EURASIAN JOURNAL OF CHEMISTRY

2023. No. 2(110)

EURASIAN JOURNAL OF CHEMISTRY

2023

No. 2(110)

April–May–June

June, 30th, 2023

CONTENTS

ORGANIC CHEMISTRY

PHYSICAL AND ANALYTICAL CHEMISTRY

INORGANIC CHEMISTRY

CHEMICAL TECHNOLOGY

ORGANIC CHEMISTRY

Oksana V. Ponomarenko[1*] [ID], Svetlana Yu. Panshina[2] [ID], Abdigali A. Bakibaev[3] [ID],
Rahmetulla Sh. Erkasov[4] [ID], Madina S. Kenzhebaj[1], Anel' S. Montaeva[1]

[1]*Sh. Ualikhanov Kokshetau University, Kokshetau, Kazakhstan;*
[2]*Karagandy University of the name of academician E.A. Buketov, Karaganda, Kazakhstan;*
[3]*National Research Tomsk State University, Tomsk, Russian Federation;*
[4]*L.N. Gumilyov Eurasian National University, Astana, Kazakhstan*
(*Corresponding author′s e-mail: oksana.ponomarenko.88@mail.ru)

Glycoluril and Its Chemical Properties

In the chemistry of heterocyclic compounds, bicyclic bisureas — glycolurils, have a special place. Glycolurils are used as a basis for the industrial production of substances that have found application in many areas of human life. The variety of glycoluril derivatives and their properties is primarily due to various substituents in the bicyclic structure. In this review, 2,4,6,8-tetraazabicyclo[3.3.0]octane-3,7-dione (glycoluril), as the main representative of bicyclic bisureas, its physico-chemical properties, and methods for the synthesis of derivatives based on it are considered. In particular, the main physico-chemical characteristics of glycoluril and the data obtained from its spectral analysis by IR, NMR spectroscopy and X-ray diffraction analysis are presented and discussed. The paper briefly outlines the known methods for the synthesis of glycolurils and related compounds, also highlights the chemical properties of glycoluril and its derivatives, as well as the ways to modify them. Coordination compounds based on N-alkylglycolurils as ligands are briefly considered. The reaction products of N-halogenation and N-acylation of glycolurils are presented and discussed. Reactions for obtaining phosphorus-, nitro- and nitroso derivatives of glycolurils; alkylation methods, Mannich reactions, thionization, alkaline hydrolysis and reduction reactions at the carbonyl group of glycolurils are also shown. There is a discussion of the macromolecules formation in the condensation reaction of glycoluril with formaldehyde as precursors for the synthesis of cucurbit[n]urils.

Keywords: glycoluril, tetraacetylglycoluril, tetramethylglycoluril, tetrachloroglycoluril, dinitrosoglycoluril, phosphorus derivatives of glycoluril, thioglycoluril.

Contents

Review Plan

Inclusion and Exclusion Criteria: This review is devoted to bicyclic bisureas, in particular glycoluril and its derivatives. The physico-chemical properties of glycoluril and methods for its modifications are described.

The review data mostly cover the publications from 1994 to 2021. However, there are older references from the period 1963–1986, as well as references to primary research sources dated on 1878, 1907, 1889 are also cited.

To write this review, we used directly our own research, as well as additional sources from databases such as Scopus, Web of Science and other online scientific search engines. The keywords used for the search were "Halogenation of Glycoluril", "Acylation of Glycoluril", "Phosphorylation of Glycoluril", "Nitration and Nitrosation of Glycoluril", "Alkylation of Glycoluril", "Thionization of Glycoluril", "Hydrolysis of Glycolurils", "Reduction of Carbamide Groups", "Trioxohexaazapropellanes". The resultant data are described in this article. No statistical methods were used in this review.

Introduction

Bicyclic bisureas, in particular 2,4,6,8-tetraazabicyclo[3.3.0.]octane-3,7-dione (glycoluril **1a**) (Fig. 1) and its derivatives occupy a special place in the chemistry of heterocyclic compounds. Substances based on glycolurils are produced on a large scale. Glycoluriles are used as components of disinfectants, pharmaceuticals [1, 2], stabilizers in polymer synthesis [3, 4], explosives and their components [5–11], etc. Recently, a new direction in the chemistry of glycolurils has been developed, namely, the creation of macrocyclic compounds with unique controllable properties. Cucurbit[n]urils, bambus[n]urils, tiara[n]urils, "molecular clamps" and supramolecular systems have been synthesized on the basis of glycoluril and its derivatives [12–19].

Glycoluril-based supramolecular systems have been proposed as materials with the properties of "molecular recognition", excipients — prolongators for drugs [20–22], components of semiconductor compositions [23] and molecular sensors for the analysis of amphiphilic components [24–27]. In addition, it is known [27–29], that glycolurils are low-toxic and do not exhibit carcinogenic properties.

1 Glycoluril as the main representative of the bicyclic bisureas

Glycoluril **1a**, as the first representative of bicyclic bisureas, was synthesized in the second half of the 19th century, and at the same time, its bicyclic structure, similar to urea, was determined [30, 31]. However, it has recently been found [32] that the glycoluril molecule **1a** is not planar and has an angle between two imidazolidinone fragments equal to 124.1° and nitrogen atoms are located equidistantly from each other. Hydrogen atoms at methine carbons are *cis*-oriented. Imidazolidinone rings are almost flat, but have a slight deviation of the C=O groups from the mean plane [32] (Fig. 1).

1a   **1a'**
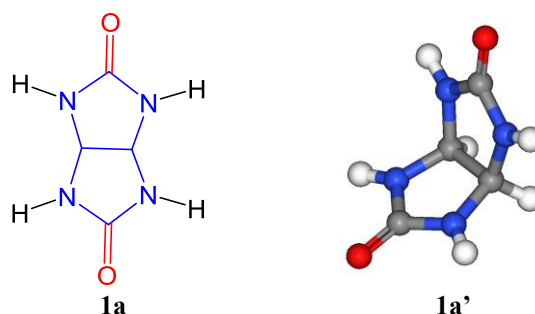
Figure 1. Structural formula of glycoluril **1a** and its spatial configuration in the crystal **1a'**
Adapted and redrawn from Ref. [32] with permission from Springer Nature

Glycoluril **1a** is a polyfunctional compound, molecule **1a** of which contains two carbamide fragments (Fig. 2). These fragments (4 donor NH-groups and 2 acceptor C=O-groups) determine the chemical properties of substance **1a**.
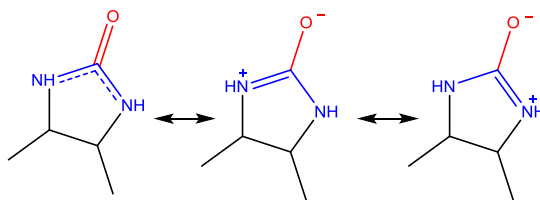
Figure 2. Resonance structures of the carbamide fragment in the glycoluril molecule **1a**

Substance **1a** is white crystals with strong intermolecular hydrogen bonds (Fig. 3). Strong internal interactions are responsible for the high melting point (360 °C with decomposition) and the low solubility of glycoluril **1a**.

a   **b**
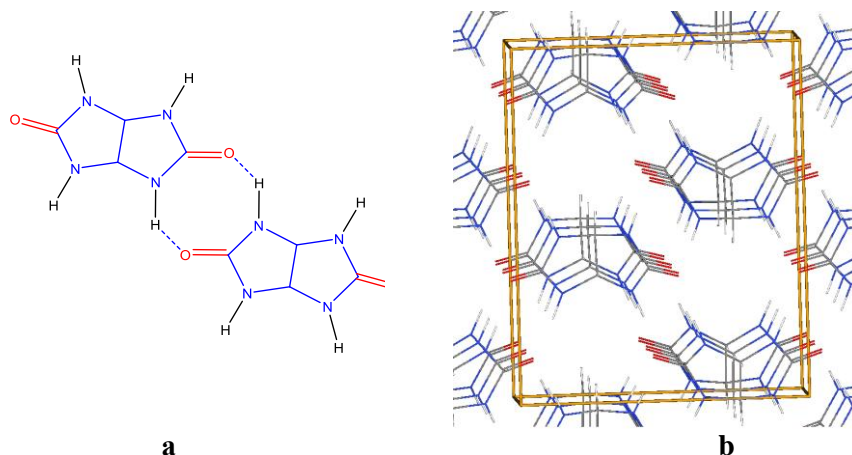
Figure 3. Hydrogen bonds in glycoluril crystals **1a**:
a — type of formation of hydrogen bonds; **b** — packing diagram of glycoluril **1a** in a crystal.
Adapted and redrawn from Ref. [32] with permission from Springer Nature

Glycoluril **1a** exists in two polymorphic forms [32] which can crystallize in water simultaneously. The effect of polymorphism of glycoluril **1a** significantly affects the physico-chemical properties. In solutions, this effect is leveled due to the equivalent effect of the solvent on the crystal structure of **1a** and does not affect the reactivity. Physico-chemical characteristics of glycoluril **1a** [33, 34] are presented in Table.

T a b l e

Physical and chemical characteristics of glycoluril 1a [33, 34]

Parameter	Value
Melting point	360°C (decomp.)
Insoluble in:	haloalkanes, alcohols, ketones, ethers
Weakly soluble in	DMSO, DMF, Ac_2O, H_2O, acids
IR spectrum, ν, cm^{-1}:	3209 (NH), 1675 (C=O).
^1H NMR (DMSO-d_6, δ, ppm):	5.24 (s. 2H, CH), 7.16 (s. 4H, NH)
^{13}C NMR (DMSO-d_6, δ, ppm):	160.3 (C=O), 64.6 (CH)

Given the specific limited solubility of glycoluril **1a** (Table), such solvents as DMSO-d_6 and D_2O are most commonly used for the identification of glycolurils by NMR methods [35].

When analyzing glycoluril **1a** in D_2O, the chemical shift of NH groups in the ^1H NMR spectrum is most often hidden due to deuterium exchange. When using the DMSO-d_6 solvent, the molecule **1a** in the ^1H NMR spectrum is shown by two chemical shifts at 5.24 ppm and 7.16 ppm, which correspond to the signals of the CH-CH and NH groups. In the ^{13}C NMR spectrum (DMSO-d_6) the structure of glycoluril **1a** is shown by peaks at δ 64.6 ppm and δ 160.3 ppm which correspond to CH-CH-carbons and carbonyl (C=O) carbons, respectively [35].

The equivalence of carbon and hydrogen atoms in the bicyclic structure indicates the spatial symmetry of the glycoluril molecule **1a**.

With the development of the chemistry of glycolurils many methods for their synthesis were created [36, 37]. The most convenient method for preparing glycolurils **1a** is the reaction of ureas **3** and their derivatives with *α*-dicarbonyl compounds **2** (Scheme 1).

1, 2, 3, 4: R^1, R^2, R^3, R^4, R^5, R^6 = H, Alk, Ar
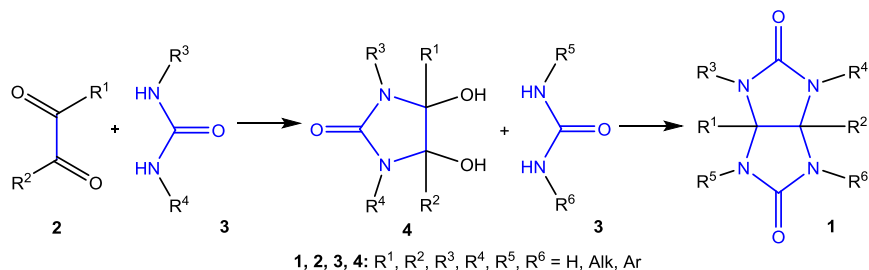
Scheme 1. Method for the synthesis of glycolurils **1** [36]

According to the mechanism of *α*-ureidoalkylation, the products of the first stage of condensation of ureas **3** and glyoxal **2** are 4,5-dihydroxyimidazolidin-2-ones **4** (DHI) – these are reaction intermediates in the further formation of glycolurils **1**. The well-known DHI **4** series and their analogues are actively used in reactions with various urea derivatives. Thus, this approach is the second method for the synthesis of various types of glycolurils **1** and their analogs (Scheme 1) [36, 37].

In accordance with the described method (Scheme 1), glycolurils unsubstituted at nitrogen atoms, glycolurils with substitution at C_1-C_5 atoms, *2-N*-substituted glycolurils, *2,4,6-N*-trisubstituted glycolurils, *2,6-N*-di-, *2,8-N*-di-, *2,4,6,8-N*-tetrasubstituted glycolurils were obtained [36, 37].

1,5-Diaminoglycoluril **1b** can be obtained from uric acid **5** by oxidation at minus 5 ºC in the presence of ammonia (Scheme 2). Based on 1,5-diaminoglycoluril **1b**, a group of Korean scientists developed a method for obtaining a tricyclic derivative of glycoluril with six NH-groups — 3,7,10-trioxo-2,4,6,8,9,11-hexaaza[3.3.3]propellane **6** (Scheme 2) [38, 39].
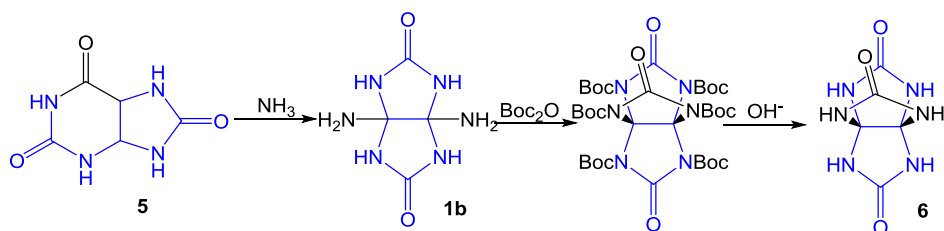
Scheme 2. The synthesis of 3,7,10-trioxo-2,4,6,8,9,11-hexaaza[3.3.3]propellane **6** [39]

Glycoluril **1a** is an active *n*-nucleophile and a significantly inactivated *p*-nucleophile. The presence of (NH–C=O) bonds with an electron-withdrawing carbonyl group makes it a less reactive base. This explains the difficulty of protonation of NH-groups, as well as the tendency for the decomposition of products formed as a result of electrophilic attack on the nitrogen atom.

In addition, the weak electrophilic properties of the carbonyl group are explained by the conjugation of two lone pairs of electrons from nitrogen atoms, which compensate for the electron-withdrawing effect of the carbonyl group. However, substance **1a** easily enters into reactions of *N*-alkylation, *N*-acylation, *N*-halogenation, *N*-nitration, *N*-nitrosation, *N*-hydroxyalkylation, etc [40].

Glycolurils form complex compounds [32]. In their structures, oxygen and nitrogen atoms are the most probable coordination centers for complexation. However, coordination through nitrogen atoms, as a rule, is sterically difficult due to its predominantly pyramidal structure, especially since this center has a reduced electron density compared to oxygen [32]. *N*-alkylglycolurils are polydentate ligands and can perform both monodentate and bidentate bridging functions with metals, with bonding through C=O groups. The bonding type depends on the coordination number of the metal atom (Fig. 4).
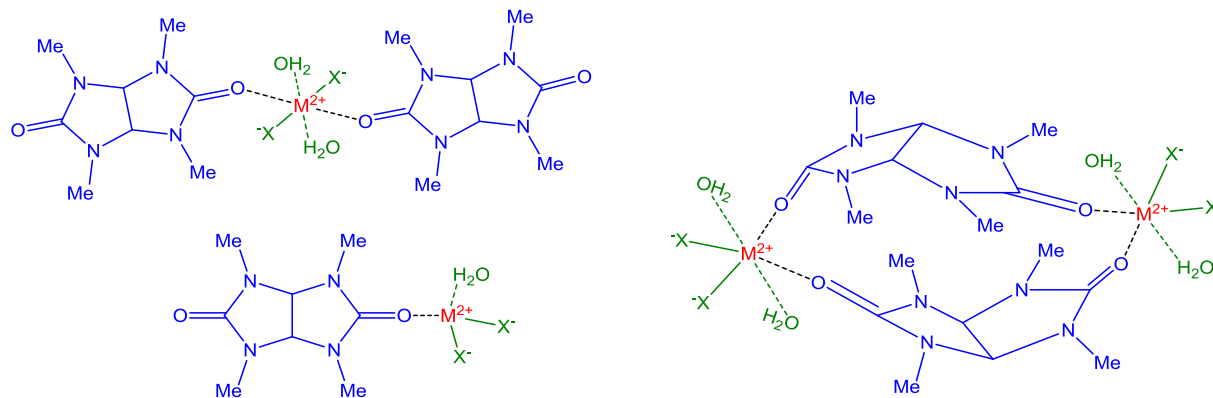
Figure 4. Coordination Options for *N*-alkylglycolurils

Thus, the structure of coordination compounds based on *N*-alkylglycolurils and salts of *d*- and *f*-metals such as Mn, Pr, Sm, Eu, and Gd were studied by X-ray diffraction analysis [32]. In all these cases, coordination compounds based on *N*-alkylglycoluril represent a centrosymmetric binuclear complex of a metal cation, where two molecules of *N*-alkylglycolurils are ligands (Fig. 5).
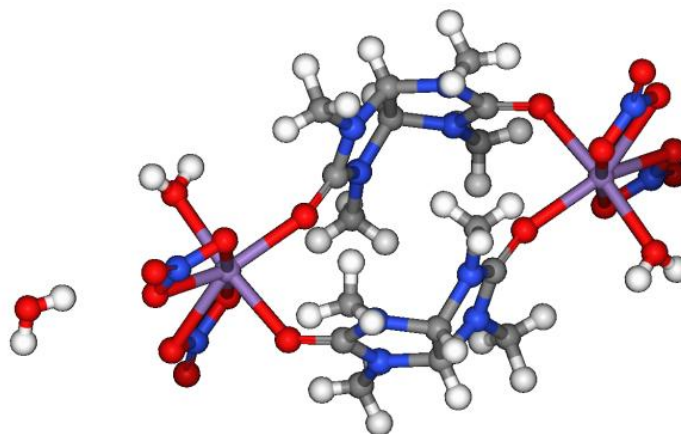
Figure 5. Centrosymmetric binuclear complex based on *N*-alkylglycoluril [41]

Derivatives of glycoluril with different numbers of substituents at *N-, C*-atoms can be synthesized both by a single-stage reaction and with step-by-step modification of the original glycoluril **1a**. The synthesis and study of the chemical properties of bicyclic bisureas allows us to reach new classes of nitrogen-containing heterocyclic compounds with various practically useful properties. Examples are such polycyclic condensed systems as cucurbit[n]urils, bambusurils, thiaraurils, "molecular clamps" [12-19], building blocks of which are glycolurils **1** (Scheme 1).

2 Halogenated glycolurils

Halogenated derivatives of glycoluril are used as oxidizers, halogenating agents, disinfectants, bleaches and detergents. The bactericidal activity of these compounds depends on the type of halogen. Thus, 2,4,6,8-tetrachloro-2,4,6,8-tetraazabicyclo[3.3.0]octane-3,7-dione (tetrachloroglycoluril) **7a** and 2,6-dichloro-2,4,6,8-tetraazabicyclo[3.3.0]octane-3,7-dione (dichloroglycoluril) **7b** are used as active chlorine atom carriers for algae control in industrial water and wastewater treatment [42].

In organic chemistry, tetrachloroglycoluril **7a** is used as a mild chlorinating agent in organic synthesis and is convenient because it has greater thermal stability than other known chloramides. The synthesis of tetrachloroglycoluril **7a** proceeds by the interaction of glycoluril **1a** and gaseous chlorine in a slightly acidic medium (Scheme 3). Substance **7a** is insoluble in water and reacts explosively with DMSO [42].
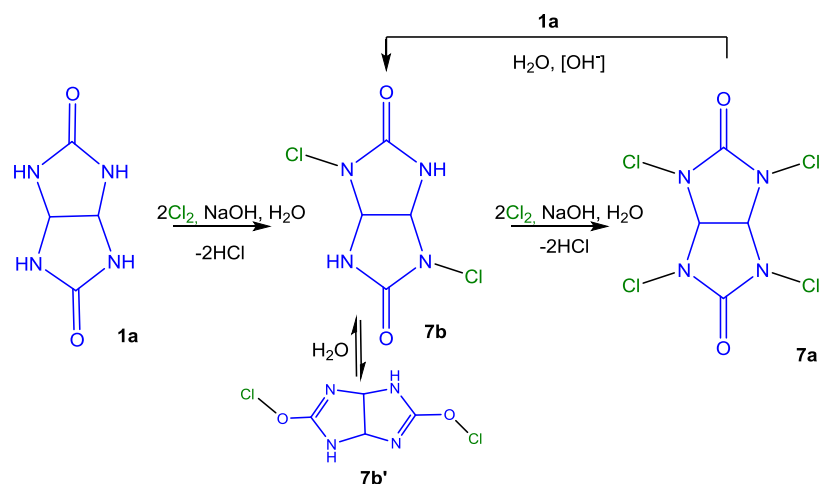
Scheme 3. The synthesis of tetrachloroglycoluril **7a** and dichloroglycoluril **7b** [42]

The highest yields of tetrachloroglycoluril **7a** were obtained in the pH range 3−7. It was shown that in the presence of an alkaline catalyst tetrachloroderivative **7a** enters into equilibrium hydrolysis with glycoluril **1a** on *N*-chlorine bond with a quantitative yield of dichloroglycoluril **7b** [43]. Dichloroglycoluril **7b** can also be selectively obtained by adjusting the amount of chlorinating reagent [43].

It is supposed [41] that dichloroglycoluril **7b** exists as two tautomeric structures **7b** and **7b'** (Scheme 3). The authors [41] attribute this assumption to the presence of three chemical shifts δ 72.8, 64.6 and 62.8 ppm of carbon atoms of the CH-CH groups and the absence of C=O carbonyl or isourea carbon signals in the ^{13}C NMR (D$_2$O) spectra. It was also found that in the study of crystalline dichloroglycoluril **7b** by IR spectroscopy, the IR spectrum contained absorption bands of carbonyl groups (1740 cm^{-1}) and bands corresponding to vibrations of ether bonds (1250 and 1100 cm^{-1}), which were absent in the IR spectrum of tetrachloroglycoluril **7a**.

A modified method for the preparation of chlorine derivatives of glycolurils **7b, d–j** at room temperature using a safe and easily processed reagent − trichloroisocyanuric acid (Scheme 4) without the use of any surfactant was proposed [44].
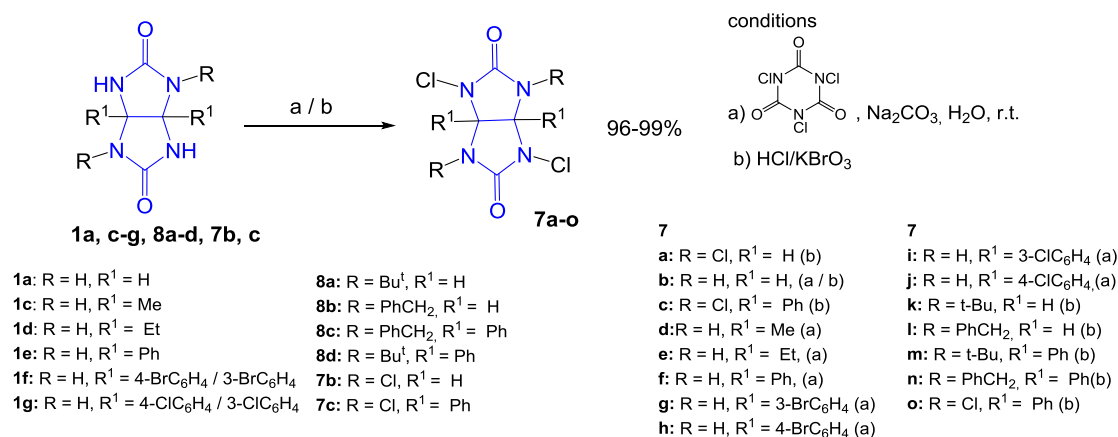
Scheme 4. A modified method for the preparation of chlorine derivatives of glycolurils

The resistance of dichloroglycoluril **7a** to the action of oxidizing agents (KBiO$_3$) made it possible to develop a preparative method for the preparation of *N*-chloroderivatives of glycolurils **7a–c, k–o** with practically quantitative yields [41]. Thus, bicyclic bisureas **1a–f, 8a–d, 7b, c** were subjected to oxidative chlorination with the HCl/KBiO$_3$ system to obtain **7a–c, k–o** (Scheme 4).

Glycoluril **1a** also reacts with molecular bromine in an alkaline medium to form tetrabrominated product **7a** (Scheme 5). Tetrabromoglycoluril **7a** has oxidizing properties and is used as additives to bactericidal, bleaching and detergents and is used as brominating agents or initiators of radical processes [43]. So, the ox-

idizing ability of halogens and hypohalides is highly dependent on the acidity of the medium, the authors [45, 46] studied interconversions in a series of *N*-halogen derivatives of glycolurils.

1a: R = H (a) Br$_2$, NaOH / H$_2$O, pH = 9...10
7a: R = Cl (b) KBr, H$_2$O, [OH$^-$]
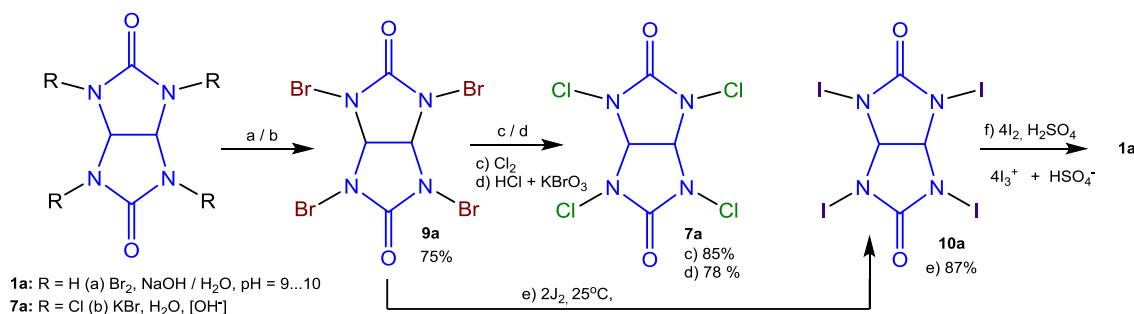
Scheme 5. Interconversions in a series of *N*-halogen derivatives of glycolurils

Based on spectral data and quantum chemical calculations, the authors of [47] determined the probability that the dissolution of tetraiodoglycoluril **8a** in sulfuric acid can lead to the formation of the triodione cation I^{3+} together with iodine-containing sulfate (IOSO$_3$H). The authors tried to prepare an I^{3+} solution by the reaction of tetraiodoglycoluril **8a** with iodine in sulfuric acid.

N-fluorine derivatives of glycolurils have not yet been obtained.

3 Acylderivatives of glycoluril

The first reports on the acetylation reactions of glycoluril **1a** with acetic anhydride to form 2,4,6,8-tetraacetyl-2,4,6,8-tetraazabicyclo[3,3,0]octane-3,7-dione (tetraacetylglycoluril) **11a** date back to the end 19th early 20th century [34].

In the development of research, it was found that the best yields of compound **11a** were achieved using catalysts (Scheme 6), [34] especially the highest yield (up to 85 %) of tetraacetylglycoluril **11a** was achieved with chloric acid.
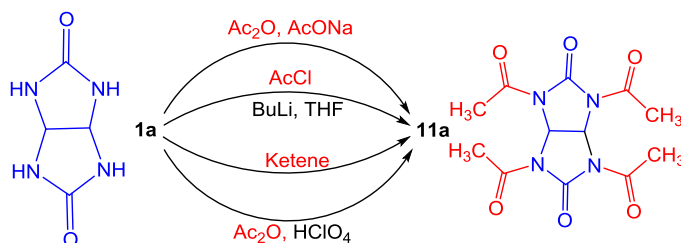
Scheme 6. Acetylation of glycoluril **1a** in the presence of various catalysts [34]

More recently, Cow Ch.N. et al. in a series of their studies [48–50] studied the reactions of *N*-acylation of the tetramethylderivative of glycoluril **12a** with further transformations (Scheme 7).
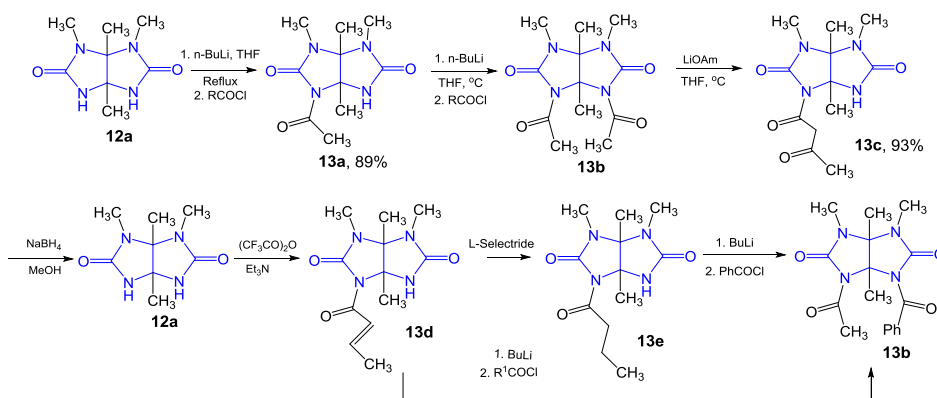
Scheme 7. The reactions of *N*-acylation of the tetramethylderivative of glycoluril **12a** [34]

Intramolecular *N-C*-transacetylation of *syn*-diacetylglycoluril **13b** by the action of lithium amylate allowed the author [51] to obtain selectively difficult-to-access *N*-acylglycolurils **13b–e** (Scheme 7). Structural features of the obtained **13b–e** compounds were determined by X-ray diffraction analysis.

Through the intermediate acylhalogenation of glycoluril **13a** with haloacylhalides **14a, b** followed by dehalogenation of *α*-haloacylglycolurils **13f–h** under the action of metals, there was carried out the synthesis of enolates [51] which underwent further condensation with another acetyl group (Scheme 8).
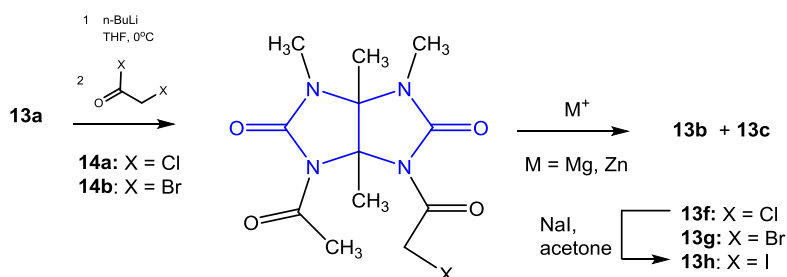
Scheme 8. Interacylation of glycolurils [34]

In the preparation of chloroacetyl derivative **13f** (42 % yield), no side reactions, such as S_N2 substitution, were observed. Bromoacetylglycoluril **13g** was similarly obtained in 44 % yield using bromoacetyl bromide **14b**. And the iodoacetyl compound **13h** was synthesized directly from glycoluril **13f** by reaction with NaI in acetone according to the general method of iodoacetylation, the resulting sodium chloride salt precipitated during the reaction [34].

Under the action of a metal atom, glycolurils **13f–h** eliminated the halogen atom and the main product of this reaction (Scheme 8) was diacetylglycoluril **13b**. When the *non*-activated Mg or Zn powder was combined with chloroacetyl glycoluril **13f** or with bromoacetyl adduct **13g** the highest yields of acetoacetate adduct **13c** were observed. It is possible that the inefficiency of the reaction is due to the poor selectivity of the metal with respect to the carbonyl groups of the substituent rather than the carbonyl groups of glycoluril **13a**. Iodoacetyl glycoluril **13h** proved to be very unstable for further reactions with it [34].

In order to expand the preparative possibilities of the *N*-acylation reactions of glycoluril **1a**, interactions **1a** with haloacylhalides **14a–c**, in particular with 1-bromoacetyl bromide **14b**, 1-chloroacetyl chloride **14a** and 3-chloropropanoic acid chloride **14c** were investigated (Scheme 9) [52].
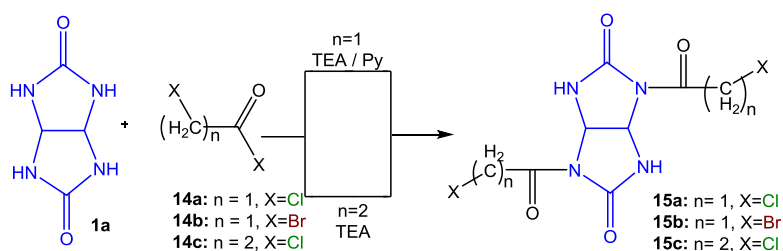
Scheme 9. *N*-haloacylation reactions of glycoluril **1a** [52]

It was shown that the reaction of glycoluril **1a** with 1-bromoacetyl bromide **14b** resulted in the formation of *bis*-acetylbromoglycoluril **15b** (yield 78 %) (Scheme 9). Under the action of 1-chloroacetyl chloride **14a** on glycoluril **1a** *bis*-acetylchloroglycoluril **15a** (yield 68 %) was formed, while using 3-chloropropanoic acid chloride **14c**, *bis*-chloropropionylglycoluril **15c** was obtained in 50 % yield.

It was shown that, despite an 8-fold excess of reagents, the authors [52] failed to obtain any tetracylhalides of glycoluril **1a** under the studied reaction conditions.

It is known that tetraacetylglycoluril **11a** undergoes hydrolysis processes, which have been studied in detail at room temperature, at pH =10 in an aqueous-alcoholic medium. Under these conditions, tetraacetylglycoluril **11a** is deacetylated stepwise to form a series of *N*-acetylglycolurils **11b–f** and final glycoluril **1a** [53] (Scheme 10). In the work [53], the directions of formation of diacetylglycolurils **11c, e** under the action of urea **3a** were proposed.
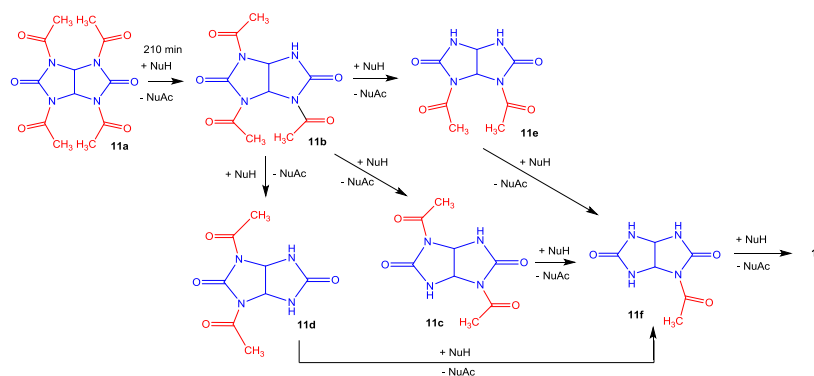
Scheme 10. The hydrolysis processes of tetraacetylglycoluril **11a** [53]

The authors of [54] successfully used the propensity to hydrolyze tetraacetylglycoluril **11a** to obtain sterically difficult-to-reach *N*-benzylglycoluril **16a** and dimer **17a** (Scheme 11). This aspect was realized through the formation of *syn*-diacetylglycoluril **11e**, where acetyl groups were used as protecting groups, which are further hydrolyzed for subsequent reactions.
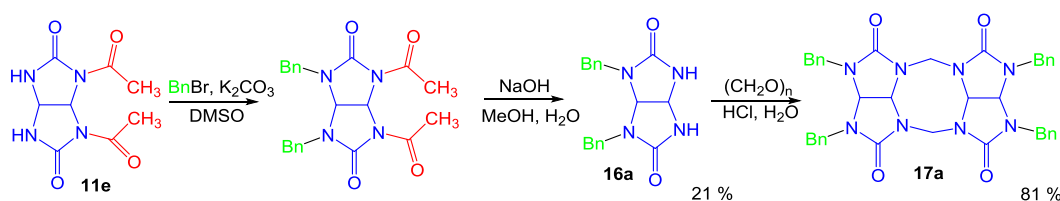
Scheme 11. The synthesis of *N*-benzylglycoluril **16a** and dimer **17a** [54]

The *N*-acetylating properties of tetraacetylglycoluril **11a** in reactions with primary aliphatic and aromatic amines were studied in detail; also a new mechanochemical method for the synthesis of some *N*-acetylamides was proposed [55]. In addition, the possibility of using **11a** as a reagent was demonstrated in separate examples of *O*-acetylation [56].

4 Phosphorus derivatives of glycoluril

Recently, the range of information on phosphorylation reactions of 2,4,6,8-tetraazabicyclo[3.3.0.]-octane-3,7-dione (glycoluril **1a**) has been expanding [57, 58]. Thus, there was investigated the transamidation reaction of glycoluril **1a** with tetraethyldiamido-*tert*-butyl phosphite [59] which resulted in the formation of glycoluril-substituted diethylamido-*tret*-butyl phosphite **18a** (Scheme 12).

The patent [60] describes in detail flame retardants — *N*-phosphorylated derivatives of glycoluril **18b** and methods for their preparation based on *N*-alkyl derivatives of glycolurils **8** (Scheme 12).
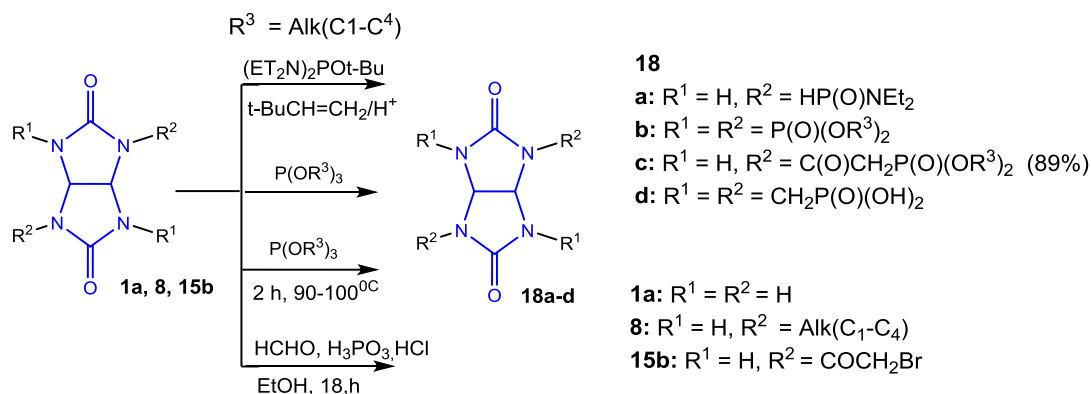
Scheme 12. The synthesis of phosphorus derivatives of glycoluril [57]

The authors of [61] carried out the acid hydrolysis of diphosphonate **18c** which was synthesized from *bis*-bromoacetylglycoluril **15b**. Hydrolysis of glycoluril **18c** leads to the corresponding diphosphonic acid.

Tetrakis(methylene phosphoric acid)glycoluril **18d** was used as an efficient catalyst for the synthesis of pyrazole-5,10-dione derivatives [62]. Substance **18d** was obtained in the "One-pot" synthesis by *N*-peralkylation of glycoluril **1a** with paraformaldehyde and phosphorous acid in refluxing ethanol (Scheme 12).

Diphosphonic complex of terraacetylglycoluril **18e** was obtained by the reaction of phosphorylation of tetraacetylglycoluril **11a** with phosphorus pentachloride (Scheme 13) [57].
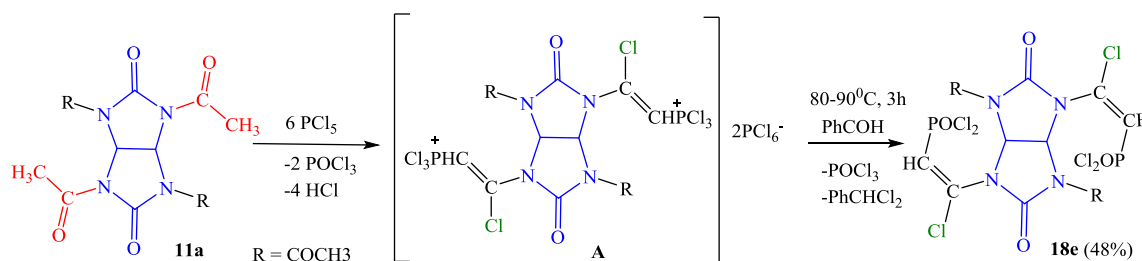
Scheme 13. The reaction of phosphorylation of tetraacetylglycoluril **11a** [57]

Probably the reaction (Scheme 13) proceeds through the addition of phosphorus pentachloride to the oxygen atom of the acetyl group **11a**, with the formation of complex **A**, which further decomposes to the product **18e**.

The phosphorylation reaction of tetra(hydroxymethyl)glycoluril **19a** with tetraethyldiamdo-*tert*-butylphosphite resulted in the formation of the oily product 2,6-di-(*N*-diethylamidomethylolphosphato)-glycoluril **18g** via the formation of intermediate **18f** (Scheme 13) [59]. Direct interaction of **19a** with phosphorus trichloride led to the isolation of a yellow crystalline substance, namely 2,6-di-(*N*-methylchloro-phosphato)-4,8-chloromethylglycoluril **18i**. Glycoluril **18i** underwent oxidation of phosphorus fragments to the pentavalent state with the formation of compound **18j** (Scheme 14).

The reaction of tetrahydroxymethylglycoluril **19a** in absolute benzene with two equivalents of dimethoxychlorophosphate and pyridine as a hydrogen chloride acceptor resulted in the formation of a mixture of products **18k** and **18l** (Scheme 14) [59].
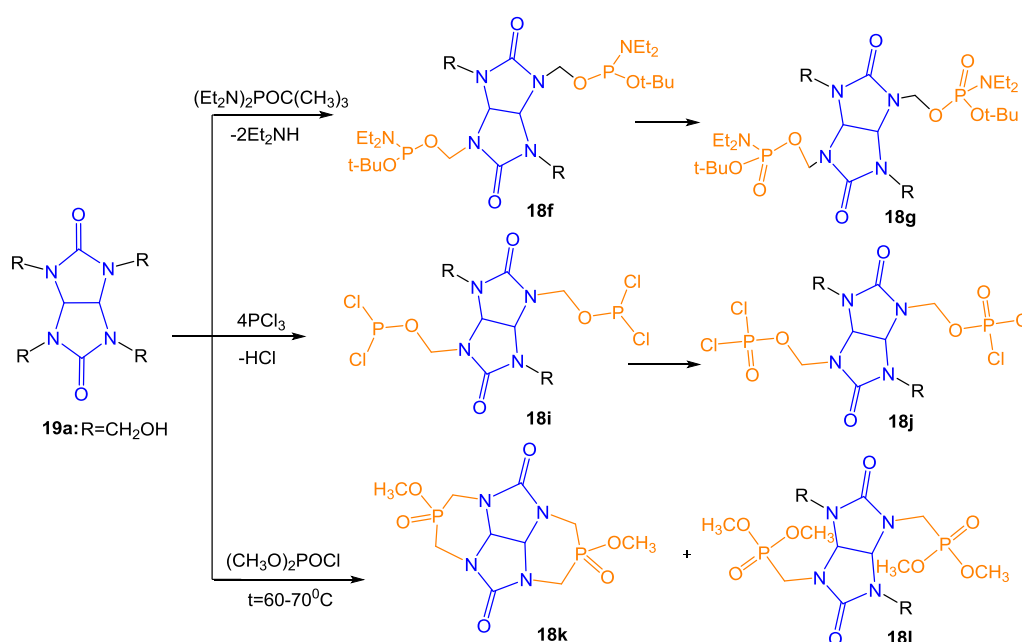
Scheme 14. The phosphorylation reaction of tetra(hydroxymethyl)glycoluril **19a** [59]

A comprehensive analysis of chemical shifts in the ^{31}P and ^{13}C NMR spectra of glycolurils and other phosphorus derivatives of bicyclic bisureas was carried out [59].

5 Nitro- and nitrosoderivatives of glycoluril

N-nitro- and *N*-nitroso derivatives of glycolurils have long attracted the attention of researchers, as they have found applications as explosives and pore-forming agents [6]. These substances, in particular 2,6-dinitro-2,4,6,8-tetraazabicyclo[3.3.0.]octane-3,7-dione (dinitroglycoluril) **20a**, were first discovered in the 1880-s [63]. And 2,4,6,8-tetranitro-2,4,6,8-tetraazabicyclo[3.3.0.]octane-3,7-dione (tetranitroglycoluril) **20b** was first obtained only in the 1970s by the French scientist Boileau [5, 64]. Further, the reactions of formation of *N*-nitroglycolurils were studied in detail [65]. Thus, in the reactions of *N*-nitration of glycoluril **1a**, the *anti-N*-dinitro-substituted product **20a** was mainly formed, but monosubstituted glycoluril **20c** was also present. Nitration of **20c** with a mixture of nitric acid and sulfuric anhydride can lead to the formation of tetranitroglycoluril **20b**. Tetranitroglycoluril **20b** was also formed by *N*-nitration of dinitroglycoluril **20a** with a mixture of nitric acid and nitric anhydride at 15 °C (Scheme 15).
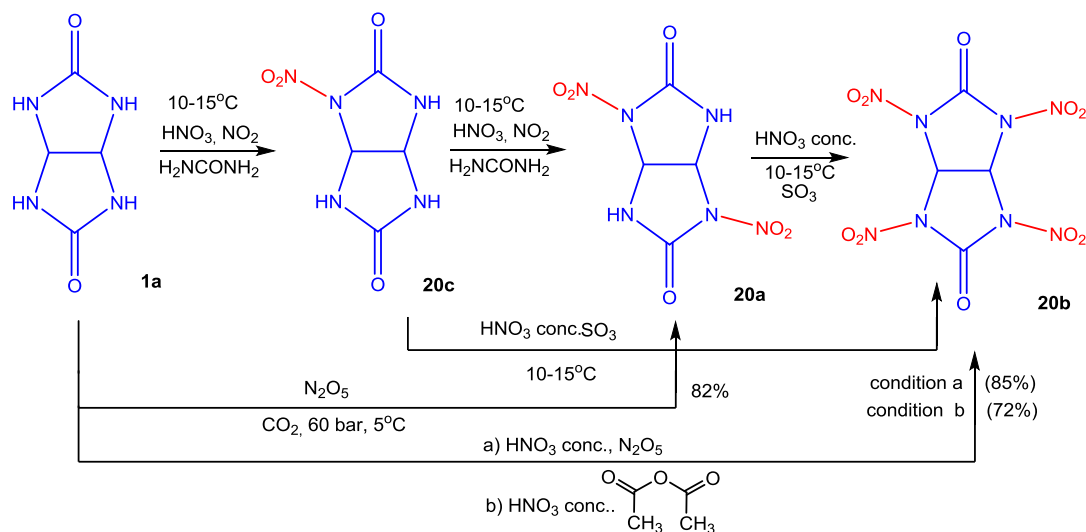
Scheme 15. The synthesis of *N*-tetranitroglycoluril **20b**

Dinitroglycoluril **20a** is synthesized selectively by *N*-nitration of glycoluril **1a** with concentrated nitric acid in the presence of urea **3a** or urea nitrate. The autoclave method [9] of synthesizing **20a** with an 82 % yield is known. It proceeds under conditions of liquid CO_2 gas at a pressure of 60 bar and a temperature of 5 °C using nitrogen pentoxide as a nitrating agent [9, 65, 66] and acetic anhydride (72 %) (Scheme 15) [67–69].

In [70], the solubility of tetranitroglycoluril **20b** in acetone, methanol, ethanol, ethyl acetate, nitromethane, and chloroform was measured in the temperature range from 295–318 K by the gravimetric method.

A number of *N*-nitroderivatives of glycoluril **20a–f** can be obtained from tetraacetylglycoluril **11a** [34]. In this reaction, mixed *N*-acetylderivatives of compounds **20d, e, f** can also be obtained in acceptable yields (Scheme 16).

Based on the known properties and methods for the preparation of glycoluril *N*-nitroderivatives, an alternative procedure [9] for the synthesis of *N*-nitroamides and *N*-nitroureanes by nitration of the corresponding *N*-alkylamides and *N*-alkylureas with nitrogen pentoxide in liquid carbon dioxide CO_2 as reaction medium was developed. The nitration procedure [9] was tested using unsubstituted glycoluril **1a** as a model.
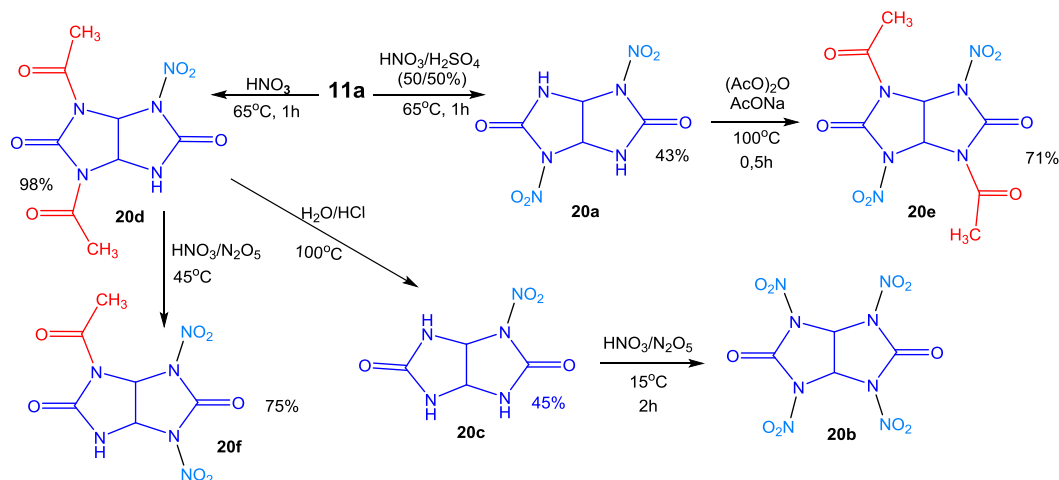
Scheme 16. Preparation of a number of *N*-nitroderivatives of glycoluril **20a-f** using tetraacetylglycoluril **11a**

The studied *N*-nitration conditions were also used in the synthesis of mono-, di-, and tetranitro-1,5-disubstituted glycolurils **20a–c, g–s** [71]. It should be noted that the authors [71] failed to obtain or observe the presence of any trinitroderivatives of glycolurils, similar to what was reported by Boileau [5] (Scheme 17).
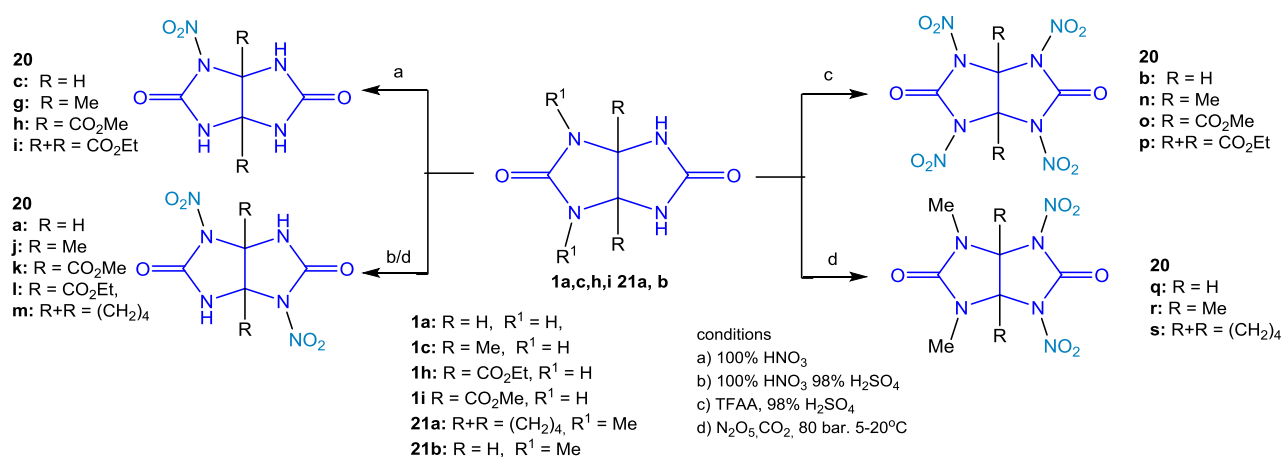
Scheme 17. Synthesis of mono-, di- and tetranitro derivatives of glycolurils

Thus, *N*-nitration of glycolurils **1a, b, g, h, 21a, b** with 100 % nitric acid leads to the exclusive formation of mononitroderivatives **20c, g–i** with a yield of more than 50 %. When using a solution of mixed acids 100 % HNO_3 and 98 % H_2SO_4, dinitroglycolurils **20a, j–m** are formed. And when using more aggressive conditions (a mixture of trifluoroacetic anhydride and 100 % HNO_3) tetranitroderivatives of glycolurils **20b, n–p** can be obtained (Scheme 17).

As a pore-forming agent in the synthesis of thermoplastic polymers, 2,6-dinitroso-2,4,6,8-tetraazabicyclo[3.3.0]octane-3,7-dione (dinitrosoglycoluril) **22a** is known [40, 72], which is obtained by *N*-nitrosation of glycoluril **1a** with sodium nitrite in the presence of a mineral acid. This reaction is accompanied by the formation of the intermediate mononitrosoglycoluril **22b** (Scheme 18).
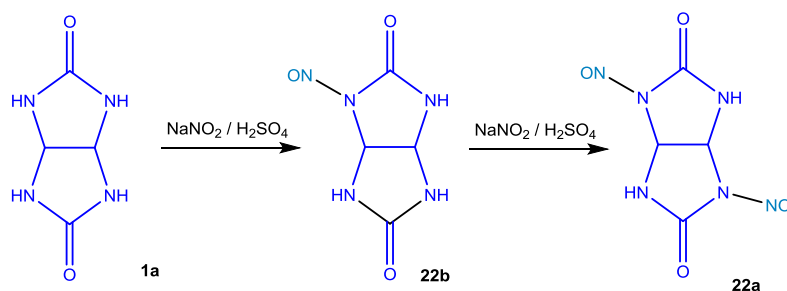
Scheme 18. *N*-nitrosation of glycoluril **1a** [41]

Mononitrosoglycoluril **22b** is always synthesized *in situ* at the first stage of nitrosation of glycoluril **1a** with alkali metal nitrites and nitric acid. A targeted isolation of mononitrosoglycoluril **22b** was carried out for further *N*-hydroxymethylation reactions [41].

In work [72], a number of *N*-nitrosoderivatives of glycoluril **22a–h** were synthesized using sodium nitrite and 1-hydroxyethylidene diphosphonic acid (HEDP) as a "green" catalyst (Scheme 19).
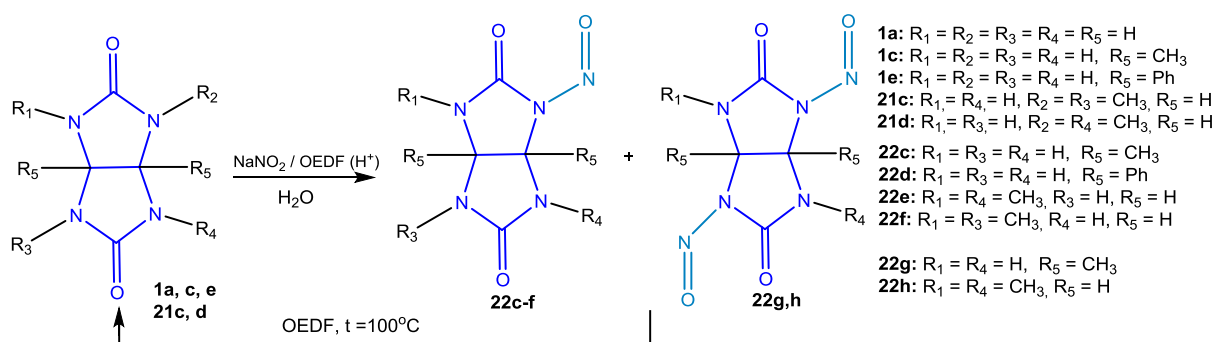
Scheme 19. The synthesis of *N*-nitrosoderivatives of glycoluril [72]

It was found [72] that when using ratios of 1 part of substrate to 2 parts of HEDP, predominantly *N*-mononitrose-substituted glycolurils **22a–f** were formed. Nitrosoglycolurils **22a–h** were isolated in 10–70 % yields. The relatively low yield of mononitrosodiphenylglycoluril **22d** was due to the low water solubility of the initial substrate **1e**.

In most cases, *N*-nitrosoderivatives are unstable and at high temperatures (100 °C) their decomposition rate increases (especially at low pH). The authors of [72] found that substances **22a–h**, when heated with 1 equivalent of HEDP, hydrolyze to the starting glycolurils **1a, c, e, 21c, d** with the destruction of the N–N bond.

6 Alkylation of glycolurils and the Mannich reaction

It is known [1, 2] that *N*-alkylsubstituted derivatives of glycoluril are pharmacologically active, which leads to a wide interest in these compounds and methods for their synthesis. However, *N*-alkylglycolurils are mainly obtained by condensation of dialkylureas **3** with 1,2-dicarbonyl compounds **2**. Direct alkylation processes at nitrogen atoms are only presented using dimethyl sulfate [73] and methyl iodide [74, 75] to obtain 2,4,6,8-tetramethyl-2,4,6,8-tetraazabicyclo[3.3.0]octane-3,7-dione (tetramethylglycoluril) **19b** (Scheme 20). Usually *N*-alkylation reactions of glycoluril **1a** are carried out in liquid ammonia at low temperatures [73–75].
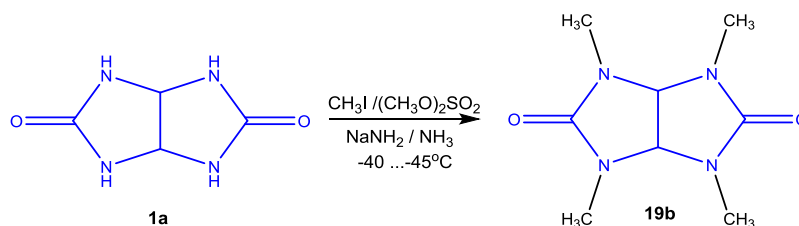
Scheme 20. *N*-Alkylation of glycoluril **1a** in the synthesis of tetramethylglycoluril **19b**

A new method for obtaining tetraalkylsubstituted glycolurils **19c–i** under milder conditions was found [76, 77]. This method describes the treatment of *N*-dialkylglycolurils **8a, b, e** with alkylating agents, namely CH_3I, C_2H_5Br, $C_6H_5CH_2Cl$, in acetonitrile in the presence of KOH base (Scheme 21).
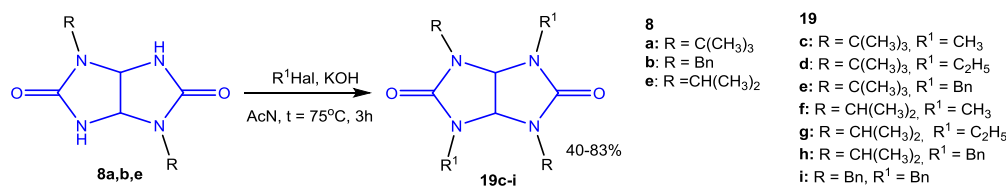
Scheme 21. Reaction of *N*-dialkylglycolurils **8a, b, e** with alkylating agents

Initially, the optimal conditions for the synthesis of dibenzyl-*ditert*-butylglycoluril **19h** with a yield of 83 % were studied. The reaction conditions under which optimal yields of tetraalkylglycolurils **19c–i** were achieved were as follows: duration 3 hours, reaction temperature 75 ºC, molar ratio 1: 4 of disubstituted glycoluril **8** to alkyl chloride, respectively. Thus, *N*-alkylation reaction of dibenzylglycoluril **8b** to obtain tetrabenzylglycoluril **19i** in 63 % yield by treating the compound with benzyl chloride in acetonitrile was successfully carried out (Scheme 21) [77].

The use of acetonitrile as a solvent contributed to obtaining better product yields, while DMSO and DMF solvents did not contribute to satisfactory yields of tetraalkylglycolurils **19c–i** [77]. The authors [77] found that benzyl chloride is the most suitable alkylating agent in the synthesis of product **19i**, in comparison with benzyl bromide. It was also shown that the *N*-alkylation reaction of 2,6-dibenzylglycoluril **8b** is currently the only way to obtain tetrabenzylglycoluril **19i**.

N-Alkylated and *N*-allylated derivatives of glycoluril are widely used [78–83].

Substance **23a** was obtained by *N*-allylation of glycoluril **1a** with allyl bromide in the presence of potassium *tert*-butoxide or with allyl chloride in the presence of sodium carbonate [78] according to Scheme 22.
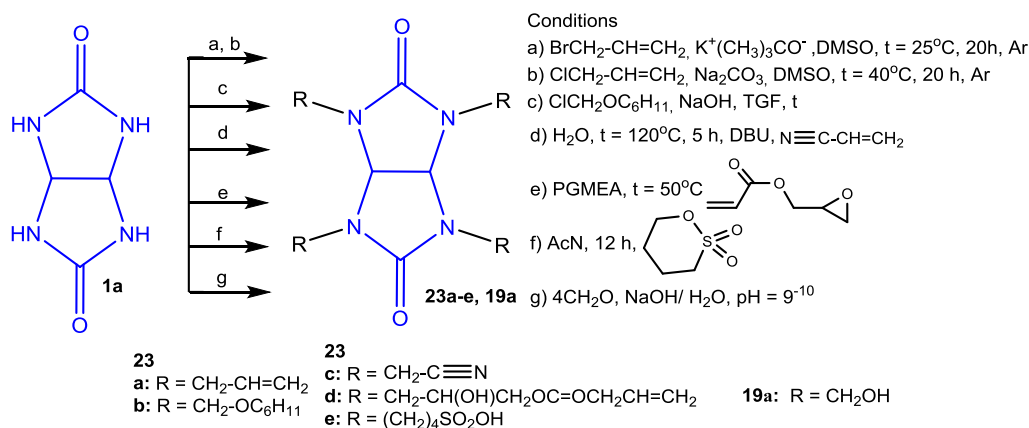
Scheme 22. Synthesis of glycolurils **23a-e**, **19a** and reaction conditions

Antireflective coating compositions for photoresistors containing a crosslinking component, tetracyclohexamethoxyglycoluril **23b,** were studied [79]. Tetrasubstitutedglycoluril **23b** was synthesized by N-alkylation of **1a** with chloromethoxycyclohexane (Scheme 22).

The synthesis of tetra(2-cyanoethyl)glycoluril **23c** with a yield of 61 % was carried out by the reaction of acrylonitrile with glycoluril **1a** in an aqueous medium in the presence of diazabicycloundecene as a base [80] (Scheme 22).

It was shown that glycoluril **1a** reacted with glycidylacrylate in 1-methoxy-2-propanol acetate at 50 °C to form tetrasubstituted glycoluril **23d** (Scheme 22) [81].

Based on bisurea **1a**, a new sulfonic derivative — tetrakis(butane-1-sulfonic acid)glycoluril **23e** was obtained in 95 % yield (Scheme 22). Substance **23e** was used as an effective catalyst for the synthesis of new spiropyrans in boiling water [82].

Thus, among *N*-hydroxyalkylglycolurils, 2,4,6,8-tetrahydroxymethyl-2,4,6,8-tetraazabicyclo[3,3,0]-octane-3,7-dione (tetrahydroxymethylglycoluril) **19a** has the greatest synthetic value. Substance **19a** was synthesized by a typical *N*-formylation reaction of glycoluril **1a** in an alkaline medium (Scheme 22) [83]. Tetrahydroxymethylglycoluril **19a** is currently widely used as a cross-linking agent in the production of glycoluril-formaldehyde resins, high-quality thermoset coatings; in the synthesis of supramolecular objects, as well as a bactericidal agent for aqueous compositions [84, 85].

In the reactions of glycoluril **1a** with formaldehyde, by changing the ratio of initial reagents, it is possible to obtain dimers **17b** and other oligomeric molecules **17c-f** [86] (Scheme 23).
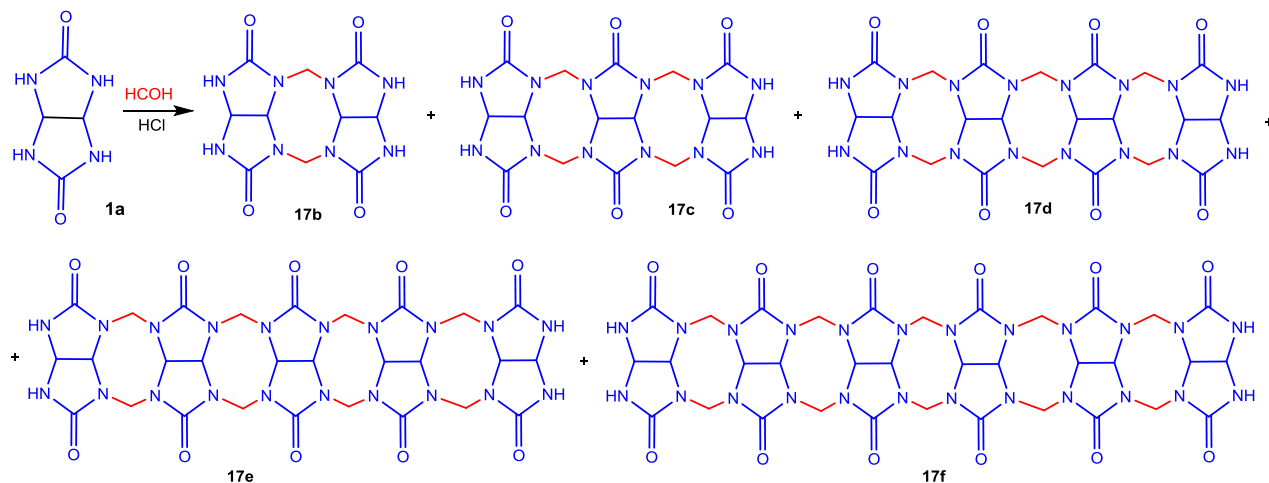
Scheme 23. Synthesis of macrocyclic derivatives of glycoluril [86]

A number of *N*-tetraaminomethylated derivatives of glycoluril **24** was obtained by the Mannich reaction, or stepwise through the intermediate tetrahydroxymethylglycoluril **19a** [41] (Scheme 24). Aminomethylated glycolurils **24** at high pH undergo decomposition at the $N–CH_2$ bond with the formation of the initial glycoluril **1a** [41].
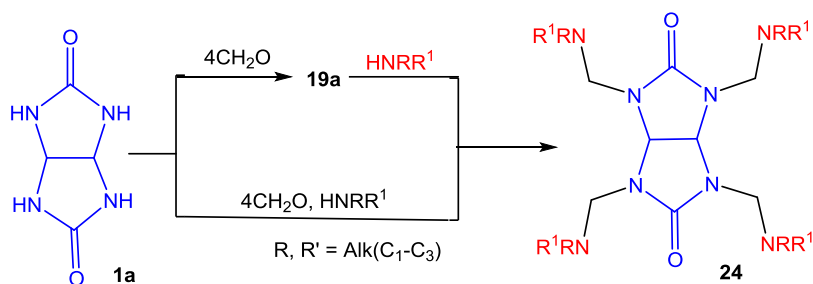
Scheme 24. The synthesis of *N*-tetraaminomethylated derivatives of glycoluril by the Mannich reaction

The reaction of glycoluril **1a** with formaldehyde became the basis for rapid progress in the chemistry of fused polycyclic glycolurils — cucurbit[n]urils, bambus[n]urils and other objects of supramolecular chemistry [86, 87]. For the synthesis of tetracyclic derivatives of glycoluril **25–30** (Scheme 25), three-component condensation of glycolurils **1a, c, e, h–j** with formaldehyde and amines was carried out [87, 88].

25 $R_1 = R_2 = H$

a: $R_3 = Me$,
b: $R_3 = (CH_2)_2OH$,
c: $R_3 = n\text{-}C_{12}H_{25}$,
d: $R_3 = n\text{-}C_{18}H_{35}$,
e: $R_3 = Cy$,
f: $R_3 = All$,
g: $R_3 = Bu$
h: $R_3 = CH_2CO_2H$
i: $R_3 = (CH_2)_5CO_2H$,
j: $R_3 = (CH_2)_{10}CO_2H$,
k: $R_3 = t\text{-}Bu$,
m: $R_3 = i\text{-}Pr$,
n: $R_3 = Et$,
o: $R_3 = (CH_2)_2CO_2H$,
p: $R_3 = (CH_2)_3CO_2H$,
q: $R_3 = CH_2CONHCH_2CO_2H$

1a: $R_1 = R_2 = H$
1c: $R_1 = R_2 = Me$
1e: $R_1 = R_2 = Ph$
1h: $R_1 = R_2 = CO_2Et$
1i: $R_1 = R_2 = CO_2Me$
1j: $R_1 + R_2 = (CH_2)_4$

26 a: $R^1 = R^2 = Me$, $R^3 = Cy$

27 $R^1 = R^2 = Ph$,
a: $R^3 = Et$,
b: $R^3 = Bn$,
c: $R^3 = Ph_2CH$

29 $R^1 = R^2 = CO_2Et$
a: $R^3 = Et$,
b: $R^3 = i\text{-}Pr$,
c: $R^3 = i\text{-}Bu$
d: $R^3 = (CH_2)_2OH$
e: $R^3 = Bn$
f: $R^3 = Bu$
g: $R^3 = Pr$
h: $R^3 = Cy$
i: $R^3 = CH_2Ar_1$,
j: $R^3 = Ar_2$

28 a: $R^1 = R^2 = CO_2Me$, $R_3 = t\text{-}Bu$

30 $R_1 + R_2 = (CH_2)_4$

a: $R^3 =$; **b:** $R^3 =$; **c:** $R^3 =$; **d:** $R^3 =$

e: $R^3 = Et$,
f: $R^3 = C_2H_4OH$,
g: $R^3 = CH_2CO_2H$
h: $R^3 = (CH_2)_2CO_2H$
i $R^3 = (CH_2)_3CO_2H$
v: $R^3 =$

r: $R^3 =$; **s:** $R^3 =$; **t:** $R^3 =$; **u:** $R^3 =$

Scheme 25. The synthesis of tetracyclic derivatives **25–30** by three-component condensation of glycolurils with formaldehyde and amines [87]

Also, the three-component condensation approach was used in the synthesis of three tetracyclic compounds **25a, b, v** by the interaction of glycoluril **1a** with formaldehyde (4 mol) and 2 mol of the corresponding amine (methylamine, 2-(hydroxyethyl)amine or 4-phenylthiazol-2-amine) (Scheme 25) [87, 88]. Tetracyclic compound **25a** was synthesized in 33 % yield and substance **25b** in 80 % yield and the yield of compound **25v** was 17 % [88].

A new method for the synthesis of compounds **25b, e, l, m** based on the condensation of glycoluril **1a** with *N,N*-bis(methoxymethyl)alkylamines (R^3 = Cy, 2-Pr, t-Bu, $(CH_2)_2OH$) in a $CHCl_3$–EtOH medium and using $SmCl_3 \cdot 6H_2O$ as a catalyst was proposed (Scheme 25) [87]. The target compounds **25b, e, l, m** were isolated by column chromatography, where the yields of **25b, e, l, m** were 70–81 %. Compound **26a** was obtained by the reaction of 1,5-dimethylglycoluril **1c** with a 30 % solution of formaldehyde and cyclohexylamine at reflux in isobutanol. Compound **27a** (in 12 % yield) was condensed using 1,5-diphenylglycoluril **1e**, formaldehyde, and ethylamine by refluxing the starting materials in MeOH solution. Compounds **27b, c** were also synthesized in 90 % yield in acetonitrile at room temperature. Dicarboxylate **28a** (90 % yield) was synthesized by the condensation reaction of dimethyl-2,5-dioxoglycoluril-3a,6a-dicarboxylate **1i**, paraformaldehyde, and *tert*-butylamine in acetonitrile at room temperature.

Three-component condensation was used mainly to obtain diethyl-2,6-dialkyl-4,8-hexaazacyclopenta[def]fluorene-3a-1,4-dicarboxylates **29a–j** (Scheme 25) by condensation of diethyl-2,5-dioxoglycoluril-3a, 6a-dicarboxylate **1h** with formaldehyde and alkyl-, aryl- or alkylarylamines [87].

In the process of synthesizing compounds **30a–i**, solutions of the corresponding amines in MeOH or MeCN were added dropwise to a mixture of glycoluril **1a** with formaldehyde. The yields of tetracyclic compounds obtained by this method varied from 10 to 76 %. To increase the yield of tetracyclic com-

pounds **30b–e** (up to 90 %), acetonitrile was used as a solvent for amines, and the reaction mixture was stirred for 12 h at room temperature [87].

The synthesis of tetracycles **30j** was carried out in various solvents. The optimal conditions found for the reactions of diethoxycarbonylglycoluril **1h** with formaldehyde and aromatic amines (aniline, *p*-toluidine, *m*-toluidine, *p*-methoxyaniline, *p*-isopropylaniline, *p*-chloroaniline, *p*-bromoaniline, *p*-iodaniline, *p*-ethynylaniline) were: dimethylformamide as a solvent and keeping the reaction mixture at 120 °C for 16 h, where the yields of products **30j** were 24–61 % (Scheme 25) [87].

Synthesis of tricyclic derivatives of glycoluril, 2a,2a^1-disubstituted 6-alkyltetrahydro-pentaaza-cyclopenta[cd]inden-1,4-diones **31-34** was carried out by three-component condensation of glycolurils **1a, e, h, j** with formaldehyde and amines or potassium of amino acid salts (in the form of solutions in an appropriate solvent) (Scheme 26) [86].

31 $R_1 = R_2 = H$
a: $R_3 = (CH_2)CO_2H$
b: $R_3 = (CH_2)_2CO_2H$
c: $R_3 = (CH_2)_3CO_2H$

32 $R_1 = R_2 = CO_2Et$,
a $R_3 = (CH_2)_2OH$,
b $R_3 = Bn$,
c $R_3 = CH_2C_6H_4Br$-p,
d $R_3 = Et$

33 $R_1 = R_2 = Ph$, $R_3 = Et$

34 $R_1 + R_2 = (CH_2)_4$,
a: $R_3 = (CH_2)_2OH$,
b: $R_3 = CH_2CO_2H$

1a: $R_1 = R_2 = H$
1e: $R_1 = R_2 = Ph$
1h: $R_1 = R_2 = CO_2Et$
1j: $R_1 + R_2 = (CH_2)_4$

2 HCOH, R^3NH_2
t, 2–12 h
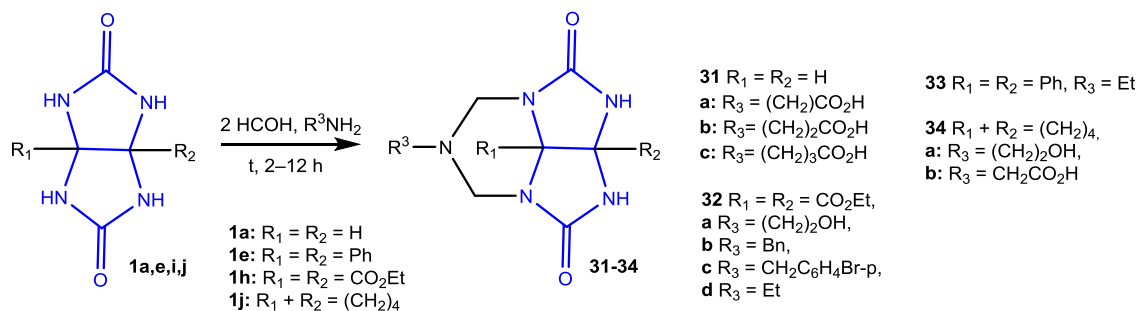
Scheme 26. The synthesis of tricyclic derivatives of glycoluril **31-34** [87]

The reactions shown in Scheme 26 were carried out in solutions of H_2O, MeOH, EtOH and MeCN. Tricyclic compounds **31a** c were obtained in 20–50 % yield by keeping the reaction mixtures at 90 °C for 2 hours. The observed products were formed by oligomerization between *N*-(hydroxymethyl)glycolurils having different degrees of hydroxymethylation at nitrogen atoms, as well as by oligomerization of these compounds with amino acids [89]. Synthesis of compound **31a** (yield 20 %) was carried out in acetonitrile, and compound **32b** in methanol. Compounds **32d** and **33** were prepared in a similar manner using EtOH instead of MeOH. The yields of products **32b–d**, **31** were 45–80 %. (Scheme 26) [87].

Tetracyclic compounds **34a, b** were isolated as side products in the reactions of compound **1j** with (2-hydroxyethyl)amine and *N*-carbamoylglycine (in the form of potassium salt) (Scheme 26) under conditions similar to those used for the synthesis of pentacyclic products **31** (H_2O, pH 9, 90 °C, 2 hours) [90].

A condensation reaction of 1-(*tert-butyl*) or 1-*cyclohexyl*glycolurils **35a, b** with formaldehyde and aliphatic amines was carried out (Scheme 27), and a result of the reaction, 2-substituted-6-alkyltetrahydro-pentaazacyclopenta[cd]inden-1,4-diones **36a–c** were obtained in high yields from 70 to 84 % (14 examples) through the formation of intermediate compounds **37** [90].

35
a: R^1 = t-Bu, R^2 = H
b: R^1 = Cy, R^2 = H
c: $R^1 = R^2 = Et$
1a: $R^1 = R^2 = H$

36
a: R^1 = t-Bu, R^2 = H
b: R^1 = Cy, R^2 = H
c: $R^1 = R^2 = Et$
d: $R^1 = R^2 = CH_2OH$ (20%)

HCOH
R^3NH_2

70 - 84%

R_3 = Et, Pr^i, Pr, Bu^n, Bu^s, Bu^t, Cy, $(CH_2)_2OH$
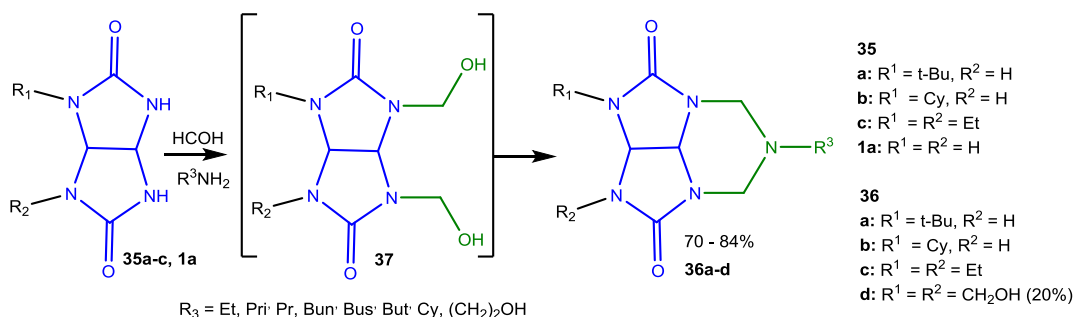
Scheme 27. The synthesis of tricyclic derivatives of glycoluril **36a–d** [87]

Condensation between glycoluril **1a**, formaldehyde and isopropylamine in acetonitrile at room temperature led to the synthesis of 2,3-bis(hydroxymethyl)-6-isopropylhexahydro-1H-2,3,4a,6,7a-pentaazacyclopenta[cd]-indene-1,4(2H)-dione **36d** in 20 % yield (Scheme 27) [87].

7 Thioderivatives of glycoluril

Mono-, and dithioglycolurils, as found in [48], can be obtained by the action of Lawesson's reagent on glycolurils. Preliminary studies of glycoluril **1a** transformations to the corresponding dithioderivative **38b** were unsuccessful, however, monothioglycoluril **38a** using Lawesson's reagent was obtained (Scheme 28).
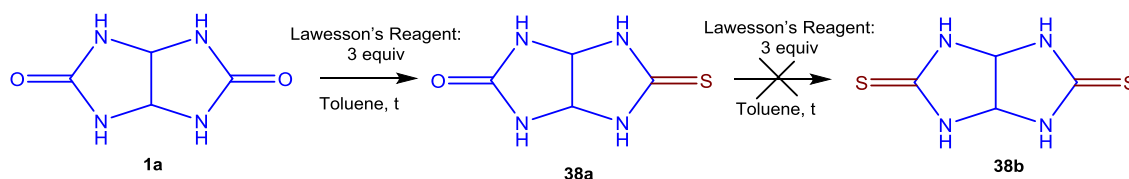
Scheme 28. The synthesis of monothioglycoluril **38a**

Heating 1,2,5,8-tetramethylglycoluryl **12a** with 1 equivalent of Lawesson's reagent readily formed thioglycoluryl **38c**, and increasing the amount of reagent to 3 equivalents led to the corresponding dithioyl derivative **38d** (Scheme 29).
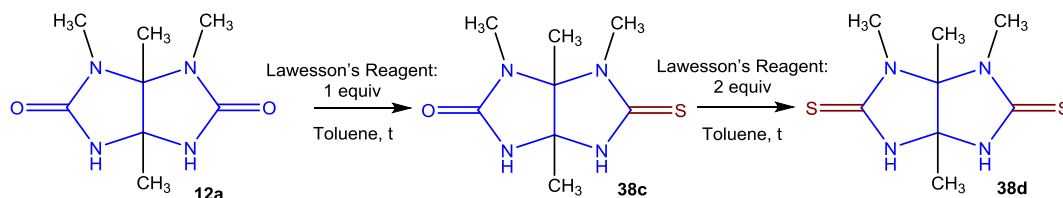
Scheme 29. Thionization of tetramethylglycoluril **12a**

Treatment of monoacylglycolurils **13a, e** with Lawesson's reagent results in highly selective monothionization of the glycoluril system with the formation of individual products **38e** or **38f**, respectively. Substitution of oxygen by sulfur occurs at 60 °C in the carbonyl group of glycoluril **13a, e**, which is the furthest away from the acylgroup of the substituent (Scheme 30).
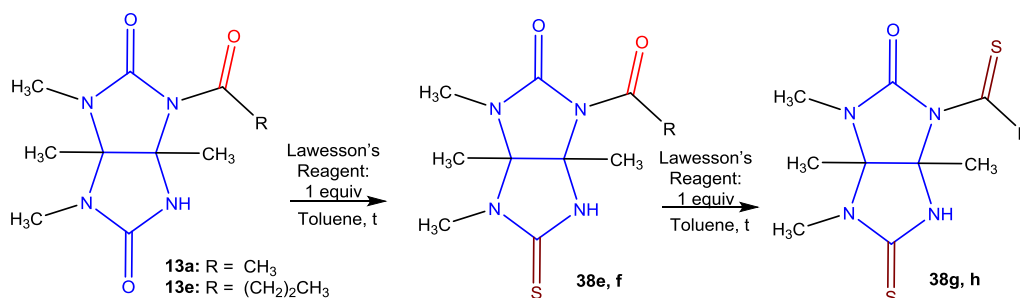
Scheme 30. Treatment of monoacylglycolurils **13a, e** with Lawesson's reagent

Alcoholysis of glycolurils **38e, f** using sodium ethoxide in THF leads to the elimination of the acetyl group, with the formation of a pure sample of glycoluril monothioderivative **38c**. The structures of thioderivatives of glycolurils were studied by X-ray diffraction analysis [48].

8 Hydrolysis of glycolurils

It is known that glycolurils are stable in a strongly acidic environment and do not enter into hydrolysis processes [91]. However, the hydrolytic properties of glycolurils under alkaline conditions are much less studied.

The authors [92] studied the ability of glycoluril **1a** and its dimethylderivatives **21c, d** to hydrolytic decomposition under alkaline conditions. It was shown that the hydrolysis of glycoluril **1a** to hydantoin **4a** at 100 °C in an alkaline medium proceeds rather quickly (10 minutes). A separate hydrolysis reaction of hydantoin **4a** under the action of aqueous NaOH leads to the formation of hydantoic acid **39a**. Dimethylderivatives of glycolurils **21c, d** react similarly (Scheme 31).
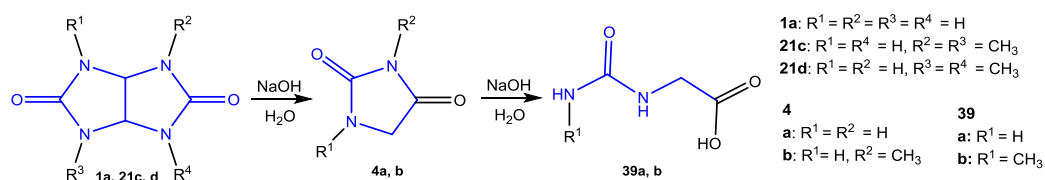
Scheme 31. Alkaline hydrolysis of glycoluril **1a** and dimethylglycoluril **21c, d** [92]

It is possible that glycolurils **21c, d** under the action of alkali at the initial stage through the elimination of the corresponding ureas form type B anions which undergo rearrangement to hydantoins **4a, b**, and the latter are easily hydrolyzed to hydantoic acids **39 a, b** (Scheme 32).
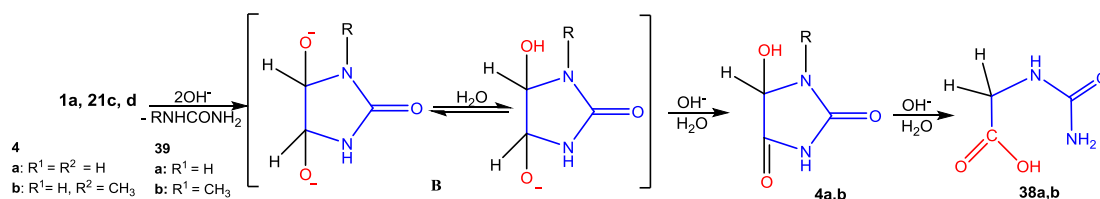
Scheme 32. Rearrangement of glycolurils **1a, 21c, d** to hydantoins **4a, b** under alkaline conditions [92]

9 Reactions on the carbonyl group of glycolurils

Reactions on the carbonyl oxygen of glycolurils in the literature are presented only by the reactions of *O*-reduction and *O*-alkylation. It is known that tetramethylglycoluril **19b** has high reaction stability to various reagents [91], and the replacement of carbonyl oxygen with a chlorine atom can sharply increase the reactivity of the latter.

The authors [93] studied the reaction between oxolyl chloride and tetramethylglycoluril **19b**, which resulted in the formation of salt **40** with a reduced carbonyl group containing chlorine atoms. The reaction was carried out in an inert atmosphere at a temperature of 80–90 °C for 6 hours (Scheme 33).
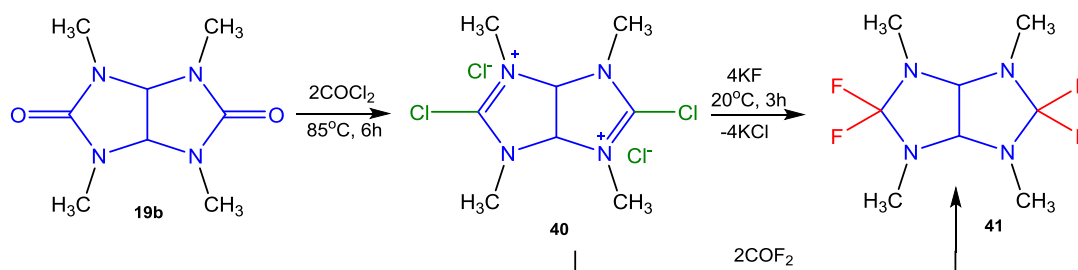
Scheme 33. The synthesis of halogen derivatives of tetramethylglycoluril **19b**

In order to obtain fluorinederivatives of glycolurils, the interaction of the chlorine salt of tetramethylglycoluril **40** with potassium fluoride in anhydrous acetonitrile was studied, as a result of which tetramethyltetrafluoroglycoluril **41** was obtained (Scheme 33). An alternative method for the preparation of tetramethyltetrafluoroglycoluril **41** is the reaction of glycoluril **40** with COF_2.

The authors [93] additionally carried out the functionalization of the chlorine-containing salt of tetramethylglycoluril **40** with amines of various structures: tetramethylguanidine, dimethyl- and diethylamine. Reactions were carried out at room temperature in anhydrous methylene chloride, where crystalline compounds **41a** c with potential biological activity were obtained (Scheme 34).
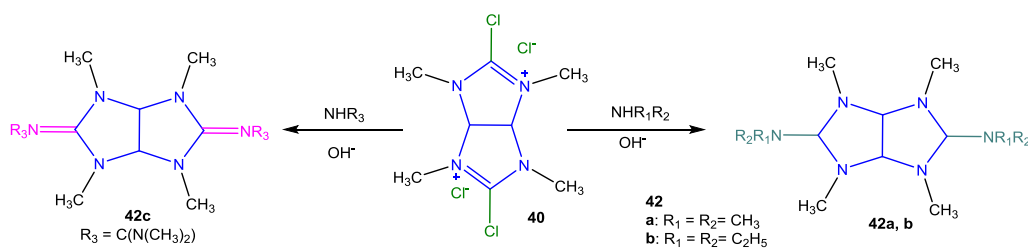
Scheme 34. The functionalization of the chlorine-containing salt of tetramethylglycoluril **39** with amines

Tetramethyltetrachloroglycoluril **40** was also obtained by the action of phosphorus oxychloride on tetramethylglycoluril **19b**. The reaction product of salt **40** with propylamine in the "One-pot" synthesis was N,N'-di(*N*-propylamino)-2,4,6,8-tetramethyl-2,4,6,8-tetraazabicyclo[3.3.0.]-octane-3,7-diylidene **42d** (Scheme 35) [57].
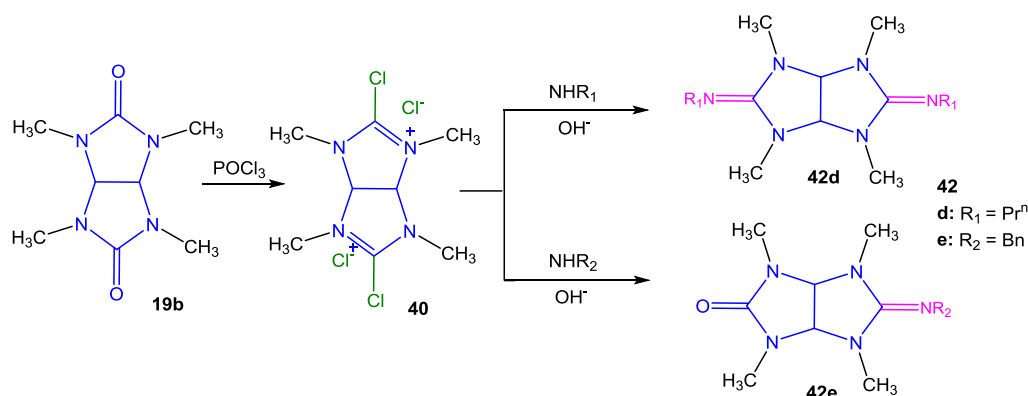
Scheme 35. The "One-pot" functionalization of the chlorine-containing salt of tetramethylglycoluril **40**

The addition of benzylamine at the second stage of the "One-pot" reaction (*in situ*) led to the formation of monosubstituted glycoluril **42e** (Scheme 35) as the main product, which can be explained by steric hindrances associated with the bulk of the benzylamine molecule and the spatial configuration of the starting compound.

Conclusion

In the present work, the main physico-chemical and spectral characteristics of glycoluril as the main representative of bicyclic bisureas were presented and discussed. The chemical properties of glycoluril and its derivatives currently known in the literature and the ways of their modification were also discussed. The review demonstrated the reactions of *N*-halogenation, *N*-acylation of glycolurils; obtaining phosphorus-, nitro- and nitroso derivatives of glycolurils; *N*-alkylation, Mannich reactions, thionization, hydrolysis and reactions at the carbonyl group of glycolurils. Methods for the preparation of macrocyclic compounds based on glycoluril were considered.

The variety of glycoluril derivatives is due to various substituents in the bicyclic structure, which directly affect the properties of the glycoluril skeleton. And the influence of substituents on the geometry and on the NMR chemical shifts of the bicyclic skeleton of glycoluril was considered in the works [33, 35].

Acknowledgments

Source of financing

References

1 Mashkovskij, M.D. (2021). Lekarstvennye sredstva: posobie dlia vrachei [Pharmaceutical products: a manual for doctors]. 15th ed. Moscow: New wave [in Russian].

2 Informatsionnyi resurs "Gosudarstvennyi reestr lekarstvennykh sredstv" [Information resource "State Register of Medicines"]. *grls.rosminzdrav.ru*. Retrieved from https://grls.rosminzdrav.ru/Grls_View_v2.aspx? routingGuid=513de8bf [in Russian].

3 Jones, F.N., Nichols, M.E., & Pappas, S.P. (2017). *Powder Coatings. In Organic Coatings*. John Wiley & Sons, Inc. https://doi.org/10.1002/9781119337201.ch28

4 Information resource "Heraeus Epurio Crosslinkers. Ultra Pure Electronic Chemicals". heraeus.com. Retrieved from https://www.heraeus.com/media/media/hec/media_hec/products_hec/ultra_pure_chemicals_pics/HEP200002_CA_Organic_Chemicals_V06_final_WEB.pdf

5 Rongzu, H., Desuo, Y., Hongan, Z., & Shengli, G.S. (2002). Qizhen Kinetics and mechanism of the exothermic first-stage decomposition reaction for 1,4-dinitro-3,6-bis(trinitroethyl)glycoluril. *Thermochimica Acta*, *389*, 65–69. https://doi.org/10.1016/S0040-6031(02)00005-9

6 Yinon, J., Bulusu, S., Axenrod, T., & Yazdekhasti, H. (1994). Mass spectral fragmentation pathways in some glycoluril-type explosives. A study by collision-induced dissociation and isotope. *Organic Mass Spectrometry*, *29*, 625–631. https://doi.org/10.1002/oms.1210291109

7 Beilfuss, W., Gradtke, R., Krull, I., & Steinhauer, K. (2006). *European Patent No. EP 1679360 (A1)*. Paris, France: European Patent Office.

8 Boileau, J., Emeury, J.-M., & Kehren, J.-P. (1984). *U.S. Patent No. 4487938 (A)*. Bethesda, MD: National Center for Biotechnology Information.

9 Boileau, J., Carail, M., Wimmer, E., Gallo, R., & Pierrot, M. (1985). Derives nitres acetyles du glycolurile. *Propellants, Explosives, Pyrotechnics*, *10*, 118–120. https://doi.org/10.1002/prep.19850100407

10 Cui, K., Xu, G., Xu, Z., Wang, P., Xue, M., & Meng, Z. et al. (2014). Synthesis and characterization of a thermally and hydrolytically stable energetic material based on N-nitrourea. *Propellants, Explosives, Pyrotechnics*, *39*(5), 662–669. https://doi.org/10.1002/prep.19850100407

11 Zharkov, M.N., Kuchurov, I.V., Fomenkov, I.V., Zlotin, S.G., & Tartakovsky, V.A.(2015). Nitraton of glycoluril derivatives in liquid carbon dioxide. *Mendeleev Communications, 25*, 15–16. https://doi.org/10.1016/j.mencom.2015.01.004

12 Lagona J., Mukhopadhyay, P., Chakrabarti, S., & Isaacs, L. (2005). The Cucurbit[n]uril Family. *Angewandte Chemie International Edition*, *44*, 4844–4870. https://doi.org/10.1002/anie.200460675

13 Khan, R., & Tuncel, D. (2019). Cucurbituril-based Functional Materials. *London: The Royal Society of Chemistry*, *1-12*(7), 289 p. https://doi.org/10.1039/9781788015950

14 She, N., Moncelet, D., Gilberg, L., Lu, X., Sindelar, V., & Briken, V. et al. (2016). Glycoluril-Derived Molecular Clips are Potent and Selective Receptors for Cationic Dyes in Water. *Chemistry A European Journal,* 22, 15270–15279. https://doi.org/10.1002/chem.201601796

15 Barrow, S.J., Kasera, S., Rowland, M.J., Barrio, J. del, & Scherman, O.A. (2015). Cucurbituril-based molecular recognition. *Chemical Review*, *115*, 12320–12406. https://doi.org/10.1021/acs.chemrev.5b00341

16 Havel, V., Babiak, M., & Sindelar, V. (2017). Modulation of Bambusuril Anion Affinity in Water. *Chemistry — A European Journal*, *23*(37), 8963−8968. https://doi.org/10.1002/chem.201701316

17 Svec, J., Necas, M., & Sindelar, V. (2010). Bambus[6]uril. *Angewandte Chemie International Edition*, *49*, 2378−2381. https://doi.org/10.1002/anie.201000420

18 Dhiman, R., Pen, S., Chandrakumar, P.K., Frankcombe, T.J., & Day, A.I. (2020). Glycoluril derived cucurbituril analogues and the emergence of the most recent example: Tiarauril. *Chemical Communications*, *56*, 2529–2537. https://doi.org/10.1039/C9CC07233K

19 Wittenberg, J.B., Costales, M.G., Zavalij, P.Y.*,* & Isaacs, L. (2011). A clipped [3]rotaxane derived from bis-nor-seco-cucurbit[10]uril. *Chemical Communications*, *47*, 9420–9422. https://doi.org/10.1039/C1CC13358F

20 Ma, D., Hettiarachchi, G., Nguyen, D., Zhang, B., Wittenberg, J.B., & Zavalij, P.Y. et al. (2012). Acyclic cucurbit[n]uril molecular containers enhance the solubility and bioactivity of poorlysoluble pharmaceuticals. *Nature Chemistry*, *4*, 503–510. https://doi.org/10.1038/nchem.1326

21 Liu, W., Lu, X., Xue, W., Samanta, S.K., Zavalij, P.Y., & Meng, Z. et al (2018). Hybrid Molecular Container Based on Glycoluril and Triptycene: Synthesis, Binding Properties, and Triggered Release. *Chemistry — An European Journal*, *24*, 14101–14110. https://doi.org/10.1002/chem.201802981

22 Gilberg, L., Zhang, B., Zavalij, P., Sindelar, V., & Isaacs L. (2015). Acyclic cucurbit[n]uril-type molecular containers: influence of glycoluril oligomer length on their function as solubilizing agents. *Organic & Biomolecular Chemistry*, *13*, 4041–4050. https://doi.org/10.1039/C5OB00184F

23 Tanaka, M., & Ishibashi, T. (2002). *U.S. Patent No. 6, 376, 157 (B1)*.

24 Assaf, K.I., & Nau, W.M. (2015). Cucurbiturils: from synthesis to high-affinity binding and catalysis. *Chemical Society Reviews*, *44*, 394–418. https://doi.org/10.1039/C4CS00273C

25 Glass, M.A., Xu, S., & Kelley, T.E. (2018). Multi-Component Sensor System for Detection of Amphiphilic Compounds. *Angewandte Chemie International Edition*, *57*, 12741–12744. https://doi.org/10.1002/ange.201807221

26 Park, K.M., Kim, J., Ko, Y.H., Ahn, Y., Murray, J., & Li, M. et al. (2018). Dye-Cucurbit[n]uril Complexes as Sensor Elements for Reliable Pattern Recognition of Biogenic Polyamines. *Bulletin of the Chemical Society of Japan*, *91*, 95–99. https://doi.org/10.1246/bcsj.20170302

27 Information resource "National Toxicology Program". *ntp.niehs.nih.gov/heraeus.com*. Retrieved from https://ntp.niehs.nih.gov/ntp/htdocs/chem_background/exsumpdf/glycoluril_508.pdf

28 Site of journal "United States Environmental Protection Agency". *epa.gov*. Retrieved from https://www.epa.gov/sites/production/files/2015-08/documents/42nd.pdf

29 Information resource "Avantor". *us.vwr.com*. Retrieved from https://us.vwr.com/assetsvc/asset/en_US/id/12277758/contents/12277758.pdf

30 Biltz, H. (1907). Zur Kenntnis der Diureine. *Berichte der Deutschen Chemischen Gesellschaft*, *40*, 4806−4816. https://doi.org/10.1002/cber.190704004138

31 Bottinger, C. (1878). Über Acetylenharnstoff'. *Berichte der Deutschen Chemischen Gesellschaft*, *11*, 1784−1787.

32 Panshina, S.Y., Ponomarenko, O.V., Bakibaev, A.A., & Malkov, V.S. (2020). Analysis of X−ray structural parameters of glycoluril and its derivatives. *Journal of Structural Chemistry*, *61*(9), 1315–1355. https://doi.org/10.1134/S0022476620090012

33 Bakibaev, A.A., Malkov, V.S., Kurgachev, D.A., & Kotelnikov. O.A. (2020). Methods of analysis of glycoluril and its derivatives. *Bulletin of the University of Karaganda — Chemistry, 100*(4), 5−34. http://dx.doi.org/10.31489/2020Ch4/5-34

34 Bakibaev, A.A., Malkov, V.S., Gorbin, S.I., Hoang, N.P., & Panshina, S.Y. (2019). Tetraatsetilglikoluril i nekotorye ego proizvodnye: sintez, svoistva i primenenie [Tetraacetylglycoluril and its derivatives: Synthesis, properties and application]. *Izvestiia vysshikh uchebnykh zavedenii. Khimiia i khimicheskaia tekhnologiia − Russian Journal Of Chemistry And Chemical Technology*, *62*, *9*, 4−19 [in Russian]. https://doi.org/10.6060/ivkkt.20196209.5924

35 Panshina, S.Y., Ponomarenko, O.V., Bakibaev, A.A., Malkov, V.S., Kotelnikov, O.A., & Tashenov, A.K. (2020). Study of glycoluril and its derivatives by ^{1}H and ^{13}C NMR spectroscopy. *Bulletin of the University of Karaganda — Chemistry*, *99*(3), 21−37. https://doi.org/10.31489/2020ch3/21-37

36 Kravchenko, A.N., Baranov, V.V., & Gaziev, G.A. (2018). Synthesis of glycolurils and their analogues. *Russian Chemical Reviews*, *87*(1), 89–108. http://dx.doi.org/10.1070/RCR4763

37 Bakibayev, A.A., Uhov, A., Malkov, V.S., & Panshina S.Yu. (2020). Synthesis of glycolurils and hydantoins by reaction of urea and 1,2-dicarbonyl compounds using etidronic acid as a "green catalyst". *Journal of Heterocyclic Chemistry*, *57*(12), 4262–4270. https://doi.org/10.1002/jhet.4132

38 Kim, Y.G., Kim, J.S., Chung, K.H., Shin, M.Y., Kim, S.H., & Ha, T.H. et al. (2017). *U.S. Patent No. 8609861*.

39 Lee, B., Shin, M., Seo, Y., Kim, M.H., Lee, H.R., & Kim, J.S., et al. (2018). Synthesis of 2,4,6,8,9,11-hexaaza[3.3.3]propellanes as a new molecular skeleton for explosives. *Tetrahedron*, *74*, 130-134. https://doi.org/10.1016/j.tet.2017.11.046

40 Bakibaev, A.A., Mamaeva, E.A., Yanovskij, V.A., Yagovkin, A.Yu., & Bystrickij, E.L. (2007). Preparativnye metody sinteza azot soderzhashchikh soedinenii na osnove mochevin [Preparative methods for the synthesis of nitrogen-containing compounds based on urea]. Tomsk: Agraf–Press [in Russian].

41 E.E. Netreba, S.V. Shabanov, A.A. Velikozhon, & N.V. Somov CCDC 1435139: Experimental Crystal Structure Determination (2017). https://dx.doi.org/10.5517/ccdc.csd.cc1k5ctx

42 Bakibaev, A.A., Yagovkin, A.Yu., & Korol`kova, S.M. (2000). Khimicheskie svoistva i primenenie imidazolin-2-onov i ikh proizvodnykh [Chemical properties and uses of imidazolin-2-ones and their derivatives]. *Izvestiia vysshikh uchebnykh zavedenii. Khimiia i khimicheskaia tekhnologiia − Russian Journal Of Chemistry And Chemical Technology*, *43*(3), 43-53 [in Russian].

43 Yagovkin, A.Yu., By`strickij, E.L., & Bakibaev, A.A. (2003). Vzaimnye prevrashcheniia N-proizvodnykh glikolurila [Mutual transformations of N-derivatives of glycoluril]. *Izvestiia Tomskogo politekhnicheskogo universiteta − Bulletin of the Tomsk Polytechnic University, 306*(3), 47-50 [in Russian].

44 Shiri, A., & Khoramabadizad, A. (2009). Preparation of several active N-chloro compounds from trichloroisocyanuric acid. *ChemInform*, *16*, 2797–2801. https://doi.org/10.1002/chin.201002041

45 Yagovkin, A.Yu. (1994). Sintez bitsiklicheskikh bismochevin oktanovogo riada i proizvodnykh imidazola s ispolzovaniem mocheviny i issledovanie ikh khimicheskikh svoistv [Synthesis of octane bicyclic bisureas and imidazole derivatives using urea and study of their chemical properties]. *Candidate's thesis*. Tomsk [in Russian].

46 Nguen, Kh.M., Chaikovskii, V.K., Filimonov, V.D., & Funk, A.A. (2012). Reaction of 1,3,5-tri-tert-butylbenzene with 2,4,6,8-tetraiodo-2,4,6,8-tetraazabicyclo[3.3.0]octane-3,7-dione. *Russian Journal of Organic Chemistry*, *48*(6), 780–782. https://doi.org/10.1134/S107042801206005X

47 Chaikovskii, V.K., Funk, A.A., Filimonov, V.D., Petrenko, T.V., & Kets, T.S. (2008) Facile iodination of aromatic compounds having electron-withdrawing substituents. Generation of triiodine cation in the system tetra-N-iodoglycoluril-iodine-sulfuric acid. *Russian Journal of Organic Chemistry*, *44*(6), 935−936. https://doi.org/10.1134/S1070428008060286

48 Cow, Ch.N., & Harrison, P.H.M. (1997). A Facile Preparation of Thioglycolurils from Glycolurils, and Regioselectivity in Thioglycoluril Template-Directed Crossed-Claisen Condensations. *The Journal of Organic Chemistry*, *62*, 8834–8840. https://doi.org/10.1021/jo9713823

49 Sun, S., Britten, J.F., Cow, Ch.N., Matta, Ch.F., & Harrison, P.H.M. (1998). The crystal structure of 3,4,7,8-tetramethylglycoluril. *Canadian Journal of Chemistry*, *76*. 301−306. https://doi.org/10.1139/CJC-76-3-301

50 Matta, Ch.F., Cow, Ch.N., & Harrison, P.H.M. (2003). Twisted amides: X−ray crystallographic and theoretical study of two acylated glycolurils with aromatic substituents. *Journal of Molecular Structure*, *660*, 81−97. https://doi.org/10.1016/j.molstruc.2003.08.005

51 Cow, Ch.N. (1997). Orchestration of reactions on glycoluril templates. *McMaster University*. http://hdl.handle.net/11375/5827

52 Panshina, S.Yu., Tajshibekova, E.K., Salkeeva, L.K., Bakibaev, A.A., & Mamaeva, E.A. (2017). Sintez i izuchenie nekotorykh bisgalogenatsilnykh proizvodnykh glikolurila [Synthesis and study of some bishalogenacyl derivatives of glycoluril]: *Vserossiiskaia nauchnaia konferentsiia s mezhdunarodnym uchastiem "Sovremennye problemy organicheskoi khimii" − Russian scientific conference with international participation "Modern Problems of Organic Chemistry"*, Novosibirsk [in Russian].

53 Khoang, N.F., Bakibaev, A.A., & Malkov, V.S. (2018). Bisdeatsetilirovanie tetraatsetilglikolurila pod deistviem mochevin [Bisdeacetylation of tetraacetylglycoluril by the action of ureas]. *Izvestiia vysshikh uchebnykh zavedenii. Khimiia i khimicheskaia tekhnologiia. − Russian Journal Of Chemistry And Chemical Technology*, *7*(7), 50-54 [in Russian]. https://doi.org/10.6060/ivkkt.20186107.5800

54 Stancl, M., Khan, M.S.A., & Sindelar, V. (2011). 1,6-Dibenzylglycoluril for synthesis of deprotected glycoluril dimer. *Tetrahedron*, *67*(46), 8937–8941. https://doi.org/10.1016/j.tet.2011.08.097

55 Bakibaev, A.A., Khoang, N.F., & Mamontov, V.V. (2018). Mechanochemical Activation of the Reaction of Tetraacetylglycoluril with Some Cyclic Primary Amines. Synthesis of Acetamides. *Russian Journal of Organic Chemistry*, *54*, 668–669. https://doi.org/10.1134/S1070428018040292

56 Arrous, S. Bakibaev, A., Hoang, P., Boudebouz, I., & Malkov, V. (2018). Convenient and Mild Method for Acylation of Betulin using Tetraacetyl Glycoluril. *International Journal of ChemTech Research*, *11*(5), 285−294. http://dx.doi.org/10.20902/IJCTR.2018.110531

57 Bakibayev, A.A., Zhumanov, K.B., Panshina, S.Yu., Gorbin, S.I., Malkov, V.S., & Tsoy, I.G., et al. (2019). Synthesis methods of phosphorylated carbamide containing acyclic and heterocyclic compounds. *Bulletin of the Karaganda university. Chemistry Series*, *3*(95), 115−157. https://doi.org/10.31489/2019ch3/115-157

58 Bakibaev, A.A., Zhumanov, K.B., Panshina, S.Yu. , Gorbin, S.I., Malkov, V.S., & Khrebtova D.V., et al (2019). NMR spectra of phosphorylated carbamide-containing heterocycles: peculiarities of chemical shifts from the valence state of the phosphorus and the size of the cycle. *News of the Academy of sciences of the Republic of Kazakhstan, Series Chemistry and Technology*, *5*(473), 100–107. https://doi.org/10.32014/2019.2518-1491.60

59 Sal`keeva, L.K. Tajshibekova, E.K., Minaeva, E.V., Sugralina, L.M., Makin, B.K., & Abajdil`din, T.S., et al. (2016). Sintez i issledovanie polifunktsionalnykh proizvodnykh glikolurila [Synthesis and research of polyfunctional derivatives of glycouril]. *Vestnik Karagandinskogo Universiteta. Seriia: Khimiia − Bulletin of the University of Karaganda — Chemistry, 84*(4),14−20.

60 Yanlin, W., & Sheng, Y. (2013). *China Patent No. 103387590 (A)*.

61 Sal'keeva, L.K., Taishibekova, E.K., Bakibaev, A.A., Minaeva, E.V., Makin, B.K., & Sugralina, L.M., et al (2017). New Phosphorylated Glycoluril Derivatives. *Russian Journal of General Chemistry*, *87*, 442−446. https://doi.org/10.1134/S1070363217030124

62 Moradi, S., Zolfigol, M., Zarei, M., Alonso, D., & Khoshnood, A. (2018). Synthesis of a Biological-Based Glycoluril with Phosphorous Acid Tags as a New Nanostructured Catalyst: Application for the Synthesis of Novel Natural Henna-Based Compounds. *ChemistrySelect*, *3*(11), 3042−3047. https://doi.org/10.1002/slct.201702544

63 Franchimont, A.P.N., & Klobbie, E.A. (1889). Contributions la Connaissance de l'Action de l'Acide Azotique sur les Corps Organiques. *Recueil des Travaux Chimiques des Pays-Bas, 8*, 283−306.

64 Boileau, J., Emeury, J.M.L., & Kehren, J.P.A. (1975). *Germany Patent No. 2435651 (A1)*.

65 Boileau, J., Wimmer, E., Carail, M., & Gallo, R. (1986). Méthodes de préparation de dérivés nitrés et nitroacétylés du glycolurile. I. *Bulletin de la Société Chimique de France*, 465−469.

66 Sherrill, W.M., & Banning, J.E. (2016). *U.S. Patent No. 9,512,127 (B2)*.

67 Born, M., Härtel, M.A.C., Klapötke, T.M., Mallmann, M., & Stierstorfer, J. (2016). Investigation on the Sodium and Potassium Tetrasalts of 1,1,2,2-Tetranitraminoethane. *Zeitschrift fur Anorganische und Allgemeine Chemie*, *642*(24), 1412–1418. https://doi.org/10.1002/zaac.201600339

68 Ha, H., Zhu, Ch., Zhang, B., Huang, H., Sun, Zh., & Wang, S. et al. (2018). *China Patent No. 105777575*.

69 Li, W., Liang, G., Cheng, X., Shi J., Wang, S., & Chen M. et al (2018). *China Patent No. 108863839*.

70 Zheng, Zh, Wang, J., Hu, Zh., & Du, H. (2017). Solubility and Dissolution Thermodynamics of Tetranitroglycoluril in Organic Solvents at 295–318 K. *Russian Journal of Physical Chemistry A*, *91*(8), 1439–1443. https://doi.org/10.1134/S0036024417080374

71 Sherrill, W.M., Johnson, E.C., & Paraskos, A.J. (2014). Synthesis and Characterization of Mono-, Di, and Tetranitrated 7,8-Disubstituted Glycolurils. *Propellants, Explosives, Pyrotechnics, 39*(1), 90−94. https://doi.org/10.1002/prep.201300048

72 Panshina, S.Yu., Bakibaev, A.A., Borodaenko, A.A., & Malkov, V.S. (2021). N-Nitrosation of Glycolurils Catalyzed by 1-Hydroxyethylidene-1,1-diphosphonic Acid. *Russian Journal of Organic Chemistry*, *57*, 1847−1852. https://doi.org/10.1134/S1070428021110063

73 Nematollahi, J., & Ketcham, R. (1963). Imidazoimidazoles. I. The Reaction of Ureas with Glyoxal. Tetrahydroimidazo[4,5-d]imidazole-2,5-diones. *The Journal of Organic Chemistry*, *28*(9), 2378−2380. https://doi.org/10.1021/jo01044a055

74 Suvorova, L.I., Eres'ko, V.A., Epishina, L.V., Lebedev, O.V., Khmel'nitskii, L.I., & Novikov, S.S. et al. (1979). The Chemistry of Bicyclic Bisureas − 2. N-Alkylation Of Bicyclic Bisureas. *Russian Chemical Bulletin*, *28*(6), 1222−1227. https://doi.org/10.1007/BF00947390

75 Nowikow, S.S., Chmelnizkij, L.I., & Lebedew, O.W. (1973). *Germany Patent No. 2237732*.

76 Sinitsyna, A.A., & Il'yasov, S.G. (2020). Alkylation Reaction in the Synthesis of Tetra-Substituted Glycoluryls. *Journal of Siberian Federal University. Chemistry*, *13*(1), 40−45. https://elib.sfu-kras.ru/handle/2311/135081

77 Sinitsyna, A.A., Il'yasov, S.G., Chikina, M.V., Eltsov, I.V., & Nefedov, A.A. (2020). A search for synthetic routes to tetrabenzylglycoluril. *Chemical Papers*, *74*, 1019–1025. https://doi.org/10.1007/s11696-019-00941-4

78 Takuma, T., Takashi, K., & Noboru, M. (2016). *U.S. Patent No. 2016289237*.

79 Takuma, T., Takashi, K., & Noboru, M. (2016). *U.S. Patent No. 2017059991*.

80 Takeshi, K., Takuma, T., Shozo, M., & Noboru, M. (2015). *Japan Patent No. 2015054843*.

81 Lee, K.W., Kwak, S.K., Lee, C., Kim, H., & Kim, S. (2014). *U.S. Patent No. 2014065543*.

82 Zarei, M., Sepehrmansourie, H., Ali Zolfigol, M., Karamian, R., & Farida, S.H.M. (2018). Novel Nano-Size And Crab-Like Biological-Based Glycoluril With Sulfonic Acid Tags As A Reusable Catalyst: Its Application To The Synthesis Of New Mono- And Bis-Spiropyrans And Their In Vitro Biological Studies. *New Journal of Chemistry*, *42*(17), 14308−14317. https://doi.org/10.1039/C8NJ02470G

83 Panshina, S.Y. Ponomarenko, O.V., Bakibaev, A.A., Sidelnikov, V.S., Kurgachev, D.A., & Malkov, V.S., et al. (2021). A study of products of tetrakis(hydroxymethyl)glycoluril dehydroxymethylation in aqueous solutions. *Russian Chemical Bulletin*, *70*, 140–147. https://doi.org/10.1007/s11172-021-3068-8

84 Panshina, S.Y., Ponomarenko, O.V., Bakibaev, A.A., & Malkov, V.S. (2020). Tetrakis(hydroxymethyl)glycoluril in N-methylenation reactions with arylamines. *Chemistry of Heterocyclic Compounds, 56*(1), 112–115. https://doi.org/10.1007/s10593-020-02633-4

85 Panshina, S.Yu., Ponomarenko, O.V., Bakibaev, A.A., & Malkov, V.S. (2019). Vydelenie i identifikatsiia oligomerov v sinteze kukurbiturilov [Isolation and identification of oligomers in the synthesis of cucurbiturils]. *Vestnik Tomskogo gosudarstvennogo universiteta. Himiia. − Bulletin of Tomsk State University. Chemistry*, *16*, 29–38 https://doi.org/10.17223/24135542/16/3 [In Russian].

86 Huang, W.H., Zavalij, P.Y., & Isaacs, L. (2008). Cucurbit[n]uril Formation Proceeds by Step-Growth Cyclo-oligomerization. *Journal of the American Chemical Society, 130*(26), 8446-8454. https://doi.org/10.1021/ja801369396

87 Barsegyan, Y.A., Baranov, V.V., & Kravchenko, A.N. (2017). Glycolurils in the synthesis of fused polyheterocyclic compounds. *Chemistry of Heterocyclic Compounds*, *53*(2), 116–122. https://doi.org/10.1007/s10593-017-2029-5

88 Salkeeva, L.K., Shibaeva, A.K., Bakibaev, A.A., Taishibekova, E.K., Minaeva, E.V., & Zhortarova, A.A., et al. (2014). New heterocycles based on tetramethylol glycoluril. *Russian Journal of General Chemistry*, *84*(2), 338−339. https://doi.org/10.1134/S1070363214020339

89 Kravchenko, A.N., Chikunov, I.E., Lyssenko, K.A., & Baranov, V.V. (2014). Glycolurils in alpha-ureido- and alpha-aminoalkylation Reactions. 3. N-(hydroxymethyl)glycolurils in Reactions with Aliphatic Amines and Amino Acids. *Chemistry of Heterocyclic Compounds*, *50*(9), 1322-1331. https://doi.org/10.1007/s10593-014-1595-z

90 Lozhkin, B.V., Sigachev, A.S., Kravchenko, A.N., Lyssenko, K.A., Kolotyrkina, N.G., & Makhova, N.N. (2007). The First Conglomerate in the Series of 2,4,6,8,10-Pentaazatricyclo[5.3.1.0$^{3.11}$]undecane-1,5-diones. *Mendeleev Communications*, *17*(2), 85−87. https://doi.org/10.1016/j.mencom.2007.03.010

91 Kravchenko, A.N. (2007) Bitsiklicheskie bismocheviny, ikh predshestvenniki i analogi: sintez, stereokhimicheskie osobennosti i svoistva [Bicyclic bisureas, their precursors and analogues: synthesis, stereochemical features and properties]. *Doctor's thesis*. Moscow [in Russian].

92 Kushcherbaeva, V.R., Bakibaev, A.A., Kurgachev, D.A., Fomchenkov, M.A., Zhaksybaeva, A.G., & Malkov, V.S. (2018). Study of hydrolytic stability of glycolurils under alkaline conditions. *Bulletin of the University of Karaganda — Chemistry*, *91*(3), 46–50. https://doi.org/10.31489/2018ch3/46-50

93 Sal'keeva, L.K., Röschenthaler, G.V., Bakibaev, A.A., Voitiček, P., Shibaeva, A.K., & Taishibekova, E.K. et al (2015). Synthesis and study of new nitrogen-containing heterocycles based on glycoluril derivatives. *Russian Journal of General Chemistry*, *85*(1), 88–91. https://doi.org/10.1134/S1070363215010156

Information about authors*

Ponomarenko, Oksana Vladimirovna (corresponding author) — PhD, Chemistry and Biotechnology Department, Sh. Ualikhanov Kokshetau University, Abai st., 76 020000, Kokshetau, Kazakhstan, e-mail: oksana.ponomarenko.88@mail.ru; https://orcid.org/0000-0002-8172-5139

Panshina, Svetlana Yur'evna — PhD, Organic Chemistry and Polymers Department, Karagandy University of the name of academician E.A. Buketov, Universitetskaya st., 28, 100024, Karaganda, Kazakhstan; e-mail: janim_svetatusik@mail.ru; https://orcid.org/0000-0001-6824-2645

Bakibaev, Abdigali Abdimanapovich — Doctor of Chemical Sciences, Professor, Leading Researcher of the Laboratory of Organic Synthesis, National Research Tomsk State University, Lenin st., 36, 634050, Tomsk, Russia; e-mail: bakibaev@mail.ru; https://orcid.org/0000-0002-3335-3166

Erkasov, Rahmetulla Sharapidenovich — Doctor of Chemical Sciences, Professor, Department of Chemistry, L.N. Gumilyov Eurasian National University, Satpayev Str., 2, 010000, Astana, Kazakhstan, e-mail: erkass@mail.ru; https://orcid.org/0000-0001-5148-8147

Kenzhebaj, Madina Sayatkyzy — 3th year Student of Chemistry Specialty, Department of Chemistry and Biotechnology, Sh. Ualikhanov Kokshetau University, Abai st., 76, 020000, Kokshetau, Kazakhstan, e-mail: madinakenzhebaj@gmail.com

Montaeva, Anel' Sabyrgel'dievna — 3th year Student of Chemistry Specialty, Department of Chemistry and Biotechnology, Sh. Ualikhanov Kokshetau University, Abai st., 76, 020000, Kokshetau, Kazakhstan, e-mail: montaeva200@gmail.com

_____

*The author's name is presented in the order: *Last Name, First and Middle Names*

Oralgazy A. Nurkenov[1,4] , Serik D. Fazylov [1,2*] , Tulegen M. Seilkhanov[3] ,
Lyazzat K. Abulyaissova[2] , Koblandy M. Turdybekov[2] ,
Tatyana S. Zhivotova[1] , Saule K. Kabieva[4] , Anel Zh. Mendibayeva[1,4]

[1]Institute of organic synthesis and coal chemistry of the Republic of Kazakhstan, Karaganda, Kazakhstan;
[2]Karagandy University of the name of academician E.A. Buketov, Karaganda, Kazakhstan;
[3]Sh. Ualikhanov Kokshetau University, Kokshetau, Kazakhstan;
[4]Karaganda Industrial University, Temirtau, Kazakhstan
(*Corresponding author`s e-mail: iosu8990@mail.ru)

Interaction of Isonicotinic Acid Hydrazide with Carboxylic Acid Anhydrides

There has been presented data on the synthesis of monoamides and cyclic imides which are derivatives of isonicotinic acid hydrazide. Cyclic anhydrides of carboxylic acids (succinic, maleic and phthalic) easily react with the hydrazide of isonicotinic acid with cycle opening, forming isonicotinoylhydrazide of dicarboxylic acids, and under more severe conditions the latter are transformed into cyclic acid imides. The structures of the synthesized compounds were studied using ^{1}H- and ^{13}C-NMR spectroscopy, as well as data from two-dimensional COSY (^{1}H-^{1}H) and HMQC (^{1}H-^{13}C) spectra. The values of chemical shifts, multiplicity and integral intensity of ^{1}H and ^{13}C signals in one-dimensional NMR spectra were determined. Homo- and heteronuclear interactions confirming the structure of the studied compounds were established using spectra in the COSY (^{1}H-^{1}H) and HMQC (^{1}H-^{13}C) formats. In the approximation of the density functional B3LYP with a base set of 6-31G(d), the enthalpy of the reactions ΔH_r in the absence and in the presence of a solvent — isopropanol (self-consistent reaction field method) were calculated quantum-chemically.

Keywords: isonicotinic acid hydrazide, anhydrides, 1,4-dicarboxylic acid monoamide, phthalic acid acylhydrazides, cyclic imides, quantum chemical calculation, heteronuclear interactions, NMR spectroscopy.

Introduction

Over the past decade, tuberculosis has once again become one of the leading causes of death in the world; at least three million people die from tuberculosis in the world every year [1, 2]. The urgency of the problem of tuberculosis incidence is associated with the spread of drug-resistant strains of the causative agent of tuberculosis, therefore there is a constant need to find new means to combat diseases caused by resistant pathological strains to improve human life. One of the main ways to find and develop new antibacterial drugs is to modify the structure of known anti-tuberculosis drugs. Isonicotinic acid hydrazide occupies a leading place in the treatment of various forms of tuberculosis and it has many different derivatives with wide variation of antitubercular activity and toxicity of compounds [3]. The introduction of an amide fragment and a carboxyl group into a molecule of biologically active substances is of practical interest, since N-substituted amides of carboxylic acids have valuable and unique properties that determine their widespread use as biologically active substances [4, 5]. It should be noted that monoamides of 1,4-dicarboxylic acids, namely succinic, maleic and phthalic acids are readily available intermediates in the synthesis of cyclic acid imides. In comparison with their predecessors, they are widely used as herbicides, insecticides, fungicides, and are also physiologically active substances of a wide spectrum of action, possessing antimicrobial, anti-tuberculosis, antiviral, antitumor and other types of activity [6–8]. As an example, we can cite such successfully used anticonvulsant drugs as ethosuximide and pufemide which are derivatives of succinimide [9, 10]. Among phthalic acid acylhydrazides obtained by the interaction of salicylic, isonicotinic and *p*-toluylic acid hydrazides, substances with high hypoglycomic activity were found [10].

In the scientific literature, work continues on the search for new tuberculostatic derivatives of isonicotinylhydrazides and methods for their preparation. Previously published works of the authors [11, 12] contain interesting data on acyl derivatives of isonicotinic acid hydrazide. Treatment of isonicotinylhydrazine with phthalic anhydride did not directly lead to the production of cyclic phthaloyl. Instead, l-isonicotinyl-2-(o-carboxybenzoyl) hydrazine was formed, which, when heated to 200–210 °C, was

cyclized to 1-isonicotinyl-2-phthaloyl hydrazine. However, the interaction of isonicotinylhydrazide with maleic anhydride under similar conditions did not lead to the production of a cyclic product, and the final product was l-isonicotinyl-2-(β-carboxyacrylyl)hydrazine [11]. In [12], the synthesis of only 4-(2-isonicotinoyl-hydrazino)-4-oxobutanoic acid obtained by the interaction of isoniazide with succinic anhydride was described and crystal structure data was given. We have previously published a number of papers on the study of hydrazine derivatives as synthons in the search for new anti-tuberculosis drugs [13–16]. Interesting results were obtained in the synthesis of β-N-(methacrylylcarbamothioyl)isonicotinohydrazide, which, when boiled in 2-propanol, underwent intramolecular cyclization to form β-N-(5-methyl-4-oxo-5,6-dihydro-4H-1,3-thiazine-2-yl)isonicotinohydrazide [17]. Previously, we also described the synthesis and study of the structure of N-(1,3-dioxoisoindoline-2-yl)isonicotinamide by the X-ray diffraction method [18]. It follows from the data obtained that bond lengths and valence angles in compounds 6 are close to the usual ones [15, 16]. The phthalimide cycle is flat with an accuracy of ±0.013 Å. The amide group is located almost perpendicular to it [19]. Thus, it follows from the analysis of the literature data that the direction of the reaction of the interaction of isonicotinic acid hydrazide with dicarboxylic acid cyclic anhydrides and the nature of the formation of final products depend on a number of factors that require further research.

Experimental

The ^{1}H and ^{13}C NMR spectra were taken on a JNM-ECA 400 spectrometer (399.78 and 100.53 MHz, respectively) using DMSO-d_6 solvent. The reaction progress and purity of the obtained compounds were monitored by thin-layer chromatography on Silufol UV-254 plates in isopropyl alcohol-benzene-ammonia systems (10:5:2). The plates were developed with iodine vapors. The reaction products were isolated by recrystallization or column chromatography on aluminum oxide. All solvents used in the work were purified and absolutized in accordance with known methods [13–17].

The general method of obtaining isonicotinoylhydrazide of 1,4-dicarboxylic acids (1–3). To 0.02 mol of isonicotinic acid hydrazide in 20 ml of ethanol or ethyl acetate, a solution of 0.02 mol of 1,4-dicarboxylic acid anhydride (succinic, maleic and phthalic) in 20 ml of ethanol or ethyl acetate was added with stirring. The reaction mixture was stirred at 40–50 °C for an hour. The precipitate was filtered out and recrystallized from ethanol.

4-(2-Isonicotinoylhydrazinyl)-4-oxobutanoic acid (1). The yield of product **1** is 86.1 %; melting point is 245–246 °C. ^{1}H NMR spectrum (DMSO-d$_6$), δ, ppm: (J, Hz): 2.42–2.43 m (4H, H-11, 11, 12, 12), 7.72 d (2H, H-3, 5, ^{3}J 6.0), 8.70 d (2H, H-2, 6, ^{3}J 6.0), 10.01 br.s. (1H, H-8), 10.61 br.s. (1H, H-9), 11.86 br.s. (1H, H-14). ^{13}C NMR spectrum, δ, md: 28.64 (C-12), 29.26 (C-11), 121.83 (C-3, 5), 140.01 (C-4), 150.91 (C-2, 6), 164.43 (C-7), 171.00 (C-10), 174.06 (C-13).

4-(2-Isonicotinoylhydrazinyl)-4-oxobut-2-enoic acid (2). The yield of product **2** is 96 %; melting point is 183–184 °C.

2-(2-Isonicotinoylhydrazinocarbonyl)benzoic acid (3). The yield of product **3** is 21 %; melting point is 219–220 °C. ^{1}H NMR spectrum (DMSO-d$_6$), δ, ppm: (J, Hz): 7.85 d (2H, H-3, 5, ^{3}J 6.0), 7.92–7.99 m (4H, H-12, 13, 14, 15), 8.82 d (2H, H-2, 6, ^{3}J 6.0), 11.70 br. s (1H, H-18), 11.70 s (2H, H-8, 9). ^{13}C NMR spectrum, δ$_C$, ppm: 121.99 (C-3, 5), 124.52 (C-12, 14), 129.95 (C-11, 16), 136.02 (C-13, 15), 138.21 (C-4), 151.31 (C-2, 6), 164.74 (C-7, 17) and 165.61 (C-10).

General method of obtaining phthalimides (4-6). A mixture of 0.01 mol of isonicotinic acid hydrazide and 0.01 mol of phthalic anhydride in 25 ml of dimetylformamide was mixed at a temperature of 120 °C in a flask with a Dean-Stark apparatus for 3.5 hours. After cooling to room temperature, the reaction mixture was diluted with 100 ml of distilled water with intensive stirring. One day later, the white precipitate was filtered out, washed with ethanol and dried at room temperature.

N-(2,5-dioxopyrrolidine-1-yl)isonicotinamide (4). The yield of product **4** is 28.7 %; melting point is 156–157 °C. ^{1}H NMR spectrum, δ, ppm: (J, Hz): 2.49 s (4H, H-11ax, 11eq, 12ax, 12eq), 7.34 d (2H, H-3, 5, ^{3}J 4.8), 8.71 d (2H, H-2, 6, ^{3}J 4.8), 9.37 c (1H, H-9). ^{13}C NMR spectrum, δ, ppm: 28.77 (C-11, 12), 121.86 (C-3.5), 139.97 (C-4), 151.07 (C-2, 6), 164.53 (C-7), 171.30 (C-10, 13).

N-(2,5-dioxo-2,5-dihydro-1H-pyrrol-1-yl)isonicotinamide (5). The yield of product **5** is 22.1 %; melting point is 288–290 °C. ^{1}H NMR spectrum, δ, ppm: (J, Hz): 3.62 br. s (1H, H-8), 6.63 d (1H, H-11, ^{3}J 15.6), 6.99 d (1H, H-12, ^{3}J 15.6), 7.34 d (2H, H-3, 5, ^{3}J 4.0), 8.73 d (2H, H-2, 6, ^{3}J 4.0). ^{13}C NMR spectrum, δ, ppm: 132.01 (C-11), 134.53 (C-12), 162.85 (C-13), 164.39 (C-11), 121.88 (C-3, 5), 139.97 (C-4), 150.98 (C-2, 6), 166.65 (C-7).

N-(1,3-dioxoisoindoline-2-yl)isonicotinamide (6). The yield of product **6** is 32 %, melting point is 220-221 °C. ^{1}H NMR spectrum, δ, ppm: (J, Hz): 7.85 d (2H, H-3, 5, ^{3}J 5.0), 8.82 d (2H, H-2, 6, ^{3}J 6.0), 7.92–7.95 m (2H, H-13, 14), 7.97-8.00 m (2H, H-12, 15), 11.72 br. s (1H, H-8). ^{13}C NMR spectrum, δC, ppm: 121.96 (C-3, 5), 124.52 (C-12, 15), 129.94 (C-11, 16), 136.03 (C-13, 14), 138.20 (C-4), 151.32 (C-2, 6), 164.73 (C-7), 165.62 (C-10, 17).

Quantum chemical calculations were carried out using Gaussian and GaussView software packages [20, 21]. The equilibrium geometry and vibrational frequencies of the molecules were calculated in the approximation of the density functional B3LYP with a base set of 6-31G(d). The enthalpy of reactions in the presence of a solvent-isopropanol at a temperature of 50 °C was calculated by the method of a self-consistent reaction field. Similar calculations were performed for reactions in the gas phase in the absence of a solvent at a temperature of 25 °C.

Results and Discussion

Continuing our search in this direction [13–18], we carried out our own research and studied the reaction of the interaction of succinic, maleic and phthalic anhydrides with isonicotinic acid hydrazide. We conducted the research in two stages. At the first stage, under the conditions we studied, cyclic anhydrides of dicarboxylic acids in mild conditions easily reacted with isonicotinic acid hydrazide with the opening of the oxolan cycle. The reaction of cyclic dicarboxylic acid anhydrides with isonicotinic acid hydrazide was carried out at a reagent ratio of 1:1 in an isopropanol medium at a temperature of 50–60 °C for 1.5 hours. It was established that under the conditions studied, the reactions under consideration can proceed with the formation of the corresponding monoamides of dicarboxylic acids **1-3** (Scheme 1).
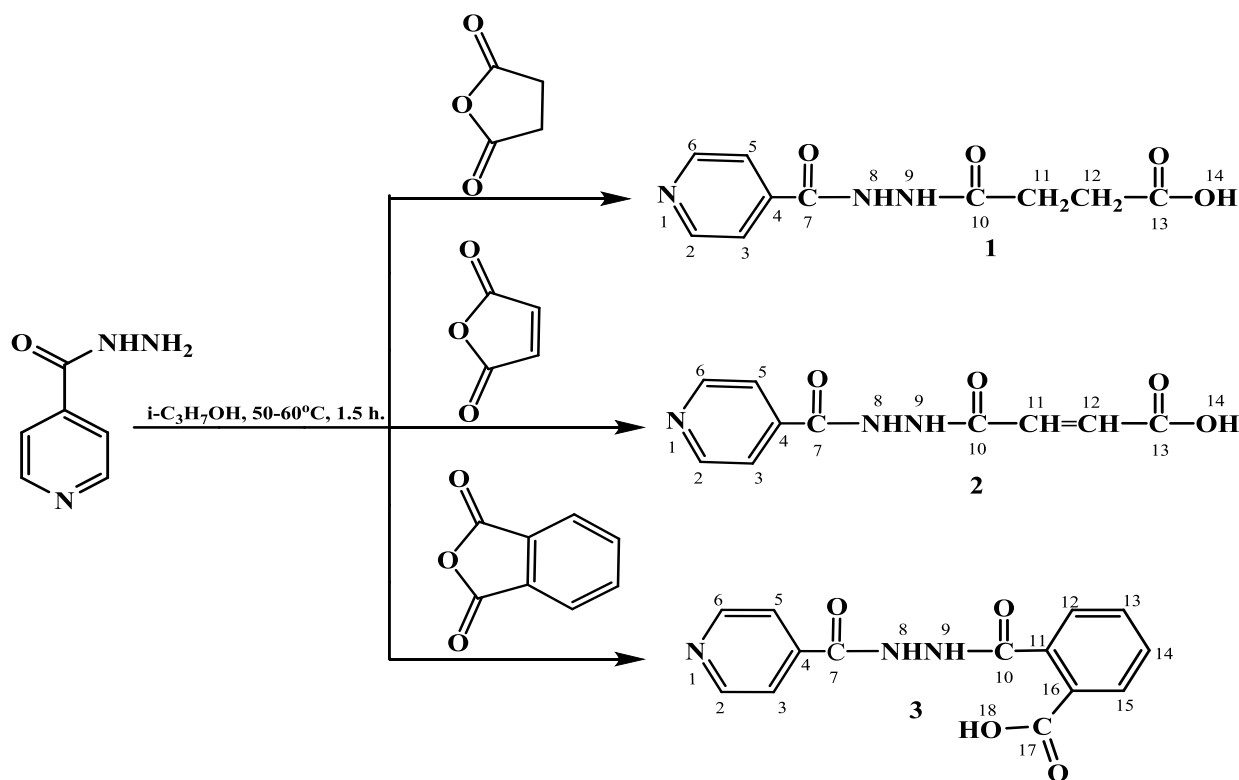
Scheme 1. Modification of isonicotinic acid hydrazide with anhydrides under mild conditions

The resulting compounds **1-3** after recrystallization are white crystalline substances that are soluble in most organic solvents, except for saturated hydrocarbons.

At the second stage, we conducted direct reactions of the interaction of the above initial reagents under harsh conditions. The reaction of succinic, maleic and phthalic acid anhydrides with isonicotinoyl hydrazide was carried out at a reagent ratio of 1:1 in a dimethylformamide solvent at a temperature of 120 °C for 3.5–5 hours (Scheme 2). The reactions proceeded in one stage, the yields of the obtained cyclic imides **4-6** ranged from 20 to 45 %.
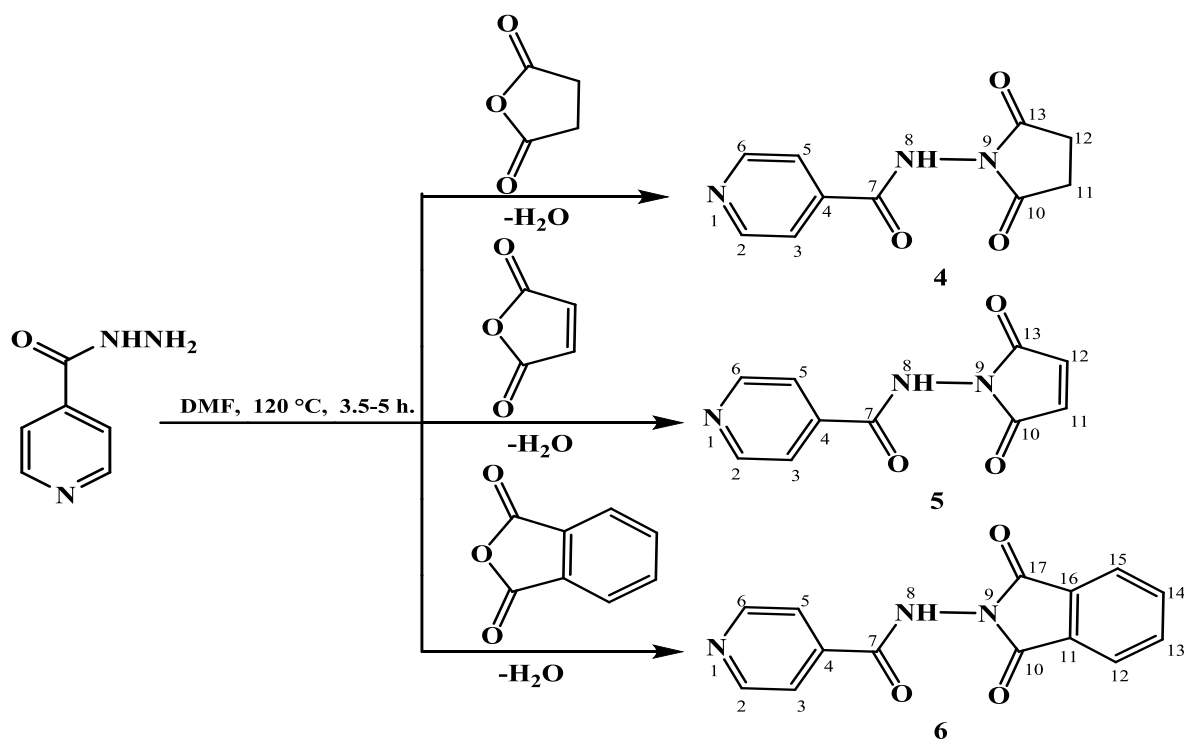
Scheme 2. Modification of isonicotinic acid hydrazide with anhydrides under severe conditions

The structures of synthesized compounds **1-6** were confirmed by ^{1}H- and ^{13}C-NMR spectroscopy, as well as by data of two-dimensional NMR, namely COSY (^{1}H-^{1}H) and HMQC (^{1}H-^{13}C) spectroscopy which allow establishing spin-spin interactions of homo- and heteronuclear nature (Fig. 1). The observed correlations in molecules **3** and **6** are shown in the diagrams. In the ^{1}H-^{1}H COSY spectra of compounds **3** and **6**, spin-spin correlations are observed through three bonds of aromatic protons of the pyridine cycle H^{3,5}-H^{2,6} cross-peaks with coordinates at 7.84, 8.82 and 8.81, 7.85. Heteronuclear interactions of protons with carbon atoms through a single bond were established using ^{1}H-^{13}C HMQC spectroscopy for the pairs present in the compound: H^{3,5}-C^{3,5} (7.84, 121.95), H^{13,14}-C^{13,14} (7.93, 124.50), H^{12,15}-C$^{12<}$ (7.93, 136.05) and H^{2,6}-C^{2,6} (8.82, 151.31).
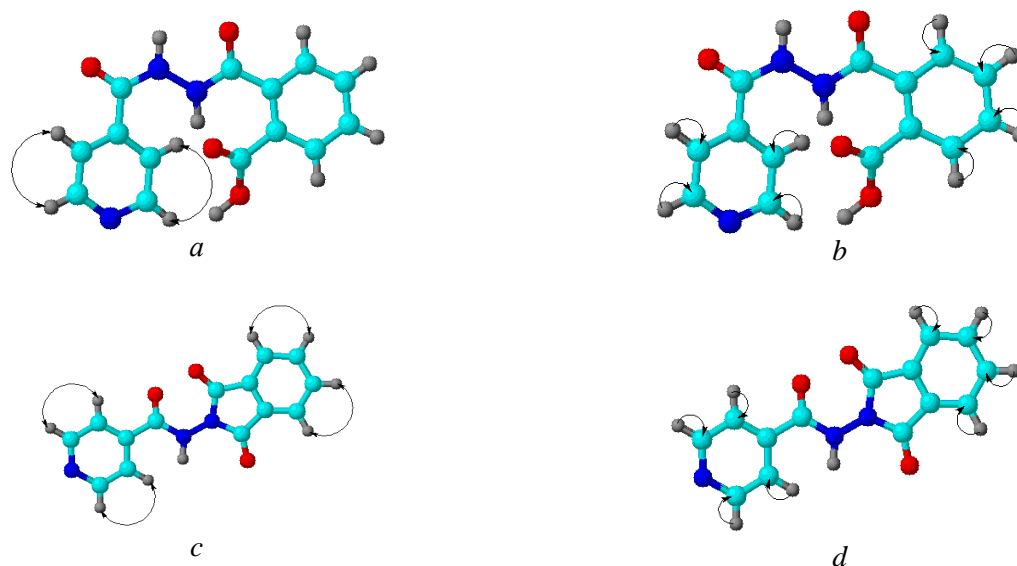
Figure 1. Correlation schemes in the COSY (*a*) and HMQC (*b*) spectra of compounds **3** and **6**

In order to theoretically substantiate the influence of the medium (solvent) on the reaction nature, quantum chemical calculations were carried out to determine the enthalpy of reactions ΔH_r. The change in the enthalpy of the system during the reaction is known to be calculated as the difference between the enthalpy of the products and the initial components. Quantum-chemically determined thermodynamic properties of molecules take into account the contribution of vibrations and rotations of the molecule. In the approximation of the density functional B3LYP with a base set of 6-31G(d) [20, 21], the enthalpy of the reactions ΔH_r in the absence and in the presence of a solvent — isopropanol (self-consistent reaction field method) were calculated quantum-chemically. Figure 3 shows 3D configurations of reagent molecules and reaction products, their thermochemical data are given in Table 1.
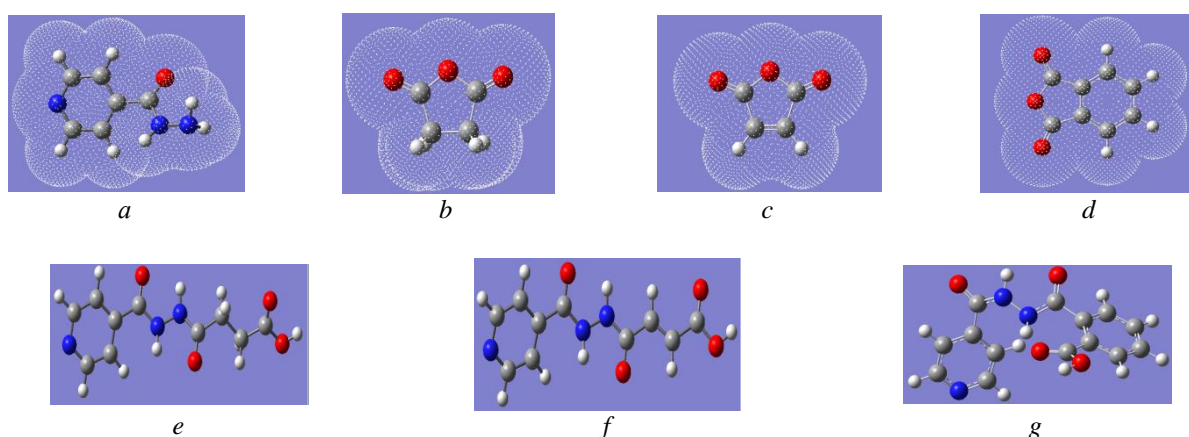
a — isonicotinic acid hydrazide; *b* — succinic anhydride; *c* — maleic anhydride; *d* — phthalic anhydride; *e* — product 1; *f* — product 2; *g* — product 3 (B3LYP/6-31G(d) method)

Figure 3. 3D configurations of reagent molecules and reaction products (the most stable conformations)

Table 1

**Theoretical values of the enthalpy of formation ($\Delta_f H$, A.U.) of compounds
(B3LYP/6-31G(d) method, t = 25 °C)**

Reaction Condition	Reagent 1	Reagent 2	Product	ΔH, kJ/mol
Reaction 1				
	isonicotinic acid hydrazide	succinic anhydride	Product **1**	
In the absence of a solvent	-472.159598	-380.436910	-852.613950	-45.80
In the presence of isopropanol	-472.169012	-380.447614	-852.628478	-31.12
Reaction 2				
	isonicotinic acid hydrazide	succinic anhydride	Product **2**	
In the absence of a solvent	-472.159598	-379.227522	-851.408555	-56.29
In the presence of isopropanol	-472.169012	-379.236069	-851.420723	-41.08
Reaction 3				
	isonicotinic acid hydrazide	succinic anhydride	Product **3**	
In the absence of a solvent	-472.159598	-532.839917	-1005.004921	-7.62
In the presence of isopropanol	-472.169012	-532.848465	-1005.021645	-10.95

As follows from the calculated data, the solvent lowers the enthalpy of the reaction (by the absolute value) which is explained by the limited mobility of molecules in the condensed phase. The consequence of this is a decrease in the activation energy, and since the reactions are exothermic, the transition states in structure should be closer to the initial reagents.

Conclusions

The results showed that the direction of the reaction of the interaction of isonicotinic acid hydrazide with cyclic dicarboxylic acids anhydrides depends on the reaction conditions. Under mild reaction condi-

tions, the corresponding isonicotinoylhydrazides of dicarboxylic acids are formed in high yield, while under harsher conditions the latter are transformed into imides of cyclic acids. In the approximation of the density functional B3LYP with a base set of 6-31G(d), the enthalpies of the reactions ΔH_r in the absence and in the presence of a solvent were calculated quantum-chemically. According to the calculated data, the solvent lowers the enthalpy of the reaction (by the absolute value), which is explained by the limited mobility of molecules in the condensed phase. The consequence of this is a decrease in the activation energy, and since the reactions are exothermic, the transition states in structure will be closer to the initial reagents.

References

1 Sadykova, L., Berikova, E., Kurakbayev, K. & Maimakov, T. (2017). Out-patient TB care in Kazakhstan. *European Journal of Biomedical and Life Sciences*, *1*, 43-48. http://dx.doi.org/10.20534/ELBLS-17-1-43-48

2 Sadykova, L., Abramavicius, S. & Maimakov, T. (2019). A retrospective analysis of treatment outcomes of drug-susceptible TB in Kazakhstan. *Medicine, 98*(26), 1-14. https://doi.org/10.1097/MD.0000000000016071

3 Rollas, S. & Küçükgüzel, S.G. (2007). Biological activities of hydrazone derivatives. *Molecules, 12*, 910-1939. https://doi.org/10.3390/12081910

4 Popolek, L., Biernasik, A., Berecka, A., Gumieniczek, A., Malm, A. & Wules, M. (2018). New hydrazide-hydrazones of isonicotinic acid: synthesis, lipophilicity and in vitro antimicrobial screening. *Chemical biology and drug design*, *91*(4), 915-923. https://doi.org/10.1111/cbdd.13158

5 Shah, M.A., Uddin, A., Shah, M.R., Ali, I., Ullah, R., Hannan, P.A. & Hussain H. (2022). Synthesis and characterization of novel hydrazone derivatives of isonicotinic hydrazide and their evaluation for antibacterial and cytotoxic potential. *Molecules, 27,* 6776. https://doi.org/10.3390/molecules27196770

6 Popolek, L. & Biernasik A. (2016). Design, synthesis and in vitro antimicrobial activity of hydrazide-hydrazones of 2-substitutea acetic acid. *Chemical biology and drug design, 88*(6), 873-883. https://doi.org/10.1111/cbdd.12820

7 Ahmed, A., Molvi, I.K., Patel, M.H., Ullah, R. & Bari A. (2020). Synthesis of novel 2,3,5-tri-substituted thiazoles with anti-inflammatory and antibacterial effect causing clinical pathogens. *Journal of infection and public health, 13*, 472-479. https://doi.org/10.1016/j.jiph.2020.02.002

8 Fazylov, S.D., Nurkenov, O.A., Seilkhanov, T.M., Karipova, G.Zh., Van Hecke, K., Suleimen, Ye.M. & Gazaliyev, A.M. (2019). Synthesis of hydrazone derivatives of isonicotinic acid under microwave activation conditions. *Bulletin of the University of Karaganda Chemistry, 3*(95), 44-37. https://doi.org/10.31489/2019Ch3/37-44

9 Naveen Kumar, H., Jummat, F. & Asmawi, M.Z. (2014). Synthesis and evaluation of isonicotinoyl hydrazone derivatives as antimycobacterial and anticancer agents. *Medicinal Chemistry Research*, *23,* 269-279.   https://doi.org/10.1007/s00044-013-0632-2

10 Dolzhenko, A.V., Kolotova, N.V., Kozminykh, V.O., Syropyatov, B.Ya., Kotegov, V.P., Godina, A.T. & Rudakova, G.V. (2003). Substituted amides and hydrazides of dicarboxylic acids. Part 13. Synthesis and hypoglycemic activity of some substituted amides and acylhydrazides of phthalic acid. *Pharmaceutical Chemistry Journal, 37*(1), 19. https://doi.org/10.1023/A:1023642927375

11 Gao, P. & Wei, Y. (2013). Efficient oxidative cyclization of N-acylhydrazones for the synthesis of 2, 5-disubstituted 1,3,4-oxadiazoles using t-BuOI under neutral conditions. *Heterocyclic Communications*, *19,* 113-119. https://doi.org/10.1515/hc-2012-0179

12 Doriguetto, A.C., Silva, C., de Paula, H.T., Rando, D.G., Ferreira, E.I. & Ellena, J.A. (2003). 4-(2-Isonicotinoylhydrazino)-4-oxobutanoic acid. *Acta Crystallographica*, 288-289. https://doi.org/10.1107/S1600536803002435

13 Nurkenov, O.A., Karipova, G.Z. & Seilkhanov, T.M. (2019). Synthesis and intramolecular heterocyclization of selected isonicotinic acid thiocarbazides. *Russian Journal of General Chemistry*, *89,* 1923-1926. https://doi.org/10.1134/S1070363219090299

14 Fazylov S.D., Nurkenov, O.A., Zhivotova, T.S. & Zhurinov, M. Zh. (2013). Ispolzovanie proizvodnykh gidrazina kak sintonov pri poiske novykh protivotuberkuleznykh preparatov [The use of hydrazine derivatives as synthons in the search for new anti-tuberculosis drugs]. *Doklady Natsionalnoi akademii nauk Respubliki Kazakhstan — Reports of the National Academy of Sciences of the Republic of Kazakhstan, 2,* 48-57 [in Russian].

15 Ibraev, M.K., Takibaeva, A.T., Gazaliev, A.M., Nurkenov, O.A. & Fazylov, S.D. (2006). Synthesis of isonicotinic acid vinyloxyethylthiosemicarbazide. *Russian Journal of Applied Chemistry, 79*, 327-328. https://doi.org/10.1134/S1070427206020327

16 Turgunalieva, D.M., Dilbaryan, D.S., Vasilchenko, A.S., Nurkenov, O.A., Fazylov, S.D., Karipova, G.Zh., Seilkhanov, T.M. & Kulakov, I.V. (2022). Synthesis and antibacterial activity of hydrazones of Isonicotinic and salicylic acids based on acetyl derivatives of coumarin and benzo[g][1,3,5]oxadiazocine. *Bulletin of the University of Karaganda Chemistry, 108*(4), 25-34. https://doi.org/10.31489/2022Ch4/4-22-2

17 Kulakov, I.V., Turdybekov, D.M., Nurkenov, O.A., Issabaeva, G.M., Makhmutova, A.S., Turdybekov, K.M. & Fazylov, S.D. (2009). Synthesis and crystal structure of β-N-(5-methyl-4-oxo-5,6-dihydro-4H-1,3-thiazin-2-yl)isonicotinohydrazide. *Chemistry of heterocyclik compounds*, 45(9), 1117-1120. https://doi.org/10.1007/s10593-009-0398-0

18 Turdybekov, K.M., Nurkenov, O.A., Fazylov, S.D., Makhmutova, A.S., Turdybekov, D.M., Seilkhanov, T.M. & Arinova, A.E. (2021). Synthesis, crystal structure, and conformation of N-isonicotinoylphthalimide. *Journal of structural chemistry*, *62*, 1279. https://doi.org/10.1134/S0022476621080151

19 Gondolova, G.G., Medzhidov, A.A. & Fatullaeva, P.A. (2018). Complexes of Fe(II) and Mn(II) with *N*-(2-Hydroxy-benzamido)phthalimide. *Russian Journal of General Chemistry, 88*(3), 607-609. https://doi.org/10.1134/S1070363218030362

20 Frisch, M.J., Trucks, G.W. & Schlegel, H.B. (2009). Gaussian 09, Revision A.02. Wallingford CT.

21 Leye, P.O., Khenchaf, A. & Pouliguen, P. (2016). The Gaussian beam summation and the Gaussian launching methods in scattering problem. *Journal of electromagnetic analysis and applications, 8*, 219-225. https://doi.org/10.4236/jemaa.2016.810020

Information about authors*

Nurkenov, Oralgazy Aktayevich — Doctor of chemical sciences, head of laboratory "Synthesis of biologically active substances", LLP "Institute of Organic Synthesis and Coal Chemistry of the Republic of Kazakhstan", Alikhanov street, 1, 100008, Karaganda, Kazakhstan; e-mail: nurkenov_oral@mail.ru; https://orcid.org/0000-0003-1878-2787;

Fazylov, Serik Drahmetovich (*corresponding author*) — Doctor of chemical sciences, chief scientific officer, LLP "Institute of Organic Synthesis and Coal Chemistry of the Republic of Kazakhstan", Alikhanov street, 1, 100008, Karaganda, Kazakhstan; e-mail: iosu8990@mail.ru; https://orcid.org/0000-0002-4240-6450;

Seilkhanov, Tulegen Muratovich — Candidate of chemical sciences, Head of the laboratory of engineering profile of NMR spectroscopy, Ualikhanov university, Abaya street, 76, 020000, Kokshetau, Kazakhstan; e-mail: tseilkhanov@mail.ru; https://orcid.org/0000-0003-0079-4755

Abulyaissova, Lyazzat Kablashevna — Candidate of chemical sciences, professor, Karagandy University of the name of academician E.A. Buketov, Universitetskaya, 28, 100024, Karaganda, Kazakhstan; *e-mail:* abu.lyazzat@gmail.com; https://orcid.org/0000-0002-7530-3378;

Turdybekov, Koblandy Muboryakovich — Doctor of chemical sciences, professor, Karagandy University of the name of academician E.A. Buketov, Karaganda, Universitetskaya, 28, 100024, Kazakhstan; e-mail: xray-phyto@yandex.kz; https://orcid.org/0000-0001-9625-0060;

Zhivotova, Tatyana Sergeevna — Doctor of chemical sciences, academic secretary, LLP "Institute of Organic Synthesis and Coal Chemistry of the Republic of Kazakhstan", Alikhanov street, 1, 100008, Karaganda, Kazakhstan; e-mail: zhts2004@mail.ru; https://orcid.org/0000-0002-0793-4653

Kabieva, Saule Kazjanovna — Candidate of chemical sciences, Head of department of "Chemical Technology and Ecology", Karaganda Industrial University, Republic ave., 30, 101400, Temirtau, Kazakhstan; e-mail: kabieva.s@mail.ru; https://orcid.org/0000-0002-4868-5278

Mendibayeva, Anel Zhanatovna — Junior researcher, LLP "Institute of Organic Synthesis and Coal Chemistry of the Republic of Kazakhstan", Alikhanov street, 1, 100008, Karaganda, Kazakhstan; e-mail: anenyawa@mail.ru; https://orcid.org/0000-0001-6123-3340

_____
*The author's name is presented in the order: *Last Name, First and Middle Names*

Nurlan Merkhatuly[1] , Amantai N. Iskanderov[1*] ,
Saltanat B. Abeuova[2] , Ablaykhan N. Iskanderov[1]

[1]Karagandy University of the name of academician E.A. Buketov, Kazakhstan;
[2]Astana International University, Astana, Kazakhstan
(*Corresponding author′se-mail: dr.amantay@ya.ru)

Synthesis of Push-Pull Azulene-Based Compounds

Nowadays, non-benzenoid aromatic hydrocarbons are widely used as synthons for the production of new organic semiconductors with interesting photophysical characteristics. For instance, a non-benzoid azulene hydrocarbon with a polar structure, a narrow energy gap between the highest free and lowest occupied molecular orbital and the ability to form stable ions can be intended as a structural moiety for the synthesis of new conjugated compounds with important optical and electronic properties. The article discusses the synthesis and investigation of the optical properties of new push-pull azulene-based compounds. It shows that Friedel-Crafts acylation is used as the key reaction for the synthesis of methyl- and phenyl-dicyanovinylated azulenes. The interaction proceeds regioselectively at the C1 and C3 positions of the five-membered azulene ring. It is identified that the synthesis of push-pull dicyanovinylated azulenes by Knoevenagel condensation of azulenyl ketones with malononitrile proceeds easily in Py and DMSO. The UF-vis spectra of the obtained azulene push-pull compounds demonstrated strong electron absorption in the visible zone with λmax at 410, 430, 434 and 452 nm associated with transport of charge between the donor azulene ring and the acceptor dicyanovinyl group. The scheme of resonant structures shows the mechanism of intramolecular donor-acceptor interaction. The structure of the synthesized push-pull dicyanovinylated nonazulenes was elucidated using modern physicochemical and spectroscopic research methods.

Keywords: functional materials, organic semiconductors, ketoazulene, diketoazulene, bis-dinitrilevinyl-azulene, mono-dinitrileazulene, donor-acceptor azulenes, π-conjugated systems.

Introduction

The increasing interest in aromatic molecules with a stretched conjugate system due to their importance as functional materials for organic optoelectronics is largely focused on obtaining phenylated, also substituted by donor-acceptor fragments of benzoid and heteroaromatic molecules. Nevertheless, up to now, non-alternative aromatic compounds have not found their extensive use as synthons for the production of new substances with valuable electro-optical characteristics. Such compounds include, in particular, azulene hydrocarbons [1, 2].

Azulene **1** (Fig. 1) is a unique nonalternant aromatic hydrocarbon consisting of condensed five- and seven-membered cycles [3]. The dipole structure (μ=1.08 D) of azulene can lead to stabilized ion radicals and is of interest as a structural block for obtaining donor-acceptor systems with advanced optoelectronic properties [1-3]. Azulene is unique not only for its polar nature, but also for the peculiarity of the energy transition and the small forbidden zone of HOMO – LUMO [4, 5]. This is due to its nonalternant structure, which induces frontal molecular orbitals to its mirror arrangement, thereby reducing the mutual repulsion between electrons. As a consequence, the energy gap of HOMO – LUMO **1** decreases in comparison with conventional aromatic hydrocarbons [6]. In addition, azulene gives strong absorption associated with the $S_0 - S_2$ optical transition, while the $S_0 - S_1$ transition leads to weak absorption in the visible range, which explains its blue color [7, 8]. Another feature of **1** is that its fluorescence mainly originates from the S_2 state, whereas the S_1-S_0 transition is insignificant [9]. This nature of the transition violates the Kasha's rule [4]. The reason for this anomalous fluorescent nature is that the energy gap between the S_1 and S_2 states is relatively large (ΔE is more than 10000 cm-1), which leads to a decrease in the transition rate from S_2 to S_1, as a result of which the radiation from S_2 to S_0 becomes dominant [10].

In this article, we report on the results of the directed synthesis and investigation of the optical properties of new push-pull methyl- and phenyldicianovinylated azulenes.
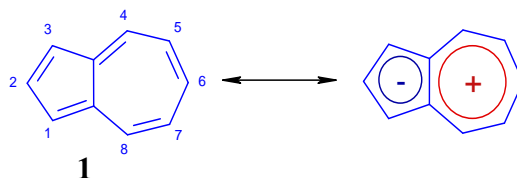
Figure 1. The polarized resonance structure of azulene **1**

Experimental

IR spectra were recorded on an Avatar-360 Fourier spectrometer (USA) in tablets with KBr. ^{1}H and ^{13}C NMR spectra were recorded on a JeolECA-500 spectrometer (Japan) [operating frequency 500.15 MHz] in CDCl$_3$, internal standard TMS. Absorption spectra were recorded on a Shimadzu UV-1800 spectrophotometer (Japan) in dichloromethane (C=10^{-4} mol/l). Mass spectra were recorded on a Shimadzu GC-MSQP-2010 Ultra chromato-mass spectrometer (Japan) with electron impact ionization (ionization energy 70 eV, column GsBP-5MS: 0.25 μm × 0.25 mm × 30 m, carrier gas helium, programmable heating from 100 to 300 °C, scanning mode for all integer m/z values in the range from 15 to 900 at a speed of 5000 amu/sec). Elemental analysis was performed on an automatic CHNS analyzer EuroVektor EA-3000 (Italy). The melting point was determined on a Melting Point M-560 instrument (Switzerland). Sorbfil PTSH-AF-UF plates (Russia) were used for TLC, eluent was hexane, hexane-ethyl acetate, and developed with a saturated solution of KMnO$_4$. Silica gel 60 (Merck) was used for column chromatography.

Initial azulene (99.5 %), acetyl chloride (99 %), benzoyl chloride (99 %), malononitrile (≥99 %), dimethyl sulfoxide (99.5 %), pyridine (≥99.0 %), methylene chloride (≥99.8 %) produced by Sigma-Aldrich were used without additional purification.

2-(1-(Azulen-1-yl)ethylidene)malononitrile (4). Monoketone **2** (150 mg, 0.86 mmol), malonitrile (100 mg, 1.5 mmol), pyridine (1 ml) and dimethyl sulfoxide (2 ml) were placed in a reaction vessel and stirred in a nitrogen atmosphere for 10 hours at 105 °C. After the end of the reaction, pyridine and dimethyl sulfoxide were distilled at reduced pressure. The product was purified by SiO$_2$ flash column chromatography (eluent was methylene chloride) and recrystallization from methylene chloride. Yield is 0.13 g (70±0.65 %), red crystals, mp 156–157±0.15 °C. IR spectrum, ν, (cm^{-1}): 2220 (CN), 1543–1385 (C$_{sp2}$-C$_{sp2}$). ^{1}H NMR spectrum, δ (ppm): 2.28 s. (3H, CH$_3$), 7.31 d (1H, H^3, J4.13 Hz), 7.64 t (2H, H^{5,7}, J 9,6 Hz), 8.0 t (1H, H^6, J 9.6 Hz), 8.05 d (1H, H^2, J 4.13 Hz), 8.08 d (1H, H^4, J 9.6 Hz), 8.13 d (1H, H^8, J 9.6 Hz). ^{13}C NMR spectrum, δ (ppm): 116.08, 117.11, 120.05, 125.25, 130.84, 136.55, 141.17, 142.60, 145.49, 146.79, 151.18, 168.38. MS, *m/z* (I_{rel},%): 218 (75.12) [M]$^+$. Found, %: C 82.62; H 4.66; N 12.94. C$_{15}$H$_{10}$N$_2$. Calculated, %: C 82.55; H 4.62; N 12.84.

2,2'-(Azulene-1,3-diylbis(ethan-1-yl-1-ylidene))dimalononitrile (5) was synthesized similarly by the interaction of diketone **3** with two equivalents of malononitrile (200 mg, 3 mmol). Yield is 0.14 g (73±0.22 %), red crystals, mp 252–253±0.16 °C. IR spectrum, ν, (cm^{-1}): 2218 (CN), 1504–1361 (C$_{sp2}$-C$_{sp2}$). ^{1}H NMR spectrum, δ (ppm): 2.28 s. (6H, CH$_3$), 7.68 t (2H, H5.7, J 9.8 Hz), 8.03 t (1H, H6, J 9.8 Hz), 8.07 s (1H, H2), 8.15 d (2H, H4.8, J 9.8 Hz). ^{13}C NMR spectrum, δ (ppm): 114.06, 115.10, 124.05, 125.19, 129.35, 130.84, 131.21, 133.35, 136.55, 139.17, 142.70, 143.39, 144.18.2, 144.18.2 MS, *m/z* (I_{rel},%): 308 (73.05) [M]$^+$. Found, %: C 77.98; H 3.96; N 18.24. C$_{20}$H$_{12}$N$_4$. Calculated, %: C 77.91; H 3.92; N 18.17.

2-(Azulen-1-yl(phenyl)methylene)malononitrile (8). Monoketone 6 (201 mg, 0.87 mmol), malonitrile (100 mg, 1.5 mmol), pyridine (2 ml) and dimethyl sulfoxide (3 ml) were placed in a reaction vessel and stirred in a nitrogen atmosphere for 10 hours at 105 °C. After the end of the reaction, pyridine and dimethyl sulfoxide were distilled at reduced pressure. The product was purified by SiO$_2$ flash column chromatography (eluent was methylene chloride) and recrystallization from methylene chloride. Yield is 0.17 g (71±0.25 %), red crystals, mp 148–149±0.17 °C. IR spectrum, ν (cm^{-1}): 2224 (CN), 1512–1374 (C$_{sp2}$-C$_{sp2}$). ^{1}H NMR spectrum, δ (ppm): 7.35 d (1H, H3, J 4.17 Hz), 7.49–7.56 m (3H$_{arom}$), 7.63–7.66 m (2H$_{arom}$), 7.69 t (2H, H^{5,7}, J 9.9 Hz), 8.04 t (1H, H^6, J9.9Hz), 8.09 d (1H, H^2, J 4.17 Hz), 8.13 d (1H, H^4, J 9.9 Hz), 8.18 d (1H, H^8, J 9.9 Hz). ^{13}C NMR spectrum, δ (ppm): 118.07, 119.09, 122.07, 123.19, 127.26, 132.85, 133.22, 134.84, 137.52, 142.16, 143.61, 146.48, 145.75, 152.17, 166.35. MS, *m/z* (I_{rel},%): 280 (78.12) [M]$^+$. Found, %: C 85.61; H 4.27; No. 9.89. C$_{20}$H$_{12}$N$_2$. Calculated, %: C 85.69; H 4.31; N 9.99.

2,2'-(Azulene-1,3-diylbis(phenylmethanylylidene))dimalononitrile (9) was synthesized similarly by the interaction of diketone 7 with two equivalents of malonitrile (200 mg, 3 mmol). Yield is

0.18 g (70±0.17 %), red crystals, mp 237–238±0.19 °C. IR spectrum, ν (cm^{-1}): 2220 (CN), 1510–1395 (C$_{sp2}$-C$_{sp2}$). ^{1}H NMR spectrum, δ (ppm): 7.50–7.48 m (8H$_{arom}$), 7.63 -7.66 m (2H$_{arom}$), 7.64 t (2H, H^{5,7}, J 9.9 Hz), 8.07 t (1H, H^6, J 9.9 Hz), 8.09 s (1H, H^2), 8.17 d (2H, H^{4,8}, J 9.9 Hz). ^{13}C NMR spectrum, δ (ppm): 116.04, 116.12, 126.05, 127.18, 128.36, 131.85, 133.22, 135.32, 137.54, 138.15, 143.68, 144.38, 145.78, 148.06, 157.16, 166.94. MS, m/z (I_{rel},%): 432 (75.10) [M]$^+$. Found, %: 83.41; H, 3.71; H 12.86. C$_{30}$H$_{16}$N$_4$. Calculated, %: C, 83.32; H, 3.73; N, 12.95.

Results and Discussion

The Friedel-Crafts acylation was used as the key reaction for the synthesis of methyl-dicyanovinylated azulenes (Scheme 1). Acylation of azulene **1** with one or two equivalents of acetyl chloride has been shown to lead regioselectively to previously described 1-mono- and 1,3-diketones **2** and **3** in 78 and 75 % yields, respectively [11]. The resulting methyl ketones then enter into a Knoevenagel condensation with CH$_2$(CN)$_2$ in the medium of pyridine and DMSO to yield push-pull 1-mono- and 1,3-bis(methyl-dicyanovinyl)azulenes **4** and **5** as red crystals in 70 and 73 % yields, respectively.
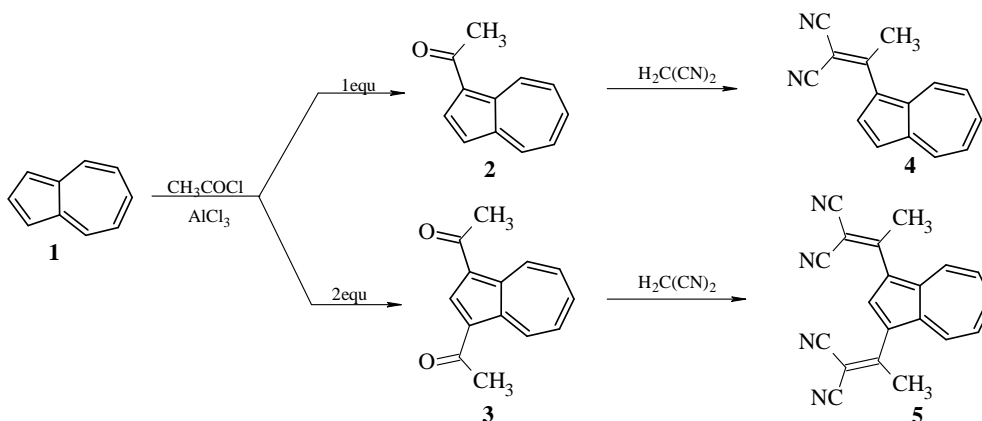
Scheme 1

The synthesis of phenyl dicyanovinylated azulenes was carried out according to Scheme 2, also using Friedel-Crafts acylation reactions and Knoevenagel condensation. Thus, the reaction of compound **1** with one or two equivalents of benzoyl chloride in dichloromethane leads to known ketones **6** and **7** in 71 and 60 % yields [12]. Then, the resulting phenyl ketones condense with CH$_2$(CN)$_2$ in the medium of pyridine and DMSO to form push-pull phenyl dicyanovinylazulenes **8** and **9** as red crystals in 71 and 70 % yields, respectively.
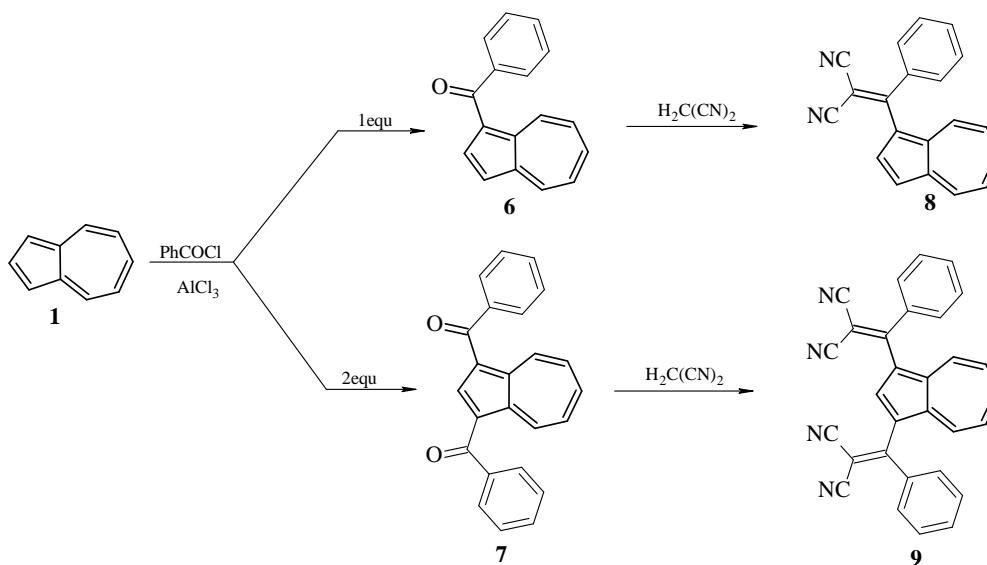
Scheme 2

To study the optical properties of the obtained compounds, push-pull analysis of azulenes **4, 5, 8,** and **9** was carried out using absorption spectrophotometry in the UV and visible regions. UV-Vis spectra of **4** and **5**, as well as **8** and **9** showed intense absorption in the visible spectrum with maxima at 430 and 410 nm, 452 and 434 nm, respectively (Table, Fig. 3), caused by intramolecular charge transfer between the azulene ring and dicyanovinyl group, as demonstrated on resonant structures (Fig. 2).

4, 8   **R = Me(4), Ph(8)**

5, 9   **R = Me(5), Ph(9)**
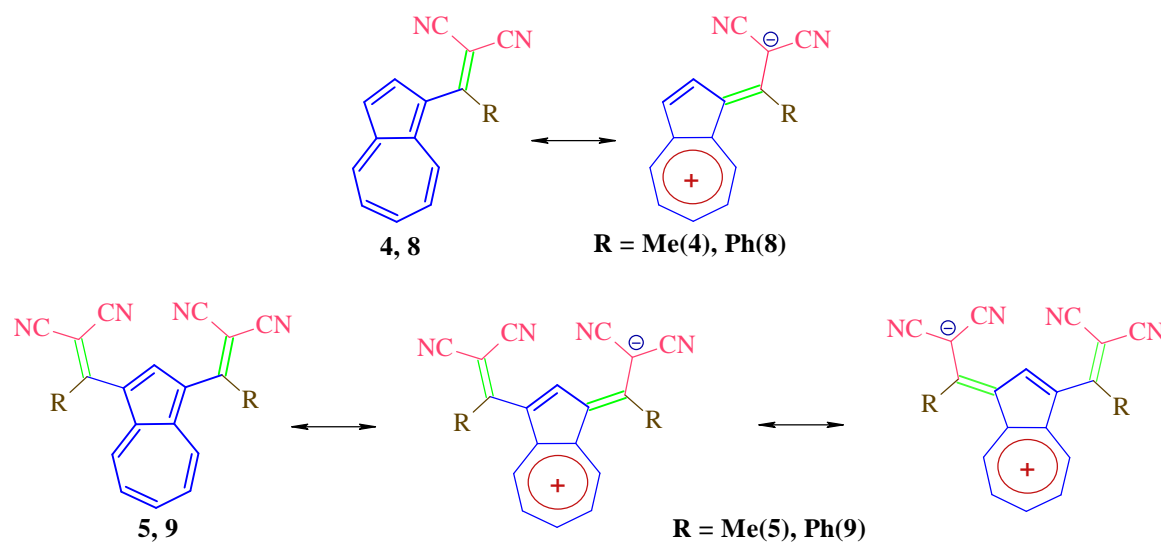
Figure 2. Resonance structures of push-pull azulenes **4, 5** and **8, 9**

T a b l e

UV-Vis light absorption data for push-pull azulenes 4, 5 and 8, 9

Compound	Solvent	C, mol/l	λ_{abs}, nm	ε, $M^{-1}cm^{-1}$
4	dichloromethane	10^{-4}	430	9552
5	dichloromethane	10^{-4}	410	8893
8	dichloromethane	10^{-4}	450	8481
9	dichloromethane	10^{-4}	434	9186
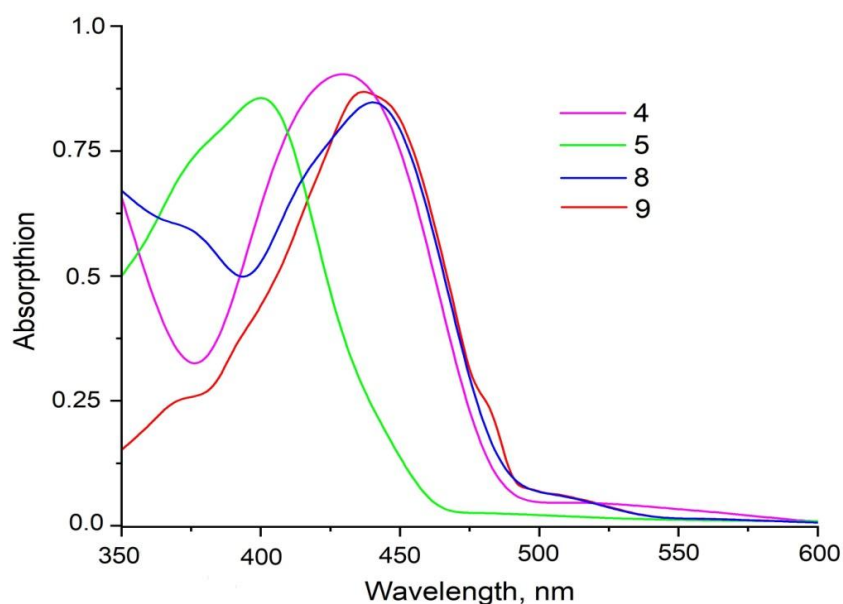
Figure 3. Push-pull absorption spectra of azulenes **4, 5** and **8, 9** in dichloromethane

Conclusions

Acylation of azulene with acetyl- and benzoyl chloride under Friedel-Crafts electrophilic substitution conditions yielded 1-mono- and 1,3-bis(methyl) and (phenyl)azulenyl ketones in high yields. In addition, by Knoevenagel condensation of the obtained azulenyl ketones with $CH_2(CN)_2$ in pyridine, push-pull 1-mono- and 1,3-bis-methyl(phenyl)dicyanovinylazulenes were synthesized in high yields. Intense absorption bands of intramolecular charge transfer in the visible region were revealed for push-pull methyl(phenyl)dicyano-vinylazulenes with absorption maxima at 430, 410, 450, and 434 nm.

Acknowledgments

References

1 Dong, J.-X., & Zhang H.-Li. (2016). Azulene-based organic functional molecules for optoelectronics. *Chin. Chem. Lett., 27,* 1097-1104. https://doi10.1016/j.cclet.2016.05.005

2 Gao, H., Ge, C., Hou, B., Xin, H., & Gao, X. (2019). Incorporation of 1,3-Free-2,6-Connected Azulene Units into the Backbone of Conjugated Polymers: Improving Proton Responsiveness and Electrical Conductivity. *ACS Macro Lett.*, *8,* 360–1364. https://doi10.1021/acsmacrolett.9b00657

3 Lopez-Alled, C.M., Park, S.J., Lee, D.J., Murfin, L.C., Kociok-Kohn, G., Hann, J.L., Wenk, J., James, T.D., Kim, H.M., & Lewis, S.E. (2021). Azulene-based fluorescent chemosensor for adenosine diphosphate. *Chem. Commun., 57,* 10608-10611. https://doi10.1039/d1cc04122c

4 Ou, L., Zhou, Y., Wu, B., & Zhu, L. (2019). The unusual physicochemical properties of azulene and azulene-based compounds. *Chin.Chem. Lett., 30,* 1903–1907. https://doi.10.1016/j.cclet.2019.08.015

5 Xin, H., Hou, B., & Gao X. (2021). Azulene-Based π‑Functional Materials: Design, Synthesis, and Applications. *Acc. of Chem. Res., 54,* 1737–1753. https://doi.10.1021/acs.accounts.0c00893

6 Puodziukynaite, E., Wang, H.W., & Lawrence, J. (2014). Azulene methacrylate poly-421 mers: synthesis, electronic properties, and solar cell fabrication. *J. of the Am. Chem. Soc., 136*, 11043–11049. https://doi.10.1021/ja504670k

7 Chen, L.Wu, B.,Qin, L., Huang, Y.Y., Zhang, X.S., & Zhang, D.(2022). A perylene five-membered ring diimide for organic semiconductors and π-expanded conjugated molecules. *Chem. Comm., 58,* 5100–5103. https://doi.org/10.1039/d2cc01061e

8 Maeng, C., Yun, Y., Son, J.Y., & Lee, P. H. (2022). Palladium-Catalyzed Oxidative Cyclization of Azulene-2-Carboxylic Acids with 1,3-Dienes for the Synthesis of Alkenyl Azulenolactones. *Adv. Synth. Catal., 364* (16), 2859–2864. https://doi.org/10.1002/adsc.202200452

9 Murai, M., Abe, M., Ogi, S., & Yamaguchi, S.(2022). Diazulenylmethyl Cations with a Silicon Bridge: A π-Extended Cationic Motif to Form J-Aggregates with Near-Infrared Absorption and Emission. *J. of the Am.Chem.Soc., 144* (44), 20385–20393. https://doi.org/10.1021/jacs.2c08372

10 Ran, F., Zheng, H.L.R., Zhang, H., Xie, F., Jin, P., Lei, Z., Wang, X.-T., & Hu, J.Y. (2022). Polarity change of OFETs based on Dithienocoronene Diimide (DTCDI)-Derived isomeric triads end-capped with Azulene. *Dyes and Pigm., 203,* 110-311. https://doi.org/10.1016/j.dyepig.2022.110311

11 Anderson, A.G., Scotoni, R., Cowles, E.J., & Fritz, C.G. (1957). Azulene. VI. Synthesis and Properties of Some 1,3-Disubstituted Azulenes. *J. Org. Chem.*, *22*(10), 1193-1196. https://doi.org/10.1021/jo01361a017

12 Westermayr, J., & Maure, R.J. (2021). Physically inspired deep learning of molecular excitations and photoemission spectra. *Chem. Sci.*, *12*, 10755-10764. https://doi.org/10.1021/jacs.2c08372

Information about authors*

Merkhatuly, Nurlan — Doctor of Chemical Sciences, Professor, Department of Inorganic and Technical Chemistry, Karagandy University of the name of academician E.A. Buketov, Universitetskaya street, 28, 100024, Karaganda, Kazakhstan; e-mail: merhatuly@ya.ru; https://orcid.org/0000-0003-4588-2150;

Iskanderov, Amantai Nurbaevich (*corresponding author*) — Master of Chemistry, Department of Inorganic and Technical Chemistry, Karagandy University of the name of academician E.A. Buketov, Universitetskaya street, 28, 100024, Karaganda, Kazakhstan; e-mail: dr.amantay@ya.ru; https://orcid.org/0000-0001-5270-5094;

Abeuova, Saltanat Bolatovna — PhD, Senior Lecturer, Astana International University, Kabanbaybatyra street, 8, Z05H0T3, Astana, Kazakhstan; e-mail: abeuova.salta@gmail.com; https://orcid.org/0000-0001-7074-3123;

Iskanderov, Ablaykhan Nurbaevich — Master of Chemistry, Department of Inorganic and Technical Chemistry, Karagandy University of the name of academician E.A. Buketov, Universitetskaya street, 28, 100024, Karaganda, Kazakhstan; e-mail: aby93@yandex.kz; https://orcid.org/0000-0002-1646-0795

_____

*The author's name is presented in the order: *Last Name, First and Middle Names*

Article

Aldana R. Galiyeva[*] , Yerkeblan M. Tazhbayev , Nazgul A. Yessentayeva , Arailym T. Daribay , Dias T. Marsel , Daniyar T. Sadyrbekov , Lyazzat Zh. Zhaparova , Zhansaule T. Arystanova

Karagandy University of the name of academician E.A. Buketov, Kazakhstan
(*Corresponding author's e-mail: aldana_karaganda@mail.ru)

PEGylation of Albumin Nanoparticles Immobilized with the Anti-Tuberculosis Drug "Isoniazid"

Polyethylene glycol (PEG) is widely used in nanomedicine to extend the circulation time of a drug in the blood and increase drug efficacy. Conjugation by attaching polyethylene glycol to an albumin macromolecule and nanoparticles is a well-established technique known as PEGylation. The aim of this research was to prepare and evaluate serum stable long circulating PEG-albumin-isoniazid nanoparticles for the treatment of Mycobacterium tuberculosis which can improve its therapeutic effect by increasing its permeability, solubility and accumulation in aveolar macrophages. For the first time, PEGylated BSA nanoparticles loaded with isoniazid were synthesized by desolvation using urea and cysteine as denaturing and stabilizing agents. Nanoparticles with an average size of up to 300 nm were obtained by varying the PEG concentration. The polydispersity index of all particle charges was less than 0.1, indicating monodisperse size. The ζ potential values indicate sufficient physical stability of the nanoparticles. SEM images showed that the particles were spherical in shape. The TGA and DSC results obtained confirm that drug loading does not affect the structure of the polymer. Based on FT-IR studies, the absence of chemical interactions between PEGylated BSA nanoparticles and isoniazid was established. In *in vitro* release studies, the nanoparticles were demonstrated to have a prologue release.

Keywords: nanoparticles, bovine serum albumin, polyethylene glycol, isoniazid, desolvation, hydrophilic drugs, anti-tuberculosis drugs.

Introduction

Recently, albumin-based nanoparticles have been actively used as pharmaceutical and functional carriers due to their low toxicity and biodegradability, as evidenced by the numerous studies conducted on the subject [1-3]. Albumin nanoparticles have several advantages as a drug delivery system, such as biodegradability, stability, particle surface modification, ease of particle size control, and they also have fewer toxicity issues such as immunogenicity [4, 5].

The process of modifying albumin molecules with various polymeric compounds has recently become a relevant area of research. There is worldwide experience in the production of drug nanoparticles by binding — linking inert macromolecules of polyethylene glycol (PEG). Immobilized by drugs PEG nanoparticles not only ensure good tolerability but also have an improved pharmacokinetic profile, promote deep penetration of molecules and provide additional protection against proteolytic enzymes [6, 7].

Polyethylene glycol is one of the medicinal synthetic polymer injectables that can be used for the organism and is approved by the Food and Drug Administration. There are numerous benefits of PEGylated nanosystems, such as those in Figure 1 [8, 9].

The desolvation method is most commonly used to synthesize albumin-based nanoparticles [10–12]. The desolvation method allows the synthesis of nanoparticles by a simple process of adding desolvating agents, such as ethanol or acetone, to albumin solutions containing drugs. Desolvating agents change the structure of albumin and reduce its solubility, leading to the formation of precipitates in the form of protein nanoparticles [2]. Once the nanoparticles are formed, they are bonded with bridging agents such as glutaraldehyde.

In previous studies, glutaraldehyde was mainly used as a crosslinking agent for the preparation of PEGylated albumin-based nanoparticles: the authors of [13] obtained PEGylated nanoparticles prepared from human serum albumin (HSA); Thadakapally, et al. [14] conducted research to obtain serum-stable long-

circulating polymeric curcumin nanoparticles and synthesized nanoparticles using serum albumin and polyethylene glycol; the authors of [15] work synthesized serum-stable long-circulating PEGylated paclitaxel-BSA nanoparticles for breast cancer treatment.
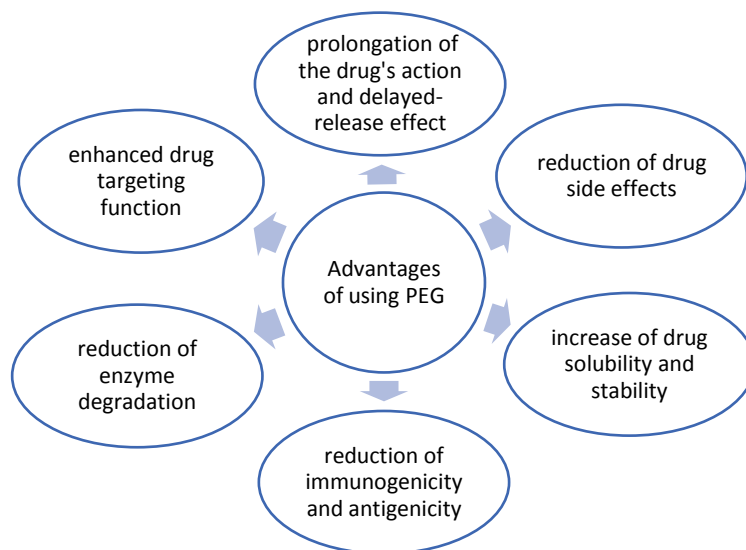
Figure 1. Advantages of PEGylated nanoparticles

In our study, we suggest replacing the synthetic stabilizer with natural materials such as urea and cysteine [16–18]. We first proposed a method for the preparation of PEG-BSA NPs using the natural components urea and L-cysteine. In this case, urea plays the role of a chaotropic agent that unfolds albumin chains and increases the availability for interaction with L-cysteine. As a result, the thiol-disulfide exchange reactions between the PEG-BSA NPs macrochains are stabilized [17].

In this research we aimed to improve the properties of the anti-tuberculosis drug isoniazid by PEGylation of bovine albumin nanoparticles. Thus, the main aim of this research was to prepare and evaluate serum stable long-term circulating PEG-albumin-isoniazid nanoparticles (PEG-BSA-INH NPs) for the treatment of Mycobacterium tuberculosis, capable of improving its therapeutic effect by increasing its permeability, solubility and accumulation in aveolar macrophages.

Experimental

Materials

Isoniazid (INH) with an in-medical purity of over 99 %, bovine serum albumin (lyophilized powder, 98 %) (BSA), L-cysteine (98.5 %) and polyethylene with MW 4000 and 6000 were supplied by Sigma Aldrich (Germany). Ethanol was purchased from DosFarm (Almaty, Kazakhstan). Urea (99.5 %) was purchased from ChemPribor SPb (St. Petersburg, Russia). Sodium hydrophosphate and potassium dihydrophosphate were used to prepare a phosphate-buffered saline solution.

Preparation of PEG-BSA-INH NPs

PEG-BSA-INH nanoparticles were prepared by desolvation with some additions as in [16–18]. According to this technique, a given amount of bovine serum albumin (concentration 20 mg/mL) and PEG with MW 4000 or 6000 (10–100 mg/mL) were dissolved in distilled water while stirring at 200 rpm. Then an aqueous solution of urea was added (its concentration was 7 mol/L) and treated with an ultrasonic bath; the ultrasonic period was 3 min. Pre-prepared isoniazid at a concentration of 4 mg/mL was added to the resulting suspension. Ethanol was then added to each albumin solution at a rate of 1 mL/min to form a colloidal dispersion of albumin nanoparticles with PEG. A given amount of L-cysteine aqueous solution (concentration 2.5 mg/mL) was then added. The reaction mixture thus obtained was stirred continuously for 2 h. The produced nanoparticles were separated by centrifugation (MiniSpin, Eppendorf, Hamburg, Germany) at 14,000 rpm for 15 min, then the suspension of nanoparticles was washed three times with distilled water.

Particle size, polydispersity index, ζ-potential and morphology of the PEG-BSA-INH NPs

The polydispersity (PDI) and particle size were determined on a laser particle size detector (Malvern Zetasizer Nano S90, Malvern Instruments Ltd., Malvern, UK) using dynamic light scattering (DLS). Each batch of nanoparticles was appropriately diluted with distilled water immediately after production. ζ-potential was determined with a Zeta potential analyzer using Phase Analysis Light Scattering (NanoBrook ZetaPALS, Brookhaven Instruments Corporation, Nova Instruments, USA). The surface morphology of PEG-BSA-INH NPs was investigated by scanning electron microscopy (MIRA 3LM TESCAN, Brno, Czech Republic, EU).

Encapsulation efficiency, loading capacity and PEG-BSA-INH NPs' yield

The amount of isoniazid loaded into PEG-BSA nanoparticles was determined by measuring the amount of unentrapped drug in the supernatant. Isoniazid was analyzed by high performance liquid chromatography (HPLC) (Shimadzu LC-20 Prominence). The encapsulation efficiency, loading capacity and yield of nanoparticles were calculated as follows:

$$\text{Encapsulation Efficiency}\,(\%) = \frac{\text{Mass of INH in NPs}}{\text{Mass of total INH}} \times 100\,\% \; ;$$

$$\text{Loading Capacity}\,(\%) = \frac{\text{Mass of INH in NPs}}{\text{Total mass of NPs}} \times 100\,\% \; ;$$

$$\text{Nanoparticles Yield}\,(\%) = \frac{\text{Total mass of NPs}}{\text{Total mass of INH} + \text{Total mass of polymer}} \times 100\,\% \; .$$

In vitro study of drug release from polymer NPs

To investigate the *in vitro* release of isoniazid from NPs: A dialysis bag (MWCO: 1 kDa) containing 3 mL of phosphate-buffered saline (PBS) with PEG-BSA-INH nanoparticles was placed in a beaker with 250 ml of PBS. The beaker was placed in a water bath, at 37 °C. Dialysates were sampled periodically (3 mL at a time). To study the degree of INH release from the polymer nanoparticles, the amount of drug released was recorded by HPLC and calculated by formula:

$$\text{Drug Release}\,(\%) = \frac{\text{Mass of released drug}}{\text{Mass of the total drug in nanoparticles}} \times 100\,\% \; .$$

Thermogravimetric analysis and differential scanning calorimetry

Polymer and nanoparticle behaviour of PEG-BSA-INH during thermal degradation was studied with a thermogravimetric analyzer and differential scanning calorimetry (LabSYS evo TGA/DTA/DSC, Setaram, France); the instrument was operated from 30 °C to 600 °C under nitrogen at a flow rate of 30 ml/min and a heating rate of 10 °C/min.

Study of prepared nanoparticles by Infrared spectroscopy

IR spectroscopy (FSM 1202, Infraspek Ltd., Russia) was used to identify the samples. FT-IR spectra were determined using the KBr method. 3 mg of the sample was mixed with 100 mg of KBr and a pellet was prepared. The IR range investigated was 4000 to 400 cm^{-1} and resolution of FT-IR spectra was 8 cm^{-1}.

Statistical analysis

The data are expressed as mean ± standard deviation. The analysis was carried out statistically by Minitab 19 Statistical Software. The data were analyzed by one-way analysis of variance (ANOVA).

Results and Discussion

PEGylation of albumin involves a chemical reaction between albumin reactive groups (amino acid side chains, N-terminal amino group or C-terminal carboxylic acid) and PEG [19]. Recently, disulfide bonds have been considered as targets for PEGylation; disulfide bridges are known to be present in small amounts in albumin macromolecules, which makes PEGylation at these sites attractive because of the possibility of producing homogeneous nanoparticles [8]. In terms of drug delivery system development, the most attractive aspect of cysteine is that it provides an accessible chemoselective site for surface modification without alter-

ing the tertiary structure of albumin [20-22]. An example of the production of albumin-specific binding sites via cysteine is the PEGylated product "CIMZIA®" (UCB Pharma S.A., Belgium) [19].

In previous work [18], we synthesized bovine albumin nanoparticles with the anti-tuberculosis drug "Isoniazid". Cysteine, which is capable of cleaving intramolecular disulfide bonds in proteins, was used to form the nanoparticles. This leads to a more complete unfolding of the polypeptide chain and facilitates cysteine attachment to intramolecular S-S bridges within the BSA globule [16–17, 22]. We suggest that the addition of urea and L-cysteine unfolds the albumin globule and opens the disulfide bridges, where PEG molecule attachment occurs more easily. Using the optimized parameters of BSA-INH NPs, we added different concentrations of PEG in the synthesis of PEGylated NPs. Thus, PEG-BSA-INH nanoparticles were obtained by desolvation (Fig. 2). The specifications of the produced NPs are shown in Table.
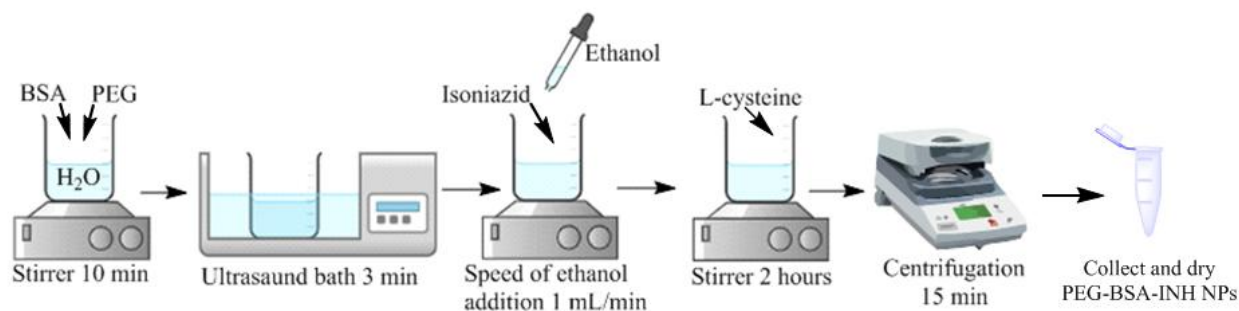
Figure 2. Scheme for producing PEG-BSA-INH nanoparticles

T a b l e

Characteristics of the PEG-BSA-INH nanoparticles

Formulation	PEG type	[PEG], mg/mL	Size, nm	PDI	ζ potential, mV	Encapsulation efficiency, %	Loading capacity, %	NPs' yield
B10	–	–	197.6±2.5	0.068±0.01	−28±6	50±3	38±4	26±3
BP410	4000	10	237.5±2.7	0.037±0.01	−34±4	68±3	18±2	47±3
BP420	4000	20	212.8±5.2	0.069±0.03	−28±1	75±1	22±2	28±6
BP440	4000	40	246.7±9.3	0.027±0.01	−41±3	74±7	19±1	22±4
BP480	4000	80	226.1±2.5	0.060±0.01	−21±7	80±5	24±5	14±2
BP4100	4000	100	225.7±5.8	0.059±0.02	−29±3	79±2	24±3	11±1
BP610	6000	10	249.7±8.1	0.040±0.02	−37±2	80±8	20±2	49±4
BP620	6000	20	245.1±5.9	0.069±0.02	−36±1	78±2	22±3	34±4
BP640	6000	40	239.8±1.6	0.039±0.03	−49±3	78±3	20±3	23±4
BP680	6000	80	271.2±9.7	0.078±0.04	−40±3	75±3	25±4	14±2
BP6100	6000	100	287.9±5.4	0.155±0.02	−44±9	77±4	27±5	11±2

PEG is known to coordinate about 3 water molecules per monomer unit, which gives PEG a large hydrodynamic volume [23]. Therefore, PEGylation of nanoparticles should lead to an increase in the hydrodynamic particle diameter as measured by DLS, which is an indirect reference to the degree of modification [24]. PEGylated and non-PEGylated BSA nanoparticles were compared with respect to particle size and polydispersity using DLS. Without PEGylation the particle diameter was 197.6±3 nm (B10 formulation). Particle size was found to be influenced by the molecular weight of the polyethylene glycol, while PEG concentrations were practically not affected. Therefore, with PEG 6000 the particles had a larger diameter than with PEG 4000. The highest added concentration of PEG 6000 (100 mg/mL) resulted in particles with a diameter 50 nm larger than those without added PEG. The polydispersity index of all particle charges was less than 0.1, indicating monodisperse size.

To confirm the stability of PEG-coated nanoparticle suspensions, the ζ-potential was measured and compared with non-PEG-coated BSA nanoparticles. Table shows the change in ζ-potential as a function of increasing concentration of added PEG. In contrast to the particle size, the ζ-potential changed significantly compared to the non-PEG-added BSA nanoparticles. In all cases, stable nanoparticle systems were produced,

with PEG-6000 obtaining nanoparticles with a ζ-potential potential of about -40 mV or more. In addition, parameters such as the encapsulation efficiency, the loading capacity and the yield of nanoparticles are also important factors in the production of nanoparticles. With increasing concentration of PEG, a decrease in the yield of nanoparticles and an increase in the loading capacity were observed as for PEG-4000 and PEG-6000 (Table).

Particle size and surface morphology of PEGylated albumin nanoparticles were performed by scanning electron microscopy (SEM). The images were analyzed using Image J software and the average particle size of BP410, BP420 and BP480 nanoparticles was 161.0±8, 201.5±2 and 226.2±3 nm, respectively. And for BP610, BP620 and BP680 nanoparticles, the average size was 231.4±5, 107.8±7, 117.7±4 nm, respectively. The morphology of the particles was smooth and spherical (Fig. 2).
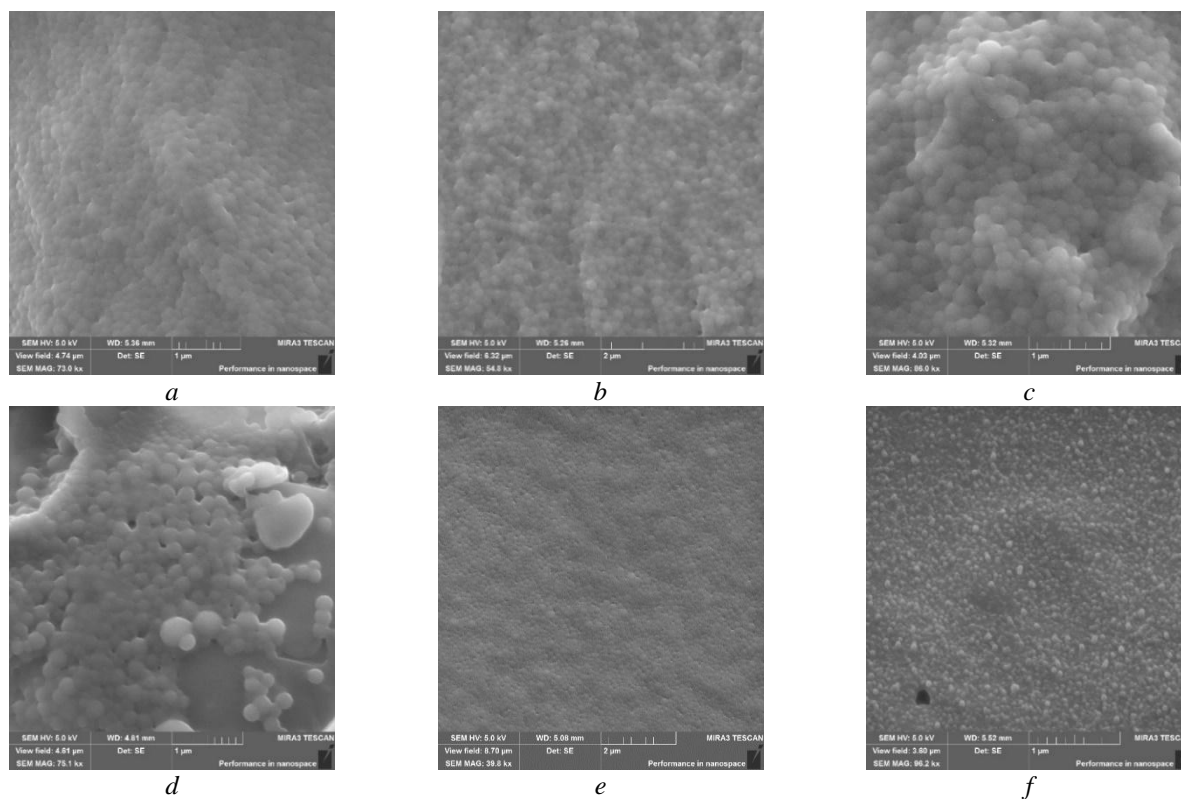
a — BP410; *b* — BP420; *c* — BP480; *d* — BP610; *e* — BP620; *f* — BP680

Figure 2. SEM images of isoniazid loaded PEG-BSA nanoparticles

Further, it was necessary to establish whether the drug substance affects the structure of the polymer. On this basis, we selected thermogravimetric analysis (TGA) and differential scanning calorimetry (DSC) as instruments (Fig. 3).

The thermal stability of isoniazid loaded nanoparticles (BP480 and BP680) as well as isoniazid, albumin, PEG4000 and PEG6000 was studied by TGA and DSC (Fig. 3). The DSC curve of isoniazid showed an endothermic peak at 177.2 °C, the associated melting, followed by another endothermic event at 345.6 °C due to the material decomposition (Fig. 3*a*). The mass loss occurred between 250 and 430 °C and was 72 % [24, 25]. The DSC data for BSA shows a three-step thermal degradation, so endothermic event at 98.9 °C related to moisture evaporation, 227.3 °C and 313 °C related to the degradation of the BSA amide bonds [26, 27]. The DSC curves for PEG4000 and PEG6000 showed an endothermic melting event at 70 °C, without mass loss (Fig. 3*c* and *d*). Thermogravimetric analysis for PEG4000 and PEG6000 showed a mass loss of more than 90 % in the temperature range of 300–440 °C. For BP480 there was an endothermic peak at 260 °C, between 220–410 °C there was a mass loss of about 40 % (Fig. 3*e*). For BP680, an endothermic peak was observed at 210 °C, with a mass loss of up to 60 % in the range of 200–440 °C. (Fig. 3*f*). However, compared to the curves of pure BSA and PEG, a significant movement towards higher temperatures was detected. This is probably due to the action of isoniazid. Data obtained by TGA and DSC analysis suggest that drug loading has no effect on the polymer structure.

a — INH; *b* — BSA; *c* — PEG 4000; *d* — PEG 6000; *e* — BP480; *f* — BP680
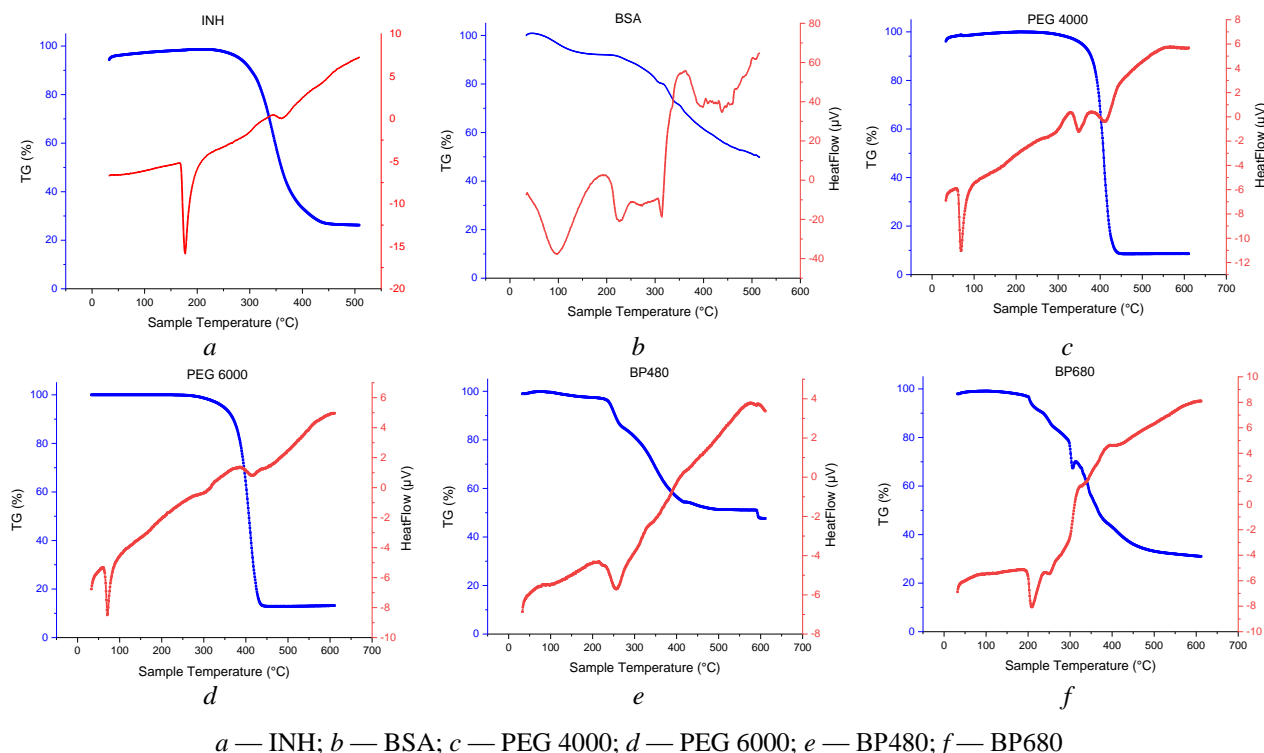
Figure 3. Thermal behavior of the components of the system and the produced nanoparticles

FT-IR analysis of samples was performed to investigate the interaction between the drug and the polymer. The FT-IR spectra of BSA, isoniazid, PEG and INH loaded PEGylated albumin nanoparticles are shown in Figure 4.
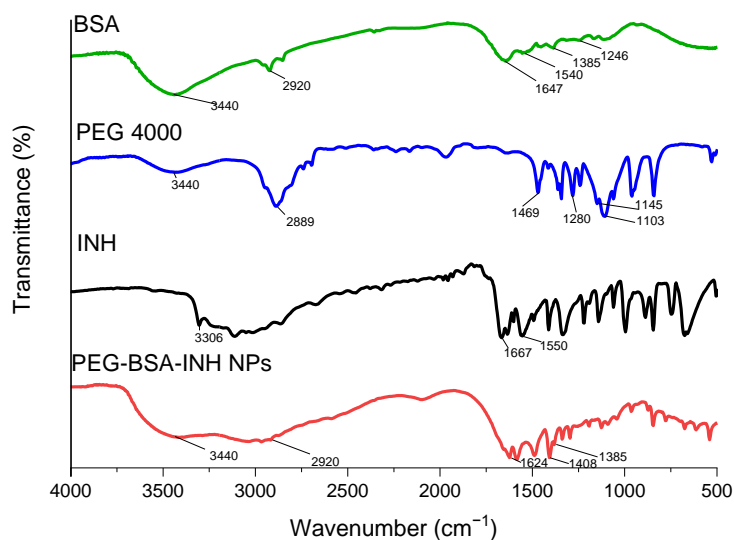
Figure 4. FT-IR spectra for isoniazid loaded PEGylated BSA nanoparticles

In FT-IR spectra of BSA, there were detected bands at 3440 cm^{-1} and 2920 cm^{-1} which show A-amide bound to N-H and B-amide bound to the free ion, respectively. The bands at 1647 cm^{-1}, 1540 cm^{-1} and 1246 cm^{-1} demonstrate C=O stretching vibrations of amide-I, N-H bending vibrations of amide-II, C-N stretching vibrations of amide-III, respectively, confirming the helical structure of BSA [17, 18]. For pure isoniazid broad strong characteristic peaks at 3306 cm^{-1} correspond to N-H stretching, C-H stretching vibrations of the heteroaromatic structure occur at 3100 cm^{-1} for asymmetric stretching, troughs at 1412 cm^{-1} are attributed to C−C symmetric ring vibrations, C-N stretch absorption of aliphatic amines is weak and occurs at 1060 cm^{-1}. The bands at 671 cm^{-1} and 1556 cm^{-1} are attributed to the C-C=O and H-N-N bend, respective-

ly [28]. There are no differences in the IR spectra of PEG due to their different molecular weights. The characteristic absorption bands for polyethylene glycol at 3440 cm^{-1} are due to the O-H stretching band, 2889 cm^{-1} is due to aliphatic C-H stretching, the bands at 1280 cm^{-1} and 1242 cm^{-1} are due to asymmetric C-O and C-O-C stretching vibrations, respectively [29, 30]. The spectrum of PEG-BSA-INH-NPs demonstrates representative peaks for the structure of albumin and isoniazid, indicating the absence of chemical interaction between PEGylated BSA nanoparticles and isoniazid.

The kinetics of drug release from nanoparticles in the creation of isoniazid loaded polymer complexes should be studied to confirm the prolonged action of the prepared NPs. The release kinetics of INH from PEG-BSA nanoparticles were investigated in phosphate buffer at pH 7.4 by dialysis. The degree of INH release from the polymer was calculated from the concentration of the released drug, which was determined by HPLC, the results of which are presented in Figure 5.
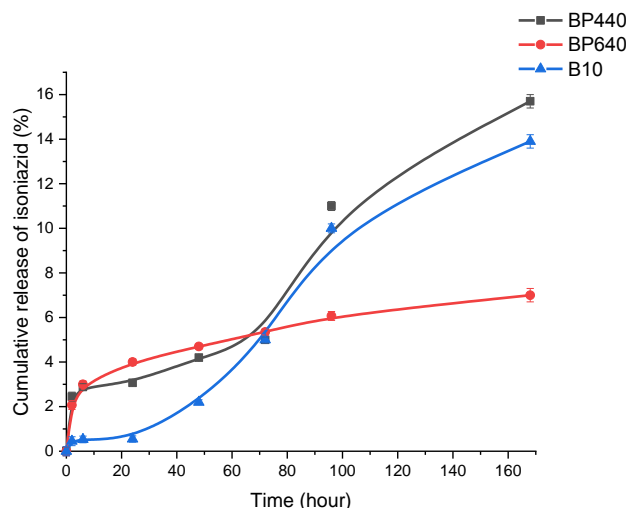
Figure 5. Investigation of isoniazid release from the polymer matrix by dialysis in phosphate-buffered saline

The data presented in Figure 5 shows that all samples demonstrate sustained release throughout the study period (7 days/ 168 hours). Thus, our study clearly demonstrates the potential for sustained release of isoniazid from PEGylated albumin nanoparticles. This makes it possible to prevent drug spikes in the blood and maintain therapeutic concentrations for a long time, indicating the potential of these particles as drug carriers for isoniazid delivery [31–34]. A study of release kinetics demonstrates a small Berst effect and prolonged release with a gradual release of isoniazid. Thus, these results provide a basis for the development of low-toxicity isoniazid prolonged-release chemotherapeutic forms.

Conclusions

PEG-BSA-INH nanoparticles were successfully synthesised by desolvation. The resulting particles were nanosized, as confirmed by DLS and SEM images. SEM images also showed that the particles were spherical in shape. Thus, the scanning microscopy results confirmed the formation of PEG-BSA-INH nanoparticles and also showed a decrease in particle size, which improved the solubility and permeability of the preparation. Based on FT-IR studies, it is clear that PEG was incorporated into the nanoparticles. Thus, the composition can be regarded as PEGylated albumin nanoparticles with isoniazid. The ζ-potential had been determined after the nanoparticles were obtained and the values indicated sufficient physical stability of the nanoparticles. In *in vitro* release studies, it was demonstrated that the nanoparticles had a prologue release. This suggests the possibility of sustained release of the drug *in vivo* as well.

Acknowledgments

References

1   Jacob, J., Haponiuk, J.T., Thomas, S. & Gopi, S. (2018). Biopolymer based nanomaterials in drug delivery systems: A review. *Materials Today Chemistry*, *9*, 43–55. https://doi.org/10.1016/j.mtchem.2018.05.002

2   Hong, S., Choi, D.W., Kim, H.N., Park, C.G., Lee, W. & Park, H.H. (2020). Protein-Based Nanoparticles as Drug Delivery Systems. *Pharmaceutics*, *12*(7), 604. https://doi.org/10.3390/pharmaceutics12070604

3   Martínez-López, A.L., Pangua, C., Reboredo, C., Campión, R., Morales-Gracia, J. & Irache, J.M. (2020). Protein-based nanoparticles for drug delivery purposes. *International Journal of Pharmaceutics*, 581, 119289. https://doi.org/10.1016/j.ijpharm.2020.119289

4   Elzoghby, A.O., Samy, W. M. & Elgindy, N.A. (2012). Albumin-based nanoparticles as potential controlled release drug delivery systems. *Journal of Controlled Release*, *157*(2), 168–182. https://doi.org/10.1016/j.jconrel.2011.07.031

5   Wang, G. & Uludag, H. (2008). Recent developments in nanoparticle-based drug delivery and targeting systems with emphasis on protein-based nanoparticles. *Expert Opinion on Drug Delivery*, *5*(5), 499–515. https://doi.org/10.1517/17425247.5.5.499

6   Suk, J.S., Xu, Q., Kim, N., Hanes, J. & Ensign, L.M. (2016). PEGylation as a strategy for improving nanoparticle-based drug and gene delivery. *Advanced Drug Delivery Reviews*, *99*, 28–51. https://doi.org/10.1016/j.addr.2015.09.012

7   Onugwu, A.L., Nwagwu, C.S., Onugwu, O.S., Echezona, A.C., Agbo, C. P., Ihim, S.A., Emeh, P., Nnamani, P.O., Attama, A.A. & Khutoryanskiy, V.V. (2023). Nanotechnology based drug delivery systems for the treatment of anterior segment eye diseases. *Journal of Controlled Release*, 354, 465–488. https://doi.org/10.1016/j.jconrel.2023.01.018

8   Santos, J.H.P.M., Torres-Obreque, K.M., Meneguetti, G.P., Amaro, B.P. & Rangel-Yagui, C.O. (2018). Protein PEGylation for the design of biobetters: from reaction to purification processes. *Brazilian Journal of Pharmaceutical Sciences*, *54*(spe). https://doi.org/10.1590/s2175-97902018000001009

9   Aukunuru, J., Thadakapally, R., Aafreen, A., Habibuddin, M. & Jogala, S. (2016). Preparation and characterization of PEG-albumin-curcumin nanoparticles intended to treat breast cancer. *Indian Journal of Pharmaceutical Sciences*, *78*(1), 65. https://doi.org/10.4103/0250-474x.180250

10   Shiehzadeh, F., Hadizadeh, F., Mohammadpour, A., Aryan, E., Gholami, L. & Tafaghodi, M. (2019). Streptomycin sulfate dry powder inhalers for the new tuberculosis treatment schedule. *Journal of Drug Delivery Science and Technology*, *52*, 957–967. https://doi.org/10.1016/j.jddst.2019.05.052

11   Ostrovskii, K.P., Osipova, N.S., Vanchugova, L.V., Shipulo, E.V., Pereverzeva, R., Treshchalin, I.D., Maksimenko, O.O. & Gel'perina, S. (2016). Use of Proteins to Increase the Aqueous Solubility of Rifapentine. *Pharmaceutical Chemistry Journal*, *50*(6), 407–412. https://doi.org/10.1007/s11094-016-1460-8

12   Srivastava, A. & Prajapati, A. (2020). Albumin and functionalized albumin nanoparticles: production strategies, characterization, and target indications. *Asian Biomedicine*, *14*(6), 217–242. https://doi.org/10.1515/abm-2020-0032

13   Fahrländer, E., Schelhaas, S., Jacobs, A. H. & Langer, K. (2015). PEGylated human serum albumin (HSA) nanoparticles: preparation, characterization and quantification of the PEGylation extent. *Nanotechnology*, *26*(14), 145103. https://doi.org/10.1088/0957-4484/26/14/145103

14   Thadakapally, R., Aafreen, A., Aukunuru, J., Habibuddin, M. & Jogala, S. (2016). Preparation and Characterization of PEG-albumin-curcumin Nanoparticles Intended to Treat Breast Cancer. *Indian journal of pharmaceutical sciences*, *78*(1), 65–72. https://doi.org/10.4103/0250-474x.180250

15   Tadakapally, R., Habbibudin, M. & Aukunuru, J. (2018). Preparation and Characterization of Peg-Albumin-Paclitaxel (PAP) Nanoparticles Intended to Treat Breast Cancer. *International Journal of PharmTech Research*, *11*(2), 143–155. https://doi.org/10.20902/ijptr.2018.11205

16   Tazhbayev, Y., Mukashev, O., Burkeev, M. & Kreuter, J. (2019). Hydroxyurea-Loaded Albumin Nanoparticles: Preparation, Characterization, and In Vitro Studies. *Pharmaceutics*, *11*(8), Article 410. https://doi.org/10.3390/pharmaceutics11080410

17   Tazhbayev, Y., Mukashev, O., Burkeyev, M. & Lozinsky, V.I. (2020). Synthesis and Comparative Study of Nanoparticles Derived from Bovine and Human Serum Albumins. *Polymers*, *12*(6), Article 1301. https://doi.org/10.3390/polym12061301

18   Tazhbayev, Y., Galiyeva, A., Zhumagaliyeva, T., Burkeyev, M. & Karimova, B. (2021). Isoniazid-Loaded Albumin Nanoparticles: Taguchi Optimization Method. *Polymers*, *13*(21), Article 3808. https://doi.org/10.3390/polym13213808

19   Porfiryeva, N.N., Moustafine, R.I. & Khutoryanskiy, V.V. (2020). PEGylated Systems in Pharmaceutics. *Polymer Science, Series C*, *62*(1), 62–74. https://doi.org/10.1134/s181123822001004x

20   El-Faham, A., Al-Rasheed, H.H., Sholkamy, E. N., Osman, S.M. & Alothman, Z.A. (2020). Simple Approaches for the Synthesis of AgNPs in Solution and Solid Phase Using Modified Methoxypolyethylene Glycol and Evaluation of Their Antimicrobial Activity. *International Journal of Nanomedicine*, *15*, 2353-2362. https://doi.org/10.2147/ijn.s244678

21   Abuchowski, A., van Es, T., Palczuk, N.C. & Davis, F.F. (1977). Alteration of immunological properties of bovine serum albumin by covalent attachment of polyethylene glycol. *The Journal of biological chemistry*, 252 11, 3578-81

22   Lozinsky, V. & Okay, O. (2014). Basic Principles of Cryotropic Gelation. *Advances in Polymer Science*, 49–101. https://doi.org/10.1007/978-3-319-05846-7_2

23   Brocchini, S., Balan, S., Godwin, A., Choi, J. -W., Zloh, M. & Shaunak, S. (2006). PEGylation of native disulfide bonds in proteins. *Nature Protocols*, *1*(5), 2241–2252. https://doi.org/10.1038/nprot.2006.346

24   Galiyeva, A.R., Tazhbayev, Ye.M., Zhumagaliyeva, T.S. & Daribay, A.T. (2022) Encapsulation of Isoniazid in Polylactide-Co-Glycolide Nanoparticles by Nanoprecipitation. *Bulletin of the University of Karaganda — Chemistry, 107(3), 208-217.* https://doi.org/10.31489/2022Ch3/3-22-17

25 Vilela Tibola, A. P. O. & Carpentieri Rodrigues, L. N. (2017). Compatibility study between isoniazid and pharmaceutical excipients used in solid dosage forms. *International Research Journal of Pharmacy*, *7*(12), 18–22. https://doi.org/10.7897/2230-8407.0712140

26 Michnik, A., Michalik, K., Kluczewska, A. & Drzazga, Z. (2006). Comparative DSC study of human and bovine serum albumin. *Journal of Thermal Analysis and Calorimetry*, *84*(1), 113–117. https://doi.org/10.1007/s10973-005-7170-1

27 Adamiano, A., Lesci, I. G., Fabbri, D. & Roveri, N. (2015). Adsorption of bovine serum albumin onto synthetic Fe-doped geomimetic chrysotile. *Journal of the Royal Society, Interface*, *12*(107), 20150186. https://doi.org/10.1098/rsif.2015.0186

28 Gunasekaran, S., Sailatha, E., Seshadri, S. & Kumaresan, S. (2009). FTIR, FT Raman spectra and molecular structural confirmation of isoniazid. *Indian J, Pure Appl. Phys., 47*, 12–18. http://nopr.niscair.res.in/handle/123456789/3152

29 Askari, F., Zandi, M., Shokrolahi, P., Tabatabaei, M. H. & Hajirasoliha, E. (2019). Reduction in protein absorption on ophthalmic lenses by PEGDA bulk modification of silicone acrylate-based formulation. *Progress in Biomaterials, 8*(3), 169–183. https://doi.org/10.1007/s40204-019-00119-x

30 Reddy Polu, A. & Kumar, R. (2011). Impedance Spectroscopy and FTIR Studies of PEG — Based Polymer Electrolytes. *E-Journal of Chemistry, 8*(1), 347–353. https://doi.org/10.1155/2011/628790

31 Mandhar, P. & Joshi, G. (2015). Development of Sustained Release Drug Delivery System: A Review. *Asian Pacific Journal of Health Sciences*, *2*(1), 179–185. https://doi.org/10.21276/apjhs.2015.2.1.31

32 Loiko, O.P., Herk, A.M. van, Ali, S.I., Burkeev, M.Z., Tazhbayev, Y.M. & Zhaparova, L.Z. (2013). Controlled release of Capreomycin sulfate from pH responsive nanocapsules. *e-Polymers, 13*(1). https://doi.org/10.1515/epoly-2013-0118

33 Burkeev, M.Z., Zhaparova, L.Z., Tazhbaev, E.M., Zhumagalieva, T.S., Ali, S.I. & van Herk, A.M. (2013). In Vitro Studies of Capreomycin Sulfate Release from Polyethylcyanoacrylate Nanoparticles. *Pharmaceutical Chemistry Journal, 47*(3), 154–156. https://doi.org/10.1007/s11094-013-0916-3

34 Galiyeva, A.R., Tazhbayev, Ye.M., Zhumagaliyeva, T.S., Sadyrbekov, D.T., Kaikenov, D.A., Karimova, B.N. & Shokenova, S.S. (2022) Polylactide-co-glycolide nanoparticles immobilized with isoniazid: Optimization using the experimental Taguchi method. *Bulletin of the University of Karaganda — Chemistry, 105(1), 69-77.* https://doi.org/10.31489/2022Ch1/69-77

Information about authors*

Galiyeva, Aldana Rymzhanovna (*corresponding author*) — Engineer, Institute of Chemical Problems, Karagandy University of the name of academician E.A. Buketov, Universitetskaya street, 28, 100024, Karaganda, Kazakhstan.; e-mail: aldana_karaganda@mail.ru; https://orcid.org/0000-0002-8551-6297

Tazhbayev, Yerkeblan Muratovich — Full Professor, Doctor of Chemical Sciences, Karagandy University of the name of academician E.A. Buketov, Universitetskaya street, 28, 100024, Karaganda, Kazakhstan; e-mail: tazhbayev@mail.ru; https://orcid.org/0000-0003-4828-2521

Yessentayeva, Nazgul Asylbekkyzy — 3rd year Doctoral Student, Department of organic chemistry and polymers, Karagandy University of the name of academician E.A. Buketov, Universitetskaya street, 28, 100024, Karaganda, Kazakhstan.; e-mail: naz.yessentayeva92@gmail.com; https://orcid.org/0000-0003-4820-8460

Daribay, Arailym Turashkyzy — Master Student, Karagandy University of the name of academician E.A. Buketov, Universitetskaya street, 28, 100024, Karaganda, Kazakhstan; e-mail: arailymdaribay@gmail.com; https://orcid.org/0000-0001-5675-0351

Marsel, Dias Temirlanuly — Master Student, Karagandy University of the name of academician E.A. Buketov, Universitetskaya street, 28, 100024, Karaganda, Kazakhstan; e-mail: marsel.dias@bk.ru; https://orcid.org/0000-0002-1204-0814

Sadyrbekov, Daniyar Tleuzhanovich — Candidate of Chemical Sciences, Researcher, laboratory of the engineering profile "Physical and chemical methods of research", Karagandy University of the name of academician E.A. Buketov, Universitetskaya street, 28, 100024, Karaganda, Kazakhstan; e-mail: acidbear@mail.ru; https://orcid.org/0000-0002-3047-9142

Zhaparova, Lyazzat Zhanybekovna — PhD, Associate Professor, Karagandy University of the name of academician E.A. Buketov, Universitetskaya street, 28, 100024, Karaganda, Kazakhstan; e-mail: lyazzh@mail.ru; https://orcid.org/0000-0003-1894-0255

Arystanova, Zhansaule Tulegenovna — Engineer, Institute of chemical problems, Karagandy University of the name of academician E.A. Buketov, Universitetskaya street, 28, 100024, Karaganda, Kazakhstan.; e-mail: zhansaule.kz@mail.ru.

*The author's name is presented in the order: *Last Name, First and Middle Names*

Article

UDC 541.1

https://doi.org/10.31489/2959-0663/2-23-13

Alexander S. Ospennikov[1] , Galina V. Kornilaeva[2] , Viktor F. Larichev[2] ,
Irina T. Fedyakina[2] , Lifeng Fu[3] , Zhuo Chen[4], Yangyang Yang[4], Andrey V. Shibaev[1,5*] ,
Eduard V. Karamov[2,6] , Ali S. Turgiev[2,6] , Liping Duan[7], William J. Liu[8], Olga E. Philippova[1]

[1]*Department of Physics, Lomonosov Moscow State University, Moscow, Russia;*
[2]*Gamaleya National Research Center for Epidemiology and Microbiology of the Russian Ministry of Health, Moscow, Russia;*
[3]*CAS Key Laboratory of Pathogen Microbiology and Immunology,*
Institute of Microbiology, Chinese Academy of Sciences (CAS), Beijing, China;
[4]*Shanghai Key Laboratory of Chemical Biology, Shanghai key Laboratory of New Drug Design,*
School of Pharmacy, East China University of Science and Technology, Shanghai, China;
[5]*Karagandy University of the name of academician E.A. Buketov, Karaganda, Kazakhstan;*
[6]*National Medical Research Center of Phthisiopulmonology and Infectious Diseases*
of the Russian Ministry of Health, Moscow, Russia;
[7]*NHC Key Laboratory of Parasite and Vector Biology, WHO Collaborating Centre for Tropical Diseases,*
National Institute of Parasitic Diseases, Chinese Center for Disease Control and Prevention, Shanghai, China;
[8]*NHC Key Laboratory of Biosafety, National Institute for Viral Disease Control and Prevention,*
Chinese Center for Disease Control and Prevention (China CDC), Beijing, China
(*Corresponding author′s e-mail: shibaev@polly.phys.msu.ru)

Activity against SARS-CoV-2 of Various Anionic Disinfectants and Their Complexes with Hydrophobically Modified Chitosan

The aim of this work was to study virucidal activity against SARS-CoV-2 of several anionic disinfectants, which are antiseptics recommended by the U.S. Environmental Protection Agency (EPA), and to prepare their complexes with hydrophobically modified chitosan active against SARS-CoV-2. Experiments were performed using a clinical isolate of SARS-CoV-2 obtained from a patient in 2020. It was shown that sodium dodecyl benzene sulfonate (SDBS) is already active at rather small concentrations (above 2 mM), which completely deactivate the virus. In the same concentration range, sodium caprylate does not show activity; and sodium lactate is active against SARS-CoV-2 only at much higher concentrations (225 mM). The most effective disinfectant — sodium dodecylbenzene sulfonate — was used to prepare complexes with hydrophobically modified chitosan. It was found that such complexes exhibit antiviral activity at very low concentrations (1.9 mM chitosan monomer units and 0.25 mM SDBS), at which the polymer without surfactant is not active against SARS-CoV-2.

Keywords: anionic disinfectants, SARS-CoV-2, chitosan, hydrophobic modification, polymer/surfactant complexes, sodium dodecyl benzene sulfonate, sodium caprylate, sodium lactate.

Introduction

In 2020, a pandemic outbreak of a new highly contagious coronavirus — SARS-CoV-2 — occurred [1–3], which in the beginning of 2023 is still a worldwide healthcare threat. The major route of viral transmission is airborne [4], however, it was reported that SARS-CoV-2 can be preserved on different surfaces for several days [5-7]. Therefore, development of effective disinfectants is very important for fighting the pandemic. Many types of disinfectants against SARS-CoV-2 are being considered [8], which include alcohol-based formulations [9, 10], quaternary ammonium compounds [11, 12], etc. Another approach consists in the use of carbonic or sulfonic acids and their salts, some of which were approved by the U.S. Environmental Protection Agency (EPA) as disinfectants. These include, for example, dodecylbenzenesulfonic, caprylic (octanoic) or lactic acid. Caprylate was reported to inactivate human immunodeficiency virus (Type-1), bovine viral diarrhea virus and pseudorabies virus [13]. Caprylic acid as an emulsion formulation is effective against several enveloped viruses such as Epstein–Barr, measles, herpes simplex, Zika, orf parapoxvirus, Ebola, Lassa, vesicular stomatitis and SARS-CoV-1, but does not inactivate a non-enveloped norovirus, showing that caprylic acid acts by disrupting the viral envelope [14]. Sanitizing fluids containing a high concentration of sodium dodecyl benzene sulfonate (SDBS) (3 wt% or 86 mM) and 70 wt% of ethanol

show virucidal activity against SARS-CoV-2, and surfactant and alcohol have a synergistic effect in virus deactivation [15]. Mixtures of dodecylbenzenesulfonic and lactic acids were reported to be effective as sanitizers, inactivating, for instance, norovirus [16]. However, a systematic study of the virucidal effect of these compounds on SARS-CoV-2 has not been performed.

One of the possible ways for improving the effectiveness of disinfectants is the preparation of their complexes with oppositely charged polymers [17]. For anionic disinfectants, chitosan and its derivatives are promising polymers for complex formation [18, 19], since chitosan is a polycation at mild acidic pH due to the protonation of amino groups. Complexes of chitosan with anionic molecules have not been regarded as antiviral agents, but they may be very promising due to several factors: 1) a single chitosan molecule bears multiple amino groups and can bind many low molecular weight anionic species within one complex, resulting in a collective transfer of disinfectant molecules onto the virion, 2) chitosan is biocompatible, which may reduce the overall toxicity of the complex as compared to anionic disinfectants alone.

The aim of this work was to investigate the virucidal activity of several anionic disinfectants (sodium dodecylbenzene sulfonate, caprylate and lactate) against SARS-CoV-2, to prepare complexes of hydrophobically modified (HM) chitosan with the most efficient anionic species and to study their virucidal properties.

Experimental

Materials

Sodium dodecylbenzene sulfonate (SDBS, hard type, purity > 95 %) was provided by Tokyo Chemical Industry (TCI). Caprylic acid (purity > 99.9 %) and lactic acid (purity > 99.9 %) were provided by Component-Reactiv, Russia. NaOH (purity > 99 %) was provided by Acros. All the solutions were prepared by using saline solution (0.9 wt% NaCl in distilled water) provided by Groteks, Russia. Caprylic and lactic acids were converted into sodium salts by dissolving in saline solution and adding appropriate amounts of NaOH. The chemical structures of the anionic compounds used in this work are presented in Figure 1.
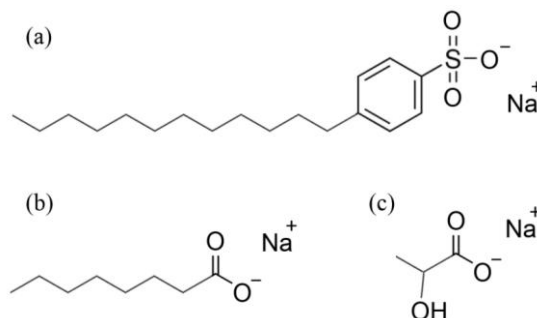
Figure 1. Chemical structure of sodium dodecylbenzene sulfonate (*a*), sodium caprylate (*b*) and sodium lactate (*c*)

Chitosan was obtained from chitin contained in the shells of Far-East crabs. The samples were grinded, and chitin pieces smaller than 0.25 mm were taken. Then, chitin was demineralized: metal salts were removed by triple washing by 1 wt% HCl and water, then by triple washing by 1M NaOH, and then by distilled water. The sample was dried and deacetylated by treatment with 2M NaOH at heating for 2 h, and then washed again by distilled water. This resulted to the conversion of chitin into chitosan. The molecular weight of chitosan was determined by static light scattering in the solvent that suppresses chitosan aggregation (0.3M acetic acid and 0.2M ammonium acetate) [20] and was equal to 170 000 g/mol.

Glacial acetic acid (purity > 99 %), dodecyl aldehyde (purity > 92 %) and sodium cyanoborohydride (purity > 95 %) were purchased from Sigma Aldrich. Ethanol was provided by Ferein (Russia) and was purified by distillation. Isopropanol (purity > 96 %) was obtained from Acros. For chitosan modification, distilled deionized water was used, which was obtained by MilliQ system (Millipore).

For virucidal activity studies, Vero E6 cells from ATCC (Manassas, USA) (CRL-1586) were cultured in high glucose Dulbecco's modified Eagle's medium (DMEM) (Sigma-Aldrich) supplemented with 5 % fetal calf serum (FCS), 2 mM L-glutamine and a mixture of antibiotics (150 u/mL penicillin and 150 u/mL streptomycin) at 37 °C in 5 % CO_2. The stock of SARS-CoV-2 (strain HCoV-19/Russia/Moscow-PMVL-12/2020 (EPI_ISL_572398) isolated from a patient) was the culture liquid withdrawn from cultures of the infected Vero E6 cells.

Hydrophobic modification of chitosan

Hydrophobic modification of chitosan was performed by the method of Rinaudo et al. [21]. First, chitosan (18 g/L) was dissolved in 0.2 M aqueous acetic acid solution by gentle stirring overnight, and pH after dissolution was ca. 0.8–1.0. Then ethanol (2:3 v/v) was added, and pH was adjusted to 5.0 by adding concentrated (1M) aqueous NaOH. After that, an appropriate amount of dodecyl aldehyde solution (20 g/L) in ethanol was added, so that its concentration in the reaction medium was 1.6 g/L. Then, sodium cyanoborohydride was added (concentration in the reaction medium 20 g/L), and the solution was stirred for 48 h at 25 °C.

The product was precipitated by adding 2M NaOH and washed twice with ethanol/water mixture (8:10 v/v) and once with isopropanol. Then, the precipitate was dissolved in aqueous HCl solution (pH 3), filtered through ceramic ROBU filters (16-40 µm pores) and lyophilized. In such a way, hydrophobically modified (HM) chitosan in hydrochloride form was obtained, which is soluble in water [22]. Its chemical structure is shown in Figure 2.
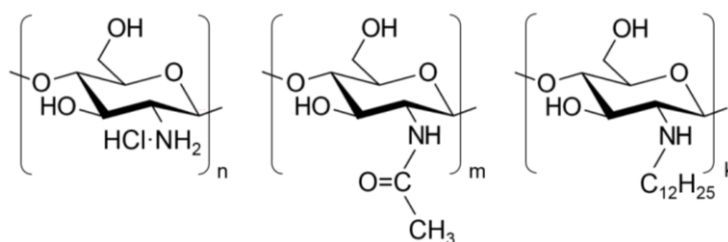
Figure 2. Chemical structure of chitosan hydrochloride modified with n-dodecyl side groups

The degree of hydrophobic modification was determined by ^{1}H NMR spectroscopy using Bruker AV-600 spectrometer. The spectrum was recorded at 30 °C in D_2O (Astrachem, Russia, isotopic purity > 99.9 %) as a solvent. Peak attribution was made according to the previously published data [21, 23]. The degree of modification (fraction of monomer units modified by *n*-dodecyl groups) was determined from the ratio of peaks at 0.89 ppm (methyl protons of *n*-dodecyl groups) and at 3.02 ppm (C2 methine protons of the saccharide ring) (Fig. 3) and was equal to 4.7 %. The degree of acetylation was calculated from the ratio of peaks at 2.09 ppm (methyl protons of acetyl groups) and at 3.02 ppm and was equal to 6.7 %.
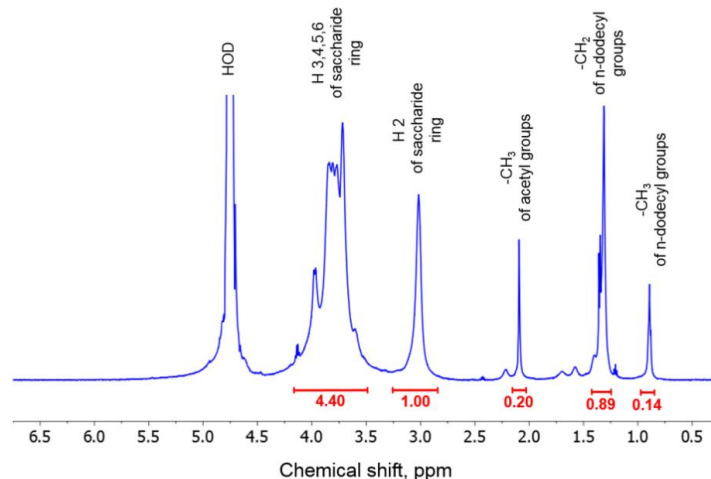
Figure 3. ^{1}H NMR spectrum of HM chitosan at 30 °C in D_2O

Preparation of chitosan / disinfectant complexes

In order to obtain polymer / disifectant complexes, solutions of chitosan hydrochloride and disinfectant were first prepared in saline (at pH 5.2), and then mixed in appropriate quantities. In the final samples, the concentration of chitosan was kept at 0.32 g/L (1.875 mM of monomer units), and the optimal molar ratio of SDBS to chitosan monomer units was 0.13. Complex formation proceeded due to interaction between anionic disinfectant species and cationic amino groups of chitosan. Complex formation was proven by the following: chitosan / SDBS mixture was dialysed against saline by using dialysis tubes with 12 000 kDa cutoff, through which only small SDBS molecules can pass. After dialysis, the composition of the complex was ana-

lyzed by 1H NMR, and the ratio of SDBS molecules to chitosan monomer units was found to be 0.12, e.g. close to the feed ratio during complex preparation, meaning that interaction between chitosan and SDBS within the complex is rather strong and does not allow SDBS molecules to freely leave the complex.

Virucidal activity

Solutions of anionic disinfectants or their complexes with HM chitosan were incubated with an equal volume of the virus stock at room temperature for 60 min. Viral particles were then separated from disinfectants by centrifugation at 27,000 rpm for 1 h to avoid their toxic effects on the cells. Viral pellets were resuspended in 300 µL of support medium (DMEM, 1 % FCS), and 10-fold dilutions in support medium were prepared for titer determination. Confluent Vero-E6 monolayers in 96-well plates were infected with the dilutions thus prepared, and, after a 2-h incubation (adsorption), the inoculum was removed. The plates were washed twice with FCS-free DMEM, filled with another type of support medium (DMEM, 2 % FCS) and further incubated at 37 °C in 5 % CO_2 for 96 h. Virus-induced cytopathic effects were assessed by microscopic examination of the cells and taken as an indication of their infection. The amount of the active virus, judged from the percentage of the infected cells, was determined by the endpoint dilution assay (titration) and expressed in fifty-percent tissue culture infective doses ($TCID_{50}$). The titer was calculated using the Spearman-Kärber method and presented as lg $TCID_{50}$/0.1 mL [24].

The virucidal efficacy of surfactants was assessed by the difference in the virus titers (A) between control A_c (without disinfectants) and experimental A_e samples:

$$A = A_c - A_e.$$

The protection index, or inhibition coefficient (IC), was calculated using the following formula:

$$IC = [(A_c - A_e)/A_c] \times 100 \%.$$

Results and Discussion

Virucidal activities of individual anionic disinfectants

First, virucidal activity of individual anionic compounds was investigated. Sodium dodecylbenzenesulfonate (SDBS) and lactate were dissolved in saline (0.9 wt% NaCl), and pH was adjusted to 5.0 by adding HCl or NaOH (initial pH values after dissolution were 9.2 for SDBS and 1.4 for lactic acid). The values of pK_a for dodecylbenzenesulfonic and lactic acid are equal to −1.8 [25] and 3.8 [26], respectively. Therefore, at pH 5.2 they are almost completely in salt forms. pK_a of caprylic acid is slightly higher: 4.89 [27]. Thus, in order to transform it into a salt and ensure its solubility in water, the solutions were prepared at slightly higher pH 6.3–6.4. Caprylic acid has a low water solubility (4.7 мM [27]), therefore, rather sophisticated approaches were previously employed to prepare its antiseptic formulations: e.g., emulsification [14] or the use of solvents different than water [28].

Virucidal activity of SDBS at different concentrations is shown in Figure 4 as the virus inhibition coefficient (IC), which shows the relative difference in the virus titers in a control experiment and in the experiment where virus suspension is brought in contact with the disinfectant. It is seen that at very low concentrations (below 0.125 mM), SDBS does not show virucidal activity (IC = 0), but upon increase of the concentration, the activity appears and increases. Rather low absolute SDBS concentrations already show high virucidal activity against SARS-CoV-2: the virus titer in the experiments is reduced by 6.5 orders of magnitude (Δlg $TCID_{50}$ = 6.5), and IC is equal to 100 % (Fig. 4).
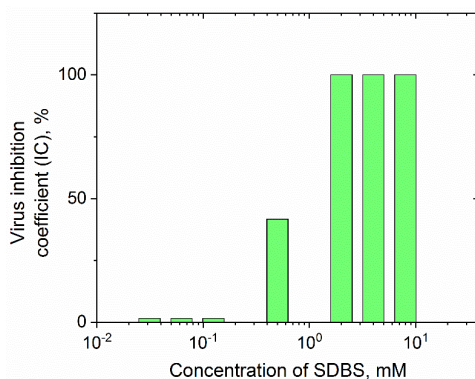
Figure 4. Inhibition coefficients of SARS-CoV-2 by SDBS solutions of different concentrations.
Solvent: 0.9 wt% NaCl in water

A possible mechanism of SDBS action against SARS-CoV-2 consists in its incorporation into the viral envelope and its subsequent disruption, as well as in denaturation of viral proteins [29]. The incorporation of SDBS into the lipid bilayer is possible due to its surface activity, since SDBS is a surfactant and consists of a polar hydrophilic benzene sulfonate head, and non-polar hydrophobic alkyl tail, which favors its interaction with the lipid bilayer. The critical micelle concentration (CMC) of SDBS equals to 0.4 mM in saline [30]. It means that SDBS is in the micellar form when it shows virucidal activity. This is reasonable, because micelles provide cooperative transfer of multiple SDBS molecules on each viral particle, increasing the probability of its disruption.

In the same concentration range where SDBS is active against SARS-CoV-2, sodium caprylate does not show any activity (Fig. 5a). This may be explained by lower surface activity of caprylate as compared to dodecylbenzenesulfonate: indeed, it has a shorter alkyl tail (C8) and is characterized by much higher CMC (400 mM [31]) than for SDBS; thus, in the studied range of concentrations, caprylate does not form micelles and is a molecular solution. This may result in a smaller amount of caprylate molecules simultaneously interacting with the envelope surface.
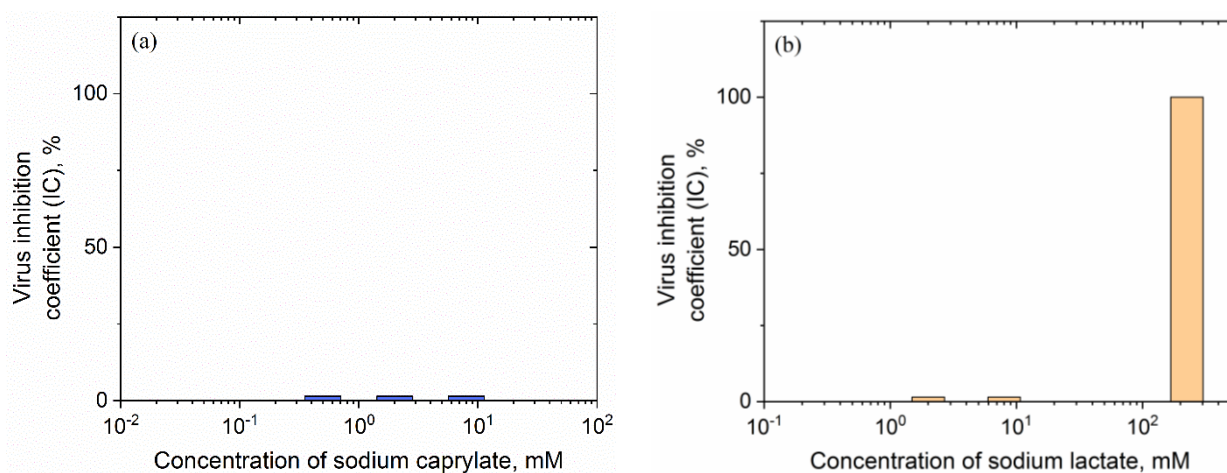
Figure 5. Inhibition coefficients of SARS-CoV-2 by sodium caprylate (*a*) and sodium lactate (*b*) solutions of different concentrations. Solvent: 0.9 wt% NaCl in water

At the same concentrations (below 8 mM), sodium lactate does not show any virucidal activity; however, it is active at a much higher concentration. 225 mM of lactate induce a complete inactivation of SARS-CoV-2: its titer is reduced by 6.5 orders of magnitude. Such a high concentration as compared to SDBS may be a result of different properties of these two molecules: SDBS is surface-active and incorporates into the lipid membranes, while lactate is not a surfactant.

Therefore, SDBS shows the highest activity against SARS-CoV-2 among three anionic disinfectants studied: it completely inactivates the virus at rather low concentrations, at which sodium caprylate and lactate do not show virucidal properties. Therefore, SDBS is the most promising disinfectant for preparation of formulations with HM chitosan.

Virucidal activities of polymer / disinfectant complexes

At the next stage, antiviral properties of chitosan / SDBS complexes were investigated. Figure 6 shows the comparison of virucidal activity of chitosan and its complex with SDBS at very low concentrations of the components. It is seen that while HM chitosan itself does not possess virucidal properties at this concentration, polymer/surfactant complexes show some activity: IC is equal to 18.2 %, meaning that the virus titer is decreased by one order of magnitude upon contact with HM chitosan / SDBS solution.
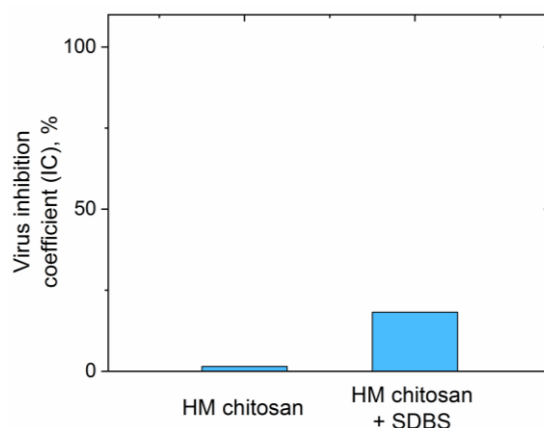
Figure 6. Inhibition coefficients of SARS-CoV-2 by HM chitosan and its mixture with SDBS.
HM chitosan monomer units: 1.875 mM, SDBS: 0.25 mM. Solvent: 0.9 wt% NaCl in water

A possible mechanism of virucidal action of HM chitosan / SDBS complexes is similar to those of SDBS and may consist in the disruption of the viral capsid when it is destabilized by incorporation of surfactant molecules. At the same time, the complexes may be more stable than SDBS micelles, since surfactant molecules in the micelle are bound together by hydrophobic interactions, while in the complex they are also bound to the polymer chain due to several distinct interactions: electrostatic interaction between anionic polar heads of the surfactant and of chitosan amino groups, Van der Waals interactions between surfactant and polymer [32], and incorporation of the polymer n-dodecyl groups into the micelles [33]. All these factors may increase the complex stability as compared to the micelles, and may also increase the SDBS micellar aggregation number (which is typical for the case of polymer/surfactant interactions [34]), thus increasing the number of SDBS molecules transferred to one virion by a single complex.

Conclusions

In this paper, the virucidal activities of several anionic disinfectants (sodium dodecylbenzene sulfonate, caprylate and lactate) against SARS-CoV-2 were investigated. The most effective disinfectant is SDBS, which deactivates the virus already at rather small concentrations (above 2 mM). In the same concentration range, caprylate and lactate do not show any activity. Sodium lactate also shows virucidal properties, but at concentrations 2 orders of magnitude higher than for SDBS. Complexes of HM chitosan with SDBS also possess antiviral properties at very low concentrations (1.9 mM chitosan monomer units and 0.25 mM SDBS), at which the polymer without surfactant is not active against SARS-CoV-2.

Acknowledgments

References

1   Wu, D., Wu, T., Liu, Q., & Yang, Z. (2020). The SARS-CoV-2 outbreak: What we know. *Intern. J. Infect. Dis., 94*, 44–48. https://doi.org/10.1016/j.ijid.2020.03.004

2   Liu, W.J., & Wu, G.Z. (2020). Convincing the confidence to conquer COVID-19: from epidemiological intervention to laboratory investigation. *Biosaf. Health, 2(4)*, 185–186. http://dx.doi.org/10.1016/j.bsheal.2020.11.005

3   Gao, G.F., & Liu, W.J. (2021). Let's get vaccinated for both flu and COVID-19: On the World flu day 2021. *China CDC Wkly., 29*, 3(44), 915–917. https://doi.org/10.46234/ccdcw2021.227

4   Prather, K.A., Marr, L.C., Schooley, R.T., McDiarmid, M.A., Wilson, M.E., & Milton, D.K. (2020). Airborne transmission of SARS-CoV-2. *Science, 370*, 6514, 303–304. http://dx.doi.org/10.1126/science.abf0521

5   Chin, A.W.H., Chu, J.T.S., Perera, M.R.A., Hui, K.P.Y., Yen, H. -L., Chan, M.C.W., Peiris, M., & Poon, L.L.M. (2020). Stability of SARS-CoV-2 in different environmental conditions. *Lancet Microbe, 1*, E10. https://doi.org/10.1016/S2666-5247(20)30003-3

6   Van Doremalen, N., Bushmaker, T., Morris, D.H., Holbrook, M.G., Gamble, A., Williamson, B.N., Tamin, A., Harcourt, J.L., Thornburg, N.J., Gerber, S.I., et al. (2020). Aerosol and surface stability of SARS-CoV-2 as compared with SARS-CoV-1. *N. Engl. J. Med., 382*, 1564–1567. https://doi.org/10.1056/NEJMc2004973

7   Liu, P., Yang, M., Zhao, X., Guo, Y., Wang, L., Zhang, J., Lei, W., Han, W., Jiang, F., Liu, W.J., Gao, G.F., & Wu, G. (2020). Cold-chain transportation in the frozen food industry may have caused a recurrence of COVID-19 cases in destination: Successful isolation of SARS-CoV-2 virus from the imported frozen cod package surface. *Biosaf. Health, 2(4)*, 199–201. https://doi.org/10.1016/j.bsheal.2020.11.003

8   Xiao, S., Yuan, Z., & Huang, Y. (2022) Disinfectants against SARS-CoV-2: A review. *Viruses, 14(8)*, 1721. https://doi.org/10.3390/v14081721

9   Kratzel, A., Todt, D., V'Kovski, P., Steiner, S., Gultom, M., Thao, T.T.N., Ebert, N., Holwerda, M., Steinmann, J., Niemeyer, D., et al. (2020). Inactivation of severe acute respiratory syndrome coronavirus 2 by WHO-recommended hand rub formulations and alcohols. *Emerg. Infect. Dis., 26*, 1592–1595. https://doi.org/10.3201/eid2607.200915

10   Singh, D., Joshi, K., Samuel, A., Patra, J., & Mahindroo, N. (2020). Alcohol-based hand sanitisers as first line of defence against SARS-CoV-2: A review of biology, chemistry and formulations. *Epidemiol. Infect., 148*, 1–23. https://doi.org/10.1017/S0950268820002319

11   Ogilvie, B., Solis-Leal, A., Lopez, J., Poole, B., Robison, R., & Berges, B. (2020). Alcohol-free hand sanitizer and other quaternary ammonium disinfectants quickly and effectively inactivate SARS-CoV-2. *J. Hosp. Infect., 108*, 142–145. https://doi.org/10.1016/j.jhin.2020.11.023

12   Karamov, E.V., Larichev, V.F., Kornilaeva, G.V., Fedyakina, I.T., Turgiev, A.S., Shibaev, A.V., Molchanov, V.S., Philippova, O.E., & Khokhlov, A.R. (2022). Cationic surfactants as disinfectants against SARS-CoV-2. *Int. J. Mol. Sci., 23(12)*, 6645. https://doi.org/10.3390/ijms23126645

13   Korneyeva, M., Hotta, J., Lebing, W., Rosenthal, R.S., Franks, L., & Petteway Jr, S.R. (2002). Enveloped virus inactivation by caprylate: A robust alternative to solvent-detergent treatment in plasma derived intermediates. *Biologicals, 30*, 153–162. https://doi.org/10.1006/biol.2002.0334

14   Fletcher, N.F., Meredith, L.W., Tidswell, E.L., Bryden, S.R., Gonçalves-Carneiro, D., Chaudhry, Y., Shannon-Lowe, C., Folan, M.A., Lefteri, D.A., Pingen, M., Bailey, D., McKimmie, C. S., & Baird, A.W. (2020). A novel antiviral formulation inhibits a range of enveloped viruses. *J. Gen. Virol., 101*, 1090–1102. https://doi.org/10.1099/jgv.0.001472

15   Jahromi, R., Mogharab, V., Jahromi, H., & Avazpour, A. (2020). Synergistic effects of anionic surfactants on coronavirus (SARS-CoV-2) virucidal efficiency of sanitizing fluids to fight COVID-19. *Food Chem. Toxicol., 145*, 111702. https://doi.org/10.1016/j.fct.2020.111702

16   Faircloth, J., Goulter, R.M., Manuel, C.S., Arbogast, J.W., Escudero-Abarca, B., & Jaykus, L.-A. (2022). The efficacy of commercial surface sanitizers against norovirus on formica surfaces with and without inclusion of a wiping step. *Appl. Environ. Microbiol., 88*, 17. https://doi.org/10.1128/aem.00807-22

17   Molchanov, V.S., Shibaev, A.V., Karamov, E.V., Larichev, V.F., Kornilaeva, G.V., Fedyakina, I.T., Turgiev, A.S., Philippova, O.E., & Khokhlov, A.R. (2022). Antiseptic polymer–surfactant complexes with long-lasting activity against SARS-CoV-2. *Polymers, 14*, 2444. https://doi.org/10.3390/polym14122444

18   Chiappisi, L., & Gradzielski, M. (2015) Co-assembly in chitosan–surfactant mixtures: thermodynamics, structures, interfacial properties and applications. *Adv. Colloid Interface Sci., 220*, 92–107. https://doi.org/10.1016/j.cis.2015.03.003

19   Onesippe, C., & Lagerge, S. (2008). Study of the complex formation between sodium dodecyl sulfate and chitosan. *Coll. Surf. A: Phys.-Chem. Eng. Asp., 317*, 1–3, 100–108. https://doi.org/10.1016/j.colsurfa.2007.10.002

20   Korchagina, E.V., & Philippova, O.E. (2012). Effects of hydrophobic substituents and salt on core–shell aggregates of hydrophobically modified chitosan: Light scattering study. *Langmuir, 28*, 7880–7888. https://doi.org/10.1021/la3013409

21   Desbrières, J., Martinez, C., & Rinaudo, M. (1996). Hydrophobic derivatives of chitosan: Characterization and rheological behavior. *Int. J. Biol. Macromol., 19*, 21-28. https://doi.org/10.1016/0141-8130(96)01095-1

22   Signini, R., & Campana Filho, S.P. (1999). On the preparation and characterization of chitosan hydrochloride. *Polymer Bulletin, 42,* 159–166. https://doi.org/10.1007/s002890050448

23   Lavertu, M., Xia, Z., Serreqi, A.N., Berrada, M., Rodrigues, A., Wang, D., Buschmann, M.D., & Gupta, A. (2003). A validated ^{1}H NMR method for the determination of the degree of deacetylation of chitosan. *J. Pharm. Biomed. Analysis, 32*, 6, 1149–1158. https://doi.org/10.1016/S0731-7085(03)00155-9

24   Flint, S.J., Racaniello, V.R., Rall, G.F., Skalka, A.M., & Enquist, L.W. (2015). The infectious cycle. In *Principles of Virology*, 4th ed.; ASM Press: Washington, DC, USA, 1, 24–52.

25   Metabocard for 4-Dodecylbenzenesulfonic Acid (Human Metabolome Database ID HMDB0059915). Retrieved from https://hmdb.ca/metabolites/HMDB0059915

26   D-Lactic acid (DrugBank Database Accession Number DB03066). Retrieved from https://go.drugbank.com/drugs/DB03066

27   Octanoic acid (PubChem Database CID379). Retrieved from https://pubchem.ncbi.nlm.nih.gov/compound/Octanoic-acid

28   Nair, M.K.M., Joy, J., Vasudevan, P., Hinckley, L., Hoagland, T.A., & Venkitanarayanan, K.S. (2005). Antibacterial effect of caprylic acid and monocaprylin on major bacterial mastitis pathogens. *J. Dairy Sci., 88*, 3488–3495. https://doi.org/10.3168/jds.S0022-0302(05)73033-2

29   Simon, M., Veit, M., Osterrieder, K., & Gradzielski, M. (2021). Surfactants — compounds for inactivation of SARS-CoV-2 and other enveloped viruses. *Curr. Opin. Colloid Interface Sci., 55*, 101479. https://doi.org/10.1016/j.cocis.2021.101479

30   Chauhan, S., & Sharma, K. (2014). Effect of temperature and additives on the critical micelle concentration and thermodynamics of micelle formation of sodium dodecyl benzene sulfonate and dodecyltrimethylammonium bromide in aqueous solution: A conductometric study. *J. Chem. Thermodyn., 71*, 205–211. http://dx.doi.org/10.1016/j.jct.2013.12.019

31 Lindman, B., Kamenka, N., Puyal, M.-C., Brun, B., & Jonsson, B. (1984). Tracer self-diffusion studies of micelle formation of a short-chain ionic surfactant, sodium n-octanoate. *J. Phys. Chem., 88*, 53-57. https://doi.org/10.1021/j150645a013

32 Blagodatskikh, I.V., Vyshivannaya, O.V., Bezrodnykh, E.A., Tikhonov, V.E., Orlov, V.N., Shabelnikova, Y.L., & Khokhlov, A.R. (2022). Peculiarities of the interaction of sodium dodecyl sulfate with chitosan in acidic and alkaline media. *Int. J. Biol. Macromol., 214*, 192–202. https://doi.org/10.1016/j.ijbiomac.2022.06.059

33 Piculell, L., Thuresson, K., & Lindman, B. (2001). Mixed solutions of surfactant and hydrophobically modified polymer. *Polym. Adv. Technol., 12*, 44–69. https://doi.org/10.1002/1099-1581(200101/02)12:1/2<44::AID-PAT944>3.0.CO;2-O

34 Hansson, P., & Lindman, B. (1996). Surfactant-polymer interactions. *Curr. Opin. Colloid Interface Sci., 1*, 5, 604–613. https://doi.org/10.1016/S1359-0294(96)80098-7

Information about authors*

Ospennikov, Alexander Sergeevich — 1st year PhD student, Department of Physics, Lomonosov Moscow State University, GSP-1, Leninskie Gory, 119991, Moscow, Russia; e-mail: ospennikov@polly.phys.msu.ru; https://orcid.org/0000-0002-1272-3658

Kornilaeva, Galina Vladimirovna — candidate of biological sciences, leading researcher, Gamaleya National Research Center for Epidemiology and Microbiology of the Russian Ministry of Health, 18 Gamaleya St., 123098, Moscow, Russia; e-mail: kornilaeva@yandex.ru; https://orcid.org/0000-0003-1819-0693

Larichev, Viktor Filippovich — doctor of medical sciences, leading researcher, Gamaleya National Research Center for Epidemiology and Microbiology of the Russian Ministry of Health, 18 Gamaleya St., 123098, Moscow, Russia; e-mail: vlaritchev@mail.ru; https://orcid.org/0000-0001-8262-5650

Fedyakina, Irina Timofeevna — candidate of biological sciences, leading researcher, Gamaleya National Research Center for Epidemiology and Microbiology of the Russian Ministry of Health, 18 Gamaleya St., 123098, Moscow, Russia; e-mail: irfed2@mail.ru; https://orcid.org/0000-0001-6421-9632

Fu, Lifeng — professor, CAS Key Laboratory of Pathogen Microbiology and Immunology, Institute of Microbiology, Chinese Academy of Sciences (CAS), NO.1 West Beichen Road, Chaoyang District, 100101, Beijing, China; e-mail: fulf@im.ac.cn; https://orcid.org/0000-0003-0431-5424

Chen, Zhuo — professor, Shanghai Key Laboratory of Chemical Biology, Shanghai key Laboratory of New Drug Design, School of Pharmacy, East China University of Science and Technology, 130 Meilong Road, 200237, Shanghai, China; e-mail: chenzhuo@ecust.edu.cn

Yang, Yangyang — professor, Shanghai Key Laboratory of Chemical Biology, Shanghai Key Laboratory of New Drug Design, School of Pharmacy, East China University of Science and Technology, 130 Meilong Road, 200237, Shanghai, China; e-mail: triyang@ecust.edu.cn

Shibaev, Andrey Vladimirovich — candidate of physico-mathematical sciences, associate professor, Department of Physics, Lomonosov Moscow State University, GSP-1, Leninskie Gory, 119991, Moscow, Russia; Karagandy University of the name of academician E.A. Buketov, Universitetskaya str., 28, 100024, Karaganda, Kazakhstan; e-mail: shibaev@polly.phys.msu.ru; https://orcid.org/0000-0002-3019-5764

Karamov, Eduard Viktorovich — doctor of biological sciences, professor, Gamaleya National Research Center for Epidemiology and Microbiology of the Russian Ministry of Health, 18 Gamaleya St., 123098, Moscow, Russia; e-mail: karamov2004@yandex.ru; https://orcid.org/0000-0003-1162-118X

Turgiev, Ali Saladinovich — leading researcher, Gamaleya National Research Center for Epidemiology and Microbiology of the Russian Ministry of Health, 18 Gamaleya St., 123098, Moscow, Russia; e-mail: turgiev@ld.ru; https://orcid.org/0000-0002-0500-6407

Duan, Liping — professor, NHC Key Laboratory of Parasite and Vector Biology, WHO Collaborating Centre for Tropical Diseases, National Institute of Parasitic Diseases, Chinese Center for Disease Control and Prevention, Shanghai 200025, China; e-mail: duanlp@nipd.chinacdc.cn

Liu, William J. — professor, NHC Key Laboratory of Biosafety, National Institute for Viral Disease Control and Prevention, Chinese Center for Disease Control and Prevention (China CDC), Beijing 102206, China; e-mail: liujun@ivdc.chinacdc.cn

Philippova, Olga Evgen'evna — doctor of physico-mathematical sciences, professor, Department of Physics, Lomonosov Moscow State University, GSP-1, Leninskie Gory, 119991, Moscow, Russia; e-mail: phil@polly.phys.msu.ru; https://orcid.org/0000-0002-1098-0255

*The author's name is presented in the order: *Last Name, First and Middle Names*

Zhanar S. Akhmetkarimova[1,2]* (iD), Gulshakhar K. Kudaibergen[2] (iD), Guldarigash K. Kaukabaeva[2] (iD), Sailau K. Abeldenov[2] (iD), Aidana B. Rysbek[2] (iD)

[1]*University of Reading, Reading, UK*
[2]*National Center for Biotechnology, Astana, Kazakhstan*
*(*Corresponding author's e-mail: z.akhmetkarimova@reading.ac.uk)*

Thiol-Ene Click Synthesis of Alginate Hydrogels Loaded with Silver Nanoparticles and Cefepime

Hydrogels used in biomedical applications, particularly for soft tissue treatment and regeneration, should have favorable mechanical properties and biocompatibility. Alginate hydrogels are suitable for developing wound dressings with desirable porosity, facilitating effective gas and vapor exchange necessary for wound healing. In this study, we present the synthesis and characterization of photocrosslinked hydrogels based on sodium alginate allyl glycidyl ether (SA-AGE). The composition and structure of the synthesized macromers were confirmed using nuclear magnetic resonance spectroscopy (1H-NMR), while scanning electron microscopy (SEM) revealed the presence of pores ranging in size from 5–32 µm. The UV light polymerization of SA-AGE hydrogel using the photoinitiator I295 was achieved within 60 minutes. The absorption of silver particles and the drug cefepime was determined through titration and UV-spectroscopy, indicating that the optimal concentration was 1 %. The antibacterial activity of the hydrogels loaded with silver nanoparticles and cefepime was evaluated against gram-negative (Pseudomonas aeruginosa) and gram-positive (Staphylococcus aureus) strains. Cytotoxicity of the hydrogels was assessed using the MTT assay with rat ADMSC cells, and the cell survival rate in the presence of the hydrogels was above 80 %, indicating their non-cytotoxic nature.

Keywords: alginate hydrogel, biopolymer, cefepime, photocrosslinked hydrogels, biocompatible, non-toxic, antibacterial activity, tissue engineering.

Introduction

The significance of wound infection has increased in the past few years, with surgical wounds being particularly affected and often resulting in severe sepsis. The primary contributors to this problem are gram-negative bacteria that have become nearly resistant to all existing antimicrobial drugs. Therefore, the development and implementation of innovative drugs and wound dressings, methods of treatment of purulent and chronic wounds are an urgent task for many researchers [1–3].

To produce an ionic polysaccharide sodium alginate, brown algae is extracted using an alkaline solution. Sodium alginate remains highly valued among naturally derived water-soluble polymers due to its numerous practical benefits. Its ability to form hydrogels in aqueous solutions in the presence of calcium ions has sparked increasing interest among researchers. The hydrogels based on sodium alginate possess remarkable properties such as high-water retention, biodegradability, and non-toxicity, making them ideal for a range of biotechnological, pharmaceutical, and medical applications [4–6]. They are particularly valuable for developing wound healing dressing and drug delivery systems [7]. Sodium alginate is known for its diverse range of biological activities, including antiviral, immunomodulatory, and hemostatic properties [8]. Alginate gels are widely used in the fields of medicine, drug delivery systems, and tissue engineering due to their ease of gelation, affordable cost, biocompatibility, low toxicity, biodegradability, hypoallergenic properties, and chelating ability [3].

Upon reviewing the available literature, our analysis indicated that there have been no previous studies on wound dressings incorporating cefepime, an antibacterial agent from the fourth generation of cephalosporin antibiotics (Fig. 1). It is worth highlighting that cefepime exerts a bactericidal effect by impeding the synthesis of microbial cell walls. Moreover, it demonstrates a wide range of activity against both gram-positive and gram-negative bacteria, including strains that are resistant to third-generation cephalosporin antibiotics and/or aminoglycoside [9].
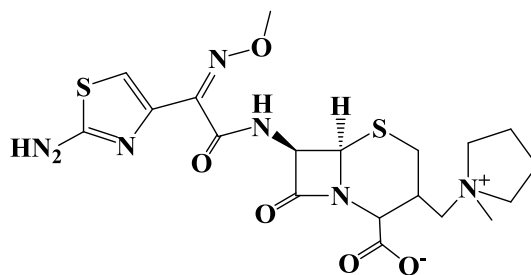
Figure 1. Chemical structure of cefepime

Cefepime demonstrates remarkable resistance to hydrolysis by most beta-lactamases and possesses rapid penetration into the cells of gram-negative bacteria. Its primary molecular target within bacterial cells is the penicillin-binding proteins. Cefepime exhibits efficacy against various gram-positive aerobes, both *in vitro* and *in vivo*, including *Staphylococcus aureus, Streptococcus pneumoniae, Streptococcus pyogenes*, and *Streptococcus viridans*. It also proves effective against gram-negative microorganisms such as *Proteus mirabilis, Pseudomonas aeruginosa, Escherichia coli, Enterobacter spp.*, and *Klebsiella pneumoniae* [10, 11].

At the same time, ionic silver exhibits bactericidal, strong antifungal, and antiseptic effects, making it a potent disinfectant against pathogenic microorganisms responsible for acute infections. When silver ions are absorbed by the cell membrane of microbes, they disrupt certain cellular functions while keeping the cell viable. This mechanism represents the interaction between silver and microbial cells [11].

To obtain novel derivatives of sodium alginate with specific properties, the click chemistry method, specifically thiol-ene reactions, was used. It is worth highlighting that click chemistry refers to a set of chemical reactions designed for the rapid and reliable synthesis of compounds by seamlessly connecting individual components. Thiol-ene reactions offer notable advantages, such as versatile reaction conditions (including radical reactions and catalytic processes) and the ability to use a wide range of substrates with various unsaturated bonds, such as acrylates, methacrylates, and ethers [12]. Over the past few years, this reaction method has become widely used in different scientific and technological domains, making a significant impact to the development of biomedical materials. Therefore, the click chemistry method, particularly thiol-ene reactions, has emerged as an excellent tool for producing materials with diverse purposes.

Hence, the aim of this study is to employ thiol-ene click synthesis to produce alginate hydrogels loaded with silver nanoparticles and cefepime, and to investigate their chemical and biological properties. Specifically, the purposes include determining the NMR structure of alginate macromers, assessing the sol-gel fraction and degradation extent of the alginate hydrogel, evaluating the antibacterial activity of the hydrogel impregnated with silver particles and cefepime using disk diffusion tests against *Pseudomonas aeruginosa* and *Staphylococcus aureus*, and lastly, examining the cytotoxicity of the hydrogel through MTT assay on the viability of rat ADMSC cells.

Experimental

Preparation and characterization of hydrogel

The synthesis of sodium alginate (SA) and allyl glycidyl ether (AGE) was performed based on a previously reported method [13], with some modifications. Briefly, a 2 % (w/v) solution of SA was prepared by mixing 10 mL of Milli-Q water. Continuous stirring was employed while adding 0.96 g of AGE to the alginate solution. Concentrated acetic acid was added to adjust the pH to 3. The reaction was carried out at 60 °C for six hours. A generous amount of cold ethanol was added to precipitate the solution. The product was then subjected to 2–3 ethanol washes and subsequently freeze-dried. The entire synthesis process of sodium alginate allyl glycidyl ether (SA-AGE) was carried out in complete darkness.

Assessment of hydrogel density, gel fractions, and degradation degree involved the use of established methods. These measurements were performed to determine the gel yield, employing a well-established equation [14]:

$$\text{Gel}(\%) = \frac{W_w}{W_i} \times 100, \tag{1}$$

where W_w and W_i — the weights of the dry and swollen samples respectively.

Following that, the hydrogels labeled as W_1 were weighed and transferred into sterile PBS tubes (0.1 M, pH 7.4) with a volume of 50 ml. During the 8-week incubation period at 37 °C, the solution was changed twice a week. At specific intervals, hydrogel samples were removed from the solution and rinsed with deionized water. After subjecting the samples to 24 hours of freeze-drying (resulting in samples labeled as W_2), the degree of degradation was determined using the subsequent equation [14, 15]:

$$DD(\%) = \frac{W_1 - W_2}{W_1} \times 100. \tag{2}$$

The gravimetric method was used to study the swelling process. The mass degree of swelling, represented as a percentage, was determined by comparing the mass of the swollen structured hydrogel to its initial mass. This equation was utilized to quantify the intensity of swelling:

$$\alpha(\%) = \frac{m_n - m_1}{m_1} \times 100, \tag{3}$$

where m_1 — the mass of the sample before the start of the study, g; m_n — the mass of the sample after a certain time, g.

Separately, concentration of 2.5 % (w/v) of SA-AGE was achieved in borosilicate vials by dissolving it in Milli-Q water. In respect of the macromer, I295 was added to the resulting solution (w/v) at different concentrations (2.5 %, 5 %, and 10 %, respectively), and UV light (365 nm) was then applied for 1 hour.

The 1H NMR spectra of the samples were recorded on a JNM-ECA 500 spectrometer (JEOL, USA) operating at a central field strength of 11.74 (500 MHz 1H), with a current below 95 Amps and field stability (drift) of less than 5 Hz/hr 1H drift. The inductance of the spectrometer was 146 H (nominal). MestreNova software was employed to process the spectral data. All samples were dissolved in D_2O at a concentration of 1 % (w/v) to obtain the spectra. The extent of MA substitution in the GG backbone was evaluated by analyzing the 1H NMR spectra. The percentage degree of MA substitution (%DM) in the GG chain was determined using the following equation [14]:

$$\%DM = \frac{H_b + H_C/2}{GG - 1/6} \times 100, \tag{4}$$

where H_C, H_b and GG -1 — the signals of the anomeric carbon hydrogen in the mannuronic units (ca.3.70-3.90 ppm), the relayed peaks of the anomeric carbon hydrogen, and in the methacrylate group the two vinyl hydrogens (5.00-5.75 ppm), respectively.

The method is based on the formation of a yellow-colored silver-dithizone complex and subsequent extraction of the silver-dithizone complex into a layer of tetrachloroethylene at pH 1.5–2.0. Colorimetry is performed using the method of standard series based on mixed-color formation [16]. 20 ml of the test solution containing 0.1–1 N sulfuric acid is placed into a separating funnel and diluted with water to a total volume of 50 ml. The mixture is titrated with a dithizone solution until the silver is completely extracted, which means that the extract, after 30 seconds of shaking, retains a green instead of the initial golden-yellow color. The accuracy of this method of determination is 0.5 %.

Cefepime was incorporated into the alginate hydrogel lowed silver nanoparticles using the absorption method. The degree of cefepime absorption was analyzed using spectrophotometry in the short-wave region. The optical density of standard and adsorbed solutions was measured using on "Eco-chem" scanning spectrophotometer, model PE-5300VI. A mixture of dimethyl sulfoxide and water (5:5) was used as a reference solution in quartz cuvettes with a 10 mm working layer thickness at a wavelength of 265 nm. The procedure for constructing a calibration curve for the analyzed substances was as follows: 0.01, 0.03, 0.05, 0.07, 0.09, 0.15, and 0.18 mL of the analyzed substance solution in water (1 mg/mL) were added into 10 mL volumetric flasks. 4.99, 4.97, 4.95, 4.93, 4.85, and 4.82 mL of water, respectively, were added to each flask. Then, 5 mL of dimethyl sulfoxide were added to each flask. The quantitative value of the adsorbed drug was determined using the calibration curve, taking into account the sample of the taken drug.

The antibacterial properties of alginate hydrogel samples were evaluated by the microbiological disc diffusion method, namely, the measurement of growth inhibition zones of test cultures *Staphylococcus aureus* and *Pseudomonas aeruginosa*. For the study, bacterial cultures of *Staphylococcus aureus* with a titer of 9.1×10^{10} CFU/ml and *Pseudomonas aeruginosa* 6×10^7 CFU/ml were selected after incubation for 14 hours in a liquid nutrient broth on a shaker at 150 rpm and temperature 37 °C. Samples of hydrogels containing particles of silver and antibiotic cefepime (in various concentrations) were placed on LB agar medium no later than 15 minutes after inoculation with sterile cotton swabs, streaking a suspension (culture fluid)

of a certain density equivalent to a turbidity standard of 0.5 according to McFarland and incubated at 37 °C. The hydrogel was pre-sterilized with a UV lamp for 15 minutes (254 nm). To compare the antibacterial activity of different samples of hydrogels containing different concentrations of silver and/or cefepime particles, the diameters of the growth inhibition zones of test cultures in millimeters were measured relative to the size of the hydrogel discs.

The dried hydrogels were examined for their morphology using a scanning electron microscope (SEM, Auriga Crossbeam 540, Carl Zeiss) operating in SE2 signal mode. The SEM was configured with an analytic column, a working distance (WD) of 4.6 mm, noise reduction Line Int. Busy SB Grid 833 V, and a scan speed of 3.

The cells were cultured at different densities ($1-5 \times 10^6$ cells per mL) in a transparent plate following the desired protocol. In the case of suspension cells, the 96-well plates were centrifuged at $1,000 \times$ g, 4 °C for 5 minutes using a microplate-compatible centrifuge, and the media was carefully removed. Then, 50 μL of serum-free media and 50 μL of MTT Reagent were added to each well. For the background control wells, 50 μL of MTT Reagent and 50 μL of cell culture media (without cells) were prepared. The plate was incubated at 37 °C for 3 hours. After incubation, 150 μL of MTT solvent was added to each well. The plate was covered with foil, placed on an orbital shaker, and shaken for 15 minutes. The absorbance was measured at OD = 590 nm. The study was carried out according to the guidelines of the Declaration of Helsinki and approved by the Local Ethics Committee of the National Center for Biotechnology [17].

For the statistical analysis, all the physical, chemical, and biological experiments on hydrogel samples were performed in triplicate. All the experimental values were expressed in the form of mean ± standard error and the limit of experimental error of each test was ± 5 %, which had been considered as statistically significant.

Results and Discussion

The preparation of SA-AGE hydrogel generally involved a reaction at pH 3 and 60 °C for 6 hours. It is worth noting that allyl glycidyl ether is a saturated three-membered heterocycle with a single oxygen atom in the cycle. Epoxides exhibit a redistribution of electron density from carbon atoms to oxygen atoms, resulting in a high level of strain within the three-membered cycle. These characteristics significantly affect their reactivity. For instance, in a neutral or basic medium, the reaction proceeds under kinetic control, and the nucleophile attacks the carbon atom with the least steric hindrance in the substrate.

The reaction between sodium alginate and allyl glycidyl ether was carried out at a pH value of 3. During the reaction, there was a significant redistribution of electron density when the epoxy ring opened. As a result, the nucleophile interacts with the substrate at the carbon atom with the highest substitution, where the majority of the positive charge is concentrated. Consequently, the SA-AGE macromer is formed as a product of epoxy ring opening under acidic conditions. These conditions are characterized by the influence of thermodynamic control on the direction of the processes (Fig. 2).
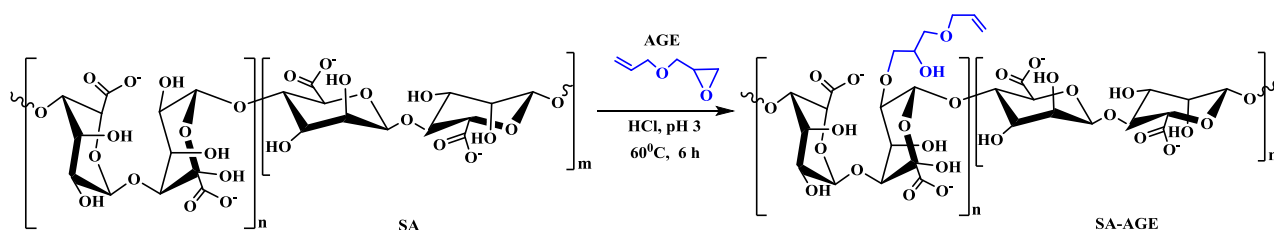
Figure 2. Reaction scheme of the SA-AGE macromer

The analysis of the 1H NMR spectrum of the SA-AGE macromer revealed that the signals of the protons of the CH-, CH₂- groups of the glucose part of the molecule appear in the region of 3.24-3.57 ppm. in the form of a complex multiplet. The anomeric proton H(1) of the carbohydrate residue appears as a doublet at 3.72 ppm. (d, J=3.9 Hz, 9H), characteristic of the β-anomer and indicating the interaction of the anomeric proton only with the neighboring trans-axial proton at C2. The methylene protons of the vinyl fragment CH=CH₂ appear as a multiplet in the region of 5.30–5.00 ppm (=CHa). The signal at 5.79 ppm. in the form of a singlet, corresponds to the vinyl protons of the epoxide. The methine proton of the OCH= fragment is written as a singlet at 1.02 ppm. The integral curve corresponds to the total number of protons (Fig. 3).
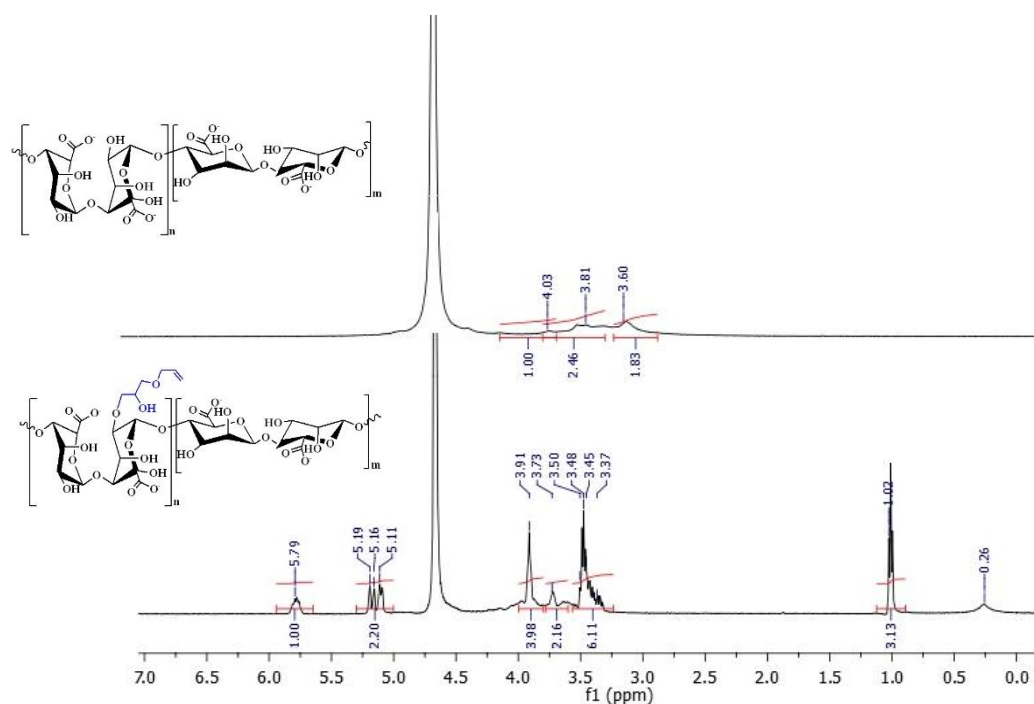
Figure 3. NMR spectra of the SA-AGE macromer

The SA-AGE structure includes a sugar group and an unsaturated double bond, making it a versatile building block for the synthesis of various medicinal copolymers. These copolymers not only exhibit prolonged release properties but also enable targeted drug delivery to specific cells in the body that possess carbohydrate-binding proteins on their surfaces (Fig. 4).
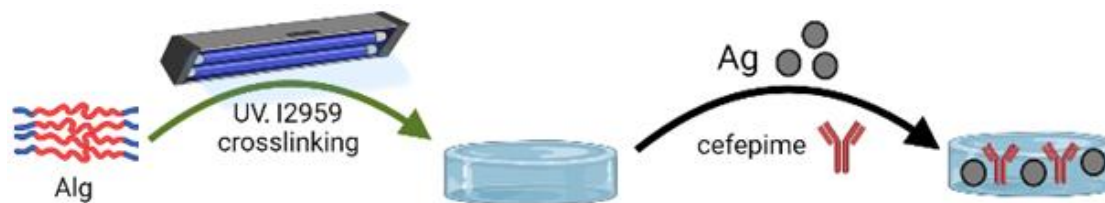
Figure 4. Scheme formation of composite hydrogel dressing with drug delivery

In order to control the speed and effectiveness of UV activation, we employed the sol-gel analysis technique, which enables the quantification of insoluble (spatially cross-linked) and soluble polymers. Following UV activation, samples with varying ratios of the thiol derivative (S-H bond) exhibited low viscosity, indicating the predominant degradation of polymer molecules in these systems. The dominant process in allyl-alginate molecules is the breaking of bonds rather than their formation, as alginate polymer derivatives primarily exhibit a deconstructing behavior. The amount of gel fraction reflects the effectiveness of polymer cross-linking, which in turn influences the immobilization efficiency of the medicine in the hydrogel matrix and its release rate. As depicted in Figure 5a, the yield of the gel fraction is significantly higher for the SA-AGE-100 sample compared to the SA-AGE-50. This difference can be attributed to the higher molecular weight polymer and its impact on the degree of cross-linking, rather than polymer modification. Unfortunately, the SA-AGE-25 sample was dissolved in Milli-Q and did not participate in subsequent experiments.
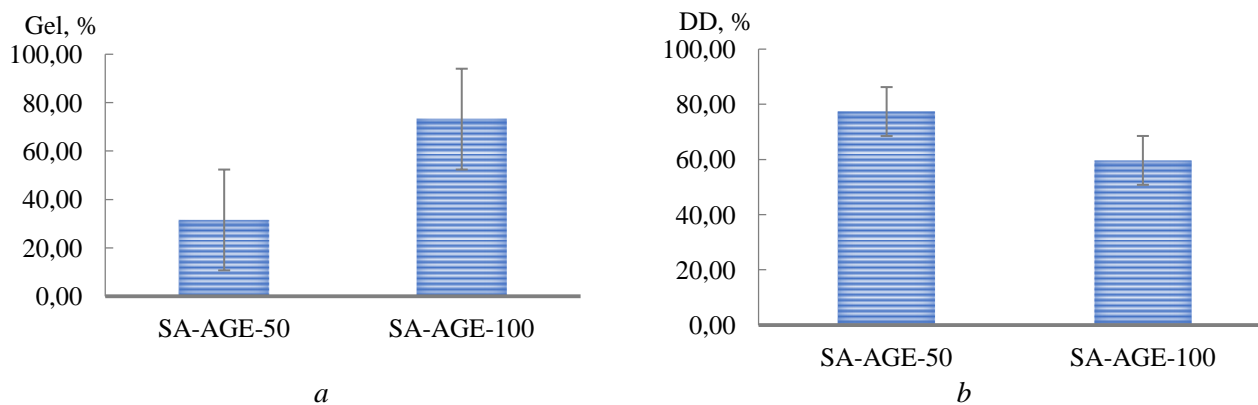
Figure 5. General properties of the SA-AGE macromer: (*a*) sol-gel, (*b*) degradation degree

As for degradation, it involves the hydrolysis process that breaks down the walls of cryogel macropores, resulting in mass loss. The study of SA-AGE-50 and SA-AGE-100 hydrogel degradation at 37 °C, over time showed a weight loss (Fig. 5*b*). Within 8 weeks, 77.35 ± 1.1 % and 59.64 ± 1.4 % degraded, respectively. It was noted that the hydrogel with a lower concentration exhibited a higher degree of degradation due to the density of crosslinking and the hydrophilic properties of the polymers. Based on the obtained data, it can be concluded that hydrogels demonstrate a low level of degradation and can be further used as scaffolds for drug delivery.
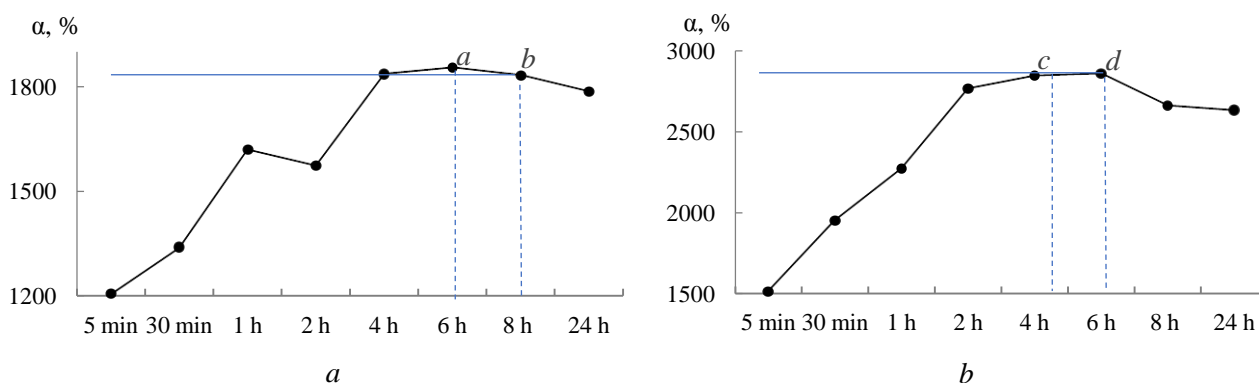
Figure 6. Sample swelling kinetic curve SA-AGE-100 (*a*) and SA-AGE-50 (*b*)

Figure 6 illustrates the continuous increase in swelling when the SA-AGE-50 and SA-AGE-100 samples are immersed in the liquid. After 6 hours (*point a*) and 4 hours (*point c*), the swelling rate starts to decrease, indicating a gradual slowdown in swelling over time and reaching the maximum possible swelling due to the initial intense swelling. At *points a* and *c*, the dissolution rate becomes equal to the swelling rate, resulting in a constant degree of swelling. After 8 hours (*point b*) and 6 hours (*point d*), the dissolution rate begins to exceed the swelling rate, leading to a decrease in the weight of the samples. It was determined that between points *a* and *b*, as well as *c* and *d*, the samples exhibit maximum swelling.

In conclusion, the experimental data obtained suggest that SA-AGE-100 exhibits a higher efficiency of crosslinking. Therefore, this specific sample was selected as the focus for further investigation of its antibacterial and toxicological activity.
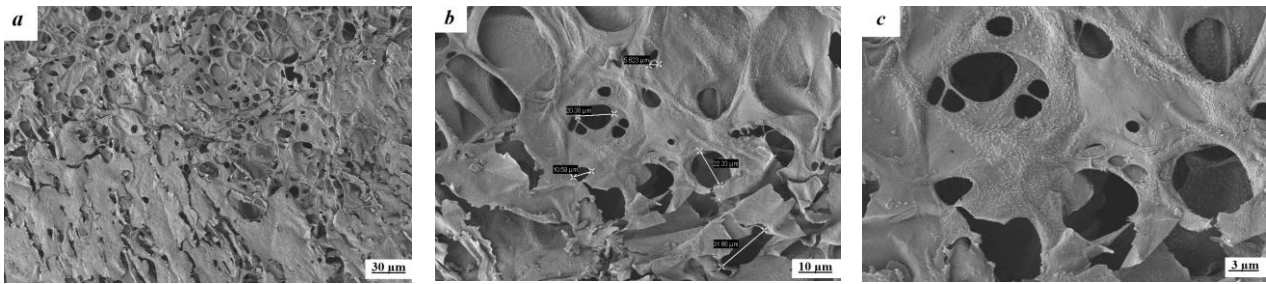
Figure 7. SEM of SA-AGE-100 hydrogel

The SEM micrographs of SA-AGE-100 showed a uniform cross-sectional morphology of the samples, which confirms the good miscibility and homogeneity between the ingredients of the composite hydrogels. The synthesized hydrogel forms a hetero-porous (with interconnected pores) polymer matrix structure in which macromolecules are connected into a stable 3D network (Fig. 7a). However, there are differences in morphology, in particular in the size and regularity of their arrangement (Fig. 7b, 7c). The electron micrograph shows differences in the porosity of the structure; there are both micropores with a dimension of 6 µm and macropores up to 32 µm. The resulting pore sizes are appropriate for drug delivery given that accommodates more silver particles and cefepime molecules, whereupon agglomerating. Thus, the pores allow for cell-cell communication with silver particles and cefepime and are available as a medical device in regenerative medicine.
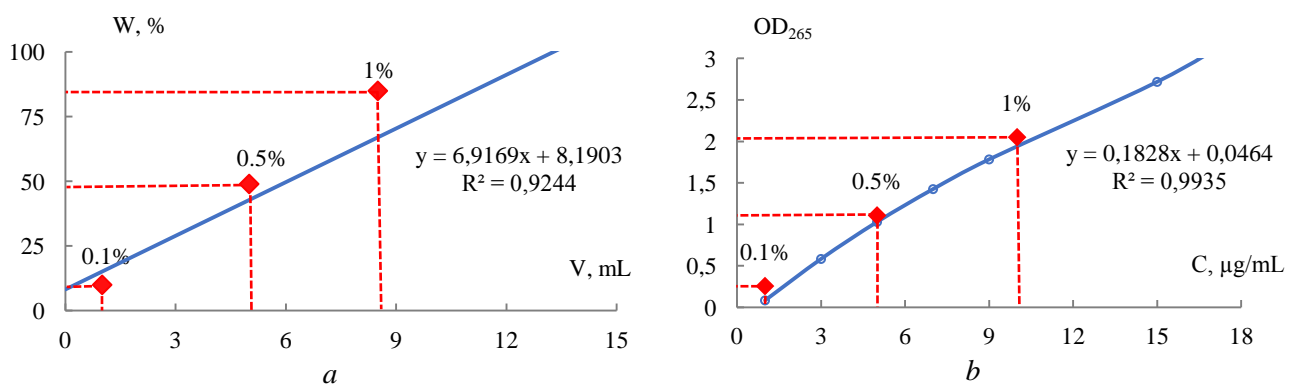
Figure 8. Quantitative analysis of the silver particles (a) and cefepime (b)

The concentration of silver and cefepime particles was quantitatively determined through photometric titration, generating the relationships between solution optical density and their respective concentrations (Fig. 8). The absorption dynamics of the antibacterial agents introduced into the samples was studied under static conditions, focusing on the volume comparison.

The intensity of absorption was assessed by measuring it at a specific wavelength, using concentration-dependent curves of the absorption intensity for silver and cefepime particles (Fig. 7a) as references. The analysis revealed an absorption degree of 85 % for silver particles (Fig. 8a) and a concentration of 10 µg/mL for cefepime (Fig. 8b). Overall, these findings indicate that the optimal concentration of impregnated silver and cefepime particles within the SA-AGE hydrogel structure was determined to be 1 % [18].

An essential requirement for a wound-healing dressing is its non-toxic nature. Therefore, the toxicity of SA-AGE-50 and SA-AGE-100 hydrogels on rat ADMSC cells was evaluated using the MTT assay (Fig. 9). The percentage of cell survival was determined by calculating the ratio of the spectral absorbance (OD_{exp}) in the experimental group to the spectral absorbance (OD_{contr}) in the control group.
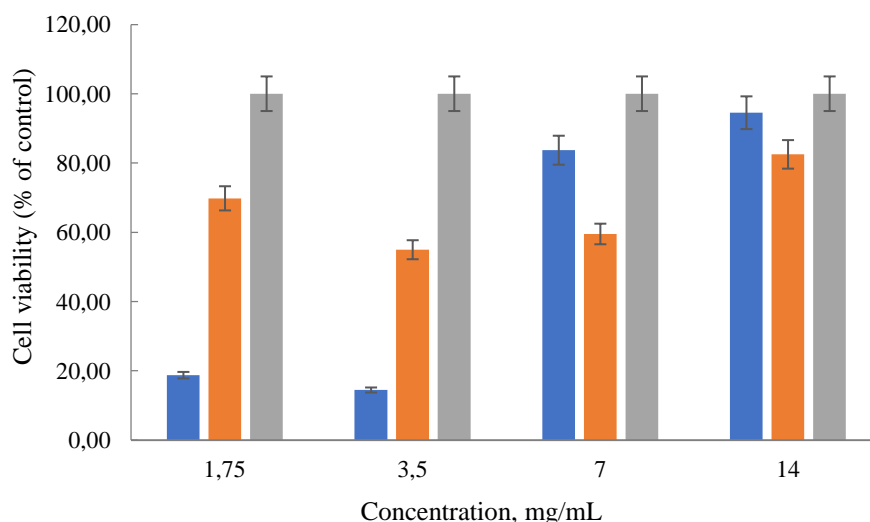
Figure 9. Cytotoxicity of SA-AGE-50 and SA-AGE-100 hydrogels to rat ADMSC cells by MTT assay

According to the international standard ISO 10993–5:2009(E), cytotoxicity is divided into six grades i.e., 0, 1, 2, 3, 4, and 5, which corresponds to 100 %, 75 %-99 %, 50 %-74 %, 25 %-49 %, 1 %-24 %, and 0 in the percentage of cell survival respectively, and grades 0 and 1 are considered non-cytotoxicity [19]. The cell survival percentage of these two hydrogels was above 80 %, indicating the absence of cytotoxicity.

T a b l e

Antibacterial activity of SA-AGE-100

Strains /samples	A 0.1 %	C 0.1 %	A 0.5 %	C 0.5 %	C 1 %	A 1 %	A-C 1 %
P. aeruginosa	5.3±0.4	10.3±1.8	3.3±0.4	11.7±0.4	12.3±0.4	4.3±0.4	12.0±0.7
S. aureus	2.0	10.3±1.6	2.0	9.0±1.3	10.7±0.4	2.7±0.4	8.7±1.1

The antimicrobial efficacy of SA-AGE-100, incorporating silver particles and cefepime, was assessed against one gram-negative strain of Pseudomonas aeruginosa and one gram-positive strain of Staphylococcus aureus. These specific strains were chosen to represent different bacterial mechanisms that possess multiple virulence factors, as well as their pathogenicity and prevalence in everyday life. Various ratios of wound dressings were prepared for the study, containing different concentrations (0.1 %, 0.5 %, and 1 %) of silver particles (A) and cefepime (C) absorbed within the alginate coating structure. Additionally, a mixture of A-C at a concentration of 1 % was also included in the research.
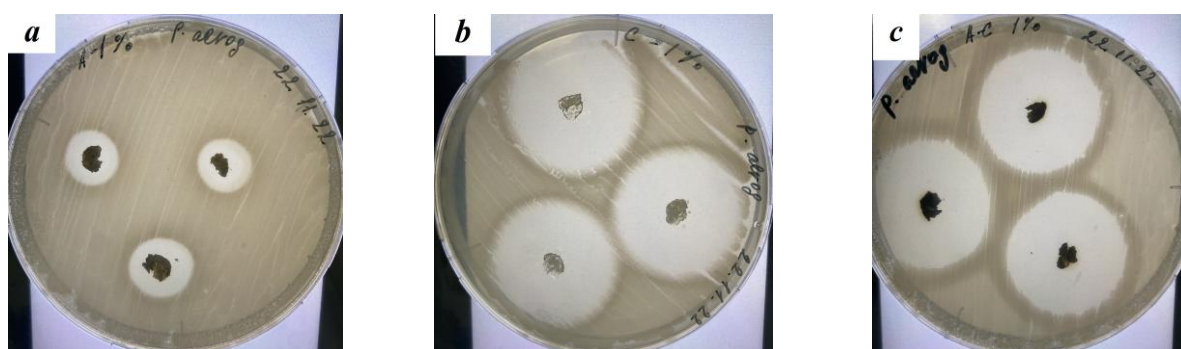
Figure 10. Evaluation of antibacterial activity of SA-AGE-100 loaded with: (*a*) silver particles 1 %; (*b*) cefepime 1 %; (*c*) mixture of silver particles 1 % and cefepime 1 %.

The study demonstrated the inhibitory effect of silver particles and cefepime on bacterial growth upon diffusion into agar (Table). Interestingly, both the mixture of silver particles and cefepime and pure cefepime

exhibited similar zones of inhibition (Fig. 10b, 10c), while the silver particles alone showed a more moderate outcome (Fig. 10*a*).

Based on our initial findings, it is evident that the adsorbed silver particles and cefepime in the alginate matrix exhibit a strong antibacterial activity. Specifically, samples C-1 and AC-1 demonstrate promising results and are therefore recommended for further investigation [20].

Conclusions

This study presents an experimental characterization of photocrosslinked SA-AGE hydrogels, aiming to evaluate and explain their physicochemical and biological properties. The obtained kinetic parameters of the swelling-dissolution process indicate that the synthesized SA-AGE hydrogel is capable of providing a diffusion prolonged release of drugs. Furthermore, when loaded with silver particles and cefepime, the synthesized hydrogel effectively delivers these substances to the tested bacterial strains, demonstrating high antibacterial activity without toxicity. However, further *in vivo* studies are necessary to assess the fate and toxicity of SA-AGE-100 before definitive conclusions can be drawn regarding the utility of the synthesized drugs. These preliminary results can serve as foundational data for the development of medical products.

Acknowledgments

References

1   Vigata, M., Meinert, C., Hutmacher, D. W., & Bock, N. (2020). Hydrogels as drug delivery systems: A review of current characterization and evaluation techniques. *Pharmaceutics, 12*(12), 1188. https://doi.org/10.3390/pharmaceutics12121188

2   Ogay, V., Mun, E. A., Kudaibergen, G., Baidarbekov, M., Kassymbek, K., Zharkinbekov, Z., & Saparov, A. (2020). Progress and prospects of polymer-based drug delivery systems for bone tissue regeneration. *Polymers, 12*(12), 2881. https://doi.org/10.3390/polym12122881

3   Qu, J., Zhao, X., Liang, Y., Xu, Y., Ma, P. X., & Guo, B. (2019). Degradable conductive injectable hydrogels as novel antibacterial, anti-oxidant wound dressings for wound healing. *Chemical Engineering Journal, 362,* 548–560. https://doi.org/10.1016/j.cej.2019.01.028

4   Shi, Q., Luo, X., Huang, Z., Midgley, A. C., Wang, B., Liu, R., ... & Wang, K. (2019). Cobalt-mediated multi-functional dressings promote bacteria-infected wound healing. *Acta Biomaterialia, 86,* 465–479. https://doi.org/10.1016/j.actbio.2018.12.048.

5   Aderibigbe, B.A., & Buyana, B. (2018). Alginate in wound dressings. *Pharmaceutics, 10*(2), 42. https://doi.org/10.3390/pharmaceutics10020042

6   Chen, K., Wang, F., Liu, S., Wu, X., Xu, L., & Zhang, D. (2020). In situ reduction of silver nanoparticles by sodium alginate to obtain silver-loaded composite wound dressing with enhanced mechanical and antimicrobial property. *International Journal of Biological Macromolecules, 148,* 501–509. https://doi.org/10.1016/j.ijbiomac.2020.01.15

7   Diniz, F. R., Maia, R. C. A., de Andrade, L. R. M., Andrade, L. N., Vinicius Chaud, M., da Silva, C. F., ... & Severino, P. (2020). Silver nanoparticles-composing alginate/gelatine hydrogel improves wound healing in vivo. *Nanomaterials, 10*(2), 390. https://doi.org/10.3390/nano10020390

8   Lin, X., Guan, X., Wu, Y., Zhuang, S., Wu, Y., Du, L., ... & Tu, M. (2020). An alginate/poly (N-isopropylacrylamide)-based composite hydrogel dressing with stepwise delivery of drug and growth factor for wound repair. *Materials Science and Engineering: C, 115,* 111123. https://doi.org/10.1016/j.msec.2020.111123

9   Farhadian, N., Karimi, M., & Porozan, S. (2021). Ceftriaxone sodium loaded onto polymer-lipid hybrid nanoparticles enhances antibacterial effect on gram-negative and gram-positive bacteria: Effects of lipid-polymer ratio on particles size, characteristics, in vitro drug release and antibacterial drug efficacy. *Journal of Drug Delivery Science and Technology, 63,* 102457. https://doi.org/10.1016/j.jddst.2021.102457

10   Alshammari, F., Alshammari, B., Moin, A., Alamri, A., Al Hagbani, T., Alobaida, A., ... & Rizvi, S. M. D. (2021). Ceftriaxone mediated synthesized gold nanoparticles: a nano-therapeutic tool to target bacterial resistance. *Pharmaceutics, 13*(11), 1896. https://doi.org/10.3390/pharmaceutics13111896

11   Zhang, M., & Zhao, X. (2020). Alginate hydrogel dressings for advanced wound management. *International Journal of Biological Macromolecules, 162,* 1414–1428. https://doi.org/10.1016/j.ijbiomac.2020.07.311

12   Kazybayeva, D. S., Irmukhametova, G. S., & Khutoryanskiy, V. V. (2022). Thiol-ene "click reactions" as a promising approach to polymer materials. *Polymer Science, Series B, 64*(1), 1–16. https://doi.org/10.1134/S1560090422010055

13 Araiza-Verduzco, F., Rodríguez-Velázquez, E., Cruz, H., Rivero, I. A., Acosta-Martínez, D. R., Pina-Luis, G., & Alatorre-Meda, M. (2020). Photocrosslinked alginate-methacrylate hydrogels with modulable mechanical properties: Effect of the molecular conformation and electron density of the methacrylate reactive group. *Materials, 13*(3), 534. https://doi.org/10.3390/ma13030534

14 Kudaibergen, G., Zhunussova, M., Mun, E. A., Arinova, A., & Ogay, V. (2021). Studying the Effect of Chondroitin Sulfate on the Physicochemical Properties of Novel Gelatin/Chitosan Biopolymer-Based Cryogels. *Applied Sciences, 11*(21), 10056. https://doi.org/10.3390/app112110056

15 Kudaibergen, G. K., & Zhunussova, M. S. (2022). Study of the effect of temperature on the properties of gelatin-chitosan cryogels. *Bulletin of the University of Karaganda — Chemistry, 106*(2), 4-11. https://doi.org/10.31489/2022Ch2/2-22-4

16 Voda pitevaia. Metody opredeleniia soderzhaniia svintsa, tsinka, serebra [Drinking water. Methods for determination of lead, zinc and silver content] (1972) *GOST 18293-72 from 25th December, 1972.* Moscow: Mezhgosudarstvennyi standart [in Russian]. Retrieved from https://online.zakon.kz/Document/? doc_id=31126624&pos=1;-16#pos=1;-16

17 WMA Declaration of Helsinki — Ethical Principles for Medical Research Involving Human Subjects (2021) Meeting of the Local Ethical Commission of the National Center for Biotechnology Company, Nur-Sultan. Protocol No.4, December 3, 2021.

18 Shoaibi, Z. A., & Gouda, A. A. (2012). Extractive spectrophotometric method for the determination of tropicamide. *Journal of Young Pharmacists*, *4*(1), 42-48. https://doi.org/10.4103/0975-1483.93572

19 Chen, Y. M., Xi, T., Zheng, Y., Guo, T., Hou, J., Wan, Y., & Gao, C. (2009). In vitro cytotoxicity of bacterial cellulose scaffolds used for tissue-engineered bone. *Journal of bioactive and compatible polymers*, *24*(1_suppl), 137–145. https://doi.org/10.1177/0883911509102710

20 Alhakamy, N. A., Caruso, G., Eid, B. G., Fahmy, U. A., Ahmed, O. A., Abdel-Naim, A. B.,... & Abdulaal, W. H. (2021). Ceftriaxone and melittin synergistically promote wound healing in diabetic rats. *Pharmaceutics, 13*(10), 1622. https://doi.org/doi.org/10.3390/pharmaceutics13101622

Information about the authors*

Akhmetkarimova, Zhanar Samatovna (*corresponding author*) — PhD, Postdoctoral Research Associate (PDRA) in Pharmacy, University of Reading, RG6 6AH, Reading, Berkshire, United Kingdom; Senior researcher, National Center for Biotechnology, Korgalzhin broad, 13/5, 010000, Astana, Kazakhstan; e-mail*: z.akhmetkarimova@reading.ac.uk; https://orcid.org/0000-0002-9782-5521;

Kudaibergen, Gulshakhar Kudaibergenovna — PhD, Senior researcher, National Center for Biotechnology, Korgalzhin broad, 13/5, 010000, Astana, Kazakhstan; e-mail: kudaibergen@biocenter.kz; https://orcid.org/0000-0002-0779-4099;

Kaukabaeva, Guldarigash Kuanyshevna — Junior researcher, National Center for Biotechnology, Korgalzhin broad, 13/5, 010000, Astana, Kazakhstan; e-mail: guldarigash.kaukabaeva@mail.ru; https://orcid.org/0000-0002-9052-5091;

Abeldenov, Sailau Kasenovich — Head of laboratory, National Center for Biotechnology, Korgalzhin broad, 13/5, 010000, Astana, Kazakhstan; e-mail: abeldenov@biocenter.kz; https://orcid.org/0000-0002-6974-9138;

Rysbek, Aidana Begalykyzy — 3rd year PhD student, Junior researcher, National Center for Biotechnology, Korgalzhin broad, 13/5, 010000, Astana, Kazakhstan; e-mail: aidanarysbek93@gmail.com; https://orcid.org/0000-0001-8290-0552

_____
*The author's name is presented in the order: *Last Name, First and Middle Names*

PHYSICAL AND ANALYTICAL CHEMISTRY

Koblandy M. Turdybekov[1*] ⓘ, Pernesh Zh. Zhanymkhanova[2] ⓘ, Gulim K. Mukusheva[1] ⓘ, Yurii V. Gatilov[3] ⓘ

[1]Karagandy University of the name of academician E.A. Buketov, Karaganda, Kazakhstan
[2]Karaganda Medical University, Karaganda, Kazakhstan
[3]N.N. Vorozhtsov Novosibirsk Institute of Organic Chemistry, Novosibirsk, Russia
(*Corresponding author′s e-mail: xray-phyto@yandex.kz)

Synthesis and Spatial Structure of (*E*)-1-(2-(4-Bromobutoxy)-6-Hydroxy-4-Methoxyphenyl-3-Phenylprop-2-en-1-one

(*E*)-1-(2-(4-bromobutoxy)-6-hydroxy-4-methoxyphenyl-3-phenylprop-2-en-1-one was synthesized from the pinostrobin molecule. The tetrahydropyran cycle was opened in acetone under heating (50–60 °C) mixtures of components for 16 hours in the presence of 3 moles of K_2CO_3 and 1,4-dibromobutane. The resulting substance is a yellow powder of the composition $C_{20}H_{21}BrO_4$, mp 83.7–86.6 °C. The structure of the obtained compound was established on the basis of the data of elemental analysis, IR and NMR spectra. As a result of X-ray diffraction analysis, it was found that the hydrogen atoms in the C8=C9 bond take the trans-conformation. The rotation of the C1…C6 phenyl ring (flat with an accuracy of ±0.008 Å) relative to the C10…C15 cycle (flat with an accuracy of ±0.004 Å) is 14.3°. In the crystal, the molecules are linked by an intramolecular hydrogen bond O4-H....O1 (distances O-H 0.95(8) Å, O····O 2.469(6) Å, H····O 1.58 (8) Å, angle O-H····O 153(7)°). The formation of (*E*)-1-(2-(4-bromobutoxy)-6-hydroxy-4-methoxy-1-phenylprop-2-en-1-one can be explained by the ease of the retro-Michael reaction of the pyran ring and the subsequent O-alkylation of the resulting chalcone. Carrying out the reaction in the presence of other bases (cesium carbonate, triethylamine) did not lead to success. The starting substance (pinostrobin) was completely converted into oligomeric compounds.

Keywords: NMR spectroscopy, IR spectroscopy, X-ray analysis, (*E*)-1-(2-(4-bromobutoxy)-6-hydroxy-4-methoxyphenyl-3-phenylprop-2-en-1-one, chalcone, flavone, phenolic compounds.

Introduction

Compounds of a number of chalcones are of interest due to the simplicity of their synthesis, as well as the possibility of using them as synthons to obtain various heterocyclic compounds with high biological activity, in particular, pyrazolines and flavones [1, 2]. Compounds containing a chalcone skeleton exhibit significant antibacterial, antiviral, antihyperglycemic, antifungal, anti-inflammatory, antimalarial, antitumor, and immunomodulatory activities, as well as chemoprotective and antioxidant properties [3–8]. In this regard, the synthesis of new chalcones seems to be an important task.

The flavonoid pinostrobin (**1**) is of particular interest for chemical modification. The availability of pinostrobin, previously isolated from the extract of the buds of *Populus balsamifera* L. [9, 10], and the analysis of its structure leads to the conclusion that its synthetic transformations are promising to obtain compounds structurally similar to a number of natural metabolites and other practically significant substances.

Experimental

The melting point was determined on a Boetius heating table. Elemental analysis was carried out on a Eurovector 3000 analyzer. TLC analysis was performed on Sorbfil plates, visualization with iodine vapor.

The IR spectrum was recorded on an Avatar 360 instrument (Thermo Nicolet) in KBr tablets.

^{1}H NMR spectra were recorded on a Bruker AV-400 spectrometer with a frequency of 400 MHz. ^{13}C NMR spectra were recorded on a Bruker AV-400 spectrometer with a frequency of 100 MHz. Solvent — $CDCl_3$, standard — TMS. The X-ray diffraction experiment was carried out on a Bruker APEX-II CCD diffractometer.

Synthesis of (E)-1-(2-(4-bromobutoxy)-6-hydroxy-4-methoxyphenyl -3-phenylprop-2-en-1-one (**2**) a yellow powder, composition $C_{20}H_{21}BrO_4$, mp 87–89 °C. To a solution of 0.5 g (1.85 mmol) of pinostrobin in 10 ml of acetone, 0.37 g (2.7 mmol) of calcined K_2CO_3 was added, and after 10 min, 1.2 equivalents (2.2 mmol) of 1,4-dibromobutane were added. The reaction mixture was stirred for 7 hours at 50 °C, 10 ml of acetone were added and stirred for another 7 hours at 50 °C. After cooling, the precipitate was filtered off, washed with acetone (3×5 ml), the combined filtrates were evaporated, the residue was recrystallized from diethyl ether, compound 2 was isolated. Yield is 72 %, mp is 87–89 °C (from ether). HPLC purity is 98.72 %. Control over the course of reactions and the purity of the obtained product were carried out by TLC on Sorbfil plates using the system petroleum ether-ethyl acetate, 2:1, R_f=0.52.

The addition of an excess (1.2 equiv.) of dibromide contributed to increasing the yield of the target product **2**. The formation of compound **2** can be explained by the ease of the retro-Michael reaction of the pyran ring and the subsequent O-alkylation of the resulting chalcone. It should be noted that the result of the conversion of pinostrobin significantly depends on the nature of the dibromoalkane. Carrying out the reaction in the presence of other bases (cesium carbonate, triethylamine) also did not lead to success. The starting substance (pinostrobin) was completely converted into oligomeric compounds.

Elemental analysis: found, %: C 61.43, H 5.02, Br 18.96. calculated, %: C 59.25, H 5.18, Br 19.73.

IR spectrum (ν, cm[-1], KBr): 3053 (OH), 2924 (OCH_3), 1631 (C=O), 1581 (C=C), 1495, 1444, 1346 (CH_3), 1112 (C-O-S), 1033 (Arom), 866, 693, 624.

X-ray diffraction study of compound **2**. Determination of unit cell parameters and intensity of 17139 diffracted reflections (3472 independent, R_{int} 0.0696) were measured on a Bruker Kappa APEX II CCD diffractometer (MoK_α, graphite monochromator, ω-scan, $2.635° \leq \theta \leq 25.817°$) at 200 K. Monoclinic crystals, space group P21/n, a=6.9892(12), b=14.249(2), c=18.413(3) Å, β=92.222(6)°, V=1832.3(5) Å^3, Z=4 ($C_{20}H_{21}BrO_4$), calculated density d=1.469 g/cm^3, absorption coefficient μ=2.264 mm^{-1}. The experimental array of reflections was corrected for absorption. Takeover accounting was carried out using SAINT [11] and SADABS [12] programs (multi-scan method, $T_{min.}$ 0.812, $T_{max.}$ 0.922).

The structure was deciphered by the method of direct phase determination. The coordinates of non-hydrogen atoms were refined taking into account the anisotropic approximation of thermal vibrations by the full-matrix least-squares method. The positions of hydrogen atoms, with the exception of hydroxyl ones, were calculated geometrically and refined in the isotropic approximation of thermal vibrations (rider model). The H atoms of the hydroxyl groups were revealed from the difference synthesis, and their positions were refined in the isotropic approximation. The structure was deciphered and the coordinates were refined using the SHELXS software package [13] and the SHELKS-2018/3 software [14]. 2268 independent reflections with I ≥ 2σ(I) were used in the calculations; the number of refined parameters was 231.

The divergence coefficients were R_1=0.0736, $_wR_2$=0.1961 (for reflections with I≥2σ(I)), R_1=0.1162, $_wR_2$=0.2139 (for all reflections), GooF=1.126. Maximum and minimum residual density: Δρ=1.522 and -0.527 e/Å^3. The coordinates of atoms in the crystal are presented in Table 1.

T a b l e 1

Coordinates of the atoms in the fractions of the cell (x10^4, Hx10^3)
and equivalent thermal parameters (Å^2, x10^3) in the structure 2

Atom	x	y	z	$U_{equiv.}$
Br1	8262(2)	9067(1)	6987(1)	68(1)
O1	7920(7)	5134(3)	3379(2)	44(1)
O2	7286(6)	5664(3)	5568(2)	34(1)
O3	7257(7)	2440(3)	6089(2)	42(1)
O4	7969(6)	3437(3)	3652(2)	40(1)

Atom	x	y	z	$U_{equiv.}$
C1	7675(8)	4616(4)	4586(3)	28(1)
C2	7382(8)	4750(4)	5345(3)	29(1)
C3	7228(8)	4016(4)	5816(3)	31(1)
C4	7377(8)	3104(4)	5563(4)	34(1)
C5	7652(8)	2915(4)	4839(3)	34(1)
C6	7754(8)	3658(4)	4358(3)	35(1)
C7	7844(8)	5352(4)	4039(3)	32(1)
C8	7869(9)	6360(4)	4219(3)	36(1)
C9	7437(8)	7005(4)	3734(3)	34(1)
C10	7408(9)	8017(5)	3864(3)	36(2)
C11	7229(9)	8649(5)	3285(4)	40(2)
C12	7233(12)	9608(5)	3393(4)	53(2)
C13	7458(10)	9965(5)	4090(4)	49(2)
C14	7631(10)	9365(5)	4673(4)	46(2)
C15	7621(9)	8399(5)	4572(3)	36(1)
C15	7085(9)	5861(4)	6333(3)	34(1)
C17	6989(9)	6918(4)	6388(3)	32(1)
C18	6678(10)	7217(5)	7166(4)	40(2)
C19	6166(10)	8237(5)	7232(4)	50(2)
C20	7385(10)	1472(4)	5879(4)	44(2)
H04	807(11)	405(5)	341(4)	5(2)

Results and Discussions

Based on pinostrobin (**1**), (*E*)-1-(2-(4- bromobutoxy)-6-hydroxy-4-methoxyphenyl-3-phenylprop-2-en-1-one (**2**) was synthesized by opening the tetrahydropyran cycle (Fig. 1). The synthesis of compound **2** was carried out by the interaction of pinostrobin with 1,4-dibrombutane in acetone in the presence of K_2CO_3.
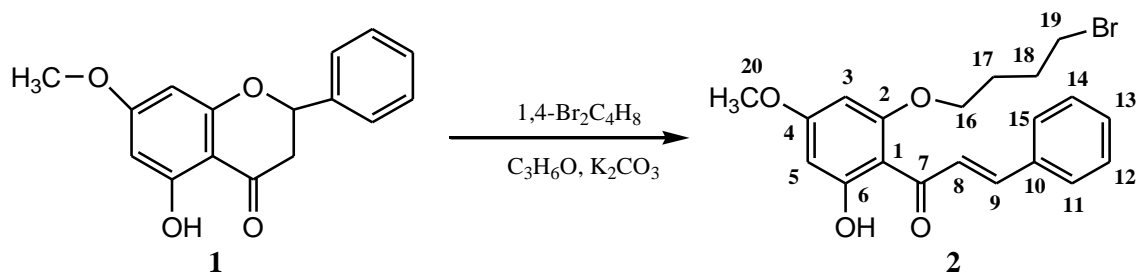
Figure 1. Synthesis scheme of (*E*)-1-(2-(4-bromobutoxy)-6-hydroxy-4-methoxyphenyl-3-phenylprop-2-en-1-one (**2**)

Structure of the synthesized compound **2** was proved by IR, ^{1}H and ^{13}C NMR spectroscopy [15].

The IR spectrum contains bands corresponding to the stretching vibrations of the OH group involved in the hydrogen bond (3053 cm^{-1}), OCH_3, C=O, C=C (2924, 1631, 1581 cm^{-1}, respectively).

The ^{1}H NMR spectrum of molecule **2** is characterized by the presence of signals of protons of substituted phenyl rings at 6.10–7.90 ppm and signal of proton of the hydroxyl group at 12.17 ppm. The aliphatic protons are observed in the area of 2.02–4.07 ppm. The protons of the methoxy group appear at 1.83 ppm as a singlet.

In the ^{13}C NMR spectrum of compound **2**, the signals of carbons of phenyl rings are observed in the range of 91.85–135.44 ppm. Carbon atoms C=C appear at 127.85 and 130.12 ppm, C=O — at 192.72 ppm. Aliphatic carbon atoms resonate in the region of 28.04-67.96 ppm and the methoxy carbon at 55.62 ppm.

Detailed assignment of ^{1}H and ^{13}C NMR signals in molecule **2** is given in Table 2.

^{1}H and ^{13}C NMR data (400 and 100 MHz, CDCl3, δ, ppm, J/Hz) for molecule 2

Atom	δH	δC	Atom	δH	δC
1	–	106.37, s	12	7.39, m (1H)	128.95, d
2	–	161.65, s	13	7.25, m (1H)	135.44, s
3	6.10, d (1H, J=2,5)	91.85, d	14	7.41, m (1H)	128.95, d
4	–	168.23, s	15	7.25, m (1H)	128.20, d
5	5.93, d (1H, J=2,5)	93.87, d	16	4.07, m (2H)	67.96, t
6	–	166.19, s	17	2.03, m (2H)	29.28, t
7	–	192.72, s	18	2.02, m (2H)	28.04, t
8	7.90, d (1H, J=15.6)	130.12, d	19	3.30, m (2H)	38.20, t
9	7.57, d (1H, J=15.6)	127.85, d	OH	12.17, s (1H)	–
10	–	130.12, d	OCH3	3.83, s (3H)	55.62, q
11	7.56, m (1H)	128.20, d			

Based on the data of elemental analysis and IR, NMR spectra, the resulting substance was identified as (*E*)-1-(2-(4-bromobutoxy)-6-hydroxy-4-methoxyphenyl-3-phenylprop-2-en-1-one. The spatial structure of compound **2** was determined by X-ray diffraction.

The general view of compound **2** is shown in Figure 2. It follows from the data obtained that the bond lengths and valence angles in compounds **2** are close to the usual ones [16].
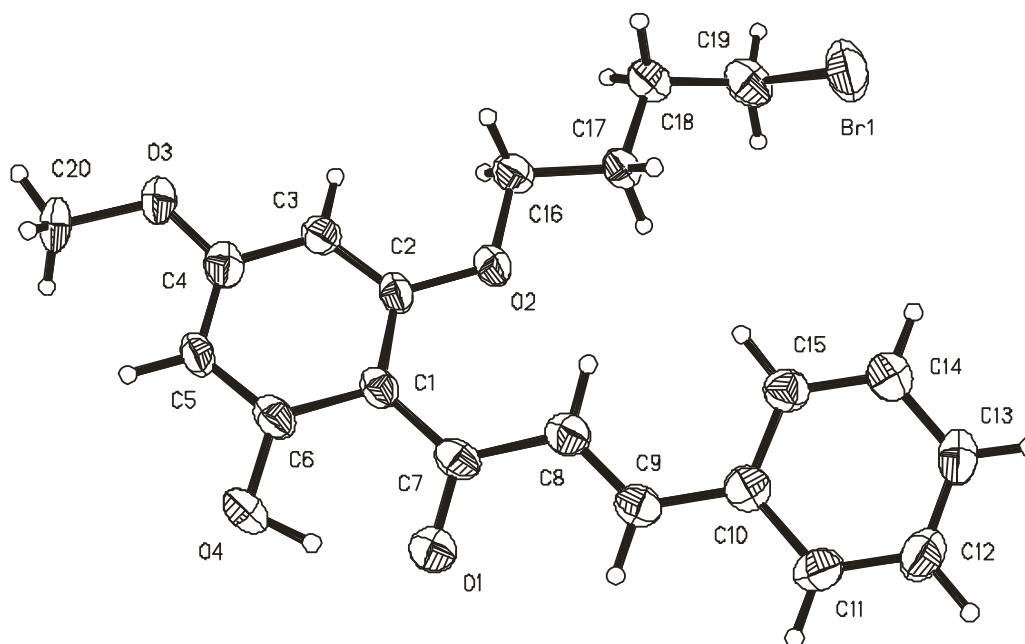
Figure 2. Crystal structural of (*E*)-1-(2-(4-bromobutoxy)-6-hydroxy-4-methoxyphenyl-3-phenylprop-2-en-1-one **(2)** (thermal vibration ellipsoids shown with a probability of 50 %)

Bond lengths (d, Å) in the structure 2

Bond	*d*	Bond	*d*
Br1-C19	1.949(7)	C5-C6	1.385(9)
O1-C7	1.258(7)	C7-C8	1.474(9)
O2-C2	1.368(7)	C8-C9	1.309(9)
O2-C16	1.448(7)	C9-C10	1.461(9)
O3-C4	1.359(8)	C10-C11	1.398(9)
O3-C20	1.436(7)	C10-C15	1.415(9)
O4-C6	1.353(7)	C11-C12	1.381(10)

Bond	*d*	Bond	*d*
C1-C6	1.429(9)	C12-C13	1.384(11)
C1-C2	1.432(8)	C13-C14	1.375(10)
C1-C7	1.462(9)	C14-C15	1.389(10)
C2-C3	1.365(8)	C16-C17	1.511(8)
C3-C4	1.386(8)	C17-C18	1.519(9)
C4-C5	1.380(9)	C18-C19	1.502(10)

T a b l e   4

Valent angles (ω, deg.) in the structure 2

Angle	ω	Angle	ω
C2-O2-C16	119.0(5)	O1-C7-C8	117.2(6)
C4-O3-C20	118.1(5)	C1-C7-C8	123.0(5)
C6-C1-C2	115.0(5)	C9-C8-C7	122.1(6)
C6-C1-C7	118.5(5)	C8-C9-C10	125.8(6)
C2-C1-C7	126.5(5)	C11-C10-C15	117.2(6)
C3-C2-O2	122.1(5)	C11-C10-C9	120.8(6)
C3-C2-C1	122.4(5)	C15-C10-C9	122.0(6)
O2-C2-C1	115.5(5)	C12-C11-C10	121.9(6)
C2-C3-C4	119.7(6)	C11-C12-C13	119.8(7)
O3-C4-C5	124.5(6)	C14-C13-C12	119.9(7)
O3-C4-C3	114.0(6)	C13-C14-C15	120.8(7)
C5-C4-C3	121.5(6)	C14-C15-C10	120.4(6)
C4-C5-C6	118.7(6)	O2-C6-C17	105.4(5)
O4-C6-C5	116.6(6)	C16-C17-C18	110.5(5)
O4-C6-C1	120.8(6)	C19-C18-C17	113.0(6)
C5-C6-C1	122.6(5)	C18-C19-Br1	112.6(5)
O1-C7-C1	119.8(5)		

Hydrogen atoms in the C8=C9 bond have a trans-conformation. The atom of the O1 ketone group is practically located in the plane of the 1,2,4,6-substituted phenyl cycle (torsion angle C6-C1-C7-O1 4.8(8)°). The keto group and the double bond C8=C9 deviate significantly from the coplanarity (torsion angle O1-C7-C8-C9 19.4(9)°). The double bond C8=C9 and C10-substituted phenyl cycle are also somewhat less conjugated (torsion angle C8-C9-C10-C15 -8.4(9)°). In general, the reversal of the phenyl cycle C1... C6 (flat with an accuracy of ± 0.008 Å) relative to the cycle C10...C15 (flat with an accuracy of ± 0.004 Å) is 14.3°.

In the crystal, the molecules are linked by an intramolecular hydrogen bond O4-H....O1 (x, y, z) (distances O-H 0.95(8) Å, O····O 2.469(6) Å, H····O 1.58 (8) Å, angle O-H····O 153(7)°) (Fig. 3).
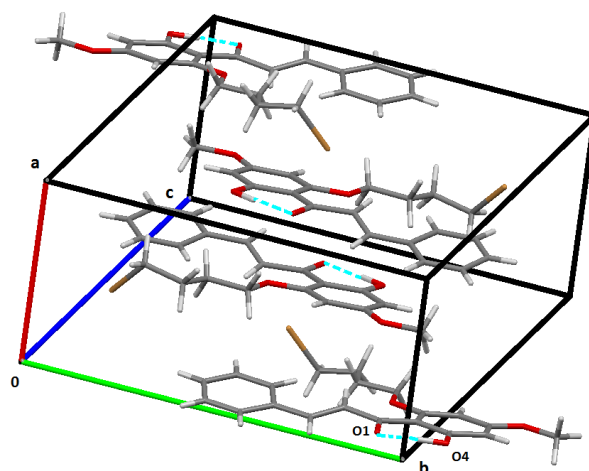
Figure 3. Crystal packing of molecules (*E*)-1-(2-(4-bromobutoxy)-6-hydroxy-
4-methoxyphenyl-3-phenylprop-2-en-1-one (**2**)

Conclusions

(*E*)-1-(2-(4-bromobutoxy)-6-hydroxy-4-methoxyphenyl-3-phenylprop-2-en-1-one was synthesized from the pinostrobin molecule by opening the tetrahydropyran ring. Synthesis of (*E*)-1- (2-(4-bromobutoxy)-6-hydroxy-4-methoxyphenyl-1-phenylprop-2-en-1-one was carried out by the interaction of pinostrobin with 1,4-dibromobutane in acetone in the presence of K_2CO_3. The structure of the obtained substance was established on the basis of elemental analysis data and IR and NMR spectra. It follows from the constant of the vicinal spin-spin interaction of H atoms at C8 and C9 that they must have cis conformations. Such a conformation would lead to a significant thermal stress between the O1 atom of the keto group and the phenyl ring. As a result of X-ray diffraction analysis, it was found that hydrogen atoms in the C8=C9 bond have a trans-conformation. The reversal of the cycle C1...C6 (flat with an accuracy of ± 0.008 Å) relative to the cycle C10...C15 (flat with an accuracy of ± 0.004 Å) is 14.3°. In the crystal, the molecules are bound by an intramolecular hydrogen bond O4-H....O1.

References

1 Daskiewicz, J. B., Comte, G., Barron, D., Di Pietro, A. & Thomasson, F. (1999). Organolithium mediated synthesis of prenylchalcones as potential inhibitors of chemoresistance. *Tetrahedron Letters*, *40*(39), 7095–7098. https://doi.org/10.1016/s0040-4039(99)01461-6

2 Ismailova, G.O., Yuldashev, N. M., Akbarhodjaeva, Kh.N. & Shertaev, M.M. (2021). Biologically Active Natural 2'-Hydroxychalcones. *Russian Journal of Bioorganic Chemistry, 47*, 660–669. https://doi.org/10.1134/s1068162021030080

3 Sivakumar, P. M., Prabhakar, P. K. & Doble, M. (2010). Synthesis, antioxidant evaluation, and quantitative structure–activity relationship studies of chalcones. *Medicinal Chemistry Research*, *20*(4), 482–492. https://doi.org/10.1007/s00044-010-9342-1

4 Tiwari, K. N., Monserrat, J. -P., Hequet, A., Ganem-Elbaz, C., Cresteil, T., Jaouen, G., Vessières, A., Hillard, E. A. & Jolivalt, C. (2012). In vitro inhibitory properties of ferrocene-substituted chalcones and aurones on bacterial and human cell cultures. *Dalton Transactions*, *41*(21), 6451. https://doi.org/10.1039/c2dt12180h

5 Awasthi, S. K., Mishra, N., Kumar, B., Sharma, M., Bhattacharya, A., Mishra, L. C. & Bhasin, V. K. (2008). Potent antimalarial activity of newly synthesized substituted chalcone analogs in vitro. *Medicinal Chemistry Research*, *18*(6), 407–420. https://doi.org/10.1007/s00044-008-9137-9

6 Achanta, G., Modzelewska, A., Feng, L., Khan, S. R. & Huang, P. (2006). A Boronic-Chalcone Derivative Exhibits Potent Anticancer Activity through Inhibition of the Proteasome. *Molecular Pharmacology*, *70*(1), 426–433. https://doi.org/10.1124/mol.105.021311

7 Satyanarayana, M., Tiwari, P., Tripathi, B. K., Srivastava, A. K. & Pratap, R. (2004). Synthesis and antihyperglycemic activity of chalcone based aryloxypropanolamines. *Bioorganic & Medicinal Chemistry*, *12*(5), 883–889. https://doi.org/10.1016/j.bmc.2003.12.026

8 Hamdi, N., Fischmeister, C., Puerta, M. C. & Valerga, P. (2010). A rapid access to new coumarinyl chalcone and substituted chromeno[4,3-c]pyrazol-4(1H)-ones and their antibacterial and DPPH radical scavenging activities. *Medicinal Chemistry Research, 20*(4), 522–530. https://doi.org/10.1007/s00044-010-9326-1

9 Kurkin, V. A., Zapesochnaya, G. G. & Braslavskii, V. B. (1990). Flavonoids of the buds of Populus balsamifera. *Chemistry of Natural Compounds*, *26*(2), 224–225. https://doi.org/10.1007/bf00607554

10 Adekenov, S.M., Baisarov, G.M., Khabarov, I.A. & Polyakov, V.V. (2020). Flavavoidy pochektopolia balzamicheskogo *Populus balsamifera L*. i sposoby ikh vydeleniia [Flavonoids of balsam poplar buds populus balsamifera and methods for their isolation]. *Khimiia Rastitelnogo Syria — Chemistry of plant raw materials*, № 2, 181–188 [in Russian]. https://doi.org/10.14258/jcprm.2020027602

11 Bruker. (2015). SAINT. Bruker AXS Inc., Madison, Wisconsin, USA.

12 Bruker. (2015). SADABS. Bruker AXS Inc., Madison, Wisconsin, USA

13 Sheldrick, G.M. (2008). Crystal structure solution with SHELXS. *Acta Crystaollogr., Sect. A*, *64*, 112–122. https://doi.org/10.1107/S0108767307043930

14 Sheldrick G.M. (2015). Crystal structure refinement with SHELXL. *Acta Crystaollogr., Sect. C. 71*, 3-8. https://doi.org/10.1107/S2053229614024218

15 Volovenko, Yu.M., Kartsev, V.G., Komarov, I.V., Turov, A.V. & Khilya, V.P. (2011). Spektroskopiia yadernogo magnitnogo rezonansa dlia khimikov [Nuclear Magnetic Resonance Spectroscopy for Chemists]. M: *ICSPP* [in Russian].

16 Allen, F. H., Kennard, O., Watson, D. G., Brammer, L., Orpen, A. G. & Taylor, R. (1987). Tables of bond lengths determined by X-ray and neutron diffraction. Part 1. Bond lengths in organic compounds. *Journal of the Chemical Society, Perkin Transactions 2*, 12, S1. https://doi.org/10.1039/p298700000s1

Information about authors*

Turdybekov, Koblandy Muboryakovich (*corresponding author*) — Doctor of chemical sciences, Professor, Karagandy University of the name of academician E.A. Buketov, Karaganda, Kazakhstan, Universitetskaya str., 28, 100024, Karaganda, Kazakhstan; e-mail: xray-phyto@yandex.kz; https://orcid.org/0000-0001-9625-0060;

Zhanymkhanova, Pernesh Zhaidarbekovna — Master of technology, Assistant professor, Karaganda Medical University, Erubaev str., 40, 100000, Karaganda, Kazakhstan; e-mail: pernesh1983@mail.ru; https://orcid.org/0000-0003-3575-9888;

Mukusheva, Gulim Kenesbekovna — Candidate of Chemical Sciences, Associate Professor, Karagandy University of the name of academician E.A. Buketov, Universitetskaya st., 28, 100024, Karaganda, Kazakhstan; e-mail: mukusheva1977@list.ru; https://orcid.org/0000-0001-6706-4816;

Gatilov, Yurii Vasilevich — Doctor of chemical sciences, Leading researcher, N.N. Vorozhtsov Institute of Organic Chemistry of Siberian Branch of Russian Academy of Sciences, Novosibirsk, Lavrentiev Avenue, 9, 630090, Russia; e-mail: gatilov@nioch.ncs.ru; https://orcid.org/0000-0002-4128-7293

_____
*The author's name is presented in the order: *Last Name, First and Middle Names*

Ulygbek B. Tuleuov[*] [iD], Akerke T. Kazhmuratova [iD], Abylaihan N. Bolatbay [iD],
Ermaut Nassikhatuly [iD], Aizhan R. Koishugulova [iD]

Karagandy University of the name of Academician E.A. Buketov, Kazakhstan
(*Corresponding author`s e-mail: bekalols1@gmail.com)

Comparative Analysis of Thermal Decomposition Kinetics of Copolymers Based on Polyethylene Glycol Fumarate with Methacrylic Acid

The thermal properties of a copolymer based on polyethylene glycol fumarate with methacrylic acid in a nitrogen atmosphere were studied in this paper. Four various heating rates and two types of a polyester resin composition were used. The analysis of thermal decomposition kinetics was implemented. Three kinetics methods namely Flynn-Wall-Ozawa, Kissinger-Akahira-Sunose and Friedman were applied. Curves of a thermogravimetric analysis demonstrated that the thermal decomposition of copolymers with different molar ratios was observed. It was determined that the kinetic data depends on the studied copolymers' composition. The obtained data showed a good convergence in various heating rates. Also, the thermodynamic characteristics were calculated namely the changes in the Gibbs energy (ΔG), enthalpy (ΔH) and entropy of activation (ΔS). The Achar-Brindley-Sharp method was used to find the invariant kinetic parameters of decomposition. Thus, the the kinetic compensation effect was applied to define a reaction model and a pre-exponential factor. A main phase of the copolymer decomposition in a narrow temperature range was determined. It was attested by a peak on the differential curve. An insignificant mass loss of the volatile-matter yield was observed in the range of 30–150 °C.

Keywords: dynamic thermogravimetry, thermal decomposition, copolymer based on polyethylene glycol fumarate with methacrylic acid, activation energy, isoconversional kinetic analysis.

Introduction

Hydrogels are the promising materials to use in the practice. They have some special physicochemical properties such as high susceptibility and sensitivity to environmental changes and shape variability [1]. The spread spectrum to use hydrogels was intensified the search for the new monomers to synthesize such polymers [2–5]. The unsaturated polyester resins are of a particular interest to obtain the above mentioned materials.

It's a well-known fact that the unsaturated polyester resins have a complex of the useful properties such as lower viscosity and efficient curing by vinyl monomers in comparison with the epoxy resins. As a result, it demonstrates their higher reactivity [6].

Despite the aforementioned advantages of the unsaturated polyesters, their reactions have not been sufficiently studied. For instance, the literature has some comprehensive data on copolymerization of the unsaturated polyester resins with the hydrophobic monomers [7–9]. However, there is almost no information on their copolymerization with the ionogenic monomers.

In addition, the ionogenic hydrophilic monomers were applied as comonomers of the unsaturated polyester resins to obtain spatially crosslinked polymers with a charged network and high sorption properties [10].

As is known the copolymers of the unsaturated polyester resins have the practical importance, but a limited number of papers on their thermal stability are observed in the literature [11]. The thermal stability with using the thermo-gravimetric analysis in nitrogen to determine the thermal and thermo-oxidative mechanisms was examined in this paper. Also the activation energy was calculated with using the various heating rates. The papers of [12–13] investigated the features of the decomposition kinetics of some unsaturated polyester resin derivatives with an acrylic acid. It was known that a thermal stability of a copolymer based on the unsaturated polyester resins with a methacrylic acid was previously researched at the initial ratios of M1:M2 (wt%) — 6.65:93.35 wt% (under nitrogen atmosphere) [14].

In continuation of the aforementioned investigations, it was interesting to estimate the impact of a temperature factor on stability of the polyethylene glycol fumarate with methacrylic acid with using the dynamic thermogravimetry methods.

Experimental

The previously synthesized [15] copolymers based on polyethylene glycol fumarate (p-EGF) with methacrylic acid (MAA) (6.65:93.35 mol.% and 89.98:10.02 mol.%) were used as subjects of this study. The thermal properties of copolymers (p-EGF:MAA) were studied on Setaram Labsys Evolution TG-DTA/DSC for the synchronous thermal analysis. A dynamic mode, a temperature range of 30-700ºC, heating in Al_2O_3 crucible at a rate of 2.5, 5, 10, 20 °C/min, inert atmosphere with a nitrogen flow rate of 30 ml/min were applied. The device was calibrated for the thermogravimetric studies and heat flow in compliance with standards of $CaCO_3$. The experimental data was processed with using the Microsoft Excel and Processing programs.

Flynn-Wall-Ozawa's integral method

The Flynn-Wall-Ozawa method [16–17], which uses the Doyle's approximation [18], is based on an equation:

$$\ln\left(\beta_i\right) = \text{Const} - 1.052\left(\frac{E_\alpha}{RT_\alpha}\right). \tag{1}$$

The activation energies for various conversion levels are calculated from a slope of $\ln(\beta_i)$ dependence on $1/T$.

Friedman's differential method

The Friedman's differential method is described by a following equation [19]:

$$\ln\left[\beta_i\left(\frac{d\alpha}{dT}\right)_{\alpha,i}\right] = \ln\left[f\left(\alpha\right)A_\alpha\right] - \frac{E_\alpha}{RT_{\alpha,i}}. \tag{2}$$

The linear dependence graphs of $\ln\left[\beta_i\left(\frac{d\alpha}{dT}\right)_{\alpha,i}\right]$ on $1/T$ give the straight lines with different slope angles of E/R. Thus, the activation energies are calculated on their basis.

Kissinger-Akahira-Sunose method

The Kissinger-Akahira-Sunose method, which uses a more accurate Murray and White approximations, is based on an equation [20]:

$$\ln\left(\frac{\beta_i}{T_{\alpha,i}^2}\right) = \text{Const} - \frac{E_\alpha}{RT_\alpha}. \tag{3}$$

The data were linearized [21]. As a result, the calculated points for all patterns were placed on the straight lines. The least squares method was used. Their tangent of a slope was corresponded to E/R. Their cut-off section on the ordinate axis was conformed to an effective order of a reaction.

Invariant kinetic parameters method

The so-called "compensation effect" was used for the invariant kinetic parameters method and the model-fitting method. So this compensation effect was found in the experiment at a single heating rate to define a reaction model and a pre-exponential factor. The Achar-Brindley-Sharp method [22] was obtained with a logarithmic equation:

$$\ln\left(\frac{dx/dt}{f(\alpha)}\right) = \ln A - \frac{E}{RT}. \tag{4}$$

The precise definition of the reaction model and pre-exponential factors could be achieved with using the foregoing compensation effect. Thus, the values of E_i and A_i were used to determine parameters. The values of a and b were applied for a compensation effect by equation [23]:

$$\ln A_i = a * E_i + b *. \tag{5}$$

Once the parameters were defined, the reaction model can be constructed in any integral or differential form with using the values of E_i and A_i by equation [24]:

$$g(a) = \frac{A}{\beta}\int_0^{T_\alpha} \exp\left(\frac{-E}{RT}\right)dt. \tag{6}$$

Thermodynamic study

The thermodynamic parameter can be calculated from a fundamental expression [25–26].

$$k = \frac{x^{ek_B T}}{h} \exp\left(\frac{\Delta S^{\neq}}{R}\right) \exp\left(-\frac{E}{RT}\right), \tag{7}$$

where χ — a transmission coefficient. It is taken to be a unity for monomolecular reactions; k_B — the Boltzmann constant; h — the Planck's constant; e — the Neper number; $\Delta S^{\neq}$ — the change of entropy for the formation of the activated complex from a reagent.

The following expression was obtained with using the pre-exponential factor A from the Arrhenius equation:

$$A = \frac{x^{ek_B T}}{h} \exp\left(\frac{\Delta S^{\neq}}{R}\right). \tag{8}$$

After rearranging an equation (8), the change of entropy of the activated complex can be calculated by the following expression (9):

$$\Delta S^{\neq} = R\left(\ln A - \ln \frac{x^{ek_B T}}{h}\right). \tag{9}$$

Changes in the Gibbs free energy and enthalpy of the activated complex can be calculated by the well-known thermodynamic equations of (10) and (11):

$$E_A = \Delta H + RT \; ; \tag{10}$$

$$\Delta G = \Delta H - T\Delta S \; . \tag{11}$$

ΔS, ΔH and ΔG were calculated at a temperature equal to the DTG peak temperature, which corresponded to the fastest decomposition temperature.

Results and Discussion

Practice demonstrated that unsaturated polyethers with a low molecular weight and an unsaturated bond are a good framework for synthesis of the spatially crosslinked highly charged cationic and amphoteric polyelectrolytes to interact with the corresponding monomers [13]. It should be noted that the crosslinked copolymers formation at any ratio of the initial comonomer mixture was obtained by the reaction. In this case, a clear pattern of dependence of the swelling ability on the content of polyester resin was observed. Thus, it was explained by a change in a grid density [27]. Previously, our paper of [28] showed that based on the above an increase in the thermal stability of copolymers with high polyester content should be expected. Therefore, it was interesting to evaluate the thermal stability in a comparison of copolymers based on polyethylene glycol fumarate with methacrylic acid, i.e. they were opposite in a molar composition.

The thermal decomposition of p-EGF–MAA copolymers was studied with a molar composition of 6.65:93.35; 89.98:10.02 mol.%. Thus, the dynamic thermogravimetric analysis in a nitrogen atmosphere at various heating rates in a temperature range of 30–600 °C was used. The kinetic data were processed by the Flynn-Wall-Ozawa, Friedman and Kissinger-Akahira-Sunose methods. They were based on the Arrhenius equation and used in studies of many organic and polymeric materials [29–33].

The resulting curves of the thermogravimetric analysis and decomposition rates are demostrated in Figure 1.
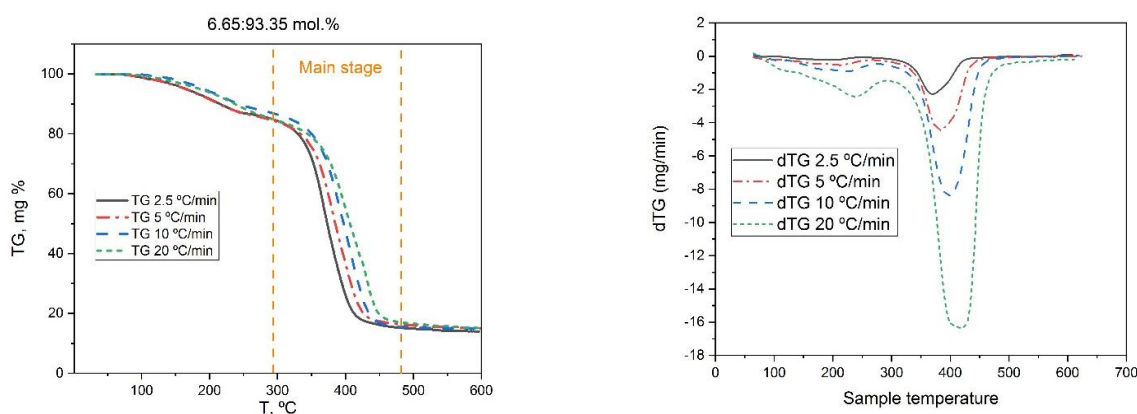
Figure 1. Temperature dependences of the mass change (TG curve), the rate of mass change (DTG) for p-EGF:MAA copolymer at various heating rates, initial ratios (a) of M_1:M_2 in mol. % — 6.65:93.35 mol.%, in a nitrogen atmosphere

Figure 1 demonstrates that transformations were not observed in a substance that lead to a change in its mass on the thermogravimetric curves at 30°C to 100 °C.

An insignificant decomposition of a sample was found for a copolymer with a composition of 6.65:93.35 mol.% at 100–300 °C with yield of some volatile products and mass loss up to ~12%. Further intensive mass loss of the sample with complete process completion at ~500 °C was observed. The total mass loss was ~80 %.

The graph in Figure 2 illustrates that the mass loss was observed noticeably faster with an increase in the heating rate. So the rate of mass loss was low at a heating rate of 2.5°C/min. Thus, the mass loss was found more intensively with an increase in the heating rate.
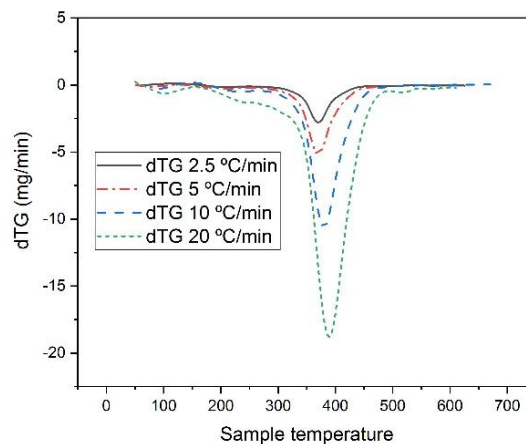
Figure 2. Temperature dependences of the mass change (TG curve), the rate of mass change (DTG) for the p-EGF:MAA copolymer at various heating rates, initial ratios of $M_1:M_2$ in mol.% — 89.98:10.02 mol.%, in a nitrogen atmosphere

The volatile-matter yield for a copolymer with a high content of polyester resin started at higher temperatures (maximum at 320 °C). The temperature range of 320–500 °C demonstrated the decomposition of a copolymer's basic mass with a total residue of ~15 %. The same rule was also used for the second sample, i.e. its heating speed raised and its mass loss rate has increased.

The comparative analysis of curves of 1 and 2 demonstrated that when a polyester content increased in a copolymer, the decomposition had higher temperatures. As noted above, it was apparently associated with an increase in a grid density.

Kinetic analysis

The isoconversion principle was used to calculate the kinetic parameters. Thus, dependences of parameters of the Flynn-Wall-Ozawa, Kissinger-Akahira-Sunose and Friedman equations at various transformation degrees were established in Figure 3.

Figure 3 showed the linearization of data for two different copolymers with slight differences, i.e. it depended on the polyester resin content. Based on these differences, the activation energies and the pre-exponential factor from a slope and line intersection of each component were calculated. Results in Table 1 demonstrated the kinetic parameters for all copolymer samples calculated with three various methods.
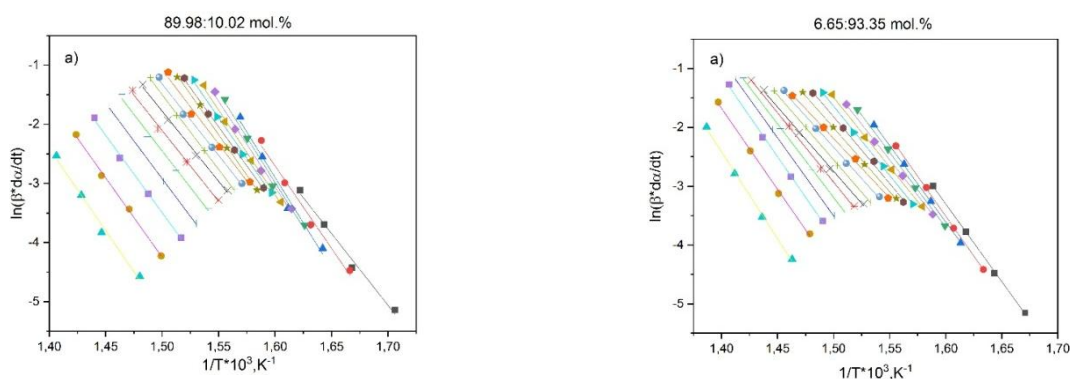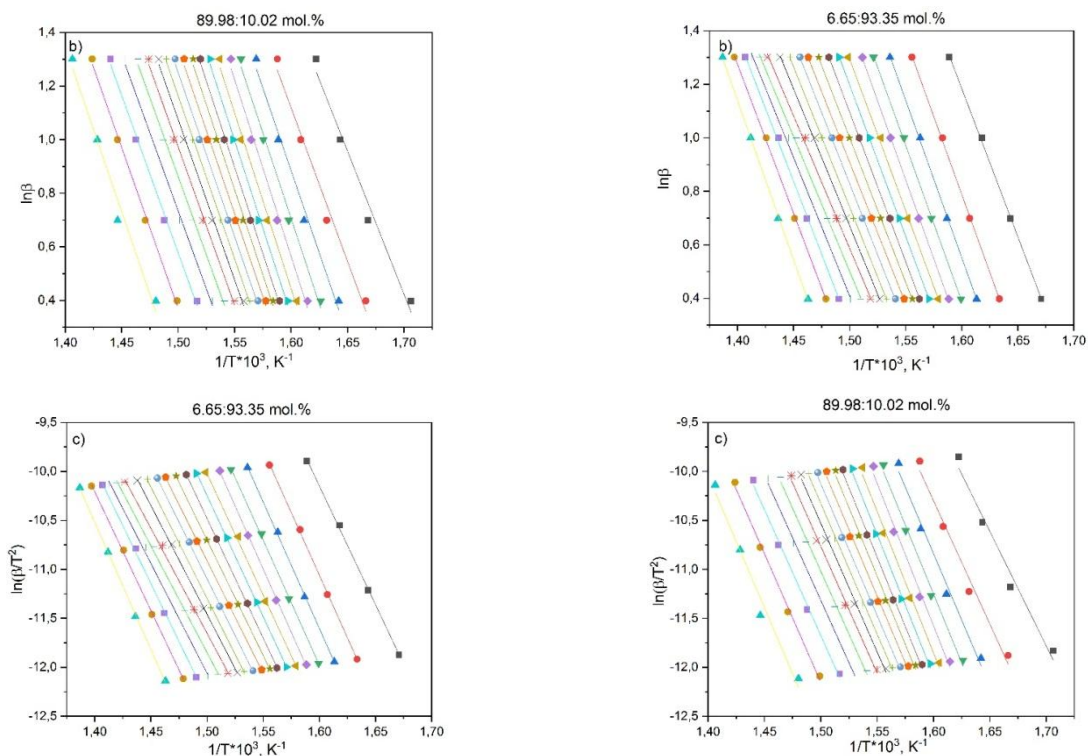
Figure 3. Linearization of thermogravimetry data for copolymers based on p-EGF:MAA at various heating rates, initial ratios (1) of $M_1:M_2$ in mol. % — 6.65:93.35 mol.%; (2) $M_1:M_2$ in mol. % — 89.98:10.02 mol. %, in a nitrogen atmosphere, using methods: (a) — Friedman; (b) Flynn-Wall-Ozawa; (c) Kissinger-Akahira-Sunose at various heating rates

T a b l e 1

Dependence of activation energy for thermal decomposition of copolymers based on p-EGF with MAA on transformation degree

α	Ea, kJ·mol^{-1}					
	Flynn-Wall-Ozawa method		Friedman method		Kissinger-Akahira-Sunose method	
	6.65:93.35%	89.98:10.02%	6.65:93.35%	89.98:10.02%	6.65:93.35%	89.98:10.02%
0.05	201.41	194.29	219.41	201.63	201.61	194.33
0.10	211.91	208.89	225.01	237.58	212.42	209.45
0.15	214.03	224.27	215.91	255.77	214.51	225.50
0.20	212.08	232.41	211.32	253.66	212.37	233.96
0.25	214.04	239.91	201.01	241.67	214.35	241.77
0.30	206.29	238.51	196.01	238.54	206.12	240.23
0.35	205.80	237.93	195.45	229.35	205.56	239.55
0.40	203.27	234.20	188.67	219.73	202.83	235.59
0.45	196.73	231.14	180.36	227.65	195.91	232.33
0.50	192.36	225.46	168.19	208.61	191.25	226.29
0.55	193.67	222.93	176.68	200.89	192.56	223.58
0.60	190.63	221.58	175.84	210.04	189.31	222.11
0.65	186.21	218.07	181.55	197.34	184.60	218.39
0.70	180.17	215.04	146.40	199.30	178.16	215.14
0.75	183.10	213.37	207.71	205.50	181.18	213.31
0.80	188.25	212.13	220.50	212.34	186.54	211.93
0.85	197.64	213.83	229.31	217.57	196.36	213.61
0.90	202.70	218.49	228.94	223.36	201.60	218.38
0.95	216.50	224.35	245.71	231.03	215.99	224.41
Average	210.9378	234.8271	211.8925	233.9814	210.185	235.553

Table 1 demonstrates some results of activation energies calculated with using three various methods. The tabular data have a good convergence with less 5% of accuracy. The Flynn-Wall-Ozawa, Kissinger-Akahira-Sunose and Friedman methods provided to estimate the activation energy in the whole process without a prior assumption of a reaction model.

The choice of these methods permitted to compare the activation energy obtained with the integral and differential methods. Thus, these methods were able to assess the correctness of the accuracy made in deriving of the equations. Figure 3 demonstrates the results of the mathematical processing for the thermogravimetric curves.

In order to define the pre-exponential factor and reaction model, the Achar-Brindley-Sharp methods and method of the invariant kinetic parameters (ABS) were applied [34]. The paper pointed out that the Achar-Brindley-Sharp method were more accurate to calculate the kinetic compensation parameters. Values of E and $\ln A$ were received for all 13 reaction models from Table 1 with using an Equation 4.
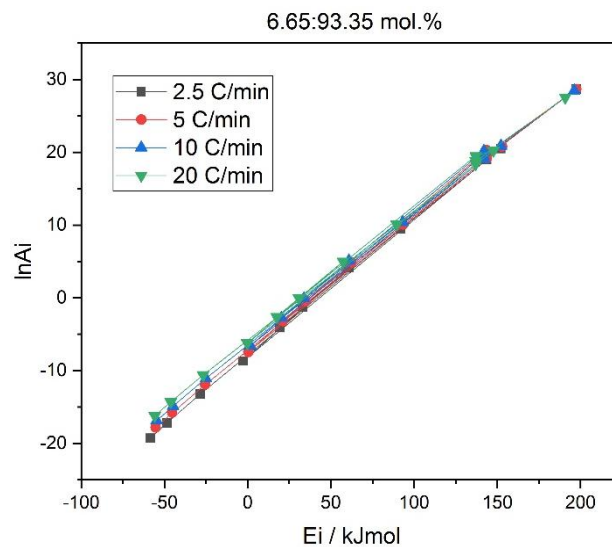
Figure 4. The observed compensation effect between the pre-exponential factor
and apparent activation energy for thermal decomposition of copolymer
based on the p-EGF:MAA, M_1:M_2 in mol.% — 6.65:93.35 mol.%, at various heating rates
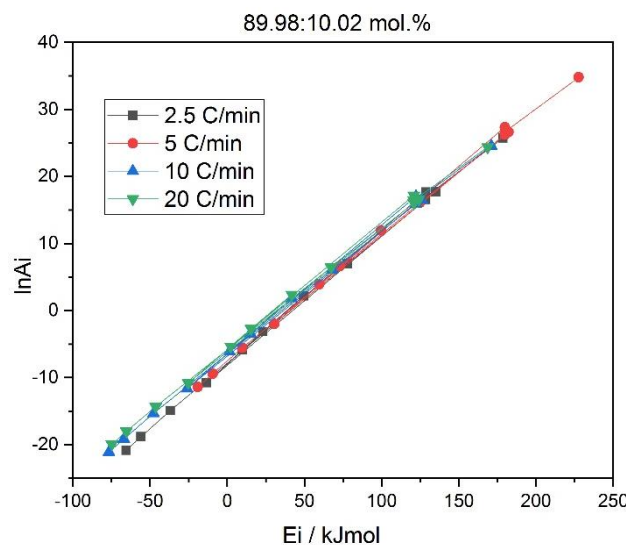
Figure 5. The observed compensation effect between pre-exponential factor
and apparent activation energy for thermal decomposition of copolymer
based on the p-EGF:MAA, M_1:M_2 in mol.% — 89.98:10.02 mol.%, at various heating rates

Figures 4–5 illustrate a correlation between $\ln A_i$ and E_i obtained by the compensation effect (CE) with using the Achar-Brindley-Sharp (ABS) method. It was observed that correlation coefficient is close to unity during the using all models ($R = 0.99$). As a result, it was indicated a good correlation between all parameters regardless of the models used. As expected, the data have a good correlation between all straight lines for all heating rates. Compensation parameters are presented in Tables 2-3.

Table 2

Compensation effect parameters for thermal decomposition of copolymer based on the p-EGF:MAA, M_1:M_2 in mol.% – 6.65:93.35 mol.% at four different heating rates

β (ºC/min)	a^*	b^*	R^2
2.5	0.1887	−7.8780	0.9993
5	0.1853	−7.2247	0.9992
10	0.1822	−6.5555	0.9992
20	0.1787	−5.8623	0.9991

Table 3

Compensation effect parameters of thermal decomposition of copolymer based on p-EGF:MAA, M_1:M_2 in mol.% — 89.98:10.02 mol.% at four different heating rates

β (ºC/min)	a^*	b^*	R^2
2.5	0.1922	−7.8805	0.9993
5	0.1899	−7.4579	0.9993
10	0.1858	−6.5204	0.9992
20	0.1834	−5.8592	0.9992

Figure 6 shows a graph of compensation parameters for copolymers based on p-EGF:MAA, M_1:M_2 in mol.% — 6.65:93.35 mol.% and p-EGF:MAA, M_1:M_2 in mol.% — 89.98:10.02 mol.%.
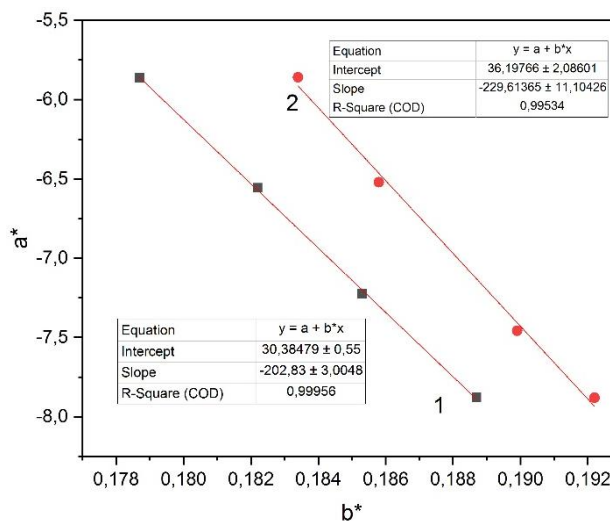
Figure 6. Graph of the correlation ratio of a^* and b^*

The kinetic parameters for copolymer base on p-EGF:MAA were obtained from a slope and line intersection of E and $\ln A$. Figure 6 illustrates that activation energy is close to values obtained by the Flynn-Wall-Ozawa, Friedman and Kissinger-Akahira-Sunose methods. They were $E = 202$ kJ/mol, $E = 229$ kJ/mol for p-EGF:MAA, M_1:M_2 in mol.% — 6.65:93.35 mol.% and M1:M2 in mol.% — 89.98:10.02 mol.%, respectively.

Using the obtained values of E_i and A_i, the dependence of $g(\alpha)$ on α was plotted in the integral form with using an equation (6) (Fig. 7).
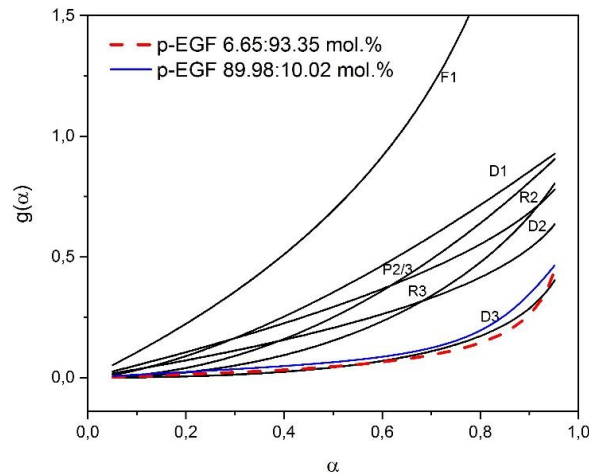
Figure 7. Theoretical curves of $g(\alpha)$ on α for some kinetic models and experimental plot
for kinetic model D3 for thermal decomposition of copolymers based on p-EGF:M_1:M_2
in mol.% — 6.65:93.35 mol.% and M1:M2 in mol.% — 89.98:10.02 mol.%, at various heating rates

Figure 7 demonstrates the most appropriate model with a shape as a three-dimensional diffusion (D3).

Thermodynamic parameters

To accurately understand the mechanism of thermal decomposition of the studied copolymers, the changes in entropy (ΔS), Gibbs free energy (ΔG) and enthalpy (ΔH) were calculated. The obtained values were summarized in Tables 4–5.

Table 4

**Thermodynamic parameters of thermal decomposition of copolymer
based on p-EGF:MAA, M_1:M_2 in mol.% — 6.65:93.35 mol.%**

β °C/min	ΔG kJ/mol	ΔH kJ/mol	ΔS J/mol*K
2.5	317.38	207.33	−297,26
5	296.78	185.88	−299,53
10	287.00	175.68	−300,69
20	320.87	210.31	−298,63

Table 5

**Thermodynamic parameters of thermal decomposition of copolymer
based on p-EGF:MAA, M1:M2 in mol.% – 89.98:10.02 mol.%**

β °C/min	ΔG kJ/mol	ΔH kJ/mol	ΔS J/mol·K
2.5	312.61	204.46	−300.56
5	329.05	221.02	−300.207
10	316.37	207.91	−301.419
20	327.20	218.79	−301.293

The thermodynamic characteristic change of Gibbs energy (ΔG), activation entropy (ΔS) and enthalpy (ΔH) were calculated with using the obtained values of activation energy. A positive value of the Gibbs energy ΔG pointed out infeasibility of the spontaneous decomposition. A negative value of ΔS stated a reduction of random effects at the gas-solid interface and a decrease in the degree of freedom of substances in the thermal decomposition.

Conclusions

The thermal decomposition of a copolymer based on polyethylene glycol fumarate with methacrylic acid was investigated in this paper. Decomposition was observed in different ways with various ratios of the polyester resin in a copolymer composition. Thus, decomposition was much later for copolymer with a large amount of polyester resin. As a result, the activation energy values had higher values.

A good convergence was found in the kinetic parameters of a copolymer obtained by the Flynn-Wall-Ozawa, Kissinger-Akahira-Sunose and Friedman methods. As a result, the received data on activation energy had the similar values at various heating rates.Thus, the process of mass loss intensified with an increase in the heating rate. It was correctly for all non-isothermal processes. The copolymer kinetic triplets were determined and showed good convergence with using methods of the Achar-Brindley-Sharp and invariant kinetic parameters. Graphs of dependence $g(\alpha)$ for various transformation degrees showed a satisfactory fit between the experimental curves and theoretical ones. As a result, the reaction model of two copolymers described with the D3 model was determined.

References

1 Okay, O. (2009). General Properties of Hydrogels. In: Gerlach, G., Arndt, KF. (eds) *Hydrogel Sensors and Actuators. Springer Series on Chemical Sensors and Biosensors, Vol 6.* Springer, Berlin, Heidelberg. https://doi.org/10.1007/978-3-540-75645-3_1

2 Li, L., Guo, J. & Xiong, R. (2021). Synthesis and swelling behavior of a fully degradable physical cross-linked high strength hydrogel. *Polymer Testing*, 94. https://doi.org/10.1016/j.polymertesting.2020.106982

3 Xiao, C. & Zhou, G. (2003). Synthesis and properties of degradable poly(vinyl alcohol) hydrogel. *Polymer Degradation and Stability, 81*(2), 297–301. https://doi.org/10.1016/S0141-3910(03)00100-9

4 Wang, Y., Zhang, X., Qiu, D., Li, Y., Yao, L. & Duan, J. (2018). Ultrasonic assisted microwave synthesis of poly (Chitosan-co-gelatin)/polyvinyl pyrrolidone IPN hydrogel. *Ultrasonics Sonochemistry*, *40*, 714–719. https://doi.org/10.1016/j.ultsonch.2017.08.003

5 Weian, Z., Wei, L. & Yue'e, F. (2005). Synthesis and properties of a novel hydrogel nanocomposites. *Materials Letters*, *59*(23), 2876–2880. https://doi.org/10.1016/j.matlet.2005.04.033

6 Boenig. H.V. (1964). Unsaturated Polyesters, Structure and Properties. Elsevier Publishing Company, Amsterdam. 222 S., DIN A 5, Preis DM 31. Fette, Seifen, Anstrichmittel, *68*(1), 30–30. https://doi.org/10.1002/lipi.19660680105

7 Anisimov Y.N., Vonsovich N.A. & Grekhova O.B. (1996). Privitaia sopolimerizatsiia vinilatsetata s nenasyshchennoi oligoefirnoi smoloi i kharakteristiki utverzhdennykh kompozitsii [Graft copolymerization of vinyl acetate with an unsaturated oligoester resin and characteristics of the cured compositions]. *Zhurnal prikladnoi khimii, 69*, 2, 312–316 [in Russian].

8 Studentsov V.N., Cheremukhina I.V. & Levkin A.N. (2003). Kompozitsionnyi material na osnove nenasyshchennoi poliefirnoi smoly [Composite material based on unsaturated polyester resin]. *Informatsionnyi listok, 5* [in Russian].

9 Talet P.A. (1955). Patent. No 2526223 SSHA.

10 Burkeev, M.Z., Magzumova, A.K., Tazhbaev, E.M., Burkeeva, G.K., Kovaleva, A.K., Khamitova, T.O. & Mataev, M.M. (2013). Effect of external factors on the swelling of hydrogels based on poly(ethylene glycol) maleate with some vinyl monomers. *Russian Journal of Applied Chemistry*, *86*(1), 63–68. https://doi.org/10.1134/S1070427213010114

11 Baudry, A., Dufay, J., Regnier, N. & Mortaigne, B. (1998). Thermal degradation and fire behaviour of unsaturated polyester with chain ends modified by dicyclopentadiene. *Polymer Degradation and Stability*, *61*(3), 441–452. https://doi.org/10.1016/S0141-3910(97)00230-9

12 Burkeev, M.Zh., Bolatbay, A.N., Sarsenbekova, A.Zh., Davrenbekov, S.Zh. & Nasikhatuly, E. (2021). Integral Ways of Calculating the Destruction of Copolymers of Polyethylene Glycol Fumarate with Acrylic Acid. *Russian Journal of Physical Chemistry A*, *95*(10), 2009–2013. https://doi.org/10.1134/S0036024421100034

13 Sarsenbekova, A.Z., Kudaibergen, G.K., Burkeev, M.Z. & Burkeeva, G.K. (2019). Comparative Analysis of the Thermal Decomposition Kinetics of Polyethylene Glycol Fumarate–Acrylic Acid Copolymers. *Russian Journal of Physical Chemistry A, 93*(7), 1252–1257. https://doi.org/10.1134/S0036024419060281

14 Burkeyev, M.Z., Tuleuov, U.B., Bolatbay, A.N., Khavlichek, D., Davrenbekov, S.Z., Tazhbayev, Y.M. & Zhakupbekova, E.Z. (2021). Investigation of the destruction of copolymers of poly(ethylene glycol)fumarate with methacrylic acid using differential equations. *Bulletin of the University of Karaganda – Chemistry*, *103*(3), 47–52. https://doi.org/10.31489/2021CH3/47-52

15 Burkeev, Kudaibergen, Tazhbayev, Hranicek, Burkeyeva & Sarsenbekova (2019). Synthesis and investigation of copolymer properties on the basis of poly(ethylene glycol)fumarate and methacrylic acid. *Bulletin of the University of Karaganda – Chemistry*, *93*(1), 32–38. https://doi.org/10.31489/2019Ch1/32-38

16 Ozawa, T. (1965). A New Method of Analyzing Thermogravimetric Data. *Bulletin of the Chemical Society of Japan*, *38*(11), 1881–1886. https://doi.org/10.1246/bcsj.38.1881

17 Flynn, J.H. & Wall, L.A. (1966). General treatment of the thermogravimetry of polymers. *Journal of Research of the National Bureau of Standards Section A: Physics and Chemistry*, *70A*(6), 487. https://doi.org/10.6028/jres.070A.043

18 Doyle, C.D. (1962). Estimating isothermal life from thermogravimetric data. *Journal of Applied Polymer Science*, *6*(24), 639–642. https://doi.org/10.1002/app.1962.070062406

19 Friedman, H.L. (2007). Kinetics of thermal degradation of char-forming plastics from thermogravimetry. Application to a phenolic plastic. *Journal of Polymer Science Part C: Polymer Symposia*, *6*(1), 183–195. https://doi.org/10.1002/polc.5070060121

20 Akahira T. & Sunose T. (1971). Method of determining activation deterioration constant of electrical insulating materials, *Res. Report Chiba Inst. Technol.* (Sci. Technol.) 22–31.

21 Petryuk I.P., Gaydadin A.N. & Yefremova S.A. (2010). Opredelenie kineticheskikh parametrov termodistruktsii polimernykh materialov po dannym dinamicheskoi termogravimetrii [Determination of the kinetic parameters of thermal degradation of polymeric materials according to dynamic thermogravimetry]. Metod. ukazaniia. Volgograd, VolgGTU, 3, 7 [in Russian].

22 Achar B.B., Brindley G.W. & Sharp J.H. (1966). Kinetics and mechanism of dehydroxylation processes, III. Applications and limitations of dynamic methods, in: L. Heller, A. Weiss (Eds.), Proc. lnt. Clay Conf. Jerusalem, Israel Prog. Sci. Transl., Jerusalem, Israel, 67–73.

23 Lesnikovich, A. I. & Levchik, S. v. (1983). A method of finding invariant values of kinetic parameters. *Journal of Thermal Analysis, 27*(1), 89–93. https://doi.org/10.1007/BF01907324

24 Vyazovkin, S., Burnham, A.K., Criado, J.M., Pérez-Maqueda, L.A., Popescu, C. & Sbirrazzuoli, N. (2011). ICTAC Kinetics Committee recommendations for performing kinetic computations on thermal analysis data. *Thermochimica Acta*, *520*(1–2), 1–19. https://doi.org/10.1016/j.tca.2011.03.034

25 Żółtowska, S., Koltsov, I., Alejski, K., Ehrlich, H., Ciałkowski, M. & Jesionowski, T. (2021). Thermal decomposition behaviour and numerical fitting for the pyrolysis kinetics of 3D spongin-based scaffolds. The classic approach. *Polymer Testing*, 97, 107148. https://doi.org/10.1016/j.polymertesting.2021.107148

26 Vlaev, L.T., Markovska, I.G. & Lyubchev, L.A. (2003). Non-isothermal kinetics of pyrolysis of rice husk. *Thermochimica Acta*, *406*(1–2), 1–7. https://doi.org/10.1016/S0040-6031(03)00222-3

27 Burkeev, M.Zh., Zhumanazarova, G.M., Kudaibergen, G.K., Tazhbayev, E.M., Turlybek, G.A. & Zhakupbekova, E.Zh. (2020). Research of the influence of external factors on copolymers based on unsaturated polyester resins. *Bulletin of the University of Karaganda – Chemistry*, *98*(2), 51–57. https://doi.org/10.31489/2020Ch2/51-57

28 Burkeev, M.Zh., Sarsenbekova, A.Zh., Bolatbay, A.N., Tazhbaev, E.M., Davrenbekov, S.Zh., Nasikhatuly, E., Zhakupbekova, E.Zh. & Muratbekova, A.A. (2020). The use of differential calculation methods for the destruction of copolymers of polyethylene glycol fumarate with the acrylic acid. *Bulletin of the University of Karaganda – Chemistry*, *99*(3), 4–10. https://doi.org/10.31489/2020Ch3/4-10

29 Fares, M.M. & El-Faqeeh, A.S. (2005). Thermal and thermoxidative degradations of starch and thermosensitive starch-g-BAM copolymers. *Journal of Thermal Analysis and Calorimetry, 82*(1), 161–166. https://doi.org/10.1007/s10973-005-0858-4

30 Zhang, G. Z., Zheng, H. C. & Xiang, X. (2013). Thermal decomposition and kinetics studies on the 2,2-dinitropropyl acrylate–styrene copolymer and 2,2-dinitropropyl acrylate–vinyl acetate copolymer. *Journal of Thermal Analysis and Calorimetry*, *111*(2), 1039–1044. https://doi.org/10.1007/s10973-012-2523-z

31 Popov, A., Bogdanov, B., Petrova, I., Gyurova, K., Nedelchev, N. & Velev, V. (2013). Thermal studies on polycaprolactam. *Journal of Thermal Analysis and Calorimetry*, *111*(2), 1539–1544. https://doi.org/10.1007/s10973-012-2496-y

32 Li, H., Pan, R., Wang, W. & Zhang, L. (2014). Thermal decomposition and kinetics studies on poly(BDFAO/THF), poly(DFAMO/THF), and poly(BDFAO/DFAMO/THF). *Journal of Thermal Analysis and Calorimetry*, *118*(1), 189–196. https://doi.org/10.1007/s10973-014-3985-y

33 Zhang, G., Zhang, J., Wang, F. & Li, H. (2015). Thermal decomposition and kinetics studies on the poly (2,2-dinitropropyl acrylate) and 2,2-dinitropropyl acrylate–2,2-dinitrobutyl acrylate copolymer. *Journal of Thermal Analysis and Calorimetry*, *122*(1), 419–426. https://doi.org/10.1007/s10973-015-4687-9

34 Sbirrazzuoli, N. (2013). Determination of pre-exponential factors and of the mathematical functions f(α) or G(α) that describe the reaction mechanism in a model-free way. *Thermochimica Acta*, *564*, 59–69. https://doi.org/10.1016/j.tca.2013.04.015

Information about authors*

Tuleuov, Ulygbek Borashevich (*corresponding author*) — 3rd year Doctoral Student, Karagandy University of the name of academician E.A. Buketov, Universitetskaya st., 28, 100024, Karaganda, Kazakhstan, e-mail: bekalols1@gmail.com; https://orcid.org/0000-0002-2664-6884

Kazhmuratova, Akerke Temirgalievna — Candidate of Chemical Sciences, Associated Professor, Karagandy University of the name of academician E.A. Buketov, Universitetskaya st., 28, 100024, Karaganda, Kazakhstan, e-mail: kazhmuratova@mail.ru; https://orcid.org/0000-0003-4044-8419

Bolatbay, Abylaihan Nurmanovich — Lecturer, Physical and Analytical Chemistry Department, Karagandy University of the name of academician E.A. Buketov, Universitetskaya st., 28, 100024, Karaganda, Kazakhstan, e-mail: abylai_bolatbai@mail.ru; https://orcid.org/0000-0001-5047-3066

Nasikhatuly, Ermaut — Lecturer, Organic Chemistry and Polymers Department Karagandy University of the name of academician E.A. Buketov, Universitetskaya st., 28, 100024, Karaganda, Kazakhstan, e-mail: ermauit@gmail.com; https://orcid.org/0000-0003-4574-0902

Koishugulova, Aizhan Ruslanovna — 2nd year Master Student, Karagandy University of the name of academician E.A. Buketov, Universitetskaya st., 28, 100024, Karaganda, Kazakhstan, e-mail: ruslanovnaaij@gmail.com; https://orcid.org/0009-0005-5244-0619

*The author's name is presented in the order: *Last Name, First and Middle Names*

Article

UDC 541.64

https://doi.org/10.31489/2959-0663/2-23-11

Gulsym K. Burkeyeva[1] ⓘ, Anna K. Kovaleva[1] ⓘ, Yerkeblan M. Tazhbayev[1] ⓘ, Zhansaya M. Ibrayeva[1*] ⓘ, Lyazzat Zh. Zhaparova[1] ⓘ, Diyara R. Meiramova[1] ⓘ, Jiri Plocek[2] ⓘ

[1]Karagandy University of the name of academician E.A. Buketov, Kazakhstan;
[2]Institute of Inorganic Chemistry of the Czech Academy of Sciences, Husinec-Rez, Czech Republic;
(*Corresponding author`s e-mail: zhansaya.ibraieva@mail.ru)

Investigation of the Influence of UV-Irradiation on Thermal Stability of Binary Systems on the Basis of Polyethylene Glycol Fumarate with Some Vinyl Monomers

This work is devoted to the investigation of continuous exposure to UV-irradiation on thermal stability of polymeric base of sealants. The copolymers of polyethylene glycol fumarate with acrylic and methacrylic acids, and acrylamide of the composition of "unsaturated polyester: vinyl monomer" ~35:65 mass.% (correspondingly) were chosen as the polymer base. The samples were analyzed on microscope to the presence of microcracks as a result of exposure to UV-irradiation on them. The studied samples were evaluated visually on color change and the appearance of turbidity. Thermal stability of the studied polymeric base was determined by establishing the temperature of the start of thermal deformation by thermogravimetry before and after the process of UV-irradiation within 21 days. It was established that for the polymeric base with acrylamide in its content the temperature of the start of thermal deformation had reduced after exposure to UV-irradiation. In contrary, for the polymeric bases with acrylic and methacrylic acids in their composition the above said thermal index almost had not changed after affecting with UV-irradiation on the samples.

Keywords: polymer base, sealants, UV-irradiation, thermal deformation, unsaturated polyesters, polyethylene glycol fumarate.

Introduction

Investigation of the processes of ageing of the materials when influencing various external factors on them is a complex research and practical task and its solution defines the safety and quality parameter of the use of a building [1–2]. When accelerating the process of operation of construction objects there are not only special requirements to the materials, but there is also the task of providing the reliance of their use within long period of time in natural conditions. In this regard it is necessary to know not only the properties of the materials, but also it is important to predict their change under the effect of negative external factors [3–7].

Sealing materials (the sealants) are used in a various area of technique and construction providing working capacity of structural elements in technique, waterproof compartments, also they define the durability of stiches of inter-wall panels, building blocks and so on [8–11]. In comparison with other classes of polymeric stuffing materials the sealants are used not only as the goods ready to use, but in the forms of fluid-flow and paste-like masses. The sealing materials are spread using rather simple technological operations in the areas of stiches, backlashes, junctures and are poured to the cracks. After technological curing time the sealants form relatively hard and elastic substance and drop into resin-like state. The polymeric film formed seal the holes and cracks hermetically and, in some cases, acts as a glue. The sealants are irreplaceable in sinking the sanitaryware products, in filling-in the stitches inside buildings with high level of humidity, where other types of constructional materials become quickly inapplicable. In housebuilding they are used for filling-in external stitches and cracks in foundations, walls, ceilings, for processing the junctures, holes and cracks inside the rooms. In the rooms with high level of humidity they are used for waterproofing the stitches and junctions. They provide the impermeability in the conditions of drops of pressure, changeable temperatures, loads and they are one of the pointers of reliability of thermo-, water- and vapor-proofing. Thus, the stability of sealants defines the consistency of work and durability of sealing sews in various constructions [10, 11].

The most promising compounds for the development of sealing materials are the solutions of unsaturated polyesters in different monomers of vinyl row [12], which preserve needed fluidity in wide range of concentrations. As a result of having reactive double bond the unsaturated polyesters are the most important rep-

resentatives of polymeric reactive oligomers which are able to react with many monomers forming the cured reaction products [13]. High indices of stability to the influence of external medium, simplicity of preparation and operation, good compatibility with other components (mechanical fillers and pigments) and availability, low primecost and ecological safety make the unsaturated polyesters more preferable co-reagent when obtaining a polymeric base of sealing materials.

Considering the characteristics of sealants are defined by the properties of fillers used as well as the initial polymeric base, the study of the behavior of latter after ageing in natural conditions is of an applied significance.

In this work a continuous effect of UV-irradiation on thermal stability of polymeric base of the sealants was studied. The copolymers of polyethylene glycol fumarate (p-EGF) with acrylic (AA) and methacrylic (MAA) acids and acrylamide (AAm) were chosen as polymeric bases.

Experimental

The reagents used in this work are ethylene glycol, acrylic and methacrylic acids, acrylamide, benzoyl peroxide, dimethylaniline ("Sigma-Aldrich"), fumaric acid ("Vekon"), aluminum chloride ("Reachem"). All of them were used without additional purification.

Initial polyester, i.e. polyethylene glycol fumarate was obtained by condensation polymerization of ethylene glycol with fumaric acid according to the procedure given in [14, 15] at a temperature of 150–160 °C in the presence of catalyst — aluminum chloride.

The objects studied — binary systems of p-EGF with AA, MAA and AAm of composition ~35:65 mass.% were obtained by radical copolymerization in the presence of optimized binary initiating system of "cold" curing (initiator (benzoyl peroxide, BP) : promoter (dimethylaniline, DMA) of the following ratio 1 %:0.15 % calculated from initial monomer mass) at a temperature of 20°C [16, 17]. Schematically the synthesis of the copolymers of p-EGF with AA, MAA and AAm is presented in Figure 1.

where R_1 — H, CH_3 groups; R_2 — H, NH_2 groups; R_I — the radical of initiator
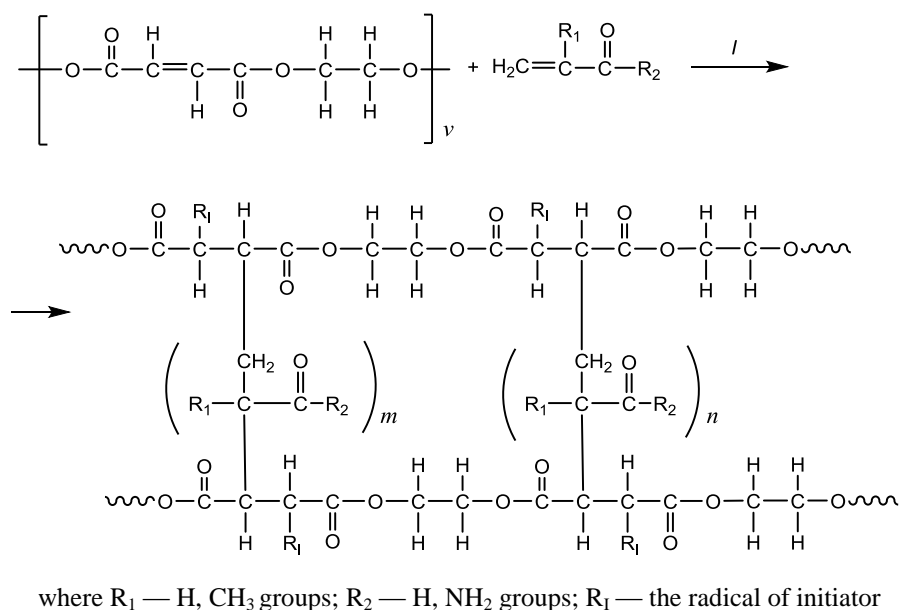
Figure 1. The scheme of polymerization of p-EGF with the monomers of vinyl row

This ratio was chosen on the basis of previous studies of the rheological properties of these binary systems. Thus, the most important parameters of sealing compositions are such parameters as the density and viscosity of the initial solutions, as well as the time of their gelatinization and curing. According to [16, 17], it was found that with an increase in the content of p-EGF, those indicators grew significantly. In particular, the dynamic viscosity of p-EGF–AA solutions rise with an increase of the amount of p-EGF from 35 to 45 mass.%, respectively, from 37.6 to 182.3 mPa·s. This also applies to density, where this indicator varies from 1.1562 to 2.069 g/cm^3. The time of gelatinization and curing of these binary systems also changes. Thus, in particular, for the p-EGF–AA system with a composition of ~35:65 mass.%, these meanings are equal to 55 and 90 min., respectively, while for the p-EGF–AA ratio of ~45:55 mass.%, they are 69 and 188 min. In view of this, the ratio of comonomers ~35:65 mass.% was chosen as an optimal.

Obtained reaction products were identified using IR-spectroscopy. The analysis of IR-spectra points on the presence of characteristic bands which appear within the interval of 1570–1590 cm^{-1}, which correspond to some quantity of non-reacted unsaturated double bonds of p-EGF. The presence of absorption bands at 1724 cm^{-1} and 3425 cm^{-1} in the IR-spectra of the copolymers of p-EGF with carboxylic acids confirms the presence of –COOH groups. There are also the absorption bands at 2859 cm^{-1} and 2915 cm^{-1}, which are characteristic for the methylene groups of MAA. The presence of the peak within the range of 1910–1950 cm^{-1} is typical for amide group –NH$_2$ (Fig. 2):
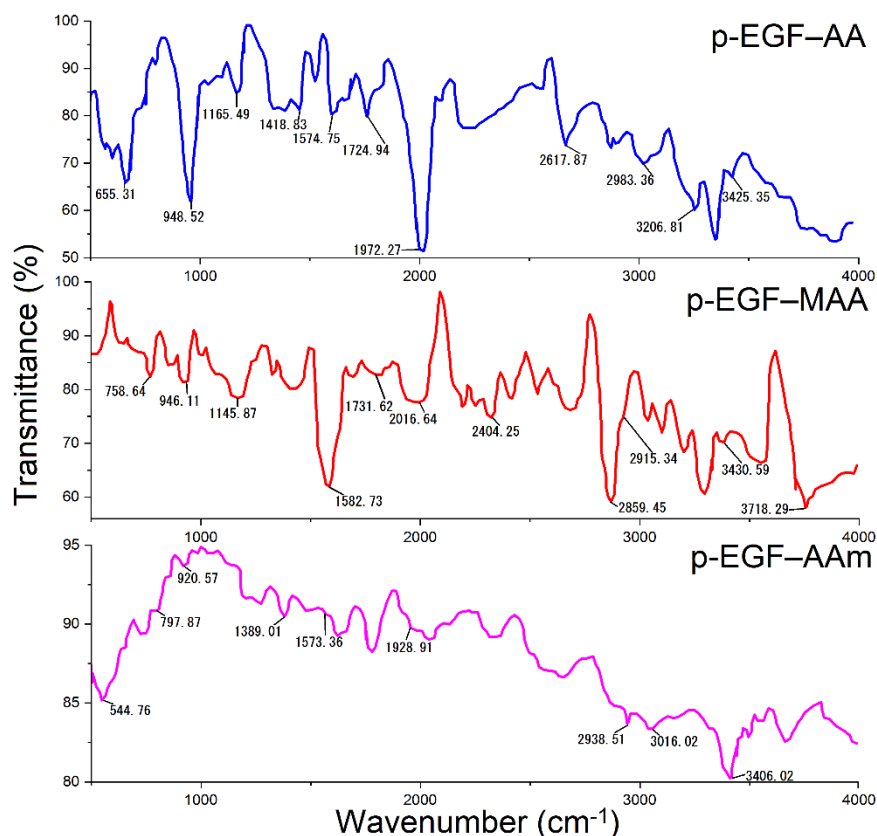
a — p-EGF–AA; *b* — p-EGF–MAA; *c* — p-EGF–AAm

Figure 2. IR-spectra of unsaturated polyester–vinyl monomer

For the study of the influence of UV-irradiation on the samples of binary systems of p-EGF with AA, MAA and AAm of the composition of ~35:65 mass.% was carried out according to all-Union State Standard 32317-2012 [18] on the device Weiss UV3 of the firm Weiss Technik (Germany). It is a camera isolated from external lighting which allows studying the irradiation of plate like samples with UV-light with the wavelengths 290 and 450 nm [19].

When studying the effect of UV-irradiation on tested samples the platelets of various thicknesses ranging from 1 to 5 mm (the platelets of each thickness were prepared three times for carrying out parallel tests which provided obtaining reliable results) were prepared. During the study the irradiation intensity was constant. So, the experiment was carried out within 3 weeks (21 days) in total. Estimation of the states of the samples after irradiation was made visually i.e. the change of color and the presence of microcracks were observed. In order to establish the thermal stability of the tested samples, their thermograms were analyzed and the temperature of thermal deformation was determined [20] within the temperature interval of 30–*200°C. The end of the process takes place when the copolymer decomposes completely at a temperature of ~550–600 °C.*

Estimation of form and shape of the samples after exposure of UV-irradiation on them was done visually and then using binocular-type microscope MicroOptix MX50 (Micro Optix, Austria).

The study of thermal properties of the samples (TGA) before and after exposure to UV-irradiation was done on a device for the synchronic thermal analysis Labsys Evolution TG-DTA/DSC ("Setaram") in dy-

namic regimen within the temperature range of 30–600 °C. Calibration of the equipment for thermogravimetry and heat current was made on $CaCO_3$ and in standards correspondingly [21]. Finely ground platelet samples after influencing with UV-irradiation and the samples of binary systems of p-EGF with AA, MAA and AAm which were not undergone to the exposure of UV-irradiation were heated in an aluminum crucible at a heating rate of 10 °C/min in nitrogen atmosphere at a flow rate of 30 ml/min. The sample's mass was ~1 g.

Results and Discussion

At present time the sealing materials on the basis of polymers play an important role almost in all fields of industry. The main volume of sealants is consumed for building and car-construction. So, the use of sealing materials allows increasing the energy-efficiency of different enterprises, including the ones working in aggressive conditions. The sealants find application in solving wide range of household problems, such as, sealing the sanitaryware. Sealing materials are of great importance in building sector as a result of improving the operational properties of construction objects, such as, heat- and vapor-isolation, waterproofing and so on.

However, during the process of operation of constructing materials they undergo to the influence of various negative factors, amongst which is UV-irradiation. While exposure to UV-irradiation within long period of time there is the change in the structure of the material and in its basic physicochemical characteristics, i.e. the photo-ageing of the product. This process is accompanied by the structural damage of polymer, appearance of the cracks (on the surface and within the thickness of the material), growing turbid of the surface and so on. Ageing causes the deterioration of the mechanical characteristics of the materials which is taken into account when calculating the building constructions by corresponding coefficients of the working conditions [22].

There are usually two types of processes take place when ageing the polymers which have reactive double bond. These are destruction and crosslinking of macromolecules. The destruction processes which take place when the product ages after affecting by UV-irradiation is called "photodestruction" [23].

With the aim of establishing the effect of UV-irradiation on binary systems of p-EGF with AA, MAA and AAm of the composition of ~35:65 mass.% the samples were analyzed visually to the change of color and appearance of turbidity. Further, a microscopic analysis on presence of microcracks on the surfaces of the samples after exposure to irradiation was done. The results of the studies obtained after visual and microscopic analyses are presented in Table.

T a b l e

The effect of UV-irradiation on the copolymers of p-EGF with AA, MAA and AAm of the composition of ~35:65 mass.%

Unsaturated polyester	Vinyl monomer	Color change, turbidity	The presence of microcracks, bubbles	Other changes
p-EGF	AA	–	–	–
	MAA	Negligible yellowish tincture	–	–
	AAm	–	–	Strong hardening, the loss of flexibility

On the basis of experimental data obtained the attention should be paid to the exposure of UV-irradiation on binary system of p-EGF with AAm. In particular, the plates prepared from the copolymers of p-EGF-AAm hardened very much and had some roughness on their surfaces as a result of prolonged exposure to UV-irradiation. In this case no change in color was observed for the given samples of p-EGF-AAm of different thicknesses, however the plates lost their flexibility completely turning into rigid framework material, which can be explained by the formation of additional crosslinks within the macromolecule due to the formation of hydrogen bonds during their partial photoinitiation [24]. It is worth noting that this kind of solidifying may cause some difficulties when further operation of the sealants which are made using this polymeric base.

Analyzing the state of plates of p-EGF with MAA after prolonged exposure to UV-irradiation it was found out that all of the samples of different thickness acquired yellowish tincture. In this case the surfaces of plates did not grow dull and did not become tarnish. Also, it was expectable that the color of the plates

with smaller thickness (1–2 mm) changed significantly in comparison with the samples with wider thickness. Taking into account that the surfaces of the copolymers either undergo cracking or erode completely very often under the exposure to UV-irradiation, in this particular case the appearing of the microcracks and other deformations on the surface of plates were not observed by microscopic analysis.

When analyzing the samples of p-EGF with AA visual changes either in color, or appearing the bubbles or turbidity were not noticed. The presence of microcracks on their surfaces was also not observed.

Further for instrumental analysis of thermal stability of the studied binary systems on the basis of p-EGF with AA, MAA and AAm a TGA was done to establish the temperature of start of thermal deformation before and after exposure to UV-light within 21 days. Analysis of obtained thermograms has shown a decrease of thermal stability of the sample of p-EGF-AAm after UV-irradiation. At the same time, there were no significant changes in temperature coefficient of the start of thermal deformation of the samples of p-EGF with AA and MAA. So, in particular, analyzing the graphs in Figure 3 (*a–c*) it is necessary to note that the temperature of the start of thermal decomposition of the copolymer of p-EGF-AAm before irradiation was 134 °C, whereas after exposure to UV-light it fell to 85 °C (Fig. 3 *a*). Similarly, the results for the other binary systems were recorded. So, the start of thermal decomposition of the copolymers of p-EGF-AA before and after exposure to UV-irradiation was at the following points: 146 °C and 132 °C (Fig. 3 *b*) accordingly, and for p-EGF-MAA these values were equal to 172 °C and 151 °C (Fig. 3 *c*):

a

b

c
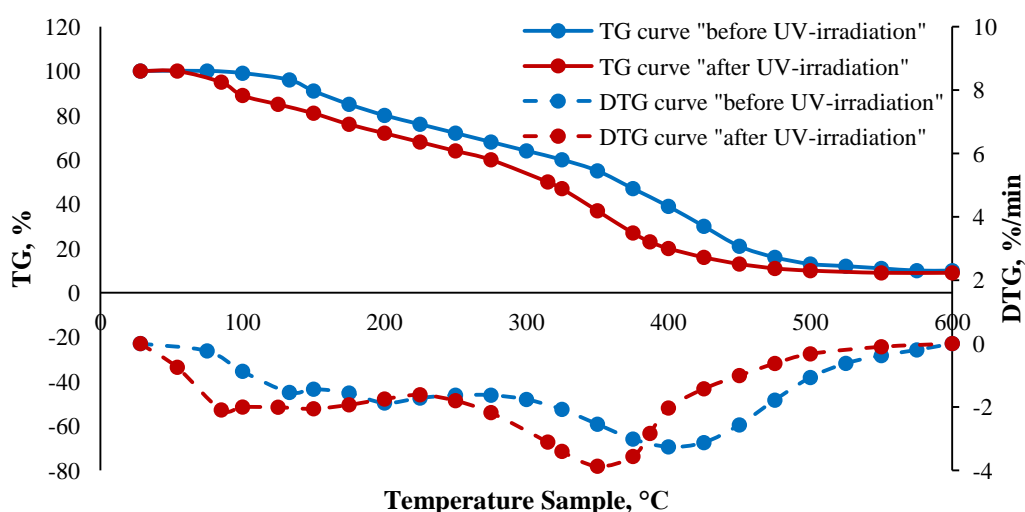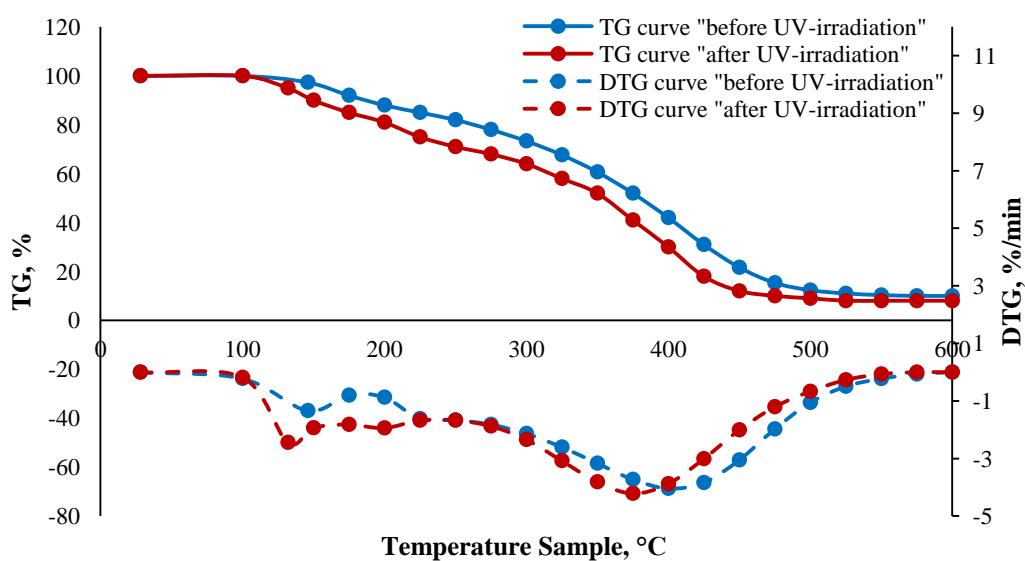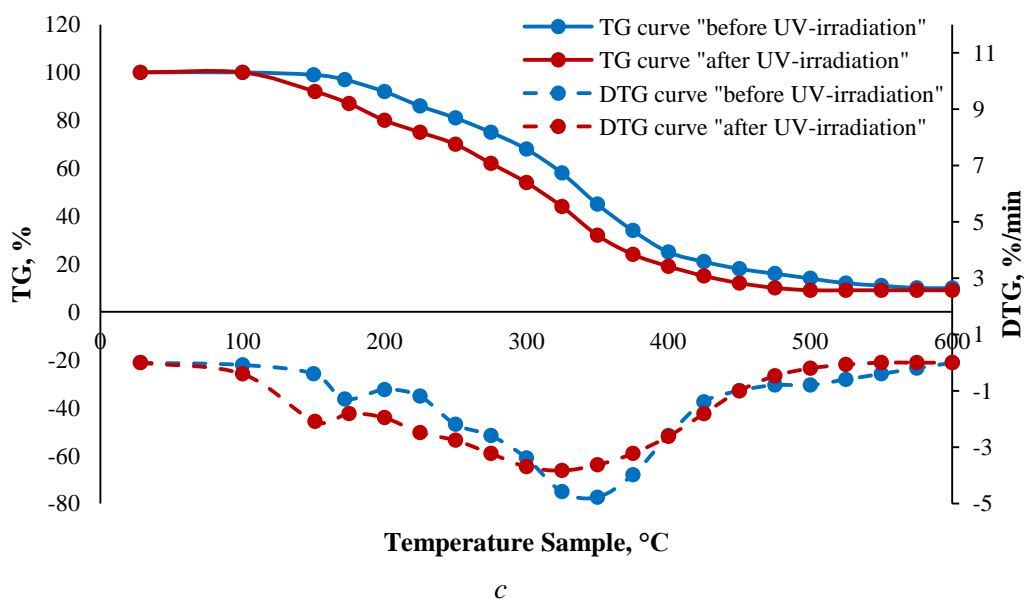
a — p-EGF–AAm 32.41:67.59 mass.%; *b* — p-EGF–AA 32.54:67.46 mass.%;
c — p-EGF–MAA 32.92:67.08 mass.%

Figure 3. TG and DTG curves of the copolymers of p-EGF–vinyl monomer
of various composition at a heating rate of 10 °C/min before and after UV-irradiation

Thus, in spite of the hardening the samples of p-EGF with acrylamide after influence of UV-light on them the temperature of the start of thermal deformation reduced considerably before and after irradiation. It is explained by the formation of additional crosslinks via hydrogen bonds which are formed during partial photoirradiation of macromolecules and are relatively fragile and can be easily decomposed under the influence of high temperature [23, 24].

So, on the basis of thermogravimetric analysis [25] a conclusion about decrease of thermal stability of synthesized copolymers based on p-EGF with AAm after the exposure to UV-irradiation can be made. Accordingly, the use of these copolymers as polymeric base for obtaining the sealants has strictly limited opportunities: in particular, they can be used in the places where they are not influenced by extensive UV-irradiation. Concerning the binary system of p-EGF-MAA it is necessary to note the possibility of its application for obtaining the sealants, however the use of the latter may be limited because of the change of their color as a result of the exposure to UV-irradiation on them. In comparison with the above said binary systems the copolymers of p-EGF with AA have shown the best physicochemical indices, including thermal stability after the radiation with UV-light. The results obtained allow us to say about preferable use of binary system of p-EGF-AA as a polymeric base of sealing materials.

Conclusions

The studies of thermal stability as a result of prolonged exposure to UV-irradiation on binary systems of p-EGF with AA, MAA and AAm of the composition of ~35:65 mass.% have shown high indices of thermostability for the copolymers of this unsaturated polyester with carboxylic acids after UV-irradiation within the range of 132–151 °C. In case of analyzing the temperature of the start of thermal deformation of the copolymer on the basis of p-EGF with AAm the reduce of this index before and after exposure of UV-irradiation on the samples from 134 to 85 °C was established; this limits the possibility of its application as a polymeric base of sealants.

The negative consequences of exposure to UV rays on copolymers of p-EGF with AAm should also include a change in their physicochemical parameters, expressed in the loss of flexibility and strong hardening. It should be noted that copolymers of p-EGF with carboxylic acids, AA and MAA, do not undergo such changes.

Thus, as a result of the experiments the conclusions can be made about preferable choice of binary systems of p-EGF with AA and MAA for obtaining the sealing materials on their basis.

References

1   Kablov, E.N. (2015). Innovatsionnye razrabotki FGUP "VIAM" GNC RF po realizatsii "Strategicheskikh napravlenii razvitiia materialov i tekhnologii ikh pererabotki na period do 2030 goda" [Innovative developments of FSUE "AIAM" of the SNRC RF for the implementation of the "Strategic Directions for the Development of Materials and Technologies for Their Processing for the Period until 2030"]. *Aviatsionnye materialy i tekhnologii — Aviation materials and technologies, 34*(1), 3–33. https://doi.org/10.18577/2071-9140-2015-0-1-3-33 [in Russian].

2   Kablov, E.N. (2016). Materialy novogo pokoleniia — osnova innovatsii, tekhnologicheskogo liderstva i natsionalnoi bezopasnosti Rossii [New generation materials are the basis of innovation, technological leadership and Russia's national security]. *Intellekt i tekhnologiia – Intellect and technology, 14*(2). 16–21. https://doi.org/10.31857/S0869587320040052 [in Russian].

3   Nikolaev, E.V. Pavlov, M.R., Andreeva, N.P., Slavin, A.V. & Skirta A.A. (2018). Issledovanie protsessov stareniia polimernykh kompozitsionnykh materialov v naturalnykh usloviiakh tropicheskogo klimata Severnoi Ameriki [Study of Aging Processes of Polymer Composite Materials in Natural Conditions of the Tropical Climate of North America]. *Novosti materialovedeniia. Nauka i tekhnika: elektronnyi nauchno-tekhnicheskii zhurnal – News of materials science. Science and technology: electronic scientific and technical journal, 30*(3–4), 08 [in Russian]. Retrieved from http://www.materialsnews.ru

4   Tanzer, J.D. & Frankel, L.S. (1992). Climate driven durability tester. *American Society for Testing and Materials Special Technical Publication, 1200.* 29-44. https://doi.org/10.1520/STP14871S

5   Andreeva, N.P., Pavlov, M.R., Nikolaev, E.V., & Slavin, A.V. (2018). Vliianie klimaticheskikh faktorov tropicheskogo i umerennogo klimata na svoistva lakokrasochnykh pokrytii na uretanovoi osnove [Influence of tropical and temperate climatic factors on the properties of urethane-based paint coatings]. *Lakokrasochnye materialy i ikh primenenie – Paints and varnishes and their application, 4,* 24–28 [in Russian].

6   Ding, S.H., Liu, D.Z. & Duan, L.L. (2006). Accelerated aging and aging mechanism of acrylic sealant. *Polymer Degradation and Stability, 91*(5), 1010–1016. https://doi.org/10.1016/j.polymdegradstab.2005.08.006

7   Nikolaev, E.V., Pavlov, M.R., Laptev, A.B. & Ponomarenko, S.A. (2017). K voprosu opredeleniia sorbirovannoi vlagi v polimernykh kompozitsionnykh materialakh [On the issue of determining sorbed moisture in polymer composite materials]. *Trudy VIAM: elektronnyi nauchno-tekhnicheskii zhurnal – Proceedings of All-Russian Research Institute of Aviation Materials: electronic scientific and technical journal, 56*(8). 07. https://doi.org/10.18577/2307-6046-2017-0-8-7-7 [in Russian].

8   Reznichenko, S.V. & Morozova, Yu.L. (2012). *Bolshoi spravochnik rezinshchika v 2 ch.* [The rubber bander's big guide in two parts]. M.: Tekhinform. 1385 [in Russian].

9   Ma, J.T., Chen, S.S., Zhou, W. & Wang, S. (2004). Effects on silicone sealant adhesion buildup on float glass substrates. *Durability of Building and Construction Sealants and Adhesives, 1453,* 97–112. https://doi.org/10.1520/stp12558s

10 Eliseev, O.A., Krasnov, L.L., Zajceva, E.I. & Savenkova, A.V. (2012). Razrabotka i modifitsirovanie elastomernykh materialov dlia primeneniia vo vseklimaticheskikh usloviiakh [Development and modification of elastomeric materials for use in all climatic conditions]. *Aviatsionnye materialy i tekhnologii, 5,* 309–314 [in Russian].

11 Yarcev, V.P. & Kiseleva, O.A. (2009). Prognozirovanie povedeniia stroitelnykh materialov pri neblagopriiatnykh usloviiakh ekspluatatsii [Predicting the behavior of building materials under adverse operating conditions] [Uchebnoe posobie]. Tambov: Izd-vo Tamb. gos. tekhn. un-ta. 124 [in Russian].

12 Burkeev, M.Zh., Kovaleva, A.K., Tazbaev, E.M., Burkeeva, G.K. & Plocek, J. (2018). Synthesis and Properties of Poly(Propylene Glycol Maleate Phthalate)–Styrene Copolymers as a Base of Composite Materials. *Russ. J. Appl. Chem., 91*(11), 1742–1749. https://doi.org/10.1134/S1070427218110022

13 Burkeyev, M.Zh., Kovaleva, A.K., Burkeeva, G.K. & Tazbayev Ye.M. (2020). Polyethylene Glycol Maleate Phthalate Terpolymerization with Acrylamide and Acrylic Acid. *Polymer. Korea., 44*(22), 123–133. https://doi.org/10.7317/pk

14 Burkeyev, M.Zh., Kovaleva, A.K., Tazhbayev, E.M. (2018). Method for producing unsaturated polyester resins based on propylene glycol and fumaric acid. Patent No. 33266 RK.Publ. C08G63/00, 8 [in Russian].

15 Burkeev, M.Zh., Kudaibergen, G.K., Burkeeva, G.K., Seilkhanov, T.M. & Tazbaev E.M. (2018). New Polyampholyte Polymers Based on Polypropylene Glycol Fumarate with Acrylic Acid and Dimethylaminoethyl Methacrylate. *Russ. J. Appl. Chem., 91*(7), 1145–1152. https://doi.org/10.1134/S1070427218070121

16 Burkeyeva, G.K., Tazhbayev, Ye.M., Muslimova, D.M., Nurseiit, G.D. & Zhaparova L.Zh. (2022). "Cold curing" of polyethylene glycol maleate with acrylic acid and some physicochemical properties of their solutions. *Bulletin of University of Karaganda. Series Chemistry, 106*(2), 25-31. https://doi.org/10.31489/2022Ch2/2-22-22

17 Burkeyeva, G.K., Kovaleva, A.K., Tazhbayev, Ye.M. & Ibrayeva, Zh.M. (2023). Development of Energy-Efficient Curing Method for Polypropylene Glycol Fumarate Using an Optimized Initiating System of "Cold" Curing. *Eurasian Journal of Chemistry (Bulletin of University of Karaganda. Series Chemistry), 109*(1), 15–23. https://doi.org/10.31489/2023Ch1/1-23-10

18 GOST 32317-2012 (EN 1297:2004). Materialy krovelnye i gidroizoliatsionnye gibkie bitumosoderzhashchie i polimernye (termoplastichnye ili elastomernye). Metod ispytaniia na starenie pod vozdeistviem iskusstvennykh klimaticheskikh faktorov: UF-izlucheniia, povyshennoi temperatury i vody [Roofing and waterproofing flexible bitumen-containing and polymeric (thermoplastic or elastomeric) materials. Test method for aging under the influence of artificial climatic factors: UV radiation, elevated temperature and water] (2014). Moscow: Standartinform, 7. https://docs.cntd.ru/document/1200108098 [in Russian].

19 Boboev, T.B., Gafurov, S. Dzh. & Istamov F.H. (2020). Issledovanie vliianiia UF-oblucheniia na skorost razrusheniia polimerov [Study of the Effect of UV Irradiation on the Rate of Destruction of Polymers]. *Prikladnaia fizika – Applied physics, 5,* 93–96. Retrieved from http://applphys.orion-ir.ru/appl-20/20-5/PF-20-5-93.pdf [in Russian].

20 Vinogradova, S.V., Korshak, V.V., Kul'chitskii, V.I., Gribkova, P.N. & Danilov V.G. (1968). Thermal stability of unsaturated polyesters and copolymers based on them. *Polymer Science, 10*(7), 1757–1764. https://doi.org/10.1016/0032-3950(68)90368-7

21 Vyazovkin, S., Burnhnam, A.K., Criado, J.M., Perez-Maqueda, L.A., Popescu, C. & Sbirrazzuolli N. (2011). Kinetic Committee recommendation for performing kinetic computations on thermal analysis data. *ICTAC: Thermochimica Acta, 520,* 1–19. https://doi.org/10.1016/j.tca.2011.03.034

22 Boubakri, A., Guermazi, N., Elleuch, K. & Ayedi, H.F. (2010). Study of UV-aging of thermoplastic polyurethane material. *Materials Science and Engineering: series A, 527*(7–8), 1649–1654. https://doi.org/10.1016/j.msea.2010.01.014

23 Rusu, M.C., Block, C., Van Assche, G. & Van Mele, B. (2012). Influence of temperature and UV intensity on photo-polymerization reaction studied by photo-DSC. *Journal of Thermal Analysis and Calorimetry, 110*(1), 287–294. https://doi.org/10.1007/s10973-012-2465-5

24 Gromov, V.F. & Homikovskij, P.M. (1979). Vliianie rastvoritelia na skorosti reaktsii rosta i obryva tsepei pri radikalnoi polimerizatsii [Influence of the solvent on the rates of chain growth and termination reactions during radical polymerization]. *Uspekhi khimii – Advances in Chemistry, 48*(11), 1943. https://doi.org/10.1070/RC1979v048n11ABEH002428 [in Russian].

25 Burkeyev, M.Zh., Tazhbayev, Ye.M., Bolatbay, A., Minayeva, E.V. & Kovaleva, A.K. (2022). Study of Thermal Decomposition of the Copolymer Based on Polyethylene Glycol Fumarate with Acrylic Acid. Journal of Chemistry. ID 3514358. https://doi.org/10.1155/2022/3514358

Information about authors*

Burkeyeva, Gulsym Kabayevna — PhD, Associate Professor of Chemical Sciences, Karagandy University of the name of academician E.A. Buketov, Universitetskaya street, 28, 100024, Karaganda, Kazakhstan; e-mail: guls_b@mail.ru; https://orcid.org/0000-0003-1993-7648;

Kovaleva, Anna Konstantinovna — PhD, Senior Researcher, Karagandy University of the name of academician E.A. Buketov, Universitetskaya street, 28, 100024, Karaganda, Kazakhstan; e-mail: cherry-girl1899@mail.ru; https://orcid.org/0000-0001-9758-648X;

Tazhbayev, Yerkeblan Muratovich — Doctor of Chemical Sciences, Professor, Karagandy University of the name of academician E.A. Buketov, Universitetskaya street, 28, 100024, Karaganda, Kazakhstan; e-mail: tazhbaev@mail.ru; https://orcid.org/0000-0003-4828-2521;

Ibrayeva, Zhansaya Mirkhankyzy (*corresponding author*) — 1st year Doctoral Student; Karagandy University of the name of academician E.A. Buketov, Universitetskaya street, 28, 100024, Karaganda, Kazakhstan; e-mail: zhansaya.ibraieva@mail.ru; https://orcid.org/0000-0002-1419-1384;

Zhaparova, Lyazzat Zhanybekovna — PhD, Associate Professor, Karagandy University of the name of academician E.A. Buketov, Universitetskaya street, 28, 100024, Karaganda, Kazakhstan; e-mail: lyazzh@mail.ru; https://orcid.org/0000-0003-1894-0255;

Meiramova, Diyara Ruslanovna — 1st year Master Student, Karagandy University of the name of academician E.A. Buketov, Universitetskaya street, 28, 100024, Karaganda, Kazakhstan; e-mail: meiramovadr19@gmail.com; https://orcid.org/0009-0009-7391-6080;

Plocek, Jiri — PhD, CSc. Institute of Inorganic Chemistry of the Czech Academy of Sciences, Czech Republic, Husinec-Rez 1001 25068 Rez; e-mail: plocek@iic.cas.cz; https://orcid.org/0000-0001-6082-5766.

_____
*The author's name is presented in the order: *Last Name, First and Middle Names*

Mukhlisa Q. Saidmuhamedova[1] , Islom H. Turdiqulov[1] , Abdumutolib A. Atakhanov[1*] , Nurbek Sh. Ashurov[1] , Muhitdin Abdurazakov[1] , Sayyora Sh. Rashidova[1] , Oleg V. Surov[2]

[1] Institute of Polymer Chemistry and Physics, Tashkent, Uzbekistan
[2] G.A. Krestov Institute of Solution Chemistry, Ivanovo, Russia
(*Corresponding author's e-mail: a-atakhanov@yandex.com)

Biodegradable Polyethylene-Based Composites
Filled with Cellulose Micro- and Nanoparticles

Composite materials filled with cellulose particles (microcrystalline cellulose and nanocellulose) have good prospects for use in various fields. Microcrystalline cellulose (MCC) and nanocellulose (NC) were isolated by chemical and physical methods and investigated. Composite materials based on polyethylene (PE) were obtained using MCC and NC as fillers (5–20 wt.%) and maleic anhydride grafted low molecular weight polyethylene (MA-g-LMPE) as a compatibilizer. The structure and morphology of the composites and fillers were characterized by Fourier transform infrared (FTIR) spectroscopy, X-ray diffraction, thermal analysis (TA), transmission electron microscopy (TEM), atomic force microscopy (AFM), and the strength properties were determined by tensile testing. An increase in the crystallinity index and mechanical strength of composites at low filler contents (up to 5 wt.%) was revealed. The size of the cellulose particles significantly affects the structure and properties of composites. Although the general picture of the effect of fillers on the crystalline structure and mechanical properties is similar, the addition of NC had a greater effect than MCC. The results of this study showed the possibility of using MCC and NC as reinforcement materials in composites, and they have biodegradable properties.

Keywords: cellulose microparticles, nanoparticles; polyethylene, composites, mechanical properties, biodegradability.

Introduction

Composite materials based on synthetic polymers reinforced with natural polymers, due to their unique physical, mechanical and operational characteristics, are widely used in various engineering fields [1–3]. Adding fillers based on natural polymers to synthetic polymers creates new materials with specific properties, including biodegradability after their end-of-life [4–6]. Micro- and nanoparticles of cellulose have good prospects in terms of their use as fillers for the preparation of composite materials due to their low density, large surface area, high mechanical properties, low toxicity, biodegradability, and renewability as raw materials [7–12]. Cellulose and its derivative-containing composites have been prepared and investigated for a wide range of vinyl polymers [13], including polycaprolactone, polyhydroxyalkanoate [14], polylactic acid [15], thermoplastic starch [16], polyacrylamide [17] and others.

The structure of polymer composites is determined not only by mixing conditions, but also by the dispersion of the polymer filler, which retains its particle shape during mixing, and the uniformity of its distribution in the polymer matrix. The effect of dispersed filler particles on the crystallization process of polyolefin was studied, and it was found that there are numerous crystallization centres on the filler surface, on which polymer crystallites grow; as a result, the crystallinity index increases [18, 19]. Filler particles are stiffer and harder than matrix materials, so they reinforce the polymer matrix. The filler addition into the polypropylene/polyethylene (PP/PE) polymer matrix increases the strength and stiffness, but reduces the elasticity of the materials [20, 21]. To eliminate the negative effect of the filler on the elasticity of polymer composites, functionalization of both polyolefin (insertion of hydrophilic groups) [22, 23] or fillers (insertion of hydrophobic groups) [24–26] has been suggested, and the addition of elastomers [27, 28] or compatibilizers [29, 30] could be used. Compatibilizers consisting of polar and nonpolar parts are located in the interfacial region, increasing the interaction between the nonpolar polymer and the polar filler and contributing to a uniform distribution of the filler.

The size and shape of the filler particles significantly affect the physical and mechanical properties of composites. Composites containing highly dispersed fillers are stronger and less viscous [31]. Moreover, oblong filler particles are stronger reinforcing agents for the polymer matrix than spherical particles [32].

The addition of functional groups into the structure of cellulose reduces its thermal stability. The process of partial esterification of cellulose occurs as cellulose nanoparticles are formed by acid hydrolysis with highly concentrated solutions of sulfuric acid [33]. At the same time, the presence of sulfate groups in the nanocellulose composition leads to lower temperature thermal stability [34, 35], which makes it difficult to use nanocellulose in high-temperature processes. Therefore, we used a hydrochloric acid solution to extract cellulose nanoparticles.

In the present work, polymer composites based on polyethylene filled with cellulose micro- and nanoparticles were obtained and their structure and properties were studied.

Experimental

Chemicals and Materials

The following chemicals and materials were used: sodium hydroxide (NaOH, 99 %), hydrogen peroxide (H_2O_2, 60 %), nitric acid (HNO_3, 65 %) and hydrochloric acid (HCl, 37 %) purchased from Fortek Ltd., Tashkent, Uzbekistan. Low-density polyethylene (PE, produced by JV "Shurtan Gas Chemical Complex" Comp. Limit., Uzbekistan) was used as a polymer matrix in compounds. Low-molecular-weight polyethylene (LMPE) with a number-average molecular weight (M_n) of 1000–2000 was supplied by JV "Uz-Kor Gas Chemical" Co. Ltd., Uzbekistan. Benzoyl peroxide (BP, 75 %), a free radical initiator, maleic anhydride (MA, 98 %), a monomer, styrene (99 %), a chain transfer agent, acetone (99.5 %), a wash solution for the products and xylene (90 %), a solvent for the initiator, were purchased from Sigma–Aldrich, USA.

Cotton Cellulose Extraction

Cotton cellulose (CC) was extracted by heating cotton linter in a 1 M sodium hydroxide solution at 120 °C for 2 h to remove hemicellulose and lignin, as reported previously [36]. It was washed with distilled water to a neutral pH solution and bleached at 120 °C for 2 h using 4 % hydrogen peroxide. The bleached fibres were filtered, and washed several times with distilled water, and dried at 100 °C for 4 h. CC had a degree of polymerization (DP) of 1200, and was used to prepare MCC.

MCC Extraction

MCC was extracted from CC by acid hydrolysis [36]. 50 g of CC was placed in a glass container and hydrolysed with 500 mL of a 4 % aqueous nitric acid solution at a boiling temperature of 100–105 °C for 2 h. The hot acid mixture was poured into 2.5 L of cold water, and the mixture was vigorously stirred with a spatula and allowed to stand overnight. The MCC obtained by this process was filtered, washed with distilled water until a neutral pH value, filtered, and dried at 100 °C for 4 h. The MCC was used to obtain nanoparticles of cellulose.

NC Isolation

NC was isolated using a reported protocol with modification [37]: the MCC (20 g) was hydrolysed with a hydrochloric acid solution (400 mL, 4N) at 70 °C for 60 min. The suspension was diluted 10-fold with cold water (5 °C), centrifuged, and dialysed until a neutral pH value, and the aqueous suspension was dispersed via ultrasonication for 1 h and homogenization for 1 h. Finally, the sample was freeze-dried.

Synthesis of compatibilizer (MA-g-LMPE)

The compatibilizer (MA-g-LMPE) was synthesized by reacting LMPE with MA according to a published method with slight modification [38]. The experiment was performed in a three-neck 250 mL round-bottom flask with a magnetic stirrer, a nitrogen inlet, and a thermometer. In a typical experiment, the reaction flask was heated in an oil bath to melt the LMPE. When the LMPE was melted completely, selected amounts of MAH and styrene were added to the flask. When the system reached homogeneity, the initiator was dissolved in xylene and added to the reaction flask. A small nitrogen flow passed through the flask during the whole reaction process. After the specified time, the reaction was stopped, and the grafted copolymer was precipitated in acetone. The precipitate was washed with acetone and filtered repeatedly to remove unreacted MAH, then dried in a vacuum oven at 60 °C to a constant weight. The compatibilizer was used as an agent to improve the compatibility of the PE and natural fillers (MCC, NC).

Composites Preparation

Compounding

Composites were prepared by high-temperature shear deformation on a rotary laboratory mixer (Brabender) at 190±2 °C. The mixture was ground for 20 min at 50 rpm. The ratios of natural fillers (MCC, NC)

to PE used in this study were (5÷95), (10÷90) and (20÷80) wt.%. The compatibilizer MA-g-LMPE was also added at 5 wt.% based on the weight of PE. Both PE and MA-g- LMPE were first melted at 170 °C, then the fillers (MCC, NC) were added.

Forming composite samples

The composites were placed in a hot compression moulding machine (Zamak, Poland) to form quadrangle-shaped composites to be used in mechanical testing. The composite samples were preheated in the mould at 180 °C for 3 min to ensure complete melting at atmospheric pressure. Then a pressure of 6 bars was applied to the mould and held for 5 min under constant temperature and pressure to form composites. After that, the forms were chilled and removed. In each tensile test, 1.5 g of sample was used to form a composite sheet with dimensions of 10 mm (width) × 75 mm (length) × 2 mm (thickness).

Characterization Methods

FTIR

The structure of samples was determined by the FTIR spectrometer "Inventio-S" (Bruker). FTIR spectra were recorded in the transmission mode in 400–4000 cm^{-1} wavenumber range with a resolution of 2 cm^{-1} and 32 scans at a temperature of 25 °C. The OPUS software was applied to determine the peaks at specific points. The samples were pressed in pellets under pressure 300 MPa containing 1 mg of the compound to be analyzed and 100 mg of potassium bromide.

Wide-angle X-ray diffraction

XRD studies were carried out according to a previously published method with a slight modification [39] on a XRD Miniflex 600 (Rigaku, Japan) with monochromatic CuKα radiation isolated by a nickel filter with a wavelength of 1.5418 Å at 40 kV and a current of 15 mA. The spectrum was recorded in the interval $2\theta = 5°–40°$. The data processing of experimental diffraction patterns, peak deconvolution, describing the peaks used by Miller indices, peak shape, and the basis for the amorphous contribution were conducted using the "SmartLab Studio II" software and PDF-2 (2020 Powder diffraction file, ICDD) data base.

The crystallite size, τ (Å), was calculated by the Scherrer equation [40, 41]:

$$\tau = \frac{K \cdot \lambda}{\beta \cdot \cos\theta},$$

where K — the correction factor (0.9); λ — the wavelength of the X-ray radiation (1.5418 Å); β — the full width at half maximum of the diffraction peak in radians; θ — the diffraction angle of the peak.

The crystal index (CrI) (%) was calculated by the following equation:

$$CrI = \frac{I_t - I_a}{I_t} \cdot 100,$$

where I_t — the total intensity; I_a — the amorphous intensity.

Thermal Analysis

Thermal analysis of the samples was recorded on a STA TG-DTA/DSC "Start-1600" (Linseis) by heating ~5 mg of samples at 10 °C/min in air atmosphere from ambient temperature to 700 °C. The results obtained by the TA method were used to calculate the crystallinity index of the polymer in composites [42], which was calculated based on the analysis of the DSC curves:

$$\chi_c = \frac{\Delta H_m}{w \Delta H_m^o},$$

where χ_c — the crystallinity index; ΔH_m — the enthalpy of the composite melting; w — the mass fraction of polymer in the composite; $\Delta H_m°$ — the enthalpy of the melting of neat polymer (χ=100 %).

TEM

Transmission electron microscopy studies were performed using PEM-100 equipment with a high accelerating voltage of 80 kV and a magnification of 104 times. The samples were prepared by the suspension method, and the studied samples were applied to a supporting film with carbon tinting after the sample was dried and contrasted with joint evaporation of platinum and carbon (in percentages of 85:15) at an angle of 45°.

AFM

Structural studies were also performed using an Agilent 5500 atomic force microscope (Agilent). Silicon cantilevers with a stiffness of 9.5 N/m^2 and a frequency of 145 kHz were used. The maximum AFM scanning area ($x÷y÷z$) is 25÷25÷1 μm. Calculations of particle size distribution by width and length were carried out using MountainsMap Premium Software, Version 6.2 (USA).

Optical Microscopy

The surface of the composites was observed by "BA 210 Digital" (Motic) optical microscope.

Sorption Measurements

The sorption measurements were carried out using a McBain balance with quartz spirals of 1 mg/mm sensitivity in the relative humidity (*P/Ps*) range 0.10–1.0 at 25 °C until sorption equilibrium was established. The change in sample mass during the sorption process was observed using a KM-8 cathetometer.

Mechanical properties of composites

Measurements of the mechanical properties (tensile strength (σ) and elongation (L)) of the composites were performed using an AG-X plus tensile tester (Shimadzu) according to standard methods at a 50 mm/min crosshead speed.

Statistical analysis

All experimental data were collected in triplicates and data expressed as average ± standard deviation. Data were compared using a one-way ANOVA with post-Bonferroni test using Graph-Pad Prism 5.04 (GraphPad Software Inc.)

Results and Discussion

FTIR studies (Fig. 1) showed that the spectra of NC and MCC are characteristic of cellulose; however, the intensities of the NC spectra were higher. Valence vibrations of the hydroxyl groups involved in intermolecular and intramolecular hydrogen bonds appeared at approximately 3400 cm^{-1}. Valence vibrations of the C-H bonds in the methylene groups of cellulose appeared in the region of 2895 cm^{-1}, vibrations of adsorbed water molecules appeared in the region of 1635 cm^{-1}. The absorption bands in the regions of 1420 cm^{-1}, 1335-1375 cm^{-1}, 1202 cm^{-1}, and 1075-1060 cm^{-1} corresponded to the strain vibrations of -H, -CH$_2$, -OH, and -CO and the valence vibrations of the C-O pyranose ring.
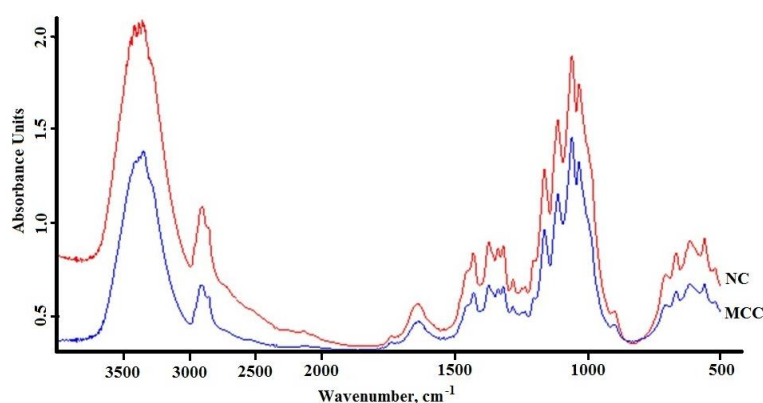
Figure 1. FTIR spectra of NC and MCC

The X-ray diffraction study showed that acid hydrolysis led to an increase in the crystallinity index of NC associated with the removal of the amorphous cellulose structure. Four crystal reflexes were observed at approximately 2θ=14.65°, 16.35°, 22,61° and 35.07° corresponding to the (10-1), (101), (002) and (040) planes (Fig. 2). The results of X-ray analysis show that during acid hydrolysis, the interplanar distance decreased, and the crystal reflexes shifted towards larger values. The unit cell size of NC was lower than that of MCC (Table 1).

T a b l e 1

Structural parameters of NC and MCC

Options	MCC			NC		
	Crystalline Reflexes					
	10-1	101	002	10-1	101	002
Position of the maximum *2θ*, (deg.)	14.48	15.94	22.56	14.65	16.35	22.61
Interlunar spacing *d*, (Å)	6.11	5.55	3.94	6.04	5.42	3.93
Crystallite size *l*, (Å)	50.4	53.9	66.5	45.2	43.8	66.3
Crystallinity index, %	86			92		
Elementary cell size, a÷b÷c (Å)	8.65÷10.36÷7.91			8.34÷10.23÷7.90		
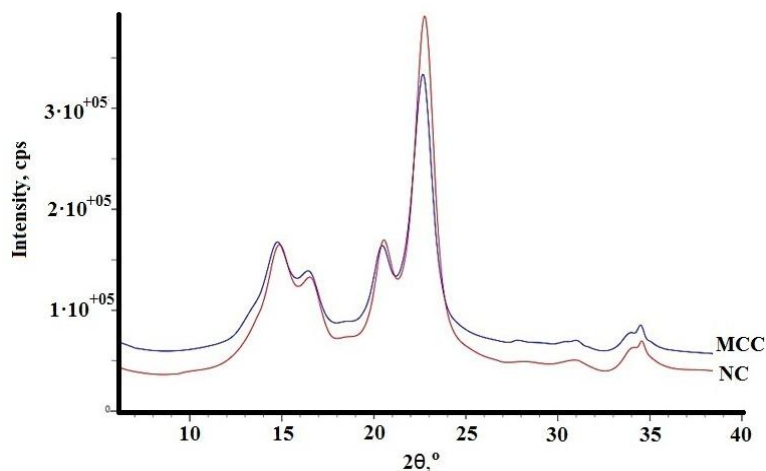
Figure 2. X-ray diffraction patterns of MCC and NC

TEM and AFM studies have shown that NC particles are in the form of whiskers with a particle size of 50–300 nm in length and 10–40 nm in width (Fig. 3 *a*, *b*). The particle size distribution ranged from 110 to 145 nm in length and 25–30 nm in width (Fig. 3 *c*, *d*).
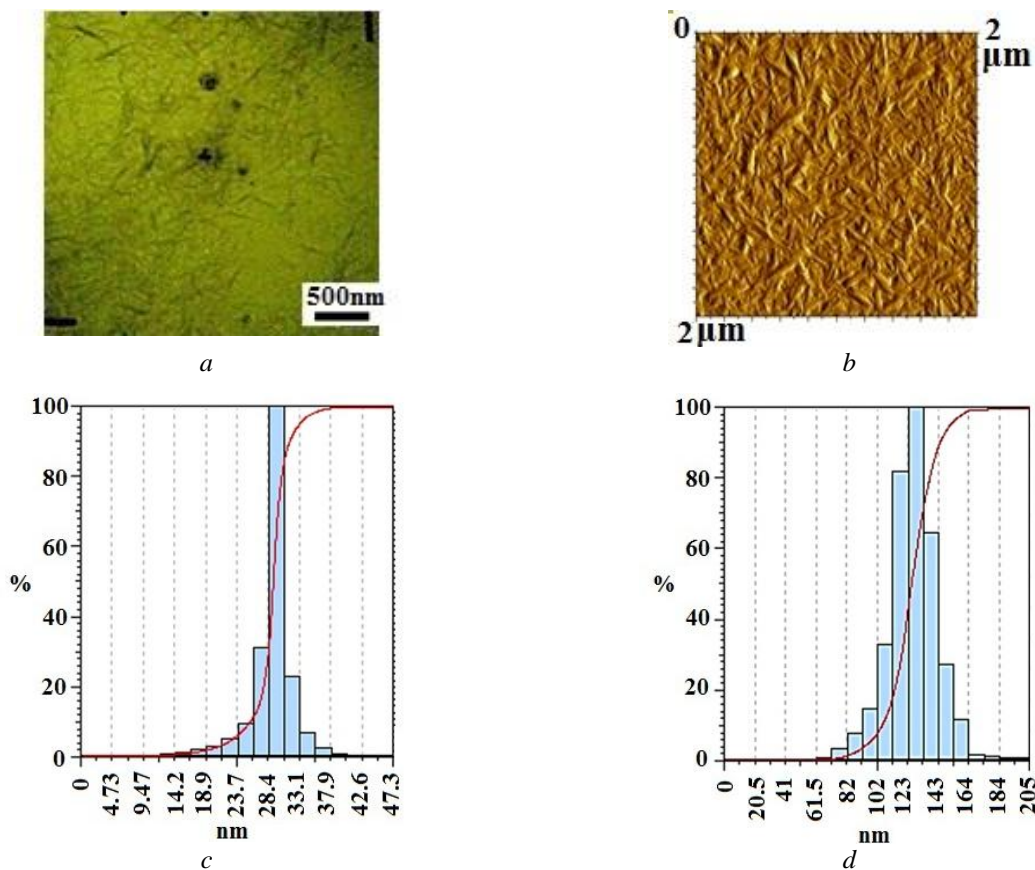
Figure 3. TEM (*a*) and AFM (*b*) images of NC and particle size distribution by width (*c*) and length (*d*)

Sorption studies using low molecular weight liquids (water and ethanol) were carried out for the NC and MCC, and the parameters of the capillary-porous structure of the samples were calculated based on isotherms of water vapour sorption (Fig. 4, Table 2).
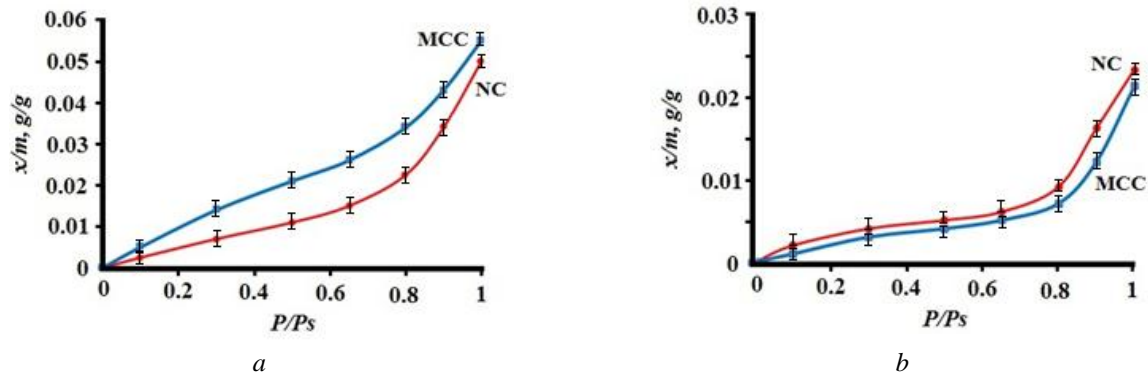
Figure 4. Isotherms of water (*a*) and ethanol (*b*) vapour sorption by MCC and NC

It was found that X_m, S_{sp} and W_o of NC compared to MCC are lower in the case of water sorption and higher in the case of ethanol sorption. This is probably due to capillary condensation of water molecules on the polymer surface, since these parameters were calculated at 100 % relative humidity.

T a b l e 2

Parameters of the capillary-porous structure

Indicator	NC	MCC	NC	MCC
	Water sorption, %		Sorption of ethanol, %	
X_m, g/g	0.0052	0.0069	0.0034	0.0022
S_{sp}, m²/g	18.28	24.44	12.21	7.38
W_o, cm³/g	0.011	0.019	0.029	0.025
r_k, A$_o$	12.04	15.55	47.5	68.69
Note: Result presented as mean ±0.04 % standard deviation, $n = 3$.				

When filler is mixed with a synthetic polymer at the micro- and nanoscale, the components of the mixture form an interpenetrating mesh structure, which provides the filled polymer with the effect of additional degradation. It is known that filler can accumulate in the less ordered regions of the polymer structure. PE/filler composites at different ratios were investigated by FTIR and X-ray to establish the effect of the filler on the structure of PE.

FTIR spectra (Fig. 5) contain absorption bands at 2922 and 2850 cm^{-1} corresponding to the asymmetric and symmetric valence vibrations of CH$_2$ groups. The absorption bands of scissor and pendulum deformation vibrations of CH$_2$ groups occur at 1466 and 720 cm^{-1}. The absorption band corresponding to the region of approximately 750-700 cm^{-1} characterizes the crystalline phase of PE, while there is only one strong absorption band at 720 cm^{-1} in the amorphous phase [43, 44].
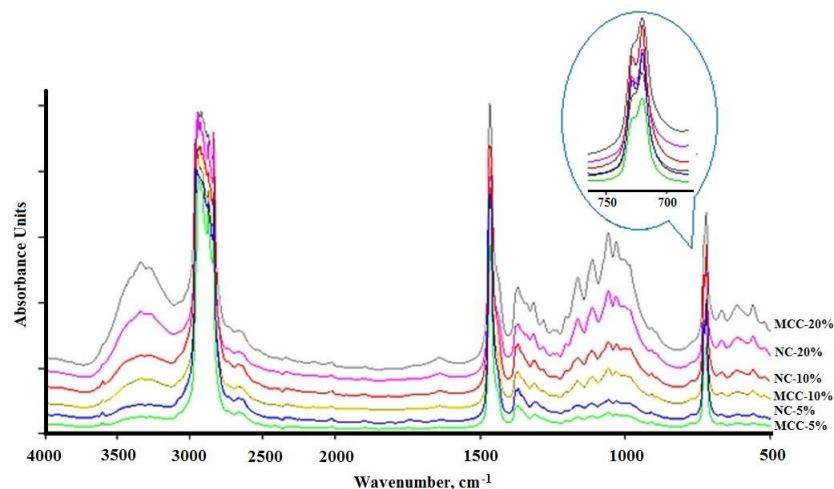
Figure 5. FTIR spectra of composites with different filler contents, wt.%: PE/MCC — 5, 10, 20 and PE/NC — 5, 10, 20

Characteristic cellulose bands are present in the 1017–1206 cm^{-1} range. The insertion of MCC and NC into PE leads to a shift of the 888 cm^{-1} band to the region of 853-861 cm^{-1}. It was also observed that some changes in the 1300–900 cm^{-1} region occur during heat treatment. This result seems to indicate the formation of PE with cellulose, inclusion compounds and H-complexes. The curves of the samples differ in the intensity of the characteristic bands at 1019, 1242, 1373, 1740 cm^{-1} and in the appearance of a new broad peak in the region of 3300-3500 cm^{-1}, which corresponds to the valence vibrations of OH-groups. More intense peaks were observed in the spectra of the PE/NC than in the spectra of the PE/MCC.

Two crystalline maximums of PE were observed in the X-ray diffraction patterns at 22° and 24.5°, corresponding to reflections (110) and (200) related to orthorhombic structure (Fig. 6). In addition, for all samples, one can observe a crystalline reflex relating to cellulose in the region of (200) corresponding to plane (110), and at high filler contents (20 %), weakly expressed reflexes relating to cellulose shifted at 15.5°, 17.2° corresponding to planes (101) and (10-1). Additionally, a decrease in the intensity of the PE crystal maximum at 24.5° and the appearance of a new crystal maximum related to cellulose in the region of 23.2° corresponding to the (10-2) plane were observed in the patterns of the same samples.
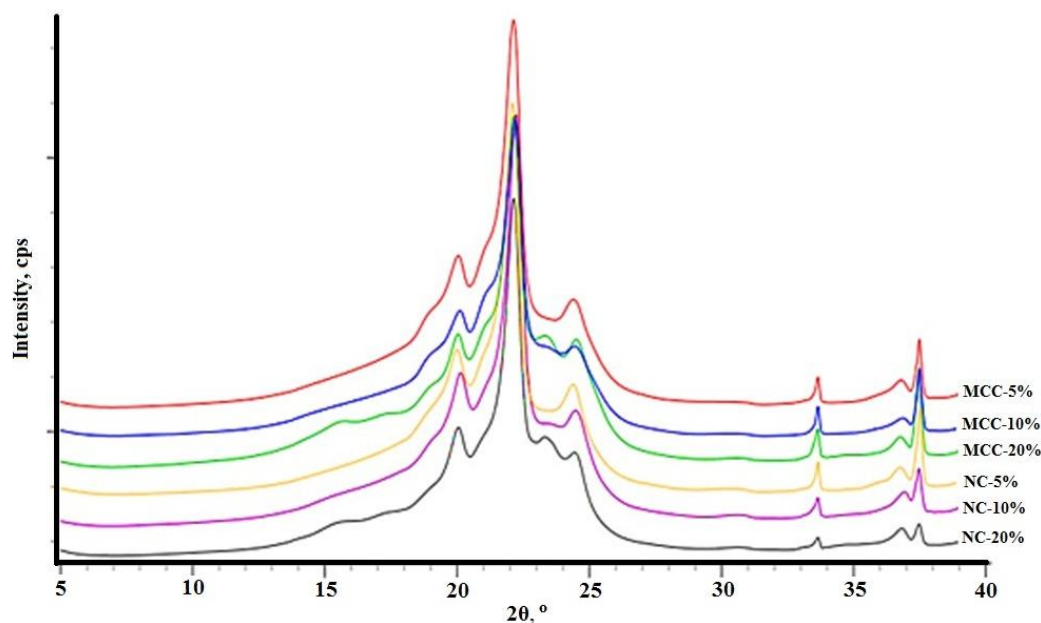

Figure 6. X-ray diffraction patterns of composites with different filler contents, wt.%:
PE/MCC — 5, 10, 20 and PE/NC — 5, 10, 20

The results showed that the crystallinity index values of all polymer composites differed from the χ of neat PE (Fig. 7).
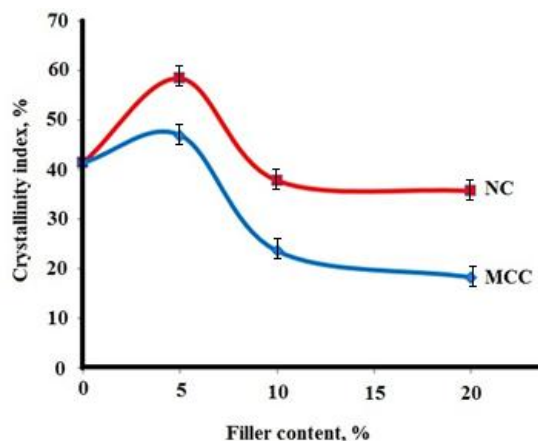

Figure. 7. Dependence of the crystallinity index of the composites on the filler content

The crystallinity was extremely dependent on the filler content and reached a maximum at a filler content of 5 wt.%. The presence of fillers up to this concentration led to the increase in the PE matrix values as an artificial seed for structure formation [45]. The reason for this behaviour may be the interphase phenomena that occur at the polymer-filler interface and the appearance of interfacial layers with characteristics that changed due to interfacial interactions.

An increase in the filler content in the range of 5–10 % led to a decrease in the crystallinity index. Most likely, an increased amount of filler contributed to their convergence; when they began to coagulate, the small particles aggregated into larger particles, while the specific surface area of the fillers decreased sharply, and, as a result, the active interactions of PE with the fillers decreased, and the fillers gradually began to have a lesser effect on the structure. A further increase in the amount of fillers up to 20 % somewhat suppressed the crystallization process and increased the number of defects in the crystallites and the amorphization of PE.

The dependence of the PE crystal lamella thickness on the filler content is shown in Figure 8. The thickness was calculated using Scherrer's formula by measuring the width at half the height of the high-intensity X-ray band corresponding to the reflections from the crystallographic planes (110).
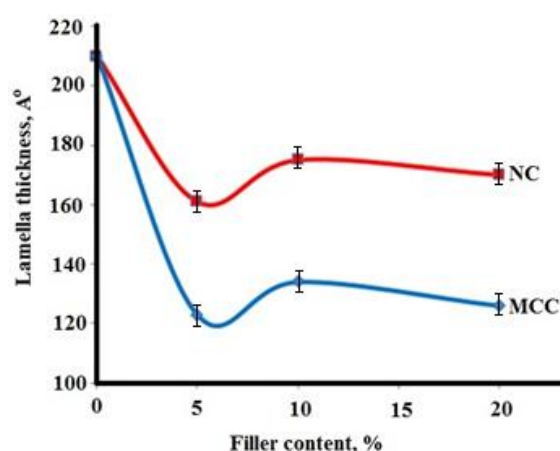
Figure 8. Dependence of lamella thickness on the filler content

As can be seen in Figure 8, the presence of fillers up to 5 % led to a decrease in the size of the crystallites because in these concentration intervals, there were many solid filler particles serving as artificial seed crystals for structure formation, as mentioned above. As a result, numerous crystallites formed, and their sizes were relatively smaller than that of neat PE. Despite a decrease in the thickness of the crystalline lamella at 5 % filler content, the PE crystallinity index reached its maximum value (Fig. 6) due to an increase in the total number of crystalline formations, the predominant number of which was crystallites grown on the artificial seed crystals. As a result, the crystallites, smaller dimensions of which enabled them to undergo denser packing in the amorphous structure, contributed to the increasing density of the final material. This reasoning is true if the growing crystalline formations filled the available amorphous space as much as possible when the growth of crystallites slowed upon meeting similar neighbouring formations.

A decrease in the χ values and the growth of the crystallites were observed in the range of filler content of 5–10 % (Fig. 7 and 8). A further increase in filler content up to 10–20 % partially suppressed the mobility of the PE macromolecules and the crystallization process, resulting in both a reduction in the crystallinity index and a decrease in crystallite size. The densities of fillers were different ($\rho_{NC} >> \rho_{MCC}$), and the denser filler particles had a more active effect on structure formation in the PE (Fig. 7).

Table 3

Crystallinity index (χ) and asymmetry index (AI) of PE and composites

PE/NC ratio, %	χ, %	AI	PE/MCC ratio, %	χ, %	AI
100:0	29	0,17	100:0	29	0,17
95:5	40	0,17	95:5	43	0,17
90:10	34	0,19	90:10	34	0,20
80:20	38	0,19	80:20	36	0,21

The thermal stability of a composite material is a desirable property in many applications. The thermal expansion of cellulose reinforced polyethylene composites has been studied using wood and fibrous cellulose as fillers [46, 47]. The viscose fibers and the MCC decreased the coefficients of the linear thermal expansion of the high density polyethylene (HDPE) matrix in the flow direction [48]. The effect of fillers on the crystalline structure of PE was also studied by thermal analysis. Calculations based on thermal analysis data showed that the values of the crystallinity index of all polymer composites were appreciably higher than the χ of neat PE (Table 3). The melting peak of the crystallizing polymer reflected the crystallite size distribution to some extent. The asymmetry of the melting peak was used to calculate indicators of the polymer crystal structure [49].

Similar results were obtained; the structure and properties of high density polyethylene-based composite films with different natural fillers (cellulose, soybean meal, and pellets) were studied [46]. Some increases in the crystallinity index and the proportion of perfect crystallites for HDPE with increasing filler content were noted. These increases occurred because the fillers acted as seed crystals in the crystal formation by forming films. We assumed that the reason for the increase in the crystallinity index was not only the presence of solid filler particles, but also the conditions of the polymer mixing process at a high temperature (180 °C). In this case, the dispersion component of the PE mixtures reflects the crystalline phase under the influence of the thermal field as it underwent modifying changes similar to those of the morphemes observed during the thermal treatment of the crystallizing polymers.

The crystallinity index values obtained by X-ray and thermal analyses do not coincide because these methods are based on the study of completely different physical and chemical phenomena. The crystallinity index of a polymer determined from X-ray data represents the total amount of ordered (crystalline) polymer areas that contribute to the coherent scattering of X-rays. When determining the crystallinity index by thermal analysis, the proportion of polymer macromolecules that are capable of absorbing energy during thermal influence and moving from an ordered to a disordered (molten) state is taken into account. However, it was noted that the general picture of the effect of fillers on the crystal structure of polyethylene remained consistent.

Optical studies have shown that filler particles can be observed in microphotographs and that their size depends on the filler. NC particles are small and needle-shaped, while MCC particles are larger.

Mechanical studies of the composites showed that filler content up to 5 % increased the strength of the composites (Fig. 9). This result is consistent with the X-ray results. Small additions of fillers that serve as structure formers contributed to the refinement of the spherulitic structure, changing the packing density of the structural elements of the spherules and the ordering of the structure of the crystallizing polymer. Apparently, these factors can increase the strength of the crystallizing polymer when small content filler is dispersed throughout the polymer matrix.
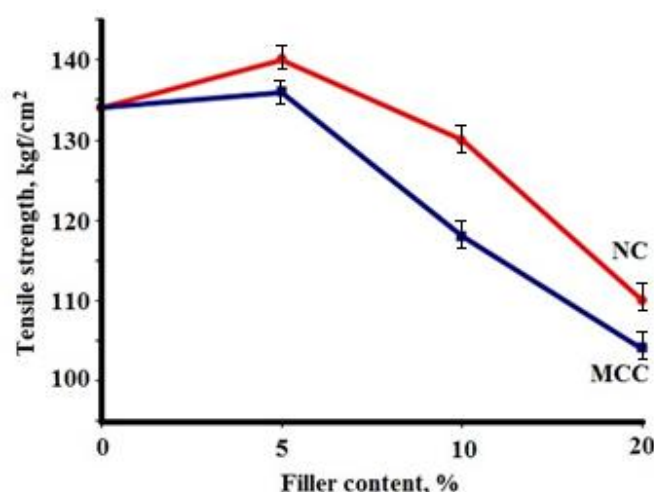

Figure 9. Mechanical characteristics of PE/MCC and PE/NC composites

As the filler content increased, a significant amount of filler particles accumulated in the polymer matrix, which no longer contributed to structure formation, and the amorphous regions stiffened. This behaviour

led to a sharp decrease in the deformation strength of the polymers with high filler contents and to brittle fracture [50].

The ability of composite materials based on polyolefin and natural fillers to be degraded and assimilated by microorganisms depends on a number of characteristics of the polymer matrix and filler, as well as the structure of the whole material. Polymer composite materials are released into the environment and exposed to physical, chemical, and biological factors [51, 52]. The properties of polymers, including their strength, colour, and shape, are irreversibly changed by degradation or ageing. The final stage of ageing is the mechanical destruction of the materials (fragmentation). Microorganisms play the main role in biological degradation. The biological degradation of composites by microorganisms includes several stages [53, 54]. The first stage of biodegradation of a synthetic polymer begins with adsorption of microorganisms on its surface; the surface hydrophility must increase for the penetration of a microorganism into the polymer structure. To test the surface hydrophility, the samples were placed in different media: water and sodium chloride solution.

A nonmonotonic change in mass was observed for all samples because the fractions with low molecular weights were washed out from the surface layers on the first day, and then the process stabilized. Some samples behaved differently based on their compositions, exhibiting sharp washout of surface layers in the first several days, followed by swelling and penetration of the solvent into the intermolecular space. The degree of polymer weight reduction depends on the percentage of soluble components, the particle size of the filler and the availability of the filler in the polymer matrix.

The change in the mechanical properties of the samples over time after composting in special humus was studied (Table 4).

T a b l e 4

**Physical-mechanical properties (tensile strain and elongation)
of composites before and after burial in soil for 90 days**

Sample	Filler content, %	Before burial in soil		After burial in soil for 90 days	
		Tensile strange, kgf/cm^2	Elongation, %	Tensile strange, kgf/cm^2	Elongation, %
PE/NC	5	140	175	122	125
	10	130	135	113	105
	20	110	100	99	85
PE/MCC	5	136	110	121	92
	10	118	60	109	52
	20	104	45	91	38
Note: Result presented as mean ±0.3 % standard deviation, $n = 5$					

As can be seen in Table 4, the mechanical strength of composites aged in the soil decreased after a certain time, and the greater the filler content was, the lower the strength. A decrease in the strength characteristics of composites enabled us to assume partial destruction of the structures of the composites; such degradation was probably connected with the initial stages of biodegradation of natural fillers in composites. The studies of the physical and mechanical properties of the composites clearly demonstrate qualitative changes in the structure of the composites during biodegradation. Changes occurring in the materials under the influence of degradation in the soil include changes in colour, loss of mass, biological fouling of the composites, and mechanical destruction.

Conclusions

A comparative study on the structures of MCC and NC was carried out, and the changes in structural characteristics were shown upon transition from microparticles to nanoparticles. Composites based on polyethylene filled with different contents of cellulose micro- and nanoparticles were obtained. The structure of the composition was studied by infrared spectroscopy, X-ray structure and thermal analyses, and the change in structure depended on the type and amount of the filler. The role of small (up to 5 wt.%) contents of polysaccharides on the structure formation of polyethylene has been revealed. It was shown that an increase in the presence of natural additives (up to 20 wt.%) leads to a decrease in the degree of polyethylene ordering, which also affects the mechanical properties of the composite. Preliminary data showed the propensity of the obtained compositions to biodegrade.

References

1   Rogovina, S.Z., Prut, E.V., & Berlin, A.A. (2019). Composite materials based on synthetic polymers reinforced with natural fibers. *J. Polym. Sci. Part A Polym. Chem., 61*(4), 417–438. https://doi.org/10.1134/S0965545X19040084

2   Azman, M.A., Asyraf, M.R.M., Khalina, A., Petru, M., Ruzaidi, C.M., Sapuan, S.M., Wan, N.W.B., Ishak, M.R., Ilyas, R.A., & Suriani, M.J. (2021). Natural fibre reinforced composite material for product design: a short review. *Polymers, 13*(12), 1917. https://doi.org/10.3390/polym13121917

3   Nurazzi, N., Asyraf, M., Khalina, A., Abdullah, N., Aisyah, H., Rafiqah, S., Sabaruddin, F., Kamarudin, S., Norrrahim, M., Ilyas, R., & Sapuan, S. (2021). A review on natural fibre reinforced polymer composite for bullet proof and ballistic applications. *Polymers, 13*(4), 646. https://doi.org/10.3390/polym13040646

4   Ibrahim, H., Farag, M., Megahed, H., & Mehanny, S. (2014). Characteristics of starch-based biodegradable composites reinforced with date palm and flax fibers. *Carbohyd. Polym., 101,* 11-19. https://doi.org/10.1016/j.carbpol.2013.08.051

5   Lu, D.R., Xiao, C.M., & Xu, S.J. (2009). Starch-based completely biodegradable polymer materials. *eXPRESS Polym. Let., 3,* 366–375. https://doi.org/10.3144/expresspolymlett.2009.46

6   Turdikulov, I.H., Mamadiyorov, B.N., Saidmuhammedova, M.Q., & Atakhanov, A.A. (2020). Obtaining and studying properties of biodestructable composite films based on polyethylene. *Open J. Chem., 6*(1), 030-036. https://doi.org/10.17352/ojc.000021

7   Omran, A.A.B., Mohammed, A.A.B.A., Sapuan, S.M., Ilyas, R.A., Asyraf, M.R.M., Koloor, S.S.R., & Petr, M. (2021). Micro- and nanocellulose in polymer composite materials: A review. *Polymers, 13,* 231. https://doi.org/10.3390/polym13020231

8   Hao, W., Wanga, M., Zhou, F., Luo, H., Xie, X., Luo, F., & Cha, R. (2020) A review on nanocellulose as a lightweight filler of polyolefin composites. *Carbohyd. Polym., 243,* 116466. https://doi.org/10.1016/j.carbpol.2020.116466

9   Lee, K.Y., Aitomäki, Y., Berglund, L., Oksman, K., & Bismarck, A. (2014). On the use of nanocellulose as reinforcement in polymer matrix composites. *Combust. Sci. Technol., 105,* 15-27. https://doi.org/10.1016/j.compscitech.2014.08.032

10   Atakhanov, A.A., Kholmuminov, A.A., Mamadierov, B.N., Turdikulov, I.H., & Ashurov, N.Sh. (2020) Rheological Behavior of Nanocellulose Aqueous Suspensions. *J Polym Sci Part A Polym Chem., 62*(3), 213–217. https://doi.org/10.1134/S0965545X20030013

11   Shen, R., Xue, Sh., Xu, Y., Liu, Q., Feng, Z., Ren, H., Zhai, H., & Kong, F. (2020). Research progress and development demand of nanocellulose reinforced polymer composites. *Polymers, 12,* 2113. https://doi.org/10.3390/polym12092113

12   Low, D.Y.S., Supramaniam, J., Soottitantawat, A., Charinpanitkul, T., Tanthapanichakoon, W., Tan, K.W., & Tang, S.Y. (2021) Recent developments in nanocellulose-reinforced rubber matrix composites: a review. *Polymers, 13,* 550. https://doi.org/10.3390/polym13040550

13   Voronova, M.I., Surov, O.V., Kuziyeva, M.K., & Atakhanov, A.A. (2022). Thermal and mechanical properties of polymer composites reinforced by sulfuric acid-hydrolyzed and tempo-oxidized nanocellulose: a comparative study. *Chem. Chem. Tech., 65*(10), 95–105. https://doi.org/10.6060/ivkkt.20226510.6596

14   Valentini, F., Dorigato, A., Rigotti, D., & Pegotti, A. (2019). Polyhydroxyalkanoates/fibrillated nanocellulose composites for additive manufacturing. *J. Polym. Environ., 27,* 1333–1341. https://doi.org/10.1007/s10924-019-01429-8

15   de Souza, A.G., Barbosa, R.F.S., & Rosa, D.S. (2020) Nanocellulose from industrial and agricultural waste for further use in pla composites. *J. Polym. Environ., 28,* 1851–1868. https://doi.org/10.1007/s10924-020-01731-w

16   Csiszár, E., Kun, D., & Fekete, E. (2021) The role of structure and interactions in thermoplastic starch–nanocellulose composites. *Polymers, 13,* 3186. https://doi.org/10.3390/polym13183186

17   Voronova, M.I., Surov, O.V., Afineevskii, A.V., & Zakharov, A.G. (2020). Properties of polyacrylamide composites reinforced by cellulose nanocrystals. *Heliyon, 6*(11), e05529. https://doi.org/10.1016/j.heliyon.2020.e05529

18   Borysiak, S. (2013). Influence of cellulose polymorphs on the polypropylene crystallization. *J. Therm. Anal. Calorim., 113,* 281-289. https://doi.org/10.1007/s10973-013-3109-0

19   Robaidi, A.A., Anagreha, N., Addousb, M., & Massadeha, S. (2013). Crystallization behavior of iPP/LLDPE blend filled with nano kaolin particles. *Jordan J. Mech. Indust. Eng., 7*(1), 35-39.

20   Sanadi, A.R., Calufield, D.F., & Rowell, R.M. (1994). Reinforcing polypropylene with natural fibers. *Plast. Eng., 50*(4), 27-28.

21   Bledzki, A.K., & Jaszkiewicz, A. (2010). Mechanical performance of biocomposites based on PLA and PHBV reinforced with natural fibres. A comparative study to PP. *Compos. Sci. Tech., 70*(12), 1687-1696. https://10.1016/j.compscitech.2010.06.005

22   Peng, Y.C., Gallegos, S.A., Gardner, D.J., Han, Y., & Cai, Z.Y. (2016). Maleic anhydride polypropylene modified cellulose nanofibril polypropylene nanocomposites with enhanced impact strength. *Polym. Compos., 37*(3), 782-793. https://doi.org/10.1002/pc.23235

23   Hirai, S., Phanthong, P., Okubo, H., & Yao, S. (2020). Enhancement of the surface properties on polypropylene film using side-chain crystalline block copolymers. *Polymers, 12*(11), 2736. https://doi.org/10.3390/polym12112736

24 Nagalakshmaiah, M., Pignon, F., El Kissi, N., & Dufresne, A. (2016). Surface adsorption of triblock copolymer (PEO–PPO–PEO) on cellulose nanocrystals and their melt extrusion with polyethylene. *RSC Advances, 6*(70), 66224-66232. https://doi.org/10.1039/C6RA11139D

25 Zhang, Y.J., Jiang, X.Y., Bai, Z.W., Wang, J.K., Qian, Z.M., & Liu, Y.X. (2018). Re-treated nanocellulose whiskers alongside a polyolefin elastomer to toughen and improve polypropylene composites. *J. Appl. Polym., Sci. 135*(15), 46066. https://doi.org/10.1002/app.46066

26 Noguchi, T., Niihara, K., Iwamoto, R., Matsuda, G., Endo, M., & Isogai, A. (2021). Nanocellulose/polyethylene nanocomposite sheets prepared from an oven-dried nanocellulose by elastic kneading. *Compos. Sci. Technol., 207,* 108734. https://doi.org/10.1016/j.compscitech.2021.108734

27 Clemons, C. (2010). Elastomer modified polypropylene–polyethylene blends as matrices for wood flour–plastic composites. *Compos Part A, 41*(11), 1559–1569. https://doi.org/10.1016/j.compositesa.2010.07.002

28 Van de Velde, K., & Kiekens, P. (2001). Influence of fiber surface characteristics on the flax/polypropylene interface. *J. Thermopl. Compos. Mat., 14*(3), 244–260. https://doi.org/10.1106/13PW-MYJU-8HCJ-B1T1

29 He, X., Zheng, S., Huang, G., & Rong, Y. (2013). Solution grafting of maleic anhydride on low-density polyethylene: effect on crystallization behaviour. *J. Macromol. Sci. Phys., 52,* 1265–1282. https://doi.org/10.1080/00222348.2013.764217

30 Chang, M.K. (2015). Mechanical properties and thermal stability of low-density polyethylene grafted maleic anhydride/montmorillonite nanocomposites. *J. Ind. Eng. Chem., 27,* 96–101. https://doi.org/10.1016/j.jiec.2014.11.048

31 Fu, S-Y., Feng, X-Q., Lauke, B., & Mai Y-W. (2008). Effects of particle size, particle/matrix interface adhesion and particle loading on mechanical properties of particulate–polymer composites. *Compos. Part B Eng., 39*(6), 933-961. https://doi.org/10.1016/j.compositesb.2008.01.002

32 Essabir, H., Hilali, E., & Elgharad, A. (2013). Mechanical and thermal properties of bio-composites based on polypropylene reinforced with nut shells of Argan particles. *Mater. Design., 49,* 442-448. https://doi.org/10.1016/j.matdes.2013.01.025

33 Yuldoshev, Sh.A., Atakhanov, A.A., Sarimsakov, A.A. (2016). Cotton cellulose microcrystalline cellulose and nanocellulose: carboxymethyllation and oxidation reaction activity. *Nano Sci. Nano Tech., 10*(3), 102-109.

34 Voronova, M.I., Lebedeva, T.N., Surov, O.V., & Zakharov, A.G. (2013). Film properties of nanocrystalline cellulose with various contents of sulfate groups. *Khimiia Rastitelnogo Syria – Chemistry of plant materials, 3,* 49-57. https://doi.org/10.14258/jcprm.1303049

35 Zaini, L.H., Janoobi, M., Tahir, P.Md., & Karimi, S. (2013). Isolation and characterization of cellulose whiskers from kenaf bast fibers. *J. Biomater. Nanotech., 4,* 37-44. https://doi.org/10.4236/jbnb.2013.41006

36 Atakhanov, A.A., Mamadiyorov, B., Kuzieva, M., Yugay, S.M., Shahobutdinav, S., Ashurov, N.S., Abdurazakov, M. (2019). Comparative studies of physic-chemical properties and structure of cotton cellulose and its modified forms. *Khimiia Rastitelnogo Syria – Chemistry of plant materials, 3,* 5–13. https://doi.org/10.14258/jcprm.2019034554

37 Atakhanov, A., Turdikulov, I., Mamadiyorov, B., Abdullaeva, N., Nurgaliev, I., & Rashidova, S. (2019). Isolation of nanocellulose from cotton cellulose and computer modeling of its structure. *Open J. Polymer Chem., 9,* 117-129. https://doi.org/10.4236/ojpchem.2019.94010

38 Atakhanov, A.A., Turdikulov, I.K., & Ashurov, N.S. (2022). Polyethylene-based oxo-degradable nanocomposite film. *Rus. J. Appl. Chem., 95*(8), 1161–1168. https://doi.org/10.1134/S1070427222080110

39 Kuzieva, M., Atakhanov, A.,·Shakhobutdinov, S., Ashurov, N., Yunusov, Kh., & Guohua, J. (2023). Preparation of oxidized nanocellulose by using potassium dichromate. *Cellulose.* https://doi.org/10.1007/s10570-023-05222-8

40 Langford, J.I., & Wilson, A.J.C. (1978). Scherrer after sixty years: A survey and some new results in the determination of crystallite size. *J App Crystall 11*(2), 102-113.

41 Nam, S., French, A.D., Condon, B.D., & Concha, M. (2016) Segal crystallinity index revisited by the simulation of X-ray diffraction patterns of cotton cellulose I and cellulose II. *Carbohydr. Polym., 13,* 1-9. http://doi.org/doi:10.1016/j.carbpol.2015.08.035

42 Wendlandt, W.W. (1974). Thermal methods of analysis. A Willey-Interscience Publication John Wiley&Sons, New York.

43 Gorokhovatsky, Yu.A., Viktorovich, A.S., Temnov, D.E., Tazenkov, B.A., Aniskina, L.B., & Chistyakova, O.V. (2006). IK-spektroskopiia elektretov na osnove polietilena i polipropilena [IR spectroscopy of electrets based on polyethylene and polypropylene]. *Izvestiia Rossiiskogo Gosudarstvennogo Pedagogicheskogo Universiteta — Izvestia of the Russian State Pedagogical University named after A.I. Herzen, 6*(15), 69-75 [in Russian].

44 Ashurov, N.S., Shahobutdinov, S.S., Kareva, N.D., Yugay, S.M., Atakhanov, A.A., & Rashidova, S.S. (2020). Issledovanie struktury i svoistv nanostrukturnykh polimernykh smesei na osnove polietilena i polipropilena [Investigation of structure and properties of nanostructured polymer mixtures based on polyethylene and polyvinyl chloride]. *Plasticheskie massy – Plastics, 3-4,* 8-11. https://doi.org/10.35164/0554-2901-2020-3-4-8-11

45 Solomko, V.P. (1980). Napolnennye Kristallizuiushchiesia Polimery [Filled crystallizable polymers]. Nauk. Dumka, Kiev [in Russian].

46 Zhong, Y., Poloso, T., Hetzer, M., & De Kee, D. (2007). Enhancement of wood/polyethylene composites via compatibilization and incorporation of Organoclay particles. *Polym. Eng. Sci., 47*(6), 797–803. http://dx.doi.org/10.1002/pen.20756

47 Zhang, F., Qiu, W., Yang, L., Endo, T., & Hirotsu, T. (2002). Mechanochemical preparation and properties of a cellulose polyethylene composite. *J. Mater. Chem., 12,* 24–6. https://doi.org/10.1039/B108255H

48 Pöllänen, M., Suvanto, M., & Pakkanen, T.T. (2013). Cellulose reinforced high density polyethylene composites — Morphology, mechanical and thermal expansion properties. *Compo. Sci. Technol., 76,* 21-28. http://dx.doi.org/10.1016/j.compscitech.2012.12.013

49 Khvatov, A.V., Popov, A.A., Kolesnikova, N.N., & Lukanina, J.K. (2007). Biodegradable polymer composite materials. *J. Balkan. Tribological. Assoc., 13*(4), 527-535.

50 Normurodov, N.F., Berdinazarov, Q.N., Abdurazakov, M., Ashurov, N.R. (2022) Mechanical and Thermal Properties of Biodegradable Composites Based on graft copolymer LLDPE-g-MA/Gelatin. *Bulletin of the University of Karaganda Chemistry*, 108(4), 35-45. https://doi.org/10.31489/2022Ch4/4-22-11

51 Clemons, C. (2010). Elastomer modified polypropylene–polyethylene blends as matrices for wood flour–plastic composites. *Compos. Part A, 41*(11), 1559–1569. https://doi.org/10.1016/j.compositesa.2010.07.002

52 Albertsson, A.C., Andersson, S.O., & Karlsson, S. (1987). The mechanism of biodegradation of polyethylene. *Polym. Degrad. Stabil., 18*, 73-87. https://doi.org/10.1016/0141-3910(87)90084-X

53 Kawai, F. (1995). Break down of plastics and polymers by microorganisms. *Biochem. Eng., 52*, 151–194. https://doi.org/10.1007/BFb0102319

54 Matsumura, S. (2005). In: Smith R (ed) Mechanism of biodegradation, Wood head, London.

Information about authors*

Saidmuhamedova, Mukhlisa Qodir qizi — Junior researcher, Institute of Polymer Chemistry and Physics, 100128, Tashkent, Uzbekistan; e-mail: polymer@academy.uz; https://orcid.org/0000-0001-5592-4997;

Turdiqulov, Islom Hayitboy o'g'li — PhD, Junior researcher, Institute of Polymer Chemistry and Physics, 100128, Tashkent, Uzbekistan; e-mail: i.turdikulov@mail.ru; https://orcid.org/0000-0001-5100-7729;

Atakhanov, Abdumutolib Abdupatto o'g'li (corresponding author) — Doctor of technical sciences, Professor, Head of laboratory "Physic and physic-chemical methods of investigation" Institute of Polymer Chemistry and Physics, 100128, Tashkent, Uzbekistan; e-mail: a-atakhanov@yandex.com; https://orcid.org/0000-0002-4975-3658;

Ashurov, Nurbek Shodievich — Candidate of physic-mathematic sciences, Senior researcher, Institute of Polymer Chemistry and Physics, 100128, Tashkent, Uzbekistan; e-mail: ansss72@mail.ru; https://orcid.org/0000-0001-5246-434X;

Abdurazakov, Muhitdin — Candidate of technical sciences, Senior researcher, Institute of Polymer Chemistry and Physics, 100128, Tashkent, Uzbekistan; e-mail: muhitdin49@mail.ru; https://orcid.org/0000-0002-7950-6092;

Rashidova, Sayyora Sharafovna — Doctor of Science, Professor, Academician, Director of Institute of Polymer Chemistry and Physics, 100128, Tashkent, Uzbekistan; e-mail: polymer@academy.uz; https://orcid.org/0000-0003-1667-4619

Surov, Oleg Valentinovich — Doctor of Science, Professor, Senior researcher, G.A. Krestov Institute of Solution Chemistry, Ivanovo, Russia; e-mail: ovs@isc-ras.ru; https://orcid.org/0000-0002-7164-364X

*The author's name is presented in the order: *Last Name, First and Middle Names*

INORGANIC CHEMISTRY

Aitolkyn A. Toibek [ID], Kenzhebek T. Rustembekov*[ID],
Vitaly N. Fomin [ID], Dauletkhan A. Kaikenov [ID]

Karagandy University of the name of academician E.A. Buketov, Karaganda, Kazakhstan
(*Corresponding author's e-mail: rustembekov_kt@mail.ru*)

New Samarium Oxotellurites: Synthesis and Characteristic

We synthesized samarium oxotellurites $SmMTeO_{4.5}$ (M — Mg, Ba) by the method of ceramic technology with solid-phase interaction (800–1200 °C) of Sm_2O_3 and TeO_2 oxides with $MgCO_3$ and $BaCO_3$ carbonates. The compounds were characterized by X-ray and electrophysics methods. It has been established that the synthesized compounds crystallize in the tetragonal syngony with the following crystallographic characteristics: $SmMgTeO_{4.5}$ — $a = 12.226$; $c = 5.783$ Å, $V^0_{un.cell} = 864.38$ Å^3, $Z = 4$, $\rho_{xray.} = 2.876$, $\rho_{pycn.} = (2.874\pm0.002)$ g·cm^{-3}; $SmBaTeO_{4.5}$ — $a = 12.717$; $c = 6.132$Å, $V^0_{un.cell} = 991.62$Å^3, $Z = 4$, $\rho_{xray.} = 3.264$, $\rho_{pycn.} = (3.260\pm0.004)$ g·cm^{-3}; for both tellurites $\alpha = \beta = \gamma = 90°$. The experimental and calculated values of 2 Th and d-sp, X-ray and pycnometric densities, as well as theoretical and experimental values of unit cell volumes are agreed satisfactorily. Thus, we can confirm correctness and reliability of the results of indexing X-ray patterns of new samarium oxotellurites. We found that increase in the ionic radii from Mg to Ba increases the lattice parameters of the synthesized oxotellurites. Oxotellurites are crystallized in the structural types of distorted perovskite P_m3_m. Based on the given study samarium oxotellurites can have semiconductor and ferroelectric properties.

Keywords: samarium oxotellurites, synthesis, crystallographic characteristics of the compounds, permittivity, resistance.

Introduction

The research object is complex oxides with the perovskite structure ABO_3 and A_2BO_4 (where A is REE and/or AEM; B is Cu, Ti, Cr, Mn, Fe, Co, Ni). It is connected with the possibility of their potential application in various fields of technology. In particular, perovskite oxides are widely used in electrocatalysis [1] and heterogeneous catalysis [2] owing to the low cost, simplicity of the synthesis process, and extraordinary ability to combine a wide range of substituting and alloying elements to modulate their properties. The oxygen sublattice is resistant to oxidizing environments and high temperatures, high electrical conductivity and mobility. Consequently, these materials are used as CO_2 laser cathodes, fuel cell electrodes, oxygen membranes, magnetoresistors and exhaust gas after burning catalysts.

Active researches are carried out to obtain materials with the required properties. The traditional way to modify the properties of inorganic compounds is to vary their composition by partial substitution of components in different sublattices. One of the approaches is based on the concept of the stereochemical effect of lone electron pairs of p-cations in medium oxidation states (I^V, Se^{IV}, Te^{IV}, As^{III}, Sb^{III}, Bi^{III}, Pb^{II}, Tl^{I}, etc.). It often results to the appearance of acentric and microporous structures [3]. In this work [4] we have predicted possible polytypes of the maximum degree of order. As well as we have discussed the crystal chemical relationships between rare earth oxyhalides and lone pair ions.

In this aspect, oxocompounds of tellurium with rare earth elements are of particular interest for research. This interest is caused because tellurium has a stereochemically active lone pair of electrons, and

also tellurium oxo compounds have semiconductor, ferroelectric properties and are nonlinear optical materials [5, 6]. In this regard, the purpose of this work is the synthesis and study of the X-ray and electrophysical properties of new phases — samarium oxotellurites of the composition $SmMTeO_{4.5}$ (M — Mg, Ba).

Experimental

Solid-phase synthesis of compounds was carried out by the ceramic technology method (800–1200 °C) with the interaction of oxides Sm_2O_3 (special purity) and TeO_2 (chemically pure) with carbonates $MgCO_3$, $BaCO_3$ (analytical grade) in stoichiometric ratios according to the method published earlier in this work [6].

X-ray diffraction patterns of the synthesized compounds using an Empyrean powder diffractometer (PANalytical) have been obtained. Data collection was performed using the Data Collector version 7.7 h. We decrypted X-ray patterns and identified phases using a specialized computer program H'Pert HighScore Plus, which provides automated quantitative phase analysis, including measurement, processing, and obtaining results, using all currently accepted analytical models. The phase composition was identified using the Crystallography Open Database and PDF-2. The pycnometric density has been determined according to the procedure [7]. Indifferent liquid was toluene.

We carried out the study of electrical properties — permittivity and resistance in the range of 293–483 K by measuring the electrical capacitance of the samples on an LCR-800 instrument (Taiwan) at an operating frequency of 1; 5 and 10 kHz continuously in dry air in thermostatic mode with holding time at each fixed temperature. The preparation of samples and their study were carried out according to the method published earlier in this work [8].

Results and Discussion

Diffraction patterns of $SmMTeO_{4.5}$ tellurites are shown in Figure 1.
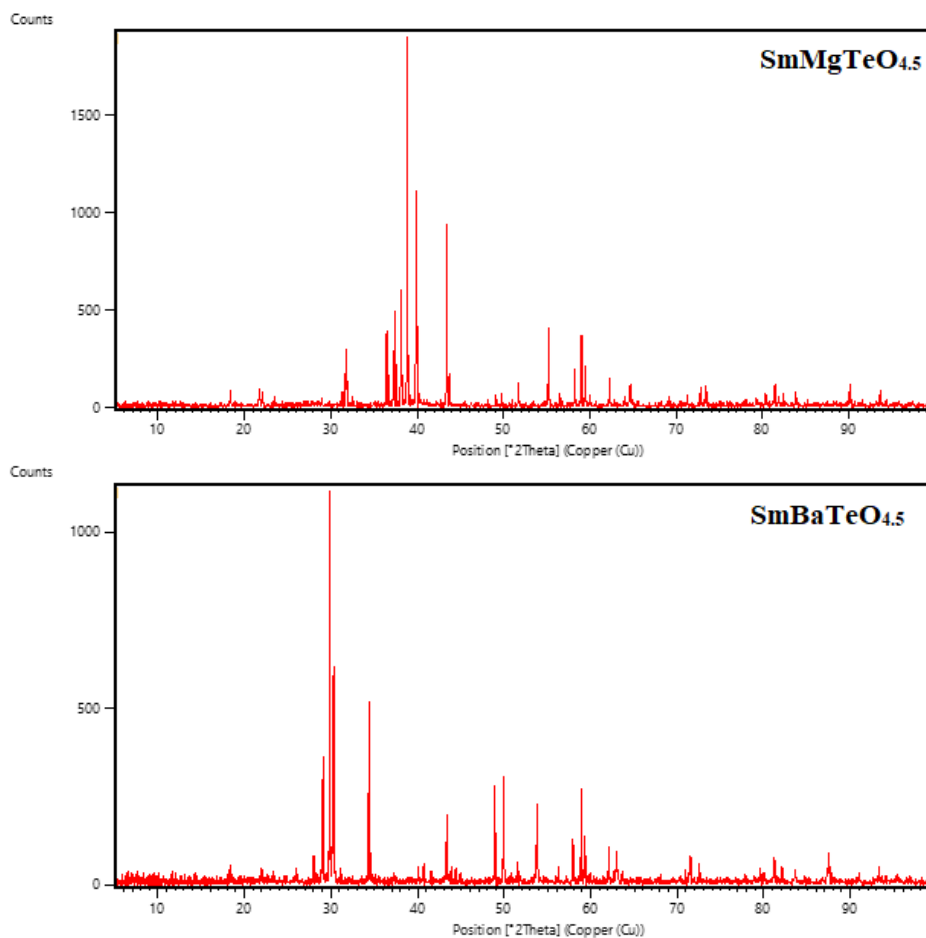
Figure 1. X-ray diffraction patterns of $SmMTeO_{4.5}$ tellurites

Table 1 shows the results of X-ray indexing of the compounds.

T a b l e 1

The results of indexing X-ray patterns of new samarium tellurites
SmMTeO$_{4.5}$ (M — Mg, Ba)

h	k	l	2Th. (c) [°]	2Th. (o) [°]	d-sp. (c) [Å]	d-sp. (o) [Å]
SmMgTeO$_{4.5}$
1	1	1	18.4354	18.3813	4.808763	4.822810
3	0	0	21.7942	21.7940	4.074674	4.074707
1	0	2	31.7540	31.7421	2.815693	2.816724
4	2	1	36.3194	36.4737	2.471547	2.461447
5	0	0	36.7308	36.6132	2.444805	2.452383
2	2	2	37.3710	37.3907	2.404382	2.403161
5	1	0	37.4850	37.5239	2.397328	2.394932
3	0	2	38.1144	38.1731	2.359178	2.355685
3	1	2	38.8456	38.8713	2.316432	2.314963
5	0	1	40.0023	39.9413	2.252079	2.255378
4	1	2	43.6769	43.6857	2.070748	2.070349
2	2	3	51.8630	51.7294	1.761502	1.765740
6	0	2	55.0857	55.1806	1.665830	1.663189
6	4	1	56.5239	56.5130	1.626808	1.627096
4	2	3	58.5173	58.2330	1.576050	1.583064
6	5	0	58.9659	59.0455	1.565126	1.563204
7	3	1	59.7391	59.4480	1.546702	1.553577
7	0	2	62.0236	62.2384	1.495103	1.490458
6	6	0	64.6473	64.6549	1.440615	1.440466
9	0	1	71.2599	71.2336	1.322293	1.322716
4	1	4	72.6615	72.7986	1.300202	1.298091
9	3	0	73.4271	73.4631	1.288525	1.287981
8	5	2	81.2899	81.3631	1.182583	1.181705
10	3	0	82.2795	82.4266	1.170849	1.169132
5	4	4	83.8338	83.8293	1.153052	1.153103
11	1	1	90.2486	90.0962	1.087012	1.088454
10	4	2	93.6117	93.5834	1.056595	1.056841
SmBaTeO$_{4.5}$
4	0	0	28.0191	28.0241	3.181951	3.181394
0	0	2	29.1527	29.0980	3.060747	3.066380
3	3	0	29.7568	29.8754	2.999972	2.988340
1	0	2	30.0031	30.2772	2.975909	2.949582
4	2	1	34.7326	34.4057	2.580740	2.604513
4	2	2	43.3801	43.3450	2.084222	2.085833
2	2	3	48.9760	48.9492	1.858368	1.859323
3	1	3	50.0795	49.9677	1.819974	1.823786
4	1	3	53.8114	53.7995	1.702229	1.702578
8	0	0	57.9159	57.9695	1.590976	1.589631
7	0	2	59.0446	58.8784	1.563227	1.567243
5	5	2	59.5328	59.3122	1.551568	1.556812
8	2	1	61.9532	62.0848	1.496632	1.493776
6	0	3	63.1755	63.0113	1.470586	1.474024
8	5	1	71.5574	71.4936	1.317525	1.318543
5	1	4	72.3722	72.5596	1.304685	1.301777
7	7	2	81.0590	81.1581	1.185369	1.184171
8	7	2	87.3902	87.4452	1.115049	1.114489

According to Table 1 and Table 2, the experimental and calculated values of 2Th. and d-sp. and the values of X-ray and pycnometric densities agreed satisfactorily with each other. That confirms the reliability and correctness of the indexing results.

Theoretical cell volumes of the synthesized tellurites were determined using the data on the cell volumes of the oxides contained in them according to the scheme:

$$V°_{un.cell} \; SmMTeO_{4.5} = 0.5 \; V°_{un.cell} \; Sm_2O_3 + V°_{un.cell} \; TeO_2 + V°_{un.cell} \; MO \; (M — Mg, Ba). \qquad (1)$$

The correctness of the indexing of X-ray diffraction patterns of the synthesized tellurites is also confirmed by the satisfactory agreement between the values calculated for the unit cell volumes of tellurites from the sum of the unit cell volumes of the initial samarium, magnesium (barium) and tellurium oxides borrowed from using the Crystallography Open Database [9] with the calculated cell volumes of the compounds from radiographic data. Thus, for $SmMgTeO_{4.5}$, $V°_{un.cell}$= 896.415 Å^3 (from the sum of $V°_{un.cell}$ of oxides) and 864.38 Å^3 (from indexing data), and for $SmBaTeO_{4.5}$, $V°_{un.cell}$= 987.790 Å^3 (from the sum of $V°_{un.cell}$ oxides) and 991.62 Å^3 (from indexing data).

It was found that with increasing ionic radii from Mg to Ba, the elementary cell volumes of the synthesized tellurites increase. Based on the indexing of X-ray diffraction patterns of the studied tellurites, we established that $SmMgTeO_{4.5}$ and $SmBaTeO_{4.5}$ compounds crystallize in the tetragonal syngony with lattice parameters, which are presented in Table 2.

T a b l e 2

Crystallographic characteristics of SmMTeO$_{4.5}$ compounds

Compound	Type of syngony	Lattice parameters, Å			Z	α, β, γ, degree.	Density, g·cm^{-3}	
		a	c	$V^0_{un.cell.}$ Å^3			xray.	pycn.
SmMgTeO$_{4.5}$	tetragonal	12.226	5.783	864.38	4	90	2.876	2.874±0.002
SmBaTeO$_{4.5}$	tetragonal	12.717	6.132	991.62	4	90	3.264	3.260±0.004

On the basis of H'Pert HighScore Plus we compared X-ray diffraction patterns of the synthesized tellurites with the X-ray parameters [I/I$_0$, d] of the starting materials and with possible tellurites of this system. It was revealed that the diffraction patterns of new tellurites have no analogs with them. These data further confirm that the synthesized tellurites are new compounds.

The data of X-ray studies show that the synthesized tellurites crystallize in the structural type of distorted perovskite P$_m$3$_m$. Therefore, it can be assumed that these compounds can have semiconductor and ferroelectric properties.

As a rule, the temperature dependence of electrophysical properties is observed in ceramic ferroelectrics. For this purpose, we studied the temperature dependences of the permittivity and resistance of the synthesized tellurites in the range of 293–483 K according to the procedure [8].

The value of the permittivity at each temperature was determined by the formula:

$$\varepsilon = C/C_0, \qquad (2)$$

where $C_0 = E_0 \; s/d$ — the capacitance of the capacitor without the test substance (air).

The dielectric constant of a standard substance, barium titanate $BaTiO_3$ has been measured at frequencies of 1; 5 and 10 kHz for the reliability of the obtained data. The experimental value of the permittivity of $BaTiO_3$ at 293 K at a frequency of 1 kHz, equal to 1296, satisfactorily agrees with its recommended value of $1400 ± 250$ [10]. In addition, the observed changes in the electrical conductivity of $BaTiO_3$ at 383 K at all frequencies are also consistent with its transition from the perovskite cubic P$_m$3$_m$ phase to the tetragonal (polar) ferroelectric phase with sp.gr. P4mm [10].

Increase in the operating frequency from 1 kHz to 10 kHz, only leads to some decrease in resistance and practically does not affect the dielectric constant of the connection. Therefore, we present the results of experiments only at a frequency of 1 kHz.

The results of experimental data on the study of the electrical properties of the compounds are shown in Table 3 and in Figures 2 and 3.

Temperature dependence of the electrical properties of tellurites of SmMTeO$_{4.5}$

| T, K	C, nF	Ohm	lgR	ε	lgε
SmMgTeO$_{4.5}$					
293	0.0085	370500	5.57	61	1.79
303	0.00851	444700	5.65	61	1.79
313	0.00857	485200	5.69	62	1.79
323	0.00845	225300	5.35	61	1.78
333	0.00774	1917000	6.28	56	1.75
343	0.00767	1656000	6.22	55	1.74
353	0.00745	1228000	6.09	54	1.73
363	0.00735	804900	5.91	53	1.72
373	0.00726	670300	5.83	52	1.72
383	0.00724	521000	5.72	52	1.72
393	0.00717	185100	5.27	52	1.71
403	0.00722	210700	5.32	52	1.72
413	0.00725	264700	5.42	52	1.72
423	0.00726	199700	5.30	52	1.72
433	0.00727	176300	5.25	52	1.72
443	0.00729	228400	5.36	52	1.72
453	0.00734	120800	5.08	53	1.72
463	0.00735	134400	5.13	53	1.72
473	0.0073	191700	5.28	53	1.72
483	0.0074	225700	5.35	53	1.73
SmBaTeO$_{4.5}$					
293	0.0189	146600	5.17	54	1.74
303	0.01875	93480	4.97	54	1.73
313	0.01901	282500	5.45	55	1.74
323	0.02301	1591000	6.20	66	1.82
333	0.0335	2700000	6.43	96	1.98
343	0.07076	2635000	6.42	204	2.31
353	0.12886	2129000	6.33	371	2.57
363	0.15916	1946000	6.29	458	2.66
373	0.03888	2620000	6.42	112	2.05
383	0.021105	736600	5.87	61	1.78
393	0.0197	220800	5.34	57	1.75
403	0.01967	1733000	6.24	57	1.75
413	0.01968	61580	4.79	57	1.75
423	0.01983	56940	4.76	57	1.76
433	0.01986	61680	4.79	57	1.76
443	0.02002	113200	5.05	58	1.76
453	0.02001	75830	4.88	58	1.76
463	0.02014	73200	4.86	58	1.76
473	0.02018	57020	4.76	58	1.76
483	0.02028	56020	4.75	58	1.77
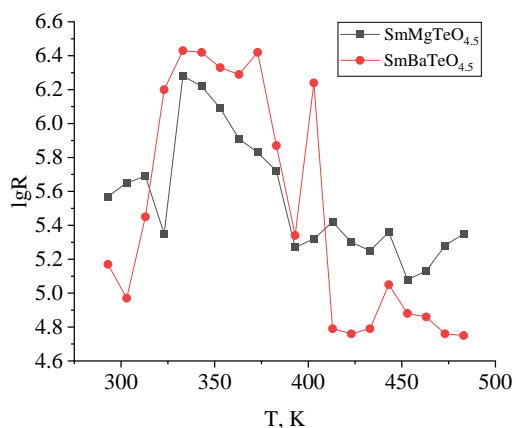
Figure 2. Temperature dependences of resistance
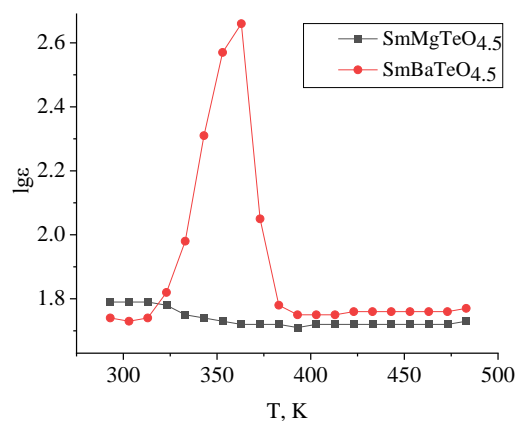
Figure 3. Temperature dependences of dielectric permittivity

An analysis of the data in Table 3 and Figures 2 and 3 shows that with increasing temperature, significant changes in the electrophysical characteristics of tellurites were found, and, as is typical for ceramic materials, such changes occur in a certain temperature range.

SmMgTeO$_{4.5}$. The dielectric constant is low. The resistances of SmMgTeO$_{4.5}$ in the interval 293–313 K and 323–333 K increase in the same way as in metals, respectively. The resistance in the range of 293–313 K increases. The rise is observed in the range of 313–323 K, at which the resistance declines with a minimum at 323 K. Then, at 333–393 K, the resistance decreases again (electrical conductivity increases), i.e. semiconductor conductivity appears.

The calculation of the band gap (ΔE) of the test compound was determined by the formula:

$$\Delta E = \frac{2kT_1T_2}{0.43(T_2 - T_1)} \lg \frac{R_1}{R_2}, \tag{3}$$

where k — the Boltzmann constant, equal to 8.6173303·10^{-5} eV·K^{-1}; R_1 and R_2 — resistances at temperatures T_1 and T_2, respectively. The band gap (ΔE) calculated by formula (3) for SmMgTeO$_{4.5}$ tellurite in the range of 333–393 K is 1.04 eV and can be attributed to narrow-probe semiconductors. In the range 443-483 K we observe variable conductivity. As the frequency increases, the resistance decreases.

SmBaTeO$_{4.5}$. This compound in the range of 303–333 K exhibits metal-like tendency, and at 333–363 K, as well as at 373–393 K and at 443–483 K — semiconductor conductivity. In the range 433–483 K we observe variable conductivity. The band gap (ΔE) calculated by formula (3) for SmBaTeO$_{4.5}$ tellurite is equal to 1.65 eV within 333–363 K, and 2.27 eV within 443–483 K. The tellurite can be attributed to a narrow-probe semiconductor.

Studies of the temperature dependence of the permittivity and resistance of double samarium tellurites have shown that these compounds can have semiconductor and ferroelectric properties. As a rule, the temperature dependence of electrophysical properties is observed in ceramic ferroelectrics. The observed anomalous jumps on the curves of the temperature dependence of the resistance of the compounds indicate Type II phase transitions, conditioned by the semiconductor and ferroelectric properties of the new double samarium tellurites [11–13]. It is known that an abrupt transition is accompanied by a structure that provides an anomalously fast three-dimensional diffusion of cations [14]. Therefore we can state that these compounds have phase transitions. The curves of the temperature dependence of the permittivity of SmBaTeO$_{4.5}$ (Fig. 3) has a λ — shaped form, which corresponds, according to [15], a ferroelectric phase transition. It is known that the ferroelectric transition temperature (Curie temperature — T$_k$) for barium titanate BaTiO$_3$ is 406 K, and for polycrystalline ceramics of the perovskite group is in the range of 453–573 K [16]. This fact indirectly indicates that barium tellurite SmBaTeO$_{4.5}$ undergoes a ferroelectric phase transition.

Conclusions

For the first time, samarium oxotellurites SmMgTeO$_{4.5}$ and SmBaTeO$_{4.5}$ were synthesized using the ceramic technology method. Syngony types, unit cell parameters, X-ray and pycnometric densities were determined by X-ray phase analysis method. It was found that with an increase in the ionic radii from Mg to Ba, the lattice parameters of the synthesized tellurites increase.

We studied the temperature dependences of the permittivity and resistance of tellurites in the temperature range 293–483 K and calculated the band gap of the compounds.

Tellurites crystallize in the structural types of distorted perovskite P_m3_m and exhibit semiconductor and ferroelectric properties.

The results obtained can be used for predicting, synthesizing and studying new derivatives of tellurium and rare earth elements and are of interest for electronic technology. The synthesized samarium oxo tellurites can find application in the field of creating materials with ferroelectric properties.

References

1   Li, X., Zhao, H., Liang, J., Luo, Y., Chen, G., Shi, X., ... & Sun, X. (2021). A-site perovskite oxides: an emerging functional material for electrocatalysis and photocatalysis. *Journal of Materials Chemistry A*, *9*(11), 6650–6670. https://doi.org/10.1039/d0ta09756j

2   Zhu, J., Li, H., Zhong, L., Xiao, P., Xu, X., Yang, X., ... & Li, J. (2014). Perovskite oxides: preparation, characterizations, and applications in heterogeneous catalysis. *ACS Catalysis*, *4*(9), 2917–2940. https://doi.org/10.1021/cs500606g

3   Charkin, D.O., Grishaev, V.Y., Volkov, S.N. et al. (2020). Synthesis and Structure of New Rare Earth Cadmium Tellurite Halides. *Russ. J. Inorg. Chem., 65*, 466–471. https://doi.org/10.1134/S0036023620040038

4   Charkin, D.O., Volkov, S.N., Grishaev, V.Y., Dolgikh, V.A., Kuznetsov, A.N., Deyneko, D.V., ... & Aksenov, S.M. (2023). A new family of rare earth–strontium tellurite chlorides, $SrLn_4(TeO_3)_4Cl_6$ (Ln= Ce, Nd, Sm): Synthesis, crystal structures, possible polytypism, and crystal-chemical relationships. *Journal of Solid State Chemistry*, *320*, 123822. https://doi.org/10.1016/j.jssc.2022.123822

5   Orgel, L.E. (1959). The stereochemistry of B subgroup metals. Part II. The inert pair. *Journal of the Chemical Society (Resumed)*, 3815. https://doi.org/10.1039/jr9590003815

6   Bekturganova, A. Zh., Sagintayeva, Zh.I., Rustembekov, K.T., Kasenova, Sh.B., Kasenov, B.K. & Stoyev, M. (2017). Sintez i rentgenograficheskoe issledovanie novykh nikelito-telluritov $La_2MNiTeO_7$ (M — Mg, Ca, Sr, Ba) [Synthesis and X-ray study of new nickelite-tellurites $La_2MNiTeO_7$ (M — Mg, Ca, Sr, Ba)]. *Izvestiia Natsionalnoi akademii nauk Respubliki Kazakhstan. Seriia Khimiia i tekhnologiia — Proceedings of the National Academy of Sciences of the Republic of Kazakhstan. Chemistry and Technology Series, 2, 422*, 99–103 [in Russian].

7   Kivilis, S.S. (1959). *Tekhnika izmerenii plotnosti zhidkostei i tverdykh tel [Technique for measuring the density of liquids and solids].* Moscow: Standargiz [in Russian].

8   Rustembekov, K.T., Dyusekeyeva, A.T., Sharipova, Z.M. & Zhumadilov, Ye.K. (2009). Rentgenograficheskie, termodinamicheskie i elektrofizicheskie svoistva dvoinogo tellurita natriia-tsinka [X-ray, thermodynamic and electrophysical properties of double sodium-zinc tellurite]. *Izvestiia TPU — Bulletin of the Tomsk Polytechnic University.* 315, 3, 16–19 [in Russian].

9   Crystallography Open Database [http://www.crystallography.net/cod/result.php]

10 Venevtsev, Yu. N., Politova, Ye. D. & Ivanov, S. A. (1985). Segnetoelektriki i antisegnetoelektriki semeistva titanata bariia [Ferroelectric and antiferroelectrics of the barium titanate family]. Moscow: Khimiia [in Russian].

11 Ok, K.M. & Halasyamani, P.S. (2005). Mixed-metal tellurites: synthesis, structure, and characterization of $Na_{1.4}Nb_3Te_{4.9}O_{18}$ and $NaNb_3Te_4O_{16}$. *Inorganic chemistry*, *44*(11), 3919–3925.

12 Rustembekov, K. T. & Bekturganova, A. Z. (2017). X-ray diffraction and thermodynamic characteristics for tellurite of the composition Li_2CeTeO_5. *Russian Journal of Physical Chemistry A*, *91*, 622–626. https://doi.org/10.1134/SOO36024417040252

13 Rustembekov, K. T., Kasenov, B. K., Bekturganova, A. Z. & Kasymova, M. S. (2019). Thermodynamic and Electrophysical Properties of $La_2SrNiTeO_7$. *Russian Journal of Physical chemistry A*, *93*(9), 1657–1661. https://doi.org/10.1134/SOO36024419090206

14 Tretyakov, Yu.D. & Putlyayev, V.I. (2006). *Vvedenie v khimiiu tverdofaznykh materialov [Introduction to the chemistry of solid-phase materials].* Moscow: Nauka [in Russian].

15 Strukov, B.A. & Levantyuk, A.P. (1983). *Fizicheskie osnovy segnetoelektricheskikh yavlenii v kristallakh [Physical basis of ferroelectric phenomena in crystals].* Moscow: Nauka [in Russian].

16 *Khimicheskaia entsiklopediia [Chemical Encyclopedia]* (1995). Moscow: Bolshaia Rossiiskaia Entsiklopediia, 4, 308 [in Russian].

Information about authors[*]

Toibek, Aitolkyn Ablaikyzy — PhD student, Karagandy University of the name of academician E.A. Buketov, Universitetskaya street, 28, 100024, Karaganda, Kazakhstan; e-mail: aitoka_95@mail.ru; https://orcid.org/0000-0002-8616-5257;

Rustembekov, Kenzhebek Tusupovich (*corresponding author*) — Academician of Kazakhstan National Academy of Natural Sciences, Doctor of Chemical Sciences, Professor, Karagandy University of the name of academician E.A. Buketov, Universitetskaya street, 28, 100024, Karaganda, Kazakhstan; e-mail: rustembekov_kt@mail.ru; https://orcid.org/0000-0003-0853-523X;

Fomin, Vitaly Nikolaevich — Candidate of Chemical Science, Head, Laboratory of the engineering profile "Physical and chemical methods of research", Karagandy University of the name of academician E.A. Buketov, Universitetskaya street, 28, 100024, Karaganda, Kazakhstan; e-mail: vitaliynikolaevich.fomin@mail.ru; https://orcid.org/0000-0002-2182-2885;

Kaikenov, Dauletkhan Asanovich — PhD, Leading Researcher, Laboratory of the engineering profile "Physical and chemical methods of research", Karagandy University of the name of academician E.A. Buketov, Universitetskaya street, 28, 100024, Karaganda, Kazakhstan; e-mail: krg.daykai@mail.ru; https://orcid.org/0000-0003-4621-7603

_____

*The author's name is presented in the order: *Last Name, First and Middle Names.*

CHEMICAL TECHNOLOGY

Toufik Chouchane[1]* iD, Atmane Boukari[1], Ouahida Khireddine[1] iD,
Sana Chibani[1] iD, Sabiha Chouchane[2] iD

[1]Research Center in Industrial Technologies CRTI, Algiers, Algeria;
[2]Faculty of Sciences, Badji Mokhtar Annaba University, Annaba, Algeria
(*Corresponding author's e-mail: t.chouchane@crti.dz)

Cu(II) Removal from Aqueous Medium Using Blast Furnace Slag (BFS) as an Effective Adsorbent

The copper adsorption by blast furnace slag (BFS) in an aqueous medium was considered based on the influencing parameters, namely the agitation speed, pH, temperature, the particle size of the solid, and the initial concentration. Physicochemical studies have shown that BFS is consisted mainly from SiO_2, CaO, Al_2O_3, and MgO with a specific surface area of 238 m^2/g. Under the optimum parameters, the maximum adsorption amount at equilibrium (140 min) corresponds to 45.16 mg/g. Exploration of adsorption isotherms revealed that the Langmuir model is more consistent with the experimental data. The values of the Freundlich (*n*) and Langmuir (*RL*) parameters indicate that the adsorption is favorable. On the other hand, the values of Temkin (*bt*) and Redlich-Peterson (*g*) parameters show that adsorption is physical. Pseudo-second order of the adsorption process was confirmed using a kinetic study. Moreover, the diffusional study specified that the transfer of copper from the solution to BFS is successively controlled by external and intraparticle diffusion. The thermodynamic parameters showed that the adsorption of Cu(II) on BFS was feasible, spontaneous, exothermic, and less entropic. The desorption phenomenon has revealed that BFS can be reused for three consecutive cycles.

Keywords: blast furnace slag, copper, adsorption in batch mode, adsorption isotherm, adsorption kinetics, desorption, depollution.

Introduction

Water pollution by metal ions is one of the most undesirable environmental problems in the world that requires immediate solutions [1–4]. Indeed, with the multiplication of inhabitants, the expansion of urbanization, and the development of industries, natural water sites have become discharges of toxic industrial pollutants [5, 6]. For this reason, it is necessary to proceed with the elimination of toxic elements from water through reliable, efficient, and rigorous treatments such as membrane technology [7], chemical precipitation [8], ion-exchange [9] and adsorption [10]. Among these used processes, the adsorption phenomenon is often considered as the most optimal, since it is effective, easy to implement and less expensive [11, 12].

In this context, we set out to develop a simple and effective process of depollution by adsorption phenomenon. Blast furnace slag from the steel complex El-Hadjar Annaba, Algeria was chosen as a low-cost adsorbent. Besides, copper was chosen as the metal pollutant.

BFS is a by-product of the metallurgical steel industry resulting from the production of cast iron in blast furnaces. The annual production of slag in the world is very high, which constitutes a serious ecological problem and a loss of important financial resources [13].

According to the literature, slag and its derivatives as effective adsorbents have been the subject of many studies, especially in cases of the adsorption of metal ions [14, 15], phosphorus [16, 17] and dyes [18, 19]. Copper is reputed as a dangerous and toxic element, due to the fact that it accumulates over time and, in addition, is not biodegradable [20]. These parameters represent a significant risk factor for humans and their environment [21]. Therefore, its removal is inevitable and more than necessary. The presence of various adsorbents used in the process of copper removal in an aqueous medium is noted in the literature, namely carbon-based adsorbents [22], clay minerals [23], and agricultural adsorbents [24].

The main purpose of this study is the valorization of blast furnace slag in the field of adsorption of metal ions in solution. The slag treatment, the kinetic study, the adsorbate/adsorbent interaction, the nature of the process, and the desorption capacity will contribute to the evaluation of BFS as an adsorbent.

Analysis by XRF and XRD were used for the physicochemical characterization of the adsorbent. BET method was applied to measure the specific surface of BFS. The effect of various parameters, such as contact time, stirring speed, pH, temperature, particle size, and initial concentration, was examined to optimize the adsorption process. Adsorption isotherms were described by the Freundlich, Langmuir, Temkin, and Redlich-Peterson models. The adsorption kinetics was represented by the models of Lagergren and Blanchard. Also, the copper ions' transfer from the solution to the adsorbent was examined by determining the stages controlling the adsorption process. The thermodynamic study was undertaken to clarify the nature of the adsorption process as a function of temperature change.

Experimental

Blast furnace slag treatment

The samples of the considered slag were treated according to the process presented by Chouchane et al. [25]. This treatment was realized according to the following steps:
– Washing BF slag with distilled water;
– Air drying of samples for 48 hours;
– Grinding and sieving of samples to specific particle sizes, 200, 300, 400 and 500 μm;
– Separation of samples by diameter size;
– Washing with distilled water and stoving at 105 °C of each batch;
– Storage in plastic boxes.

Analytic methods

The copper ions were determined by atomic absorption spectrometry (Perkin Elmer 3110). The pH of the solution was measured with a pH meter (Ericsson). The characterization of the solid samples was carried out by X-ray fluorescence (Siemens SRS 3000), and scanning electron microscope combined with energy dispersive analysis (Zeiss EVO MA25). The specific surface of the solid samples was measured using the Brunauer, Emmett and Teller model (BET model).

Experimental protocol

Several discontinuous mode tests were applied to study the nature of the copper adsorption phenomenon on the BF slag. The adsorption process was carried out by adding 1 g of prepared BFS to a 1 liter aqueous solution containing copper ions. Copper solutions were prepared from copper nitrate ($Cu(NO_3)_2 \cdot 3H_2O$) then dissolved in bidistilled water. Mixing of the solution was provided by a multi-speed stirrer. The temperature of the solution was controlled by a thermometer and adjusted using a water bath. The kinetics of copper elimination was determined by taking 5 ml samples every 20 minutes with a pipette, and these samples were filtered through filter paper. The kinetics of copper elimination were examined according to the protocol proposed by Chouchane et al. [25].

The determining parameters used in this adsorption process are the initial concentration (C_0, mg/l), the agitation speed (V_{ag}, rpm), the hydrogen potential (pH), the temperature (T, °C), and the particle size ($\varnothing_S$, μm). Moreover, the solution volume (V, L) is 1 liter and the solid mass (M, g) is 1 g throughout the study. The experimental conditions used are as follows:
– Equilibrium time, C_0 = 30 mg/L; V_{ag} = 100 rpm; pH = 4.7; T = 20 °C; $\varnothing_S$ = 400 μm;

– Effect of agitation speed, $C_0 = 30$ mg/L; $V_{ag} = 50, 100, 150, 200$ rpm; pH = 4.7; $T = 20$ °C; $\emptyset s = 400$ µm;

– Effect of initial pH, $C_0 = 30$ mg/L; $V_{ag} = 150$ rpm; pH = 2; 3.9, 4.7, 5.2; T= 20 °C; $\emptyset_S = 400$ µm;

– Effect of temperature, $C_0 = 30$ mg/L; $V_{ag} = 150$ rpm; pH = 4. 20, 40, 50 °C; $\emptyset_S = 400$ µm;

– Effect of particles size, $C_0 = 30$ mg/L; $V_{ag} = 150$ rpm; pH = 4.7; $T = 20$ °C; $\emptyset_S = 200, 300, 400, 500$ µm;

– Effect of initial concentration, C_0, 10–100 mg/L; $V_{ag} = 150$ rpm; pH = 4,7; $T = 20$ °C; $\emptyset_S = 300$ µm.

The copper adsorption efficiency was calculated using Equation 1

$$\% R = \frac{C_0 - C_e}{C_0} \times 100, \tag{1}$$

where C_0 — the initial concentration solution (mg/L); C_e — the concentration of the solution at equilibrium (mg/L).

Desorption

The desorption process was performed using 10 g of the saturated BFS. The BFS collected by filter paper was washed, dried, and baked at 105 °C. Regeneration of saturated slag was accomplished using distilled water and different eluents, namely sulfuric acid (0.1N), nitric acid (0.1N), and hydrochloric acid (0.1N). Desorption was performed with stirring (100rpm) at room temperature. The efficiency of the desorption process was evaluated using Equation 2:

$$\text{Desorption rate} = \frac{q_{des}}{q_{ads}} \times 100, \tag{2}$$

where q_{ads} — the adsorbed quantity at equilibrium (mg/g) for cycle I; q_{ads} — the desorbed quantity at equilibrium (mg/g) of each cycle.

The experimental protocol for copper desorption from saturated BFS was applied according to the approach carried out by Chouchane et al. [25].

Results and Discussion

Characterization of BF slag

According to our previous work [25] and subsequent recent analyses, BFS consists of silica (37.16 %), lime (40.11 %), alumina (14.34 %), magnesium oxide (5.34 %), and a low percentage of oxides. Indeed, the results of the analyses carried out by XRF, XRD, and SEM-XDE specified that BFS consists mainly of SiO_2, CaO, Al_2O_3, and MgO. These studies also revealed the presence of a small amount of oxides, namely Fe_2O_3, MnO, K_2O, and Na_2O, as shown in Table 1 and Figures 1 and 2. BFS grains were found to be conchoidal in shape, with a wide grain size distribution, smooth surfaces of the grain edges visible, and no visible porous structure in the images shown in Figure 3. According to the research results the specific surface was shown to be 238 $m^2.g^{-1}$.
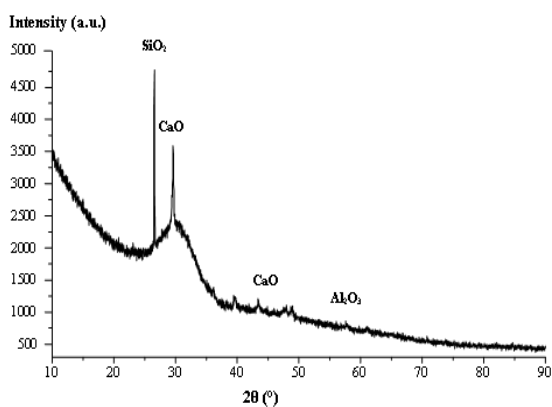


Figure 1. Diffractogram of BFS sample [25]
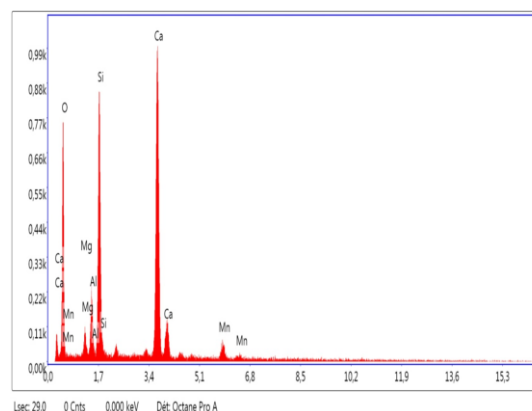
Figure 2. EDX results
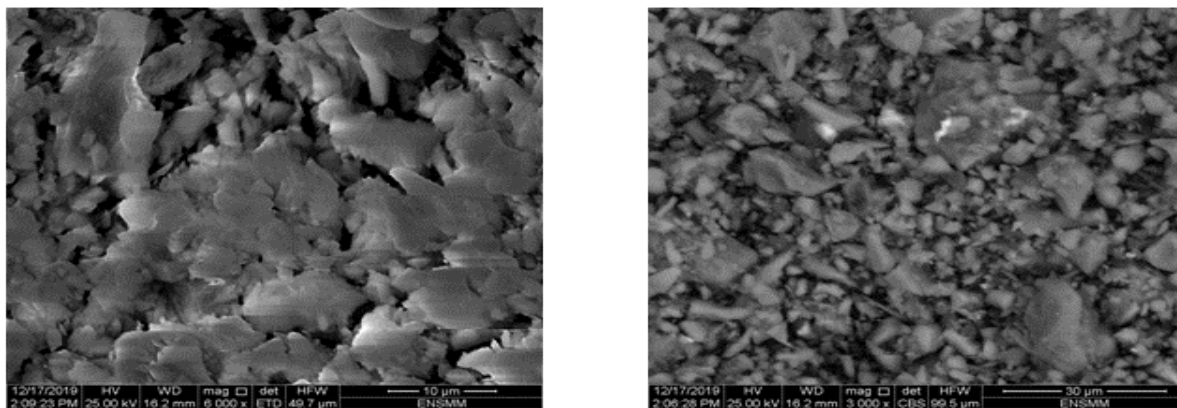
Figure 3. SEM images of BFS

Contact time effect

In the adsorption process, the contact time effect is a determining factor because it informs us about the equilibrium time and the stages of pollutant removal. The kinetic study of the copper adsorption on BFS showed that equilibrium is reached after 140 minutes of stirring under specific experimental conditions (Fig. 4). Indeed, the adsorbed amount becomes constant (C_e/C_0 = constant) after 140 minutes of stirring. This effect is regenerated due to the progressive reduction of active adsorption sites until total saturation of the adsorbent [26]. This finding prompted us to take 140 min as equilibrium contact time.

T a b l e 1

Composition of blast furnace slag (BFS) [25]

| Substance	% mass
CaO	40.11
Al_2O_3	14.34
SiO_2	37.16
MgO	5.34
Fe_2O_3	1.91
MnO	0.69
K_2O	0.28
Na_2O	0.37
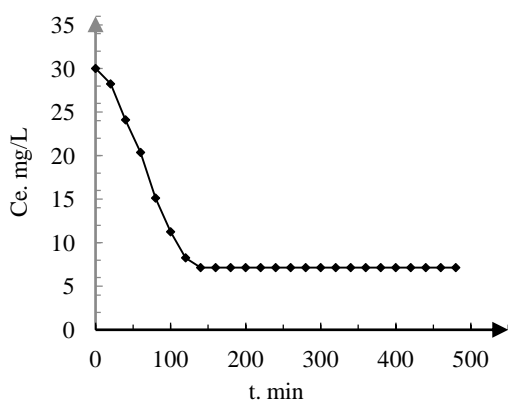
Figure 4. Contact time effect
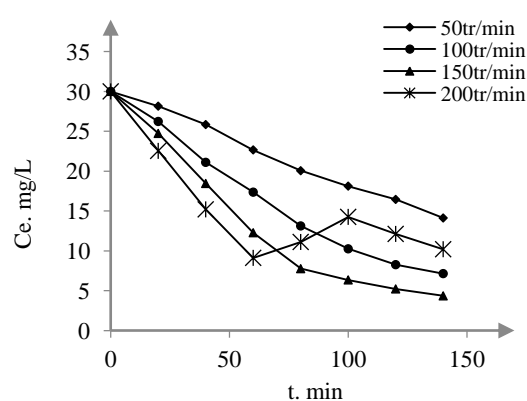
Figure. 5. Effect of agitation speed

Agitation speed effect

Agitation of the solution is an extremely decisive operation in adsorption processes. In fact, it favors the diffusion of the adsorbate toward the solid [27, 28]. Stirring speeds utilized were 50, 100, 150, and 200 rpm, respectively (Fig. 5).

Figure 5 shows that the amount of copper adsorbed by BFS gradually increased with increasing stirring speed until it reached 150 rpm. However, fluctuations in the value of the residual concentration after 80 minutes of agitation were noticed at 200 rpm. These fluctuations are probably caused by copper desorption from the BFS after strong agitation [29]. Based on this outcome, we conclude that the solution stirring contributed effectively to the diffusion of copper ions from the solution into the adsorbent, which gives it an important role in external diffusion [30]. In addition, we identified 150 rpm as the optimal agitation speed.

Effect of initial solution pH

The pH of the medium is a significant element in this process, since it affects both the shape of the ions and the surface of the adsorbent [31]. Several media were used during these experimental tests, namely pH 2, pH 3.9, pH 4.7, and pH 5.2 (Fig. 6).

Experimental data showed that Cu(II) adsorption is unfavourable at pH 2 (Fig. 6). This phenomenon is explained by the presence of H^+ protons, which obstruct the adequate transfer of Cu(II) ions from the solution to the adsorbent [32]. Moreover, a change in pH from 2 to 4.7 had a positive effect on the adsorption process [33], where we observed that the residual concentration at equilibrium decreased from 19.87 mg/L to 4.35 and the removal rate increased from 33.7 % to 85.5 %.

For solutions at pH 5.2, the values of the capacity and adsorption rate are less important and regressed from 25.67 to 18.11 mg/g and from 85.5 to 60.36 % respectively. This result could be explained by the fact that precipitation dominates the removal of the copper and adsorption has an almost negligible effect [34]. It is important to note that the pH threshold for Cu^{2+} speciation into hydroxides is approximately 5.0–5.5 [35].
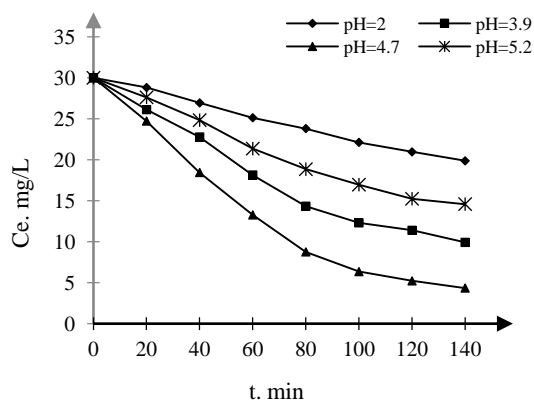

Figure 6. Effect of initial pH
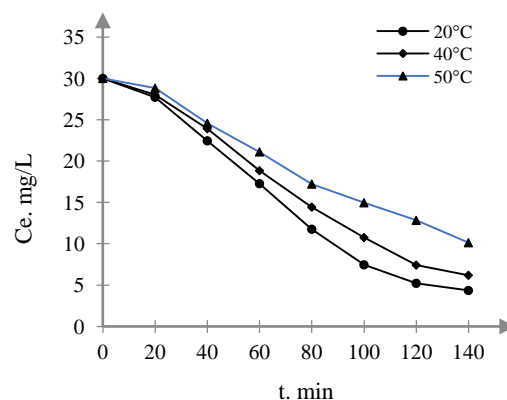
Figure 7. Effect of temperature

Effect of Temperature

The temperature of the solution is an important characteristic in the adsorption process, since it makes a huge contribution to the fixation of metals on the surface of a solid [36]. For this purpose, the effect of temperature on the Cu(II) adsorption process on BFS was studied (Fig. 7).

The experimental data revealed that the temperature has an inversely proportional effect on the Cu(II) adsorption process and this phenomenon is more favorable at 20 °C (Fig. 7). This result allowed us to predict that the copper adsorption on BFS in solution is exothermic [37]. The inefficiency of the copper adsorption process as temperature rises is most likely due to the destruction of active binding adsorption sites [38] or the reduction in attractive Cu(II)/BFS bonds [39]. Furthermore, evaporation of the solution can occur at high temperatures, which affects the concentration of Cu(II) ions in the solution.

Effect of the granulometry of the solid

The granulometry of the adsorbent has a significant effect on the rate of ion transfer from the adsorbate to the solid [40]. In this perspective, we proceeded to evaluate the effect of particle size on copper adsorption using different diameters, namely 200, 300, 400, and 500 μm (Fig. 8).

From the kinetic study, it was observed that copper adsorption is better for particles with sizes corresponding to 300 μm and begins to weaken with increasing particle size. Indeed, the adsorption yield decreased from 91.73 % to 85.5 % and then to 70.5 % as the size of the particles widened. An increase in particle size led to a narrowing of the specific surface area, which in turn led to a decrease in the adsorption capacity of the solid [41, 42]. The experimental results also showed that the copper adsorption on the BFS with

a diameter of 200 μm is estimated as unfavourable (Fig. 8). This repercussion could probably be clarified by the appearance of the coalescence phenomenon [43].

Effect of the initial solution concentration

The elimination of copper on BFS under the effect of the initial concentration [10-100 mg/L] was studied under our experimental conditions, namely $V_{ag} = 150$ rpm; pH = 4.7; Ø = 300 μm, $T = 20$ °C. Maximum adsorption capacity at equilibrium was calculated using Equation 3:

$$q_e = \frac{C_0 - C_e}{m} \times V, \tag{3}$$

where C_0 — the initial solution concentration (mg/L); C_e — the solution concentration at equilibrium (mg/L); m — the adsorbent mass (1 g); V — the solution volume ($V = 1$ L).

The dependence of the adsorbed capacity (q_e) on the initial concentration (C_0) is shown in Figure 9. As can be seen in Figure 9, the adsorbed amount increased in proportion the initial concentration up to a certain amount ($C_0 = 80$ mg/L), after which the adsorbed amount remained constant. Indeed, with an increase in the concentration of the initial solution, the probability of BFS/Cu(II) contact rises, which contributes to an increase in the adsorbed amount. But once the adsorption sites are saturated, the increase in the initial concentration could not affect the adsorption process [44, 45]. The amount adsorbed (q_e) at the saturation level is 45.16 mg/g, which represents the maximum capacity adsorbed by 1 g of BFS.

Based on these results, we concluded that the sorption rate is controlled by the initial concentration, which varies from 10 to 80 mg/L. On the other hand, the maximum amount adsorbed per gram of BFS is 45.16 mg/g.
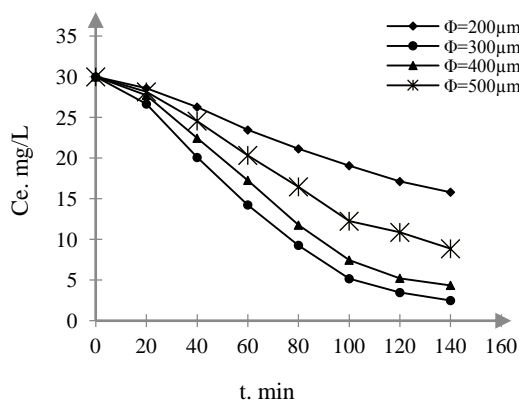
Figure 8. Effect of the granulometry of the solid
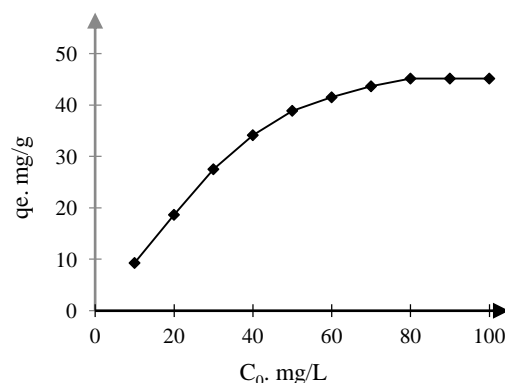
Figure 9. Effect of initial concentration

Adsorption isotherms

In order to study the correlation between adsorbent and adsorbate and determine the best adopted presentation for the experimental data, we applied the adequate adsorption isotherms, namely Freundlich [46], Langmuir [47], Temkin [48] and Redlich-Peterson [49]. Their empirical formulas are given by Equations 4-7, respectively.

$$\ln q_e = \ln k + \frac{1}{n} \ln C_e; \tag{4}$$

$$\frac{C_e}{q_e} = \frac{1}{q_{max}} C_e + \frac{1}{q_{max} b}; \tag{5}$$

$$q_e = B_T \ln A_T + B_T \ln C_e; \tag{6}$$

$$\ln \frac{C_e}{q_e} = g \ln C_e - \ln k_R, \tag{7}$$

where q_e — the adsorbed capacity at equilibrium (mg/g); C_e — the concentration of solution at equilibrium (mg/L); q_{max} — the maximum adsorbed capacity (mg/g); b — the thermodynamic constant of the adsorption equilibrium (L·mg^{-1}); k_F and $1/n$ — the Freundlich constants related to adsorption and affinity; A_T — Temkin isotherm equilibrium binding constant (L/g); b_T — Temkin isotherm constant; R — the universal gas

constant (8.314 J/K·mol); T — the temperature (298K); B_T — the constant related to heat of sorption (KJ·kmol^{-1}); k_R — the intercept (L/g); g — the Redlich-Peterson isotherm constants.

The parameter values of the Freundlich, Langmuir, Temkin, and Redlich-Peterson models are grouped in Table 2. The presentations of these models are sequentially shown in Figures 10 to 13.

As can be seen from the data presented in Table 2, the Langmuir's model is best suited for this process. Indeed, the correlation coefficient of the Langmuir model ($R^2 = 0.99$) is higher than those of all other considered models. Moreover, the adsorbed capacity measured from the Langmuir model was closest to the experimental adsorption value.

Based on these results, it was confirmed that the adsorption process takes place on a homogeneous monolayer surface. This leads us to specify that all active sites of adsorption have similar interactions with copper [47].

Figure 14 shows that the adsorption isotherm is L-type, undergoes a fast phase in the low concentration range, is followed by a medium-weak phase, and ends with a phase constant (the appearance of a long horizontal plateau). This identification provides information about the formation of a monolayer [6, 26]. In the same context, Chouchane et al. [25] reported that the adsorption of nickel on the blast furnace slag was accomplished on a homogeneous monolayer. Zahar, M.M.S., Muhammad, S.N. et al. also stated in [50] that the manganese sorption in solution on steel slag occurred on a homogeneous monolayer layer.
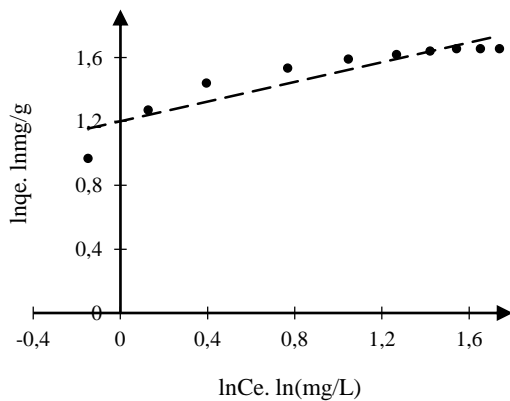
Figure 10. Presentation of the Freundlich model
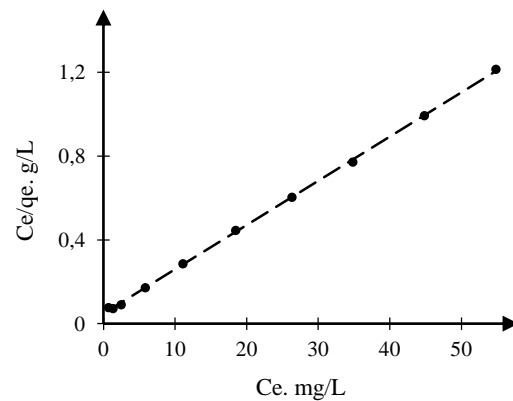
Figure 11. Presentation of the Langmuir model
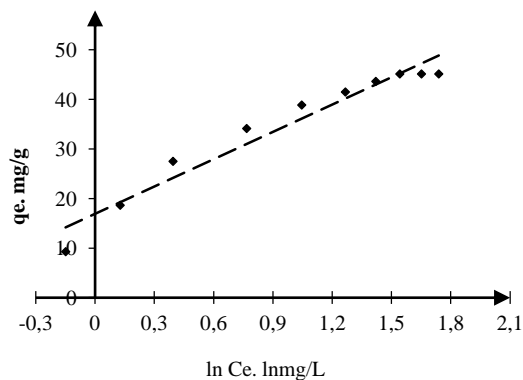
Figure 12. Presentation of the Temkin model
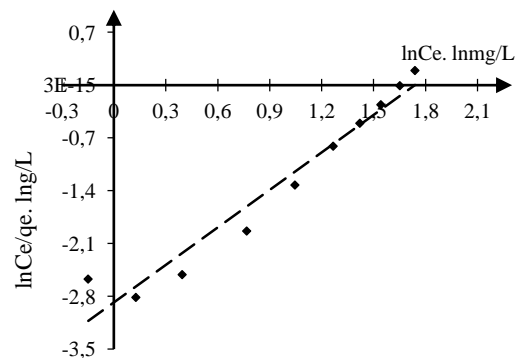
Figure 13. Presentation of the Redlich-Peterson model

According to the value of the Temkin model parameter ($b_t = 0.261$), we conclude that the adsorption of copper on BFS in solution is physical [25]. On the other hand, the parameter values of the Freundlich ($n = 3.7$) and Redlich-Peterson ($g = 0.68$) models confirm that this adsorption process is favorable [1, 20, 44, 49].

The quality of the adsorption process can also be defined by the Equilibrium parameter of Langmuir equation R_L. The R_L qualifies the adsorption process as favorable if it is between 0–1 ($0 < R_L < 1$), unfavora-

ble if it is greater than 1 ($R_L > 1$) and linear if it is equal to 1 ($R_L = 1$) [51]. This ratio was calculated as follows (Equation 8):

$$R_L = \frac{1}{1 + C_0 b},$$ (8)

where R_L — the Ratio indicates the quality of the adsorption; B — the Langmuir isotherm constant; C_0 — the initial solution concentration.

As can be seen from Figure 15, the R_L value decreases from 0.18 to 0.02 as C_0 increases. This result also confirmed the favorable nature of copper adsorption by BFS.

Table 2

Isotherm parameters for adsorption of copper by BF slag

Models	Parameters			
Freundlich	qe_{exp}, mg/g	K_F, (mg·g^{-1})(ml·mg^{-1})$^{1/n}$	n	R^2
	45.16	0.183	3.25	0.836
Langmuir	qe_{exp}, mg/g	q_{max}, mg/g	B, L·mg^{-1}	R^2
	45.16	46.31	0.437	0.997
Temkin	qe_{exp}, mg/g	A_T, L/g	b_T, KJ·mol^{-1}	R^2
	45.16	1.06	0.214	0.944
Redlich-Peterson	qe_{exp}, mg/g	g	k_R, L/g	R^2
	45.16	0.651	17.77	0.993
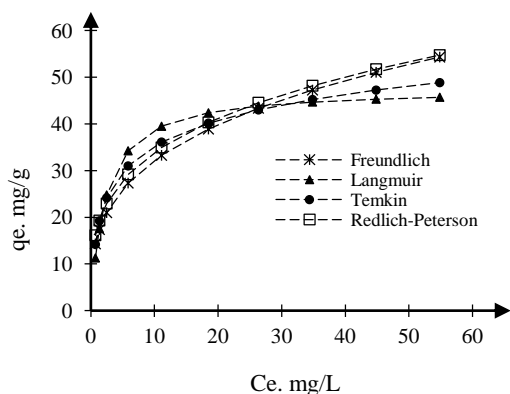
Figure 14. Presentation of the Freundlich model
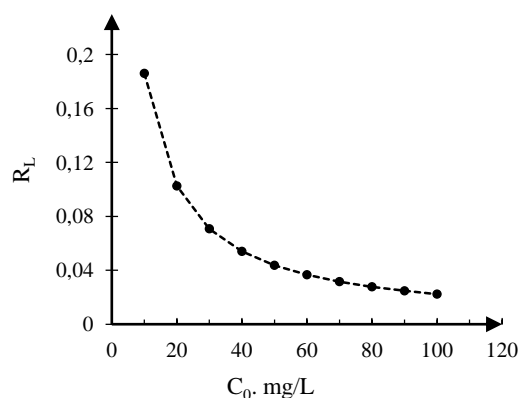
Figure 15. Presentation of the Langmuir model

Adsorption Kinetics

The kinetic study is a significant step in the solid-liquid adsorption process because it facilitates the understanding of the adsorption rate and the behavior of the adsorbents compared to the adsorbates at time t and at equilibrium [52]. The pseudo first and pseudo-second orders were determined under optimal conditions by the frequently used kinetic models, namely the Lagergren and Blanchard models, respectively.

The Lagergren relationship [53] was formulated to illustrate sorption kinetics in a liquid-solid environment. Its relation is represented by Equation 9:

$$\log(q_e - q) = -k_L t + \log q_e.$$ (9)

Blanchard's model [54] was formulated to describe the pseudo-second order of the adsorption process. It is represented by Equation 10:

$$\frac{t}{q} = \frac{1}{k_b q_e^2} + \frac{t}{q_e},$$ (10)

where q_e — the adsorbed capacity at equilibrium (mg/g); q — the adsorbed capacity at time t (mg/g); k_L — the constant of Lagergren model (min^{-1}); k_b — the constant of Blanchard model (g/mg·min); t — the time of adsorption process (min).

The parameters of the Lagergren and Blanchard models are represented in Table 3. These two models are shown graphically in Figures 16 and 17.

From the literature, the Lagergren and Blanchard models are satisfied (if the R^2 correlation coefficients are greater than 0.9, and the experimental and calculated adsorption capacities are close [34, 35, 55, 56].

As can be seen in Table 3, the correlation coefficient of the Blanchard model (0.988) is higher than that of the Lagergren model (0.912), and the experimental adsorption capacity (45.16 mg/g) was close to that calculated per the Blanchard equation (45.88 mg/g). This result indicates the existence of a proportionality between the adsorption active sites and the adsorbed copper ions, which is compatible with the pseudo-second-order model. The pseudo-first-order model with the lowest regression ($R^2 = 0.912$) indicates that adsorption can occur on a monolayer surface, which reaffirms our previous results, namely that the Langmuir model is best suited to the process of copper adsorption on slag [57].
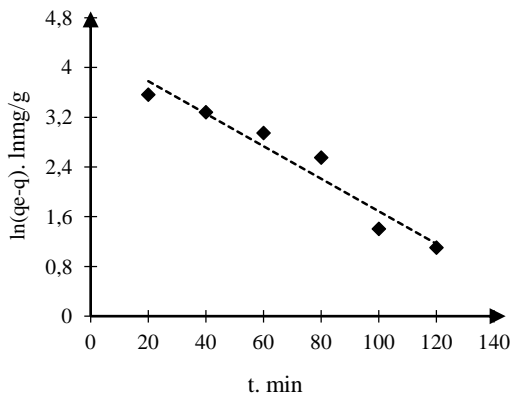
Figure 16 Pseudo-first order kinetic
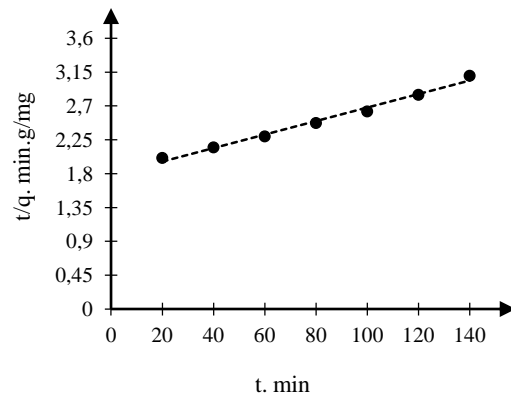
Figure 17 Pseudo-second order kinetic

Based on these results, it was concluded that the Blanchard model is best suited to describe the kinetics of copper adsorption on BFS. In the same context, Xue et al. [34] reported that copper removal from basic oxygen furnace slag follows pseudo-second order kinetics. Chouchane et al. [25] also indicated that the adsorption of nickel on the slag at different temperatures follows the kinetics of the pseudo-second order.

In order to study the mechanism of the transfer of copper ions from the solution to the surface of the BFS, we tried to identify the limiting stages of this phenomenon, namely the external and the Intraparticle diffusion.

External diffusion is represented by Equation 11 [58]:

$$\ln C_e = k_{ext} t + C_{ext}, \tag{11}$$

where C_e — the concentration of solution at equilibrium (mg/L); t — the time measured in minute; k_{ext} — the diffusion constant (min^{-1}); C_{ext} — the intercept (ln(mg/L).

According to the bibliography, copper adsorption is controlled by external diffusion if the plot of the function $\ln C_e = f(t)$ is linear and also if the correlation coefficient is greater than 0.9 [35, 59]. As can be seen from Table 5 and Figure 18, the plot is linear and the correlation coefficient exceeds 90 % ($R^2 = 0.99$). This result shows that the adsorption of copper by the blast furnace slag is controlled by external diffusion.

The Weber-Morris model equation (internal diffusion) is represented below (Equation 12) [60]:

$$q = k_w (t)^{1/2} + C_{int}, \tag{12}$$

where q — the quantity adsorbed at time t (mg/g); t — the time measured in minute; k_w — the diffusion rate constant in the pores (mg/m·min$^{1/2}$); C_{int} — the intercept and it's tied to the boundary layer.
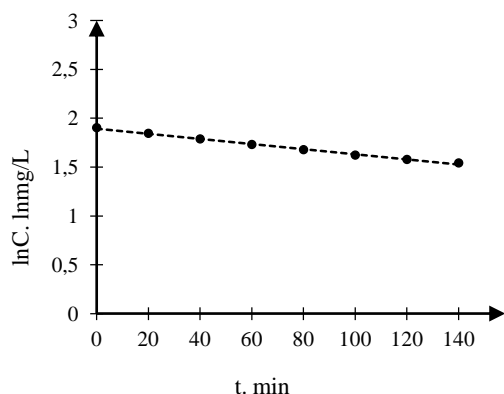
Figure 18. External diffusion kinetic
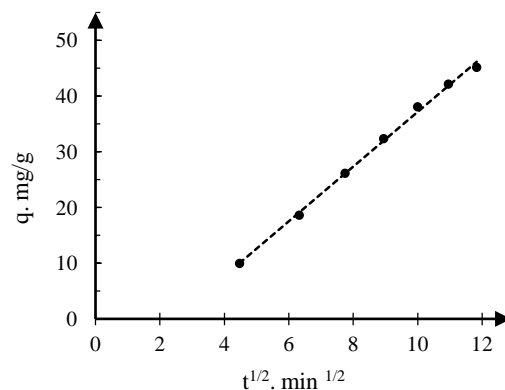
Figure 19. Intra-particle diffusion kinetic

The parameters of Weber-Morris model are presented in Table 3 and the graphic representation is illustrated in Figure 19. It is known from previous studies that the adsorption process is controlled by internal diffusion if the plot of the function $q_e = f\left(t^{1/2}\right)$ is linear and passes through the origin [1, 26, 61].

As can be seen in Figure 19, the plot of the function $q_e = f\left(t^{1/2}\right)$ is multilinear, but does not pass through the origin ($C \neq 0$), which means that internal diffusion is not the only mechanism controlling copper adsorption kinetics. Furthermore, multi-linearity argues for the existence of various mechanisms controlling the adsorption process, which reaffirms our inference that copper adsorption by BFS is controlled by both external and internal diffusion [25, 62, 63].

T a b l e 3

Kinetic model parameters

Models	Parameters			
Lagergren	qe_{exp}, mg/g	K_{lag}, min^{-1}	qe_{theo}, mg/g	R^2
	45.16	2.9×10^{-2}	50.58	0.912
Blanchard	qe_{exp}, mg/g	K_b, g/mg min	qe_{theo}, mg/g	R^2
	45.16	1.8×10^{-3}	45.88	0.988
Internal diffusion	qe_{exp}, mg/g	C_{int}	k_w, mg/g.min	R^2
	45.16	11.97	4.31	0.995
Internal diffusion	qe_{exp}, mg/g	C_{ext}	K, min^{-1}	R^2
	45.16	1.86	0.02	0.998

Thermodynamic study

Under the effect of the temperature of the solution and the conditions of the experiment, a thermodynamic study was carried out to give a more detail about the character of the copper adsorption process. Parameters such as free enthalpy variation (ΔG_0), enthalpy change (ΔH^0) and entropy change (ΔS^0) were determined to define the nature of the adsorption process. These variables were determined from the following equations (Equations 13–15):

$$\Delta G^0 = -RT \ln k_d ; \tag{13}$$

$$\Delta G^0 = \Delta H^0 - T\Delta S^0 ; \tag{14}$$

$$\ln k_d = \frac{\Delta H^0}{R} \times \frac{1}{T} + \frac{\Delta S^0}{R} . \tag{15}$$

The distribution coefficient k_d was calculated from the ratio of the adsorbed quantity to the residual concentration at equilibrium [59, 64]:

$$k_d = \frac{C_i - C_e}{C_e} \times \frac{V}{M} = \frac{q_e}{C_e} , \tag{16}$$

where q_e — the adsorbed quantity at equilibrium (mg/g); C_i — the initial concentration of solution (mg/L); C_e — the residual concentration at equilibrium (mg/L); T — the absolute temperature (K); R — the universal gas constant; k_d — the distribution coefficient (L/g); V — the volume of solution (1 L); M — the mass of the adsorbent (1g).

The plot of the function $\ln k_d = f\left(\dfrac{1}{T}\right)$ at different temperatures is presented in Figure 20. The thermodynamic parameter values are grouped in Table 4.

Initially, it was observed that the adsorption efficiency was inversely proportional to the temperature, as presented in Figure 7. This result led us to predict that the nature of the adsorption process is exothermic. Following the thermodynamic study, this prediction was verified by the negative value of ΔH^0 displayed in Table 3 [20, 25, 65].

Table 4 also shows that the values of ΔG^0 and ΔS^0 are negative. Negative values of ΔG^0 inform us about the spontaneity and feasibility of the adsorption process [6, 66, 67]. Furthermore, the negative value of ΔS^0 informs us about the decrease in the randomness of copper adsorption at the solid/solution interface [6, 57, 68]. Indeed, this weakening in randomness is probably due to the structural stability of BFS during the adsorption process.

It was also observed from Table 4 that the absolute value of the Gibbs free energy increased with increasing temperature. This effect indicates that higher temperatures help to increase the driving force of adsorption [69]. It was found from Figure 20 that the distribution coefficient k_d decreases with increasing temperature. This result points out that the high-temperature adsorption process is less efficient [59].
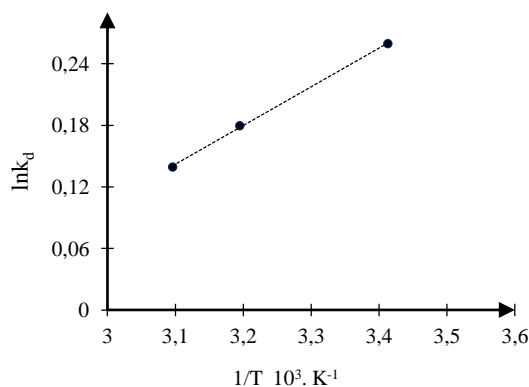
Figure 20. Van't Hoff plot for copper adsorption

T a b l e 4

Thermodynamic parameters of the copper adsorption on BFS

T, K	$\Delta G°$, kJ/mol	$\Delta H°$, kJ/mol	$\Delta S°$, J/mol·K)
293	−17.45		
313	−18.42	−3.13	−8.54
323	−18.92		

Desorption study

The desorption of the copper ions from the charged BFS is a very important process since it allows us to reuse the same adsorbent and avoids the storage of another type of pollution [1, 3]. For this study, we performed desorption of the Cu(II) adsorbed on the loaded BFS in various solutions.
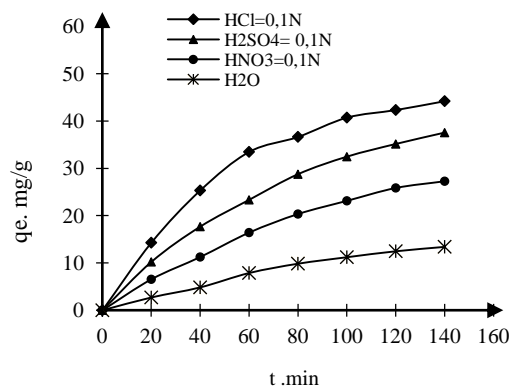
Figure 21. Desorption kinetics
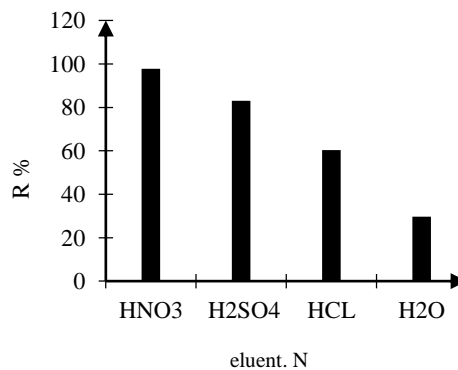
Figure 22. Desorption rate (%)

The kinetics of Cu(II) desorption, as well as the effects of the solutions used, are depicted in Figures 21 and 22. Table 5 shows the results of the various cycles used (adsorption and desorption).

Table 5

Adsorption and desorption performance of copper

	qe_{ads}, mg/g	qe_{des}, mg/g	Desorption rate, %
Cycle I	45.16	44.19	97.85
Cycle III	42.64	39.93	93.64
Cycle V	38.36	35.11	91.52
Cycle VI	32.18	22.27	69.2
Cycle VII	20.14	7.15	35.5

The results of the experiments revealed that desorption of Cu(II) from the surface of saturated BFS is more efficient with 0.1N HCl. Indeed, as can be seen in Figure 22, the desorption rates were 98.91 %, 84.19 %, 70.64 %, and 27.34 % in the presence of HCl, H_2SO_4, HNO_3, and H_2O respectively. Consequently, hydrochloric acid (HCl, 0.1 N) was retained as the regeneration eluent.

Based on the data in Table 5, it was found that the blast furnace slag as an adsorbent could be exploited over three consecutive cycles where the adsorption rate is greater than 91 %. However, a glaring regression was displayed for the last two cycles. This alteration is certainly caused by the loss of mass and/or the deterioration of the surface of the adsorbent used [26, 58, 69].

Conclusions

In general, based on the results of the study, it can be concluded that the adsorption of copper on the blast furnace slag is feasible and favorable with a yield of 91.7 %. The physicochemical analysis indicated that blast furnace slag mainly consists of lime, silica, alumina, and magnesium oxide, with a moderately high specific surface (238 m²/g). Experimental data showed that the maximum adsorption capacity is 45.16 mg/g after 140 minutes under the optimal conditions, namely: V_{ag} = 150 rpm; pH = 4,7; $\varnothing_S$ = 300 μm, T = 20 °C, M_S = 1 g. Modeling of the experimental data revealed that the copper adsorption process is more consistent with Langmuir's model (R^2 = 0.99). Adsorption is best described by the pseudo-second order kinetics model, with a correlation coefficient of 0.99. The adsorption mechanism was studied, and it was discovered that the adsorption process is physical, with copper diffusion from solution toward the adsorbent controlled by external and internal diffusion in sequential order. The thermodynamic study demonstrated that the adsorption process is feasible, exothermic, spontaneous, and has less entropy. The executed desorption process indicated that the BFS can be effectively regenerated over three consecutive cycles in the presence of hydrochloric acid (HCl, 0.1 N) as an eluent. Based on the data obtained, it can be concluded that adsorption on the BFS will be an effective outcome in toxic metal elimination processes.

References

1 Çelebi, M. & Gökirmak Söğüt, E. (2022). High-efficiency removal of cationic dye and heavy metal ions from aqueous solution using amino-functionalized graphene oxide, adsorption isotherms, kinetics studies, and mechanism. *Turkish Journal of Chemistry*, *46*, 1577–1593. https://doi.10.55730/1300-0527.3462

2 Yan, X, Wang, J., Zhu, L., Wang, J., Li, S. & Kim, M. (2021). Oxidative stress, growth inhibition, and DNA damage in earthworms induced by the combined pollution of typical neonicotinoid insecticides and heavy metals. *Science of the Total Environment*, 754. https://doi.10.1016/j.scitotenv.2020.141873.

3 Asliyüce Çoban, S., Safarik, I. & Denizli, A. (2021). Heavy metal removal with magnetic coffee grain. *Turkish Journal of Chemistry, 45*, 157–166. https://doi.10.3906/kim-2006-47

4 Amin, A, Shima, S, Hafez, W. & Desouky, O. (2021). Biorecovery of Cupper (II) using Klebsiella pneumoniae Isolated from Wastewater Effluents. *Egyptian Journal of Chemistry, 64*, 6623–6633. https://doi.10.21608/EJCHEM.2021.78714.3847

5 Ayandiran, T.A., Fawole, O.O. & Dahunsi, S.O. (2018). Water quality assessment of bitumen polluted Oluwa River. South-Western Nigeria. *Water Resources and Industry, 19*, 13–24. https://doi.10.1016/j.wri.2017.12.002

6 Tunçeli, A., Ulaş, A., Acar, O. & Türker, A.R. (2022). Adsorption isotherms, kinetic and thermodynamic studies on cadmium and lead ions from water solutions using Amberlyst 15 resin. *Turkish Journal of Chemistry, 46*, 193–205. https://doi.10.3906/kim-2107-28

7 Kanagaraj, P., Nagendran, A., Rana, D., Matsuura, T., Neelakandan, S., Karthikkumar, T. & Muthumeenal, A. (2015). Influence of N-phthaloyl chitosan on poly (etherimide) ultrafiltration membranes and its application in biomolecules and toxic heavy metal ion separation and their antifouling properties. *Applied Surface Science*, *329*, 165–173. https://doi.10.1016/j.apsusc.2014.12.082

8 Luo, J.M., Tao, X.Y., Zhang, J., Xia, Y., Huang, H., Zhang, L.Y., Gan, Y.P., Liang, C. & Zhang, W.K. (2016). Sn^{4+} ion decorated highly conductive Ti_3C_2MXene, promising lithium-ion anodes with enhanced volumetric capacity and cyclic performance. *ACS Nano*, *10*, 2491–2499. https://doi.10.1021/acsnano.5b07333

9 Dabrowski, A., Hubicki, Z., Podkoscielny, P. & Robens, E. (2004). Selective Removal of the Heavy Metal Ions from Waters and Wastewaters by Ion-exchange Method. *Chemosphere*, *56*(2), 91–106. https://doi.10.1016/j.chemosphere.2004.03.006

10 Ma, H.F., Yang, J., Gao, X, Liu, Z., Liu, X. & Xu, Z. G. (2019). Removal of chromium (VI) from water by porous carbon derived from corn straw, influencing factors, regeneration and mechanism. *Journal of Hazardous Materials*, *369*, 550–560. https://doi.10.1016/j.jhazmat.2019.02.063

11 Kaprara, E., Tziarou, N., Kalaitzidou, K., Simeonidis, K., Balcells, L., Pannunzio, E.V., Zouboulis, A. & Mitrakas, M. (2017). The use of Sn(II) oxy-hydroxides for the effective removal of Cr(VI) from water, optimization of synthesis parameters. *Science of The Total Environment*, 605–606, 190–198. https://doi.10.1016/j.scitotenv.2017.06.199

12 Guerra, E.R., Aristizabal, J., Arce, B., Zurob, E., Dennett, G., Fuentes, Ro., Suescún, A.V., Cardenas, L., Rodrigues da Cunha, T.H., Cabezas, R., García-Herrera, C. & Parra, H.C. (2021). Nanostructured Didymospheniageminata-based membrane for efficient lead adsorption from aqueous solution. *Journal of Environmental Chemical Engineering*, *9*(4), 105269. https://doi.org/10.1016/j.jece.2021.105269

13 Yusuf, M., Chuah, L., Khan, M.A. & Choong, T.S. (2014). Adsorption of Nickel on Electric Arc Furnace Slag, Batch and Column Studies. *Separation Science and Technology, 49*(3), 388–397. https://doi.10.1016/j.jece.2021.105269

14 Zhou, H., Ai J., Gao, H., Zhang, W. & Wang, D. (2020). Removal of arsenic in groundwater using Slag based calcined layered double hydroxides (CLDHs) with dual functions of adsorption and photo-catalysis. Colloids and Surfaces A. *Physicochemical and Engineering Aspects*, *604*, 125300. https://doi.10.1016/j.colsurfa.2020.125300

15 El-Dars, F.MS.E., Elngar, M.A.G., Abdel-Rahim, S.Th, El-Hussiny, N.A. & Shalabi M.E.H. (2015). Kinetic of nickel (II) removal from aqueous solution using different particle size of water-cooled blast furnace slag. *Desalination and Water Treatment*, *54*, 769–778. https://doi.10.1080/19443994.2014.904071

16 Vu, M.T., Nguyen, L.N, Johir, M.A.H, Ngo, H.H., Skidmore, C. Fontana, A., Galway, B., Bustamante, H. & Nghiem, L. D. (2020). Phosphorus removal from aqueous solution by steel making slag — Mechanisms and performance optimization. *Journal of Cleaner Production*, 284, https://doi.10.1016/j.colsurfa.2020.125300

17 Scott, I.S.P.C. & Penn, J.C. (2021). Estimating the variability of steel slag properties and their influence in phosphorus removal ability. *Chemosphere*, 276, 130205. https://doi.10.1016/j.chemosphere.2021.130205

18 Xue, Y., Hou, H. & Zhu, S. (2009). Adsorption removal of reactive dyes from aqueous solution by modified basic oxygen furnace slag, Isotherm and kinetic study. *Chemical Engineering Journal*, *147*, 272–279. https://doi.10.1016/j.cej.2008.07.017

19 Dhmees, AS., Khaleel, N. M. & Mahmoud, S.A. (2018). Synthesis of silica nanoparticles from blast furnace slag as cost-effective adsorbent for efficient azo-dye removal. *Egyptian Journal of Petroleum*, *27*(4), 1113–1121. https://doi.10.1016/j.ejpe.2018.03.012

20 Donat, R. (2022). Removal of Cd^{2+} metal ions from aqueous solutions by Na-alginate-containing composite biosorbent. *Turkish Journal of Chemistry*, *46*, 754–765. https://doi.10.55730/1300-0527.3365

21 Shotop, M.Y. & Al-Suwiti, I.N. (2021). The possible role of vitamins E and C in reducing the toxicity of copper nanoparticles in the kidney and liver of the rats (Rattusnorvegicus*). Journal of King Saud University-Science*, *33*(2), 101357. https://doi.10.1016/j.jksus.2021.101357

22 Tauetsile, P.J., Oraby, E.A. & Eksteen, J.J. (2018). Adsorption behaviour of copper and gold Glycinates in alkaline media onto activated carbon. Part 2, Kinetics. *Hydrometallurgy*, *178*, 195–201. https://doi.10.1016/j.hydromet.2018.04.016

23 Ben Ali, M., Wang, F., Boukherroub, R., Lei, W. & Xia, M. (2019). Phytic acid-doped polyanilinenanofibers-clay mineral for efficient adsorption of copper (II) ions. *Journal of Colloid and Interface Science*, *553*, 688–698. https://doi.10.1016/j.jcis.2019.06.065

24 Bashir, M., Tyagi, S. & Annachhatre, A.P. (2020). Adsorption of copper from aqueous solution onto agricultural Adsorbents, Kinetics and isotherm studies. *Materials Today, Proceedings 28*, 1833–1840. https://doi.10.1016/j.jcis.2019.06.065

25 Chouchane, T., Khireddine, O. & Boukari, A. (2021). Kinetic studies of Ni(II) ions adsorption from aqueous solutions using the blast furnace slag (BF slag). Journal *of Engineering and Applied Science*, *68*, 34. https://doi.10.1186/s44147-021-00039-3

26 Chouchane, T. & Boukari, A. (2022). Impact of influencing parameters on the adsorption of nickel by kaolin in an aqueous medium, *Analytical and Bioanalytical Chemistry Research*, *9*(4), 381–399. https://doi.10.22036/ABCR.2022.325691.1716

27 Fatemeh Hosseini, S., Reza Talaie, M., Aghamiri, S., Khademi, M.H., Gholami, M. & Esfahany, M.N. (2017). Mathematical modeling of rapid temperature swing adsorption, the role of influencing parameters. *Separation and Purification Technology*, *183*, 181–193. https://doi.10.1016/j.seppur.2017.03.017

28 Saranya, M., Srinivasan, L., Gopal Reddi, M.R., Gomathi, T., Sudha, P.N. & Anil, S. (2017). Adsorption Studies of Lead(II) from aqueous solution onto Nanochitosan / Polyurethane / Polypropylene glycol ternary blends. *International Journal of Biological Macromolecules*, *104*(B), 436–1448. https://doi.10.1016/j.ijbiomac.2017.06.004

29 Haerifar, M. & Azizian S. (2012). Fractal-like adsorption kinetics at the solid/solution interface, *The Journal of Physical Chemistry C*, *116*(24), 13111–13119. https://doi.10.1021/jp301261h

30 Zhuang, H., Zhong, Y. & Yang, L. (2020). Adsorption equilibrium and kinetics studies of divalent manganese from phosphoric acid solution by using cationic exchange resin. *Chinese Journal of Chemical Engineering*, *28*(11), 2758-2770. https://doi.10.1016/j.cjche.2020.07.029

31 Ren W., Chang H., Mao T. & Tenga Y. (2019). Planarity effect of polychlorinated biphenyls adsorption by graphenenanomaterials, The influence of graphene characteristics, solution pH and temperature. *Chemical Engineering Journal*, *362*, 160–168. *https://doi.10.1016/j.cej.2019.01.027*

32 Padmavathy, K.S., Madhu, G. & Haseena, P.V.A. (2016). Study on effects of ph, adsorbent dosage, time, initial concentration and adsorption isotherm study for the removal of hexavalent chromium (Cr (VI)) from wastewater by magnetite nanoparticles. *Procedia Technolog*, *24*, 585–594. https://doi.10.1016/j.protcy.2016.05.127

33 Gupta, N. & Sen, R. (2017). Kinetic and equilibrium modelling of Cu (II) adsorption from aqueous solution by chemically modified Groundnut husk (Arachishypogaea). *Journal of Environmental Chemical Engineering*, *5*(5), 4274–4281. https://doi.10.1016/j.jece.2017.07.048

34 Xue, Y., Wu, S. & Zhou, M. (2013). Adsorption characterization of Cu(II) from aqueous solution onto basic oxygen furnace slag. *Chemical Engineering Journal*, *231*, 355–364. https://doi.10.1016/j.cej.2013.07.045

35 Jiang, S., Huang, L., Nguyen, T.A.H., Sik, O.k. Y., Rudolph, V., Yang, H. & Zhang D. (2016). Copper and zinc adsorption by softwood and hardwood biochars under elevated sulphate-induced salinity and acidic pH conditions. *Chemosphere*, *142*, 64–71. https://doi.10.1016/j.chemosphere.2015.06.079

36 Anayurt, R.A., Sari, A. & Tuzen, M. (2009). Equilibrium, thermodynamic and kinetic studies on biosorption of Pb (II) and Cd (II) from aqueous solution by macrofungus (Lactariusscrobiculatus) biomass. *Chemical Engineering Journal*, *151*(1-3), 255–261. https://doi.10.1016/j.cej.2009.03.002

37 Esvandi, Z., Foroutan, R., Peighambardoust, S.J., Akbari, A. & Ramavandi, B. (2020). Uptake of anionic and cationic dyes from water using natural clay and clay/starch/$MnFe_2O_4$ magnetic nanocomposite. *Surfaces and Interfaces*, *21*. https://doi.10.1016/j.surfin.2020.100754

38 Hu, C., Zhu, P., Cai, M., Hu, H. & Fu, Q. (2020). Comparative adsorption of Pb(II), Cu(II) and Cd(II) on chitosan saturated montmorillonite, Kinetic, thermodynamic and equilibrium studies. *Applied Clay Science*, *143*, 320–326. https://doi.10.1016/j.clay.2017.04.005

39 Shafiee, M., Foroutan, R., Fouladi, K., Ahmadlouydarab, M., Ramavandi, B. & Sahebi, S. (2019). Application of oak powder/Fe_3O_4 magnetic composite in toxic metals removal from aqueous solutions. *Advanced Powder Technology*, *30*(3), 544–554. https://doi.10.1016/j.apt.2018.12.006

40 Matsui, Y., Nakao, S., Sakamoto, A., Taniguchi, T., Pan L., Matsushita, T. & Shirasaki, N. (2016). Adsorption capacities of activated carbons for geosmin and 2-methylisoborneol vary with activated carbon particle size, Effects of adsorbent and adsorbate characteristics. *Water Research*, *85*, 95–102. https://doi.10.1016/j.watres.2015.08.017

41 Sekar, M., Sakthi, V. & Rengaraj, S. (2004). Kinetics and equilibrium adsorption study of lead(II) onto activated carbon prepared from coconut shell. *Journal of Colloid and Interface Science*, *279*(2), 307–313. https://doi.10.1016/j.jcis.2004.06.042

42 Ngah, W.W. & Hanafiah, M.A.K.M. (2008). Adsorption of copper on rubber (Heveabrasiliensis) leaf powder, Kinetic, equilibrium and thermodynamic studies. *Biochemical Engineering Journal*, *39*(3), 521–530. https://doi.10.1016/j.bej.2007.11.006

43 Chouchane, T., Chouchane, S., Boukari, A. & Mesalhi, A. (2015). Adsorption of binary mixture «Lead Nickel» by koalin. *Journal of Materials and Environmental Science*, 6(4), 924–941. ISSN: 2028-2508, CODEN: JMESCN

44 Mustapha S., Shuaib D.T., Ndamitso M.M., Etsuyankpa M.B., Sumaila A., Mohammed U.M. & Nasirudeen M.B. (2019). Adsorption isotherm, kinetic and thermodynamic studies for the removal of Pb(II), Cd(II), Zn(II) and Cu(II) ions from aqueous solutions using Albizia lebbeck pods. *Applied Water Science*, 9(6), 142. https://doi.10.1007/s13201-019-1021-x

45 Abdolali, A., Ngo, H.H., Guo, W., Zhou, J.L., Zhang, J., Liang, S., Chang, S.W., Nguyen, D.D. & Liu, Y. (2017). Application of a breakthrough biosorbent for removing heavy metals from synthetic and real wastewaters in a lab-scale continuous fixed-bed column. *Bioresource Technology*, 229, 78–87. https://doi.10.1016/j.biortech.2017.01.016

46 Freundlich, H.M.F. (1906). Over the adsorption in solution. *Journal of Physical Chemistry*, 57, 385–470. https://doi.org/10.1515/zpch-1907-5723

47 Langmuir, I. (1918). The adsorption of gases on plane surfaces of glass, mica and platinum. *Journal of the American Chemical Society*, 40, 1361–1403. https://doi.10.1021/ja02242a004

48 Temkin, M.I. (1940). Kinetics of ammonia synthesis on promoted iron catalysts. *Acta physiochim, URSS, 12,* 327-356.

49 Redlich, O. & Peterson, D.L. (1959). A Useful Adsorption Isotherm. *The Journal of Physical Chemistry, 63*(6), 1024-1024. https://doi.org/10.1021/j150576a611

50 Zahar, M.M.S., Kusin, F.M. & Muhammad, S.N. (2015). Adsorption of manganese in aqueous solution by steel slag. *Procedia Environmental Sciences*, 30, 145–150. https://doi.10.1016/j.proenv.2015.10.026

51 Mert Sivri, F., Hoda, N., Topuz, A., Budama Akpolat, L. & Eroğlu, E. (2022). Adsorption of dimethyl disulfide onto activated carbon cloth. *Turkish Journal of Chemistry*, 46, 859–868. https://doi.10.55730/1300-0527.3374

52 Maran, J.P., Sivakumar, V. & Sridhar, R. (2013). Thirugnanasambandham K. Development of model for barrier and optical properties of tapioca starch based edible films. *Carbohydrate Polymers*, 92(2), 1335–1347.

53 Gandhi, N., Sirisha, D. & Chandra Sekhar, K.B. (2016). Adsorption of Fluoride (F-) from Aqueous Solution by Using Pineapple (Ananas comosus) Peel and Orange (Citrus sinensis) Peel Powders. *International Journal of Environmental Bioremediation & Biodegradation*, 4(2), 55-67. https://doi.10.12691/ijebb-4-2-4

54 Ho, Y.S. & McKay, G. (1999). Pseudo-second order model for sorption processes. *Process Biochemistry*, 34(5), 451–465. https://doi.10.1016/S0032-9592(98)00112-5

55 Su, J., Lin, S., Chen, Z., Megharaj, M. & Naidu, R. (2011). Dechlorination of p-chlorophenol from aqueous solution using bentonite supported Fe/Pd nanoparticles, synthesis, characterization and kinetics, *Desalination*, 280(1–3), 167–73. https://doi.10.1016/j.desal.2011.06.067

56 Bhattacharya, A., Gupta, A., Kaur, A. & Malik, D. (2014). Efficacy of Acinetobacter sp. B9 for simultaneous removal of phenol and hexavalent chromium from co-contaminated system. *Applied Microbiology and Biotechnology*, 98, 9829–9841. https://doi.10.1007/s00253-014-5910-5

57 Alalwan, H.A., Mohammed, M.M., Sultan, A.J., Abbas, M.N., Ibrahim, T.A., Aljaafari H.A.S. & Alminshid A.A. (2021). Adsorption of methyl green stain from aqueous solutions using non-conventional adsorbent media, Isothermal kinetic and thermodynamic studies. *Bioresource Technology Reports*, 14. https://doi.10.1016/j.biteb.2021.100680.

58 Liu, T., Lawluvy, Y., Shi, Y., Ighalo, J.O., He, Y., Zhang, Y. & Yap, P.-S (2022). Adsorption of cadmium and lead from aqueous solution using modified biochar, A review. *Journal of Environmental Chemical Engineering*, 10(1), 106502. https://doi.10.1016/j.jece.2021.106502

59 Chouchane T., Yahi M., Boukari A., Balaska A. & Chouchane S. (2016). Adsorption of the copper in solution by the kaolin. *Journal of Materials and Environmental Science*, 7(8), 2825–2842. ISSN: 2028-2508, CODEN: JMESCN

60 Weber, Jr W.J. & Morriss, C. (1963). Kinetics of adsorption on carbon from solution. *Journal of the Sanitary Engineering Division*, 89(2), 31–60. https://doi.10.1061/JSEDAI.0000430

61 Ofomaja, A.E. (2010). Intraparticle diffusion process for lead(II) biosorption onto mansonia wood sawdust. *Bioresource Technology*, 101(15), 5868–5876. https://doi.10.1016/j.biortech.2010.03.033

62 Gao, R., Liu D., Huang, Y. & Li G. (2020). Preparation of diatomite-modified wood ceramics and the adsorption kinetics of tetracycline. *Ceramics International*, 46(12), 19799–19806. https://doi.10.1016/j.ceramint.2020.05.014

63 Cheung W.H., Szeto Y.S. & McKay G. (2007). Intraparticle diffusion processes during acid dye adsorption onto chitosan. *Bioresource Technology*, 98(15), 2897–2904. https://doi.org/10.1016/j.biortech.2006.09.045

64 Dehbi, A., Dehmani, Y., Omari, H., Lammini, A., Elazhari, K. & Abdallaoui, A. (2019). Hematite iron oxide nanoparticles (α-Fe₂O₃), synthesis and modelling adsorp- tion of malachite green. *Journal of Environmental Chemical Engineering*, 8(1). 103394. https://doi.10.1016/j.jece.2019.103394

65 Fonseca-Correa, R.A., Giraldo, L. & Moreno-Piraján, J.C. (2019). Thermodynamic study of adsorption of nickel ions onto carbon aerogels. *Heliyon*, 5(6), e01789. https://doi.10.1016/j.heliyon.2019.e01789

66 Rajabzadeh, M., Aghaie, H. & Bahrami, H. (2020). Thermodynamic study of Iron (III) removing by the synthesized a-Alumina powder and evaluating the corresponding adsorption isotherm models using Response Surface Method. *Arabian Journal of Chemistry*, 13(2), 4254–4262. https://doi.10.1016/j.arabjc.2019.07.006

67 Kamaraj R. & Vasudevan S. (2016b). Facile one-pot synthesis of nano-zinc hydroxide by electro-dissolution of zinc as a sacrificial anode and the application for adsorption of Th⁴⁺, U⁴⁺, and Ce⁴⁺ from aqueous solution. *Research on Chemical Intermediates*, 42, 4077–4095. https://doi.10.1007/s11164-015-2259-z

68 Kalhori, E.M., Yetilmezsoy, K., Uygur, N., Zarrabi, M. & Shmeis, R.M.A. (2013). Modeling of adsorption of toxic chromium on natural and surface modified lightweight expanded clay aggregate (LECA). *Applied Surface Science*, *287*, 428–442. https://doi.10.1016/j.apsusc.2013.09.175

69 Wang, S., Zhong, S., Zheng, X., Xiao, D., Zheng, L., Yang, Y., Zhang, H., Ai B. & Sheng, Z. (2021). Calcite modification of agricultural waste biochar highly improves the adsorption of Cu(II) from aqueous solutions. *Journal of Environmental Chemical Engineering*, *9*(5). https://doi.10.1016/j.jece.2021.106215

Information about authors*

Chouchane, Toufik (*corresponding author*) — Research Director and research team leader, Leading researcher, Research Center in Industrial Technologies CRTI, P.O. Box 64, Cheraga 16014 Algiers Algeria; e-mail: chouchane_toufik@yahoo.fr; t.chouchane@crti.dz; https://orcid.org/0000-0001-8979-0667

Boukari, Atmane — Searcher, Research Center in Industrial Technologies CRTI, P.O. Box 64, Cheraga 16014 Algiers Algeria; e-mail: a.boukari@crti.dz;

Khireddine, Ouahida — Searcher, Research Center in Industrial Technologies CRTI, P.O. Box 64, Cheraga 16014 Algiers Algeria; e-mail: o.khireddine@crti.dz; https://orcid.org/0000-0001-6890-5744

Chibani, Sana — Searcher, Research Center in Industrial Technologies CRTI, P.O. Box 64, Cheraga 16014 Algiers Algeria; e-mail: s.chibani@crti.dz; https://orcid.org/0000-0002-0339-8320

Chouchane, Sabiha — Professor, Faculty of Sciences, Badji Mokhtar Annaba University, Annaba Algeria; e-mail: chouchsam01@yahoo.fr; https://orcid.org/0000-0003-2587-4372

_____

*The author's name is presented in the order: *Last Name, First and Middle Names*

Arman B. Yeszhanov[1,2*] iD, Ilya V. Korolkov[1,2] iD, Aigerim Kh. Shakayeva[1,2] iD, Lana I. Lissovskaya[1,2] iD, Maxim V. Zdorovets[1,2] iD

[1]*Institute of Nuclear Physics of the Republic of Kazakhstan, Almaty, Kazakhstan;*
[2]*L.N. Gumilyov Eurasian National University, Astana, Kazakhstan*
(*Corresponding author's e-mail: a.yeszhanov@inp.kz)

Preparation of Poly(Ethylene Terephthalate) Track-Etched Membranes for the Separation of Water-Oil Emulsions

Rapid industrial growth in the petrochemical, pharmaceutical, metallurgical and food industries, as well as stormwater that accumulates pollution from the roadway and the territories of motor transport enterprises, gas stations, car washes and other municipal services have led to the formation of a large amount of oily wastewater. Oil-containing wastewater is a multicomponent, multiphase water system and, as a rule, is in a state stabilized by various factors, which greatly complicates their processing. Pollution of water sources with oil-containing compounds leads to negative consequences for both living organisms and human health. Therefore, the need to treat oily wastewater is an urgent problem. In this article, poly(ethylene terephthalate) track-etched membranes (PET TeMs) with pore diameters of ~ 5.1 µm and pore density of $1 \cdot 106$ pore/cm^2 were modified by formation of polyelectrolyte complexes of PET TeMs surface with poly(allylamine) (PAAm) and tested for oil-water separation by using hexadecane/water (at pH=2) and chloroform/water (at pH=2) emulsions. Fourier-transform infrared (FTIR) spectroscopy, scanning electron microscope (SEM), energy dispersive X-ray (EDX) analysis, contact angle measurements were used for membrane characterization. The efficiency of oil-water separation was evaluated by flux measurements. Results showed separation performance of 267 mL/m^2·s for hexadecane/water (pH=2) and 100 mL/m^2·s for chloroform/water (pH=2) at vacuum pressure of 700 mbar.

Keywords: track-etched membranes, oily wastewater, poly(allylamine), hexadecane, chloroform, poly(ethylene terephthalate), water treatment, separation.

Introduction

At present, due to the growth of industrial production, environmental pollution is significantly increasing, as a result, there is a deterioration in the condition of objects of domestic and drinking water use [1–5]. The most common pollution of water bodies (oceans, seas, lakes, rivers, groundwater, glaciers) is oil and its products, such as gasoline, kerosene, oils, fuel oil, etc. In water bodies, oil and oil products create various forms of pollution, such as oil film floating on the water, oil products dissolved or emulsified in water, heavy fractions settled to the bottom, products adsorbed by the bottom soil or the shore of a reservoir. The negative consequences of pollution are showed in various mechanisms of exposure and damage to living organisms, including humans [6–8]. Contaminated industrial oily wastewater can also form explosive and flammable gases and mixtures or toxic substances, therefore, various methods are used to treat and neutralize them [9–11].

Such methods as coagulation [12, 13], flocculation [14, 15], flotation [16, 17], sorption [18], electromagnetic separation [19, 20] can be used to solve the problem of wastewater treatment from oil pollution. Currently, membrane separation methods (ultrafiltration, reverse and direct osmosis) are the most promising for the purification of water-oil emulsions, due to their high energy efficiency, selectivity, and economy [21–24]. Various types of membranes can be used, while track-etched membranes (TeMs) are poorly understood. However, the small thickness, non-tortuosity of pores, extremely narrow pore size distribution, and controlled pore geometry per unit area make them promising for use in the process of separating oil-in-water emulsions [25–29]. In addition to the use of TeMs in water filtration, they can be used in microelectronics, bio- and nanotechnologies (for example, as a means of delivering medicines), medicine, pharmaceutical, food and perfume industries, chemical industry, ecology and other fields [29–31]. Polytetrafluoroethylene (PTFE), polyvinylidene fluoride (PVDF), polypropylene (PP) membranes are mainly

used to separate oil-water emulsions, however, the use of polyethylene terephthalate (PET) TeMs has been little studied [32–35].

Since the surface of PET TeMs has semi-hydrophobic properties, it is necessary to increase hydrophilicity for effective separation of water-oil emulsions [36, 37]. Polyallylamine (PAAm) is a hydrophilic monomer that can be used to separate oil-in-water emulsions. In addition, polyallylamine is available and has not been previously studied for surface modification of PET TeMs. For this purpose, the hydrophilization of oxidized PET TeMs by polyallylamine was studied in this article.

Previously, we have shown that PET TeMs modified by photoinitiated graft polymerization of stearyl methacrylate [38], as well as by soaking in a trichlorooctylsilane solution [39], performed well in the separation of oil-water emulsion. In this paper, we studied a simpler and more energy efficient method of modifying PET TeMs to obtain a pH-responsive surface by soaking in a (poly)allylamine (PAAm) solution for use in the separation of chloroform/water (pH=2) and hexadecane/water (pH=2) systems in various ratios.

Experimental

Materials

Sodium hydroxide, benzophenone, N'N-dimethylformamide, 2-propanol, poly(allylamine hydrochloride), methanol, ethanol, chloroform, hexadecane were purchased from Sigma-Aldrich. Deionized water (18.2 MΩ) was used in all experiments.

Preparation of track-etched membranes (TeMs)

The PET TeMs were prepared as described below. Ion tracks on PET films were generated by irradiation with Kr ions using the accelerator DC-60 (Astana branch of Institute of Nuclear Physics) with an energy of 1.75 MeV/nucleon and ion fluences $1 \cdot 10^6$ ion/cm^2. Then the membranes were processed by photosensitization for 30 min on both sides and were chemically treated in 2.2M NaOH solution at certain periods of time. After chemical etching in a 2.2 M NaOH solution at 85 °C, membranes with a pore diameter of ~5.1 µm were obtained.

Pre-oxidation of PET track-etched membranes in H_2O_2/UV system

PET TeMs were oxidized in a solution of 0.3 M H_2O_2 at pH=3 (HCl). Oxidation was carried out for 180 min under UV lamps (190W). After the oxidation, samples were washed in deionized water and dried [25].

Preparation of poly(allylamine) solution

0.6 g of polyallylamine hydrochloride was neutralized by reaction with 0.224 g of NaOH in 10 ml of methanol. The reaction kept for 24 h at 60 °C. Then solution was separated from the precipitate and 40 ml of ethanol was added. Then, oxidized PET TeMs were kept in a 6 % poly(allylamine) solution for 6h. After that, before determining the contact angle (CA), the samples were additionally kept in a solution of pH=2 and pH=9 for 30 min.

Methods of characterization

For identification of chemical groups before and after modification, FTIR spectra were recorded using FTIR spectrometer InfraLUM® FT-08 with an ATR accessory. The measurements were carried out in the range from 400 to 4000 cm^{-1}, 32 scans with 2 cm^{-1} resolution at a temperature of 21–25 °C.

The water and hexadecane contact angles were measured by using Digital Microscope with 1000× magnification by the sessile drop method at room temperature. Before measuring the contact angle, the samples were soaked for 30 minutes at a certain value of pH. The average drop volumes of water at different pH was 15 µl, the average value of the CA was obtained by measuring the sample in a few different positions.

Hitachi TM3030 scanning electron microscope with a Bruker XFlash MIN SVE microanalysis system at an accelerating voltage of 15 kV was used to study the membrane morphology and elemental composition of the surface before and after modification.

The gas permeability test was used to evaluate the effective pore sizes of the membranes at a pressure drop of 20 kPa according to the method described in [40].

A burst strength procedure was performed to evaluate the mechanical properties of oxidized and modified PET TeMs. Burst strength was evaluated at pressure that damages a circular sample of 1 cm^2 surface area. Burst strength is 0.28 MPa for pristine PET TeMs with pore diameter of ~5.1 µm, and there is a slight decrease to 0.20 MPa after modification with PAAm.

Performance of modified membranes in oil-water separation

The separation of water-oil mixtures with modified PET TeMs was carried out by filtration according to the scheme presented in our previous works [38, 39].

The performance of the obtained membranes was tested out as follows. First, the modified PET TeMs were kept in a pH=2 solution for 30 minutes. Then, the samples were dried and fixed in a vacuum filtration unit. Chloroform and hexadecane at pH=2 were dispersed in a volume of 20 ml in the different ratios (chloroform/water (pH2) = 1:50 and 1:100 (vol.), hexadecane/water (pH2) = 1:50 and 1:100 (vol.)) using an IKA T18 digital ULTRA-TURRAX disperser at a speed of ~ 22000 rpm. Next, the mixture was poured into a glass funnel, a hose was connected from the IKA VACSTAR Control vacuum pump, setting the desired pressure value. Next, the filtration of the mixture was observed by recording the time at which the liquid passes through the pores of the membrane.

The performance (Q) of the filtered water-oil mixture was calculated by Equation (1):

$$Q = \frac{V}{S \cdot T}, \tag{1}$$

where Q — the performance (ml/s·cm^2); S — the filtration area of sample (cm^2); V — the volume of solution (ml); T — the filtration time (s).

The separation efficiency (R, %) was calculated using Equation (2):

$$R = \frac{V_2}{V_1} \cdot 100 \% , \tag{2}$$

where V_2 — the volume of water collected after separation; V_1 — the volume of water in water-in-oil emulsion before separation.

Results and Discussion

To separate "oil-in-water" type of emulsion, it is necessary to obtain membranes with a surface that can pass water and retain an organic medium. With this aim, we proposed a simple method for the formation of a polyelectrolyte complex by negatively charged pre-oxidized PET membrane surface contained carboxylic and hydroxylic groups and polyallylamine. One part of the amino groups of polyallylamine interacts with the membrane surface, and the other part can be ionized by soaking in solutions with acidic pH. For example, after soaking in pH=2, NH$_2$ groups are converted into charged NH$_3^+$ groups, which make the membrane surface hydrophilic, since the charged groups have a dipole.

Figure 1 shows the contact angle (CA) values for water and hexadecane, measured for oxidized PET TeMs and modified PET TeMs-PAAm at different pH value (before measurement, the membranes were soaked in water with the appropriate pH).

Contact angle of water and hexadecane with oxidized PET TeMs,		After modification with PAH (PET TeMs-PAAm) (6 %),	
pH=7	Hexadecane	pH=7	Hexadecane
44°±4	–	68°±4	13°±5
Contact angle of pH = 2 solution and hexadecane PET TeMs-PAAm (6 %),		Contact angle of pH = 9 solution and hexadecane PET TeMs-PAAm (6 %),	
pH=2 (HCl)	Hexadecane	pH=9 (NaOH)	Hexadecane
59°±11	29°±5	72°±5	21°±5
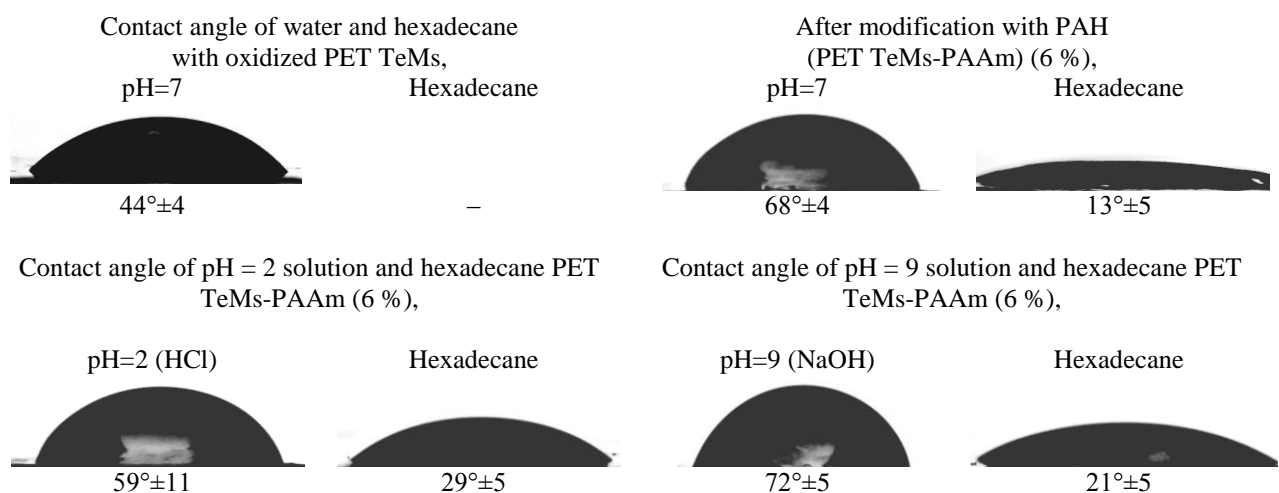
Figure 1 Contact angle of water, hexadecane, solutions pH = 2 and pH = 9
of the oxidized and modified PET TeMs-PAAm

As can be seen in Figure 1, the oxidized PET TeMs have water CA of 44°, however, hexadecane immediately passed through the pores of the membranes and this membrane cannot be used for water-oil separation, while PET TeMs-PAAm at pH=7 showed water CA of 68° and hexadecane of 13°, at pH=2 water CA is 59° and hexadecane of 29°. In this case, a drop of water passes through the pores of the membranes, while

a drop of hexadecane does not pass. This indicates that such membranes can be used to separate water-oil mixtures.

The FTIR spectra of the pristine PET TeMs contain absorption peaks at 2972 cm^{-1} (aromatic C-H), 2910 cm^{-1} (aliphatic C-H), 1716 cm^{-1} (C=O), 1471 cm^{-1} (CH$_2$ vibr.), 1410 cm^{-1} (CH vibr.), 1341 cm^{-1} (CH$_2$), 1246 cm^{-1} (stretching vibrations of C(O)-O bonds), 1019 cm^{-1} (CCC ring), 970 cm^{-1} (O-CH$_2$) [41]. The presence of polyallylamine on the surface causes the appearance of peaks at ~2924 cm^{-1} and ~980 cm^{-1} related to the –CH group, at ~3400 cm^{-1} and 1624 cm^{-1} related to the amino groups –NH$_2$ and –NH (Fig. 2).
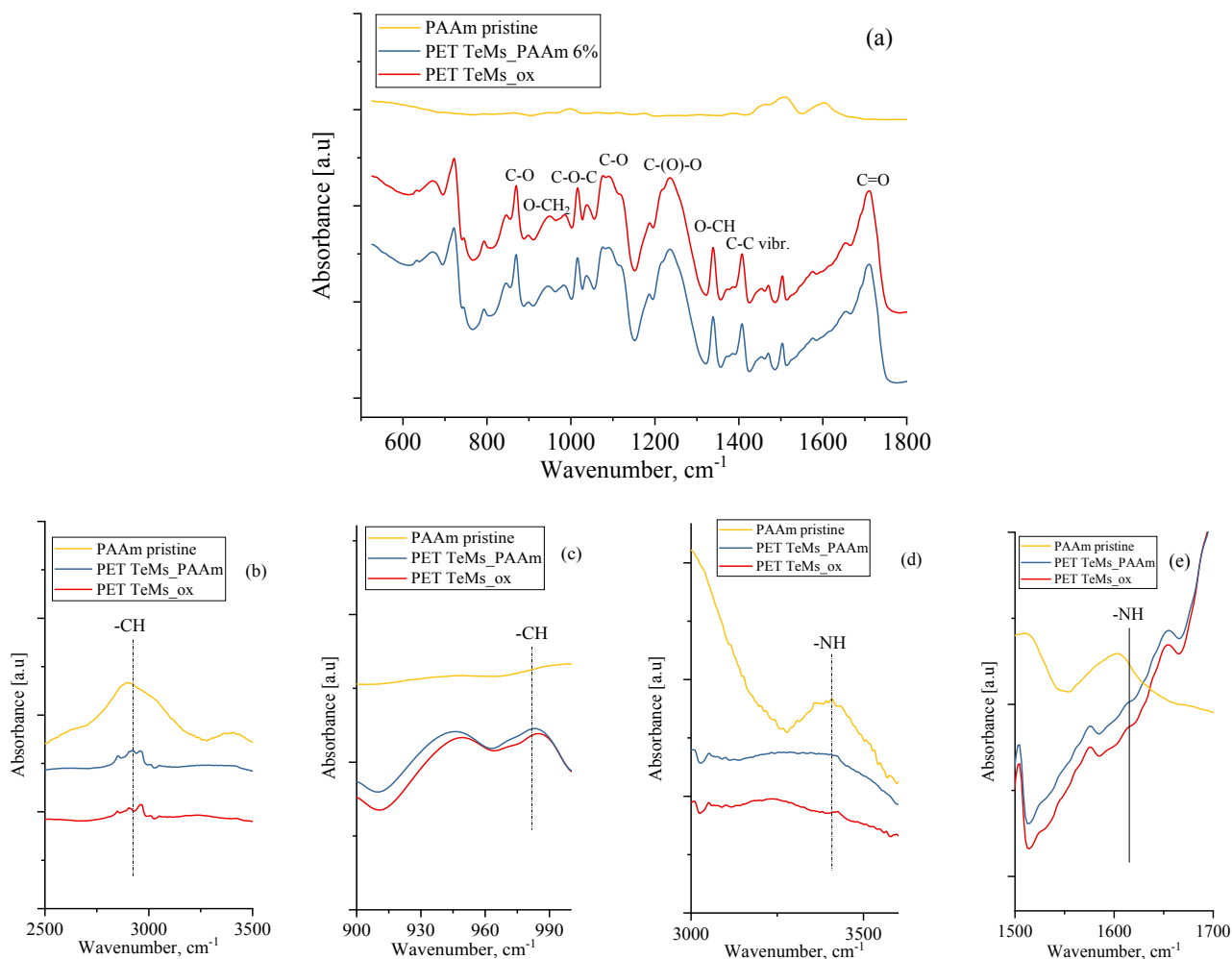

Figure 2. FTIR spectra of oxidized and modified PET TeMs-PAAm in the ranges of:
550–1800 cm^{-1} (*a*), 2500–3500 cm^{-1} (*b*), 900–1000 cm^{-1} (*c*), 3000–3550 cm^{-1} (*d*), 1500–1700 cm^{-1} (*e*)

EDX spectra of the surface of modified PET TeMs-PAAm are shown in Figure 3.
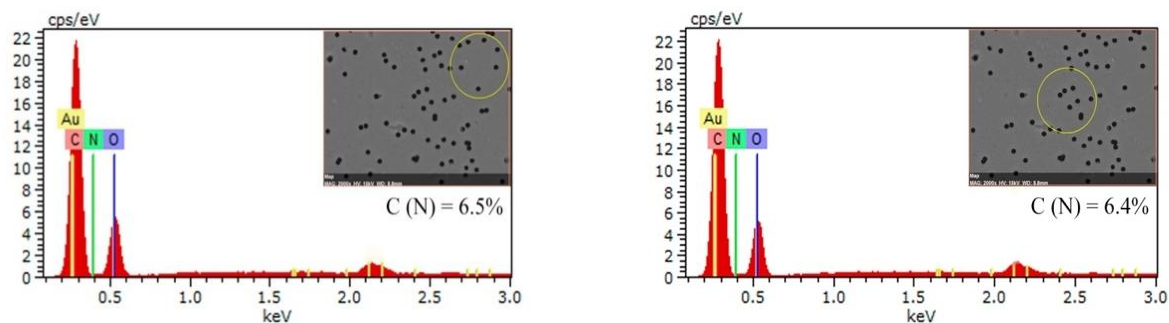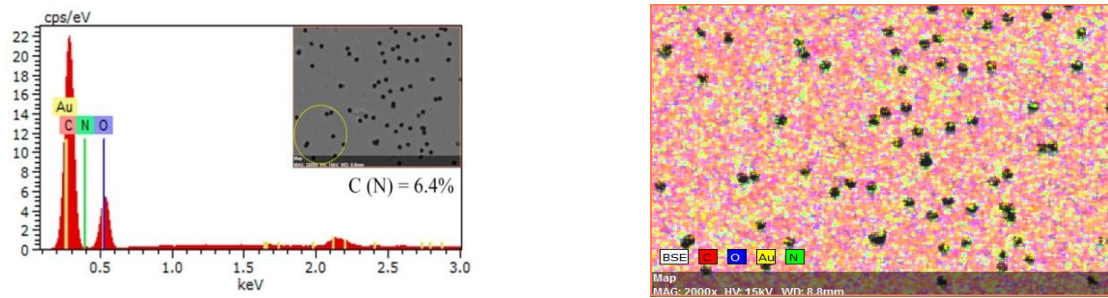
Figure 3. EDX spectra of modified PET TeMs-PAAm (6 %)

Figure 3 shows, that there is a uniform coverage of nitrogen (from PAAm) on the membrane surface. The presence of carbon and oxygen on the surface refers to PET TeMs. It should be noted that the gold content is present due to vacuum deposition prior to SEM analysis. Elemental analysis showed that the average content of nitrogen was ~6.4 %.

Table shows that the effective pore diameter decreases slightly after modification. This is probably due to the formation of a polyallylamine layer on the surface and inner pore walls of PET TeMs.

T a b l e

Characteristics of the pristine (oxidized) and modified PET TeMs-PAAm

Sample	CA (pH=2), °	CA (hexadecane), °	Effective pore diameter, nm
PET TeMs ox.	44°±4	-	5061±19
PET TeMs-PAAm (6 %)	68°±4	13°±5	4862±16
PET TeMs-PAAm (6 %) (after soaking at pH = 2)	59°±11	29°±5	4810±9
PET TeMs-PAAm (6 %) (after soaking at pH = 9)	72°±5	20°±5	4806±15

The results of performance of modified PET TeMs-PAAm using chloroform-water (pH=2) solution (1:50), hexadecane-water (pH=2; 1:100) emulsions are shown in Figure 4. Since the hexadecane/water (pH=2) emulsion is more viscous, their ratio was greater than when using a mixture of chloroform/water (pH=2; 1:100 to 1:50). This resulted in greater performance of the hexadecane/water (pH=2) emulsion compared to chloroform/water (pH=2) at different pressures. At a pressure of 700 mbar, the average performance of chloroform/water (pH=2) was 100 ml/s·cm^2, and the mixture of hexadecane/water (pH=2) was 267 ml/s·cm^2. The performance was studied over 10 cycles, the surface stability of the modified layer of the membrane was observed. The degree of separation in almost all cases was more than 98 % and only slight decrease in flux was detected. Moreover, CA was controlled after each cycle of separation, which showed changes in CA within the standard error. Thus, a simple and effective method for the modification of PET TeMs with a pH-responsive surface has been developed, which can be successfully applied to separate oil-water emulsions.
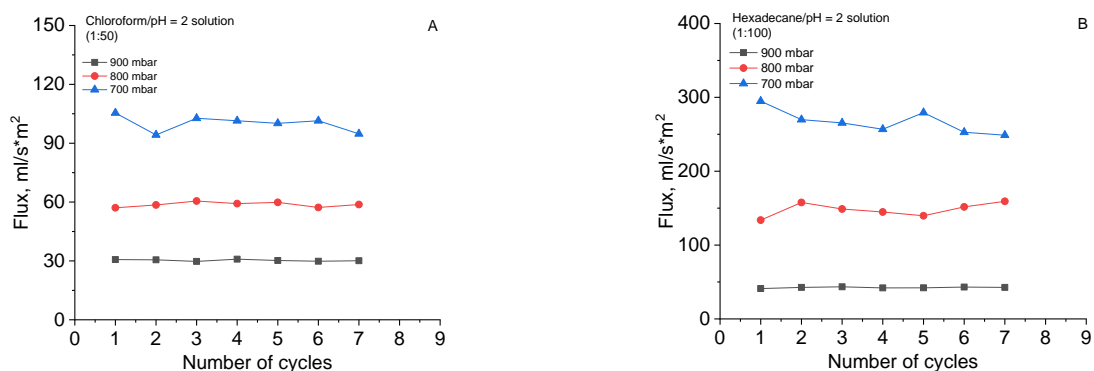
Figure 4. The fluxes of modified PET TeMs-PAAm with pore density 1·10^6 for chlorofom/pH=2 solution (1:50) and hexadecane/pH=2 solution (1:100) oil-water emulsions after each cycle at different pressure

Conclusions

In this study, we presented the results of modification of PET TeMs by soaking in poly(allylamine) solution. The effect of pH solutions and monomer concentrations providing the highest contact angle for hexadecane was studied. PET TeMs with pore diameters 5.1 μm ($1 \cdot 10^6$ pore density) were tested in oil-water emulsion separation by using hexadecane/water (pH=2; 1:100) and chloroform/water (pH=2; 1:50) as a model emulsions. Membranes showed that the average performance of chloroform/water (pH=2) was 100 ml/s·cm^2, and the mixture of hexadecane/water (pH=2) was 267 ml/s·cm^2.

Acknowledgments

References

1   Zhang, N., Yang, X., Wang, Y., Qi, Y., Zhang, Y., Luo, J., Cui, P. & Jiang, W. (2022). A review on oil/water emulsion separation membrane material. *Journal of Environmental Chemical Engineering*, *10*(2), 107257. https://doi.org/10.1016/j.jece.2022.107257

2   Baig, U., Faizan, M. & Sajid, M. (2020). Multifunctional membranes with super-wetting characteristics for oil-water separation and removal of hazardous environmental pollutants from water: A review. *Advances in Colloid and Interface Science*, *285*, 102276. https://doi.org/10.1016/j.cis.2020.102276

3   Dansawad, P., Yang, Y., Li, X., Shang, X., Li, Y., Guo, Z., Qing, Y., Zhao, S., You, S. & Li, W. (2022). Smart membranes for oil/water emulsions separation: A review. *Advanced Membranes*, *2*, 100039. https://doi.org/10.1016/j.advmem.2022.100039

4   Shan, W., Du, J., Yang, K., Ren, T., Wan, D. & Pu, H. (2021). Superhydrophobic and superoleophilic polystyrene/carbon nanotubes foam for oil/water separation. *Journal of Environmental Chemical Engineering*, *9*(5), 106038. https://doi.org/10.1016/j.jece.2021.106038

5   Li, J. J., Zhou, Y. N. & Luo, Z. H. (2017). Mussel-inspired V-shaped copolymer coating for intelligent oil/water separation. *Chemical Engineering Journal*, *322*, 693–701. https://doi.org/10.1016/j.cej.2017.04.074

6   Yin, Z., Yuan, F., Li, M., Xue, M., Zhou, D., Chen, Y., Liu, X., Luo, Y., Hong, Z., Xie, C. & Ou, J. (2021). Self-cleaning, underwater writable, heat-insulated and photocatalytic cellulose membrane for high-efficient oil/water separation and removal of hazardous organic pollutants. *Progress in Organic Coatings*, *157*, 106311. https://doi.org/10.1016/j.porgcoat.2021.106311

7   Sarbatly, R., Krishnaiah, D. & Kamin, Z. (2016). A review of polymer nanofibres by electrospinning and their application in oil–water separation for cleaning up marine oil spills. *Marine Pollution Bulletin*, *106*(1–2), 8–16. https://doi.org/10.1016/j.marpolbul.2016.03.037

8   Askin, S., Kizil, S. & Bulbul Sonmez, H. (2021). Creating of highly hydrophobic sorbent with fluoroalkyl silane cross-linker for efficient oil-water separation. *Reactive and Functional Polymers*, *167*, 105002. https://doi.org/10.1016/j.reactfunctpolym.2021.105002

9   Heidari, M. K., Fouladi, M., Sooreh, H. A. & Tavakoli, O. (2022). Superhydrophobic and super-oleophilic natural sponge sorbent for crude oil/water separation. *Journal of Water Process Engineering*, *48*, 102783. https://doi.org/10.1016/j.jwpe.2022.102783

10   Cui, W., Fan, T., Li, Y., Wang, X., Liu, X., Lu, C. J., Ramakrishna, S. & Long, Y. Z. (2022). Robust functional Janus nanofibrous membranes for efficient harsh environmental air filtration and oil/water separation. *Journal of Membrane Science*, *663*, 121018. https://doi.org/10.1016/j.memsci.2022.121018

11   Tjale, L., Richards, H., Mahlangu, O. & Nthunya, L. N. (2022). Silica nanoparticle modified polysulfone/polypropylene membrane for separation of oil-water emulsions. *Results in Engineering*, *16*, 100623. https://doi.org/10.1016/j.rineng.2022.100623

12   Almojjly, A., Johnson, D., Oatley-Radcliffe, D. L. & Hilal, N. (2018). Removal of oil from oil-water emulsion by hybrid coagulation/sand filter as pre-treatment. *Journal of Water Process Engineering*, *26*, 17–27. https://doi.org/10.1016/j.jwpe.2018.09.004

13   Jang, D., Lee, J. & Jang, A. (2023). Impact of pre-coagulation on the ceramic membrane process during oil-water emulsion separation: Fouling behavior and mechanism. *Chemosphere*, *313*, 137596. https://doi.org/10.1016/j.chemosphere.2022.137596

14   Dickinson, E. (2019). Strategies to control and inhibit the flocculation of protein-stabilized oil-in-water emulsions. *Food Hydrocolloids*, *96*, 209–223. https://doi.org/10.1016/j.foodhyd.2019.05.021

15   Wang, X., Lin, Q., Ye, A., Han, J. & Singh, H. (2019). Flocculation of oil-in-water emulsions stabilised by milk protein ingredients under gastric conditions: Impact on in vitro intestinal lipid digestion. *Food Hydrocolloids*, *88*, 272–282. https://doi.org/10.1016/j.foodhyd.2018.10.001

16   Qiu, Y., Mao, Z., Sun, K., Zhang, L., Yang, L., Qian, Y. & Lei, T. (2022). Cost-efficient clean flotation of amorphous graphite using water-in-oil kerosene emulsion as a novel collector. *Advanced Powder Technology*, *33*(11), 103770. https://doi.org/10.1016/j.apt.2022.103770

17 Gao, J., Tong, Z., Bu, X., Bilal, M., Hu, Y., Ni, C. & Xie, G. (2023). Effect of water-in-oil and oil-in-water with Span 80 on coal flotation. *Fuel*, *337*(December 2022), 127145. https://doi.org/10.1016/j.fuel.2022.127145

18 Akpomie, K. G. & Conradie, J. (2021). Ultrasonic aided sorption of oil from oil-in-water emulsion onto oleophilic natural organic-silver nanocomposite. *Chemical Engineering Research and Design*, *165*, 12–24. https://doi.org/10.1016/j.cherd.2020.10.019

19 Kovaleva, L., Zinnatullin, R., Musin, A., Gabdrafikov, A., Sultanguzhin, R. & Kireev, V. (2021). Influence of radio-frequency and microwave electromagnetic treatment on water-in-oil emulsion separation. *Colloids and Surfaces A: Physicochemical and Engineering Aspects*, *614*(December 2020). https://doi.org/10.1016/j.colsurfa.2020.126081

20 Telmadarreie, T., Berton, P. & Bryant, S. L. (2022). Treatment of water-in-oil emulsions produced by thermal oil recovery techniques: Review of methods and challenges. *Fuel*, *330*(July), 125551. https://doi.org/10.1016/j.fuel.2022.125551

21 Al-Husaini, I. S., Yusoff, A. R. M. & Wirzal, M. D. H. (2022). Efficient oil/water separation using superhydrophilic polyethersulfone electrospun nanofibrous ultrafiltration membranes. *Journal of Environmental Chemical Engineering*, *10*(5), 108341. https://doi.org/10.1016/j.jece.2022.108341

22 Matindi, C. N., Hu, M., Kadanyo, S., Ly, Q. V., Gumbi, N. N., Dlamini, D. S., Li, J., Hu, Y., Cui, Z. & Li, J. (2021). Tailoring the morphology of polyethersulfone/sulfonated polysulfone ultrafiltration membranes for highly efficient separation of oil-in-water emulsions using TiO2 nanoparticles. *Journal of Membrane Science*, *620*, 118868. https://doi.org/10.1016/j.memsci.2020.118868

23 da Silva, J. R. P., Merçon, F., da Silva, L. F., Andrade Cerqueira, A., Braz Ximango, P. & da Costa Marques, M. R. (2015). Evaluation of electrocoagulation as pre-treatment of oil emulsions, followed by reverse osmosis. *Journal of Water Process Engineering*, *8*, 126–135. https://doi.org/10.1016/j.jwpe.2015.09.009

24 Zhang, H., Fang, S., Ye, C., Wang, M., Cheng, H., Wen, H. & Meng, X. (2008). Treatment of waste filature oil/water emulsion by combined demulsification and reverse osmosis. *Separation and Purification Technology*, *63*(2), 264–268. https://doi.org/10.1016/j.seppur.2008.05.012

25 Korolkov, I. V., Mashentseva, A. A., Güven, O., Niyazova, D. T., Barsbay, M. & Zdorovets, M. V. (2014). The effect of oxidizing agents/systems on the properties of track-etched PET membranes. *Polymer Degradation and Stability*, *107*, 150–157. https://doi.org/10.1016/j.polymdegradstab.2014.05.008

26 Mashentseva, A., Borgekov, D., Kislitsin, S., Zdorovets, M. & Migunova, A. (2015). Comparative catalytic activity of PET track-etched membranes with embedded silver and gold nanotubes. *Nuclear Instruments and Methods in Physics Research Section B: Beam Interactions with Materials and Atoms*, *365*, 70–74. https://doi.org/10.1016/j.nimb.2015.07.063

27 Korolkov, I. V., Mashentseva, A. A., Güven, O., Gorin, Y. G. & Zdorovets, M. V. (2018). Protein fouling of modified microporous PET track-etched membranes. *Radiation Physics and Chemistry*, *151*, 141–148. https://doi.org/10.1016/j.radphyschem.2018.06.007

28 Korolkov, I. V., Yeszhanov, A. B., Zdorovets, M. V., Gorin, Y. G., Güven, O., Dosmagambetova, S. S., Khlebnikov, N. A., Serkov, K. V., Krasnopyorova, M. V., Milts, O. S. & Zheltov, D. A. (2019). Modification of PET ion track membranes for membrane distillation of low-level liquid radioactive wastes and salt solutions. *Separation and Purification Technology*, *227*, 115694. https://doi.org/10.1016/j.seppur.2019.115694

29 Zhumanazar, N., Korolkov, I. V., Yeszhanov, A. B., Shlimas, D. I. & Zdorovets, M. V. (2022). Electrochemical detection of lead and cadmium ions in water by sensors based on modified track-etched membranes. *Sensors and Actuators A: Physical*, 114094. https://doi.org/10.1016/j.sna.2022.114094

30 Chakarvarti, S. K. (2016). Track-Etch Membranes as Tools for Template Synthesis of Nano-/Microstructures and Devices. *Encyclopedia of Membranes*, 1910–1924. https://doi.org/10.1007/978-3-662-44324-8_473

31 Wang, C., Wu, Z., Liu, B., Zhang, P., Lu, J., Li, J., Zou, P., Li, T., Fu, Y., Chen, R., Zhang, L., Fu, Q. & Li, C. (2021). Track-etched membrane microplate and smartphone immunosensing for SARS-CoV-2 neutralizing antibody. *Biosensors and Bioelectronics*, *192*, 113550. https://doi.org/10.1016/j.bios.2021.113550

32 Zhao, J., Liu, H., Xue, P., Tian, S., Lv, Z., Wang, R., Lv, X. & Sun, S. (2023). High-performance PVDF water treatment membrane based on IL-Na+MMT for simultaneous removal of dyes and oil-water emulsions. *Journal of Environmental Chemical Engineering*, *11*(1), 109093. https://doi.org/10.1016/j.jece.2022.109093

33 Xu, J., Cui, J., Sun, H., Wu, Y., Xue, C., Xie, A. & Li, C. (2023). Facile preparation of hydrophilic PVDF membrane via tea polyphenols modification for efficient oil-water emulsion separation. *Colloids and Surfaces A: Physicochemical and Engineering Aspects*, *657*, 130639. https://doi.org/10.1016/j.colsurfa.2022.130639

34 Venault, A., Jumao-as-Leyba, A. J., Chou, F. C., Bouyer, D., Lin, I. J., Wei, T. C. & Chang, Y. (2016). Design of near-superhydrophobic/superoleophilic PVDF and PP membranes for the gravity-driven breaking of water-in-oil emulsions. *Journal of the Taiwan Institute of Chemical Engineers*, *65*, 459–471. https://doi.org/10.1016/j.jtice.2016.05.011

35 Yu, Y., Zhang, L., Li, X., Ye, J. & Meng, J. (2023). Multifunctionalization of PTFE membrane surface for biofouling resistance and oil/water separation performance improvement. *Journal of Environmental Chemical Engineering*, *11*(1), 109158. https://doi.org/10.1016/j.jece.2022.109158

36 Zhang, Y., Ying, L., Wang, Z., Wang, Y., Xu, Q. & Li, C. (2021). Unexpected hydrophobic to hydrophilic transition of PET fabric treated in a deep eutectic solvent of choline chloride and oxalic acid. *Polymer*, *234*, 124246. https://doi.org/10.1016/j.polym.2021.124246

37 Kolahchi, A. R., Ajji, A. & Carreau, P. J. (2015). Improvement of PET surface hydrophilicity and roughness through blending *AIP Conference Proceedings*, *1664*, 30001. https://doi.org/10.1063/1.4918391

38 Yeszhanov, A. B., Muslimova, I. B., Melnikova, G. B., Petrovskaya, A. S., Seitbayev, A. S., Chizhik, S. A., Zhappar, N. K., Korolkov, I. V., Güven, O. & Zdorovets, M. V. (2022). Graft Polymerization of Stearyl Methacrylate on PET Track-Etched Membranes for Oil–Water Separation. *Polymers*, *14*(15). https://doi.org/10.3390/polym14153015

39 Korolkov, I. V., Narmukhamedova, A. R., Melnikova, G. B., Muslimova, I. B., Yeszhanov, A. B., Zhatkanbayeva, Z. K., Chizhik, S. A. & Zdorovets, M. V. (2021). Preparation of Hydrophobic PET Track-Etched Membranes for Separation of Oil–Water Emulsion. *Membranes 2021, Vol. 11, Page 637*, *11*(8), 637. https://doi.org/10.3390/membranes11080637

40 Mulder, M. (1996). Transport in Membranes. *Basic Principles of Membrane Technology*, 210–279. https://doi.org/10.1007/978-94-009-1766-8_5

41 Yeszhanov, A.B. & Dosmagambetova S.S. (2020). Phenol solutions treatment by using hydrophobized track-etched membranes. *Bulletin of the University of Karaganda — Chemistry, 3(*99*)*, 99–109. https://doi.org/10.31489/2020Ch3/99-109

Information about authors*

Yeszhanov, Arman Bakhytzhanovich (*corresponding author*) — Master degree of chemistry science, junior scientific researcher, Astana Branch of the Institute of Nuclear Physics, Abylay khana 2/1, 010000, Astana, Kazakhstan; e-mail: a.yeszhanov@inp.kz; https://orcid.org/0000-0002-1328-8678

Korolkov, Ilya Vladimirovich — PhD, senior researcher, Institute of Nuclear Physics, Abylay khana 2/1, 010000, Astana, Kazakhstan; e-mail: i.korolkov@inp.kz; https://orcid.org/0000-0002-0766-2803

Zdorovets, Maxim Vladimirovich — Candidate of Physical and Mathematical Sciences, Director, Astana Branch of the Institute of Nuclear Physics, Abylay khana 2/1, 010000, Astana, Kazakhstan; e-mail: mzdorovets@inp.kz; https://orcid.org/0000-0003-2992-1375

Shakayeva, Aigerim Khairatovna — engineer, Astana Branch of the Institute of Nuclear Physics, Abylay khana 2/1, 010000, Astana, Kazakhstan; e-mail: aigerim_19-03@mail.ru; https://orcid.org/0000-0001-5731-1115

Lissovskaya, Lana Igorevna — engineer, Astana Branch of the Institute of Nuclear Physics, Abylay khana 2/1, 010000, Astana, Kazakhstan; e-mail: ms.defrance@mail.ru; https://orcid.org/0000-0002-3894-6366

_____

*The author's name is presented in the order: *Last Name, First and Middle Names*

Sairagul Tyanakh[1]* , Murzabek I. Baikenov[1] , Feng-Yun Ma[2], Vitaliy N. Fomin[1] , Gulzhan G. Baikenova[3] , Anuar S. Ashimhanov [1], Raikhan S. Seitzhan[1]

[1]Karagandy University of the name of academician E.A. Buketov, Karaganda, Kazakhstan
[2]Xinjiang University, Xinjiang, China
[3]Karaganda Economic University of Kazpotrebsoyuz, Karaganda, Kazakhstan
(*Corresponding author's e-mail: saika_8989@mail.ru)

Determination of Optimal Conditions for Catalytic Hydrogenation of Oil Sludge (Atasu-Alashankou)

The optimal conditions of catalytic hydrogenation of oil sludge (Atasu-Alashankou) and the change in the kinematic viscosity of the fraction to 350℃ from the studied factors using the method of probabilistic-deterministic planning were experimentally determined. During the hydrogenation process of oil sludge, the maximum total yield of light fractions reached 62.1 %, and the kinematic viscosity decreased from 2.2 to 1.2 mm^2/s. It was established the initial hydrogen pressure and the amount of added nanocatalyst microsilicate with cobalt (catalyst 1) have the greatest influence on the yield of the middle fraction from oil sludge under experimental conditions. It was shown that catalyst 1 increases the yield of diesel fraction components during the hydrogenation process of oil sludge. For the first time, we established the individual and group chemical composition of the fraction up to 350℃ before and after processing. The use of nanocatalyst 1 in amounts of 1.2–1.5 % led to an increase in the yield of the fraction up to 350℃ and diesel fraction components. This is due to the yield of paraffinic hydrocarbons increasing from 57.6 (initial fraction) to 80.7 %, as well as a decrease in aromatic hydrocarbons from 14.1 to 12.9 % and polycyclic aromatic hydrocarbons from 9.56 to 4.3 %.

Keywords: optimization, oil sludge, catalyst, microsilicate, cobalt, nickel, viscosity, hydrogenation, optimization, correlation, matrix.

Introduction

Oil-producing and oil-refining manufactories, as well as oil transported through pipelines, are sources of environmental pollution. Oil-containing waste called oil sludge, the most common type of industrial waste. For every ton of oil produced, 7 tons of sludge are generated [1–2]. Its approximate composition is: water (from 30 to 80 %), oil products (from 10 to 50 %), and solid inclusions (from 1 to 40 %) [1–2]. The organic part of the waste in oil sludge is distributed as follows: 7–10 % are oil hydrocarbons, 5–10 % are in an emulsified and dissolved state, and the remaining hydrocarbons are on the surface of the oil sludge in the form of a film [1–2]. The inorganic part of the oil sludge contains silicon and iron oxides (sand, corrosion products), a small amount (less than 1 %) of aluminum, sodium, and zinc [3].

Currently, known technologies for oil sludge processing contain physical, mechanical, and biological methods [4]. However, none of the listed methods are efficient in processing and disposal of oil sludge and still causing damage to the environment. We propose a combined method for oil sludge processing, which includes preliminary fractionation in order to remove mechanical impurities and solid inclusions, followed by catalytic hydrogenation of the obtained wide fraction.

The oil-containing sludge (Atasu-Alashankou), which formed during the transportation of Kazakh oil through the pipelines, contains drilling mud, used oil, emulsified solid particles, and crude oil. In the studies [5–6], the results of the optimal conditions determination for electro-hydraulic treatment of oil are given.

Literature analysis showed there is no data available for catalytic hydrogenation of oil sludge. Previously, the optimal conditions for electrohydraulic treatment of oil sludge were determined in [5–6]. The data obtained in [5–6] were used for the process of hydrogenation of a wide fraction of oil sludge in the presence of a nanocatalyst.

The purpose of the work is to determine the dominant factors (temperature, initial hydrogen pressure, duration of the experiment, number of nanocatalysts added) for the yield and quality of the individual

chemical composition of the target hydrogenate during destructive hydrogenation of a wide fraction of oil sludge.

The literature does not contain data on the use of factor planning of the experiment to study the process of catalytic hydrogenation of oil sludge and the determination of parameters for hydrogenation of oil sludge, which makes this study relevant.

Experimental

The object of research for experimental work in order to determine the optimal conditions and kinetic parameters of oil sludge hydrogenation was the raw material obtained during the transportation of oil through the pipelines of the KazTransOil company in the West Kazakhstan oil fields of the Republic of Kazakhstan. The physicochemical characteristics of the oil sludge (Atasu-Alashankoou) and the method of synthesis of the nanocatalyst are presented in [6].

Physical and chemical characteristics of oil sludge (Atasu-Alashankou): density — 0.87 g/cm^3, viscosity — 30 cSt, ash content A — 0.36 %, C — 72.3 %, H — 11.1 %, N — 0.1 %, O — 16.1 %. The atomic ratio of hydrogen to carbon in oil sludge is 1.8.

The microsilicate is used as a carrier and catalyst — a product of the Karaganda silicon plant Tau-Ken.temir LLP.

The individual and quantitative chemical composition of the starting microsilicate was determined by X-ray spectral analysis. Content of components, %: SiO_2 — 95.5; TiO_2 — 0.02; Al_2O_3 — <0.95; Fe_2O_3 — <1.0; CaO — 0.5; MgO — 0.4; MnO — 0.04; P_2O_5 — 0.06; K_2O — <0.1; Na_2O — 0.3.

The starting microsilicate was pre-ground, then samples with a particle size of 0.1 mm were taken by sieve analysis. The initial microsilicate was leached using a 20 % hydrochloric acid solution to remove alkali and alkaline earth metals. Chemical composition of the initial microsilicate after leaching by X-ray — spectral analysis is following, %: SiO_2 — 97.439; TiO_2 — 0.023; Al_2O_3 — <0.95; Fe_2O_3 — <1.0; CaO — 0.414; MgO — 0.304; MnO — 0.033; P_2O_5 — 0.057; K_2O — <0.1; Na_2O — 0.276.

The given data demonstrate the chemical composition of the starting microsilicate and after leaching changed almost slightly.

For the preparation of nanocatalysts, we used the method of impregnating the catalyst support with the active substance followed by calcination. Impregnation was carried out by immersing the support (leached microsilicate) in a 1.5 % salt solution of $Ni(NO_3)_2 \cdot 6H_2O$ and $Co(NO_3)_2 \cdot 6H_2O$. Impregnated support (microsilicate) with solutions of nickel nitrate and cobalt nitrate of microsilicate (20 g) was heated for 2 hours at 80–90 °C temperature, and the prepared samples were dried at 105 °C temperature for 2 hours. Then, the obtained catalysts were calcined in a muffle furnace at 650 °C temperature for 2 hours. 2 catalyst samples were prepared to study the effect on thermal decomposition of nickel oxide, cobalt oxide and iron oxide: Sample 1 (microsilicate + Co 1.5 % + oil sludge, particle size 0.1 mm), Sample 2 (microsilicate + Ni 1.5 % + oil sludge, particle size 0.1 mm). Previously, we carried out work [7] with a nanocatalyst obtained by the impregnation method; the particle size of the starting microsilicate and prepared catalyst samples was established using a laser *Nano-S90* particle size detector.

After the oil sludge processing, the hydrogenate was fractionated up to 350 °C. The individual and group chemical composition of the fraction up to 350 °C was determined by the chromato-mass-spectrometry on the HP 5890/5972 MSD device (Agilent, USA).

Identification of substances was performed by the NIST98 mass spectral database.

Chromatography conditions:

Column: DB-5, 30 m × 0.2 mm × 0.5 μm.

Carrier-gas: helium, 0.8 ml/min.

Thermostat: 50 °C — 4 min;

50–150 °C — 10 °C/min

150–300 °C — 20 °C/min

300 °C — 4 min

Atomizer: 250 °C

Atomizer: 200 °C

The determination of the kinematic viscosity of the fraction up to 350 °C, obtained in the process of hydrogenation of oil sludge of the studied samples was carried out at a temperature of 30 °C by the automatic viscometer SYD-265B-1 (P.R. China).

Results and Discussion

A probability-deterministic design of experiment has been used in order to determine the optimal conditions for the hydrogenation of oil sludge [5]. The dependence of the yield of the middle fraction and the changes in the kinematic viscosity of the wide fraction in of oil sludge on the studied factors usually is nonlinear. Hence, it is more rational to use design methods that are based on the Protodyakonov-Malyshev nonlinear multiple correlation to process statistical data [8–10]. The authors [8–10] proposed an empirical formula for multiple nonlinear correlations in the form of a power one less than the number of partial functions:

$$Y_p = \frac{\overset{n}{\underset{i=1}{P}} Y_i}{Y_{mid}^{n-1}}, \tag{1}$$

where Y_{mid} — the total average of all considered values of the generalized function; Y_p — generalized functions of $X1$, $X2…$ factors; Y_i — partial function; n — number of partial functions (factors); $P_{i=1}^{n}$ — product of all the partial functions.

Experimental work was conducted in order to develop a mathematical model of the process of catalytic hydrogenation of oil sludge using a matrix of the design of experiment compiled by the Protod'yakonov-Malyshov method [8–12]. The obtained results were processed by the probabilistic-deterministic design of experiment program (PDDoE) [10–12]. The sequence of program operations is reduced to finding the partial dependence of the yield of the middle fraction and the change in the viscosity of the middle fraction obtained from the oil sludge.

As a result equations of the multiple correlation R [8–9] and tr coefficient [8–9] have been obtained. The selected intervals and levels of changes in factors, the matrix of the design of experiment of oil sludge hydrogenation are given in Tables 1 and 2.

T a b l e   1

Levels and intervals of the variation of the studied factors

Factors	Levels			
	1	2	3	4
X_1, amount of the catalyst 1 added to the oil sludge (catalyst 1 — microcatalyst coated with 1.5 % Co)	0.001	1.0	1.5	2.0
X_2, initial hydrogen pressure, P=MPa	0.0	3.0	4.0	5.0
X_3, temperature, T °C	350	370	390	410
X_4, duration, min	0.0	3.0	45	60
X_5, amount of the catalyst 2 added to the oil sludge (catalyst 2 — microcatalyst coated with 1.5 % Ni)	2.0	1.5	1.0	0.001

T a b l e   2

Matrix of the 5-factor 4-level design of experiment

№	X_1	X_2	X_3	X_4	X_5	$Y_{exp,}$ yield of the fraction up to 350 °C, %	$Y_{P,}$ yield of the fraction up to 350 °C, %	$Y_{exp,}$ kinematic viscosity of the fraction up to 350 °C, mm*s^{-2}	$Y_{P,}$ kinematic viscosity of the fraction up to 350 °C, mm*s^{-2}
1	2	3	4	5	6	7	8	9	10
1	1	1	1	1	1	32.2	34.4	1.38	1.38
2	2	2	2	2	1	68.4	61.4	1.34	1.34
3	3	3	3	3	1	62.05	66.4	1.335	1.33
4	4	4	4	4	1	74.8	71.4	1.37	1.37
5	1	2	3	4	2	72.13	63.58	1.33	1.34
6	2	1	4	3	2	64.85	62.12	1.44	1.51
7	3	4	1	2	2	55.64	49.96	1.29	1.25
8	4	3	2	1	2	48.12	50.86	1.291	1.25
9	1	3	4	2	3	48.72	58.93	1.345	1.37

1	2	3	4	5	6	7	8	9	10
10	2	4	3	1	3	48.54	50.78	1.26	1.21
11	3	1	2	4	3	61.36	66.68	1.28	1.24
12	4	2	1	3	3	51.29	50.40	1.4	1.46
13	1	4	2	3	4	51.63	50.33	1.18	1.14
14	2	3	1	4	4	48.22	53.58	1.25	1.23
15	3	2	4	1	4	64.87	59.36	1.42	1.50
16	4	1	3	2	4	61.76	62.83	1.29	1.27

Table 3 and 4 show the calculated values of the partial functions for the yield of the fraction up to 350 °C from oil sludge in the process of hydrogenation and the viscosity changes caused by various conditions of the process.

T a b l e 3

Calculated values of the partial functions for Y_P

Functions	Levels				Total average	R	t_r
	1	2	3	4			
$Y_1 = -3.192x^2 + 10.615x + 51.005$	51.17	57.5025	60.98	59.005	57.164	0.95	13.6
$Y_2 = -0.5993x^2 + 3.0321x + 55.444$	55.44	59.22	57.874	55.66	57.05	0.99	69.64
$Y_3 = 0.266x - 43.911$	46.83	57.37	61.12	63.32	57.164	0.88	5.6
$Y_4 = 55.619x^{0.0203}$	48.43	58.63	57.455	64.14	57.164	0.8594	6.63
$Y_5 = 3.4762x^2 - 4.756x + 56.214$	56.2	57.48	59.51	60.61	58.45	0.48	0.87

T a b l e 4

Calculated values of the partial functions for Y_P

Functions	Levels				Significance		
	1	2	3	4	Total average	R	t_r
$Y_1 = 1.309 + 0.01467X_1$	1.31	1.32	1.33	1.34	1.325	0.99	441.5879
$Y_2 = -0.01524X_2^2 + 0.07196X_2 + 1.3$	1.30	1.37	1.35	1.27	1.325	0.98	45.5597
$Y_3 = 6.081*10^{-5}X_3^2 - 0.04461X_3 + 9.464$	1.30	1.27	1.32	1.39	1.325	0.96	22.2321
$Y_4 = 6.122*10^{-5}X_4^2 - 0.00555X_4 + 1.413$	1.41	1.31	1.26	1.30	1.325	0.95	14.0683
$Y_5 = 1.285 + 0.03549X_5$	1.35	1.33	1.32	1.28	1.325	0.99	3535.1803

As a result of processing the experimental data, partial functions for the catalytic hydrogenation of oil sludge and the change in viscosity of the middle fraction were obtained. Point graphs are presented in Figures 1 and 2. They are generalized by the Protoiakonov-Malychev equation. The significance of partial and generalized dependencies was tested using the coefficient of nonlinear multiple correlation R [8–9] and its significance t_r for the 95 % confidence level [8–9]. It turned out that out of all the partial dependencies, only 5 (on the amount of added catalyst 2 (X_5)) was insignificant. Therefore, it was not included in the generalized equation (2).

$$Y_{P_1} = 57.14^{-3} y_1 y_2 y_3 y_4 ; R = 0.70 \ t_r = 5.0. \tag{2}$$

$$Y_{P_2} = \begin{pmatrix} (1.309 + 0.01467X_1) + (-0.01524X_2^2 + 0.07196X_2 + 1.3) + (6.081 \cdot 10^{-5}X_3^2 - \\ -0.04461X_3 + 9.464) + (6.122 \cdot 10^{-5}X_4^2 - 0.00555X_4 + 1.413) + (1.285 + 0.03549X_5) \end{pmatrix} - 5.3004; \tag{3}$$
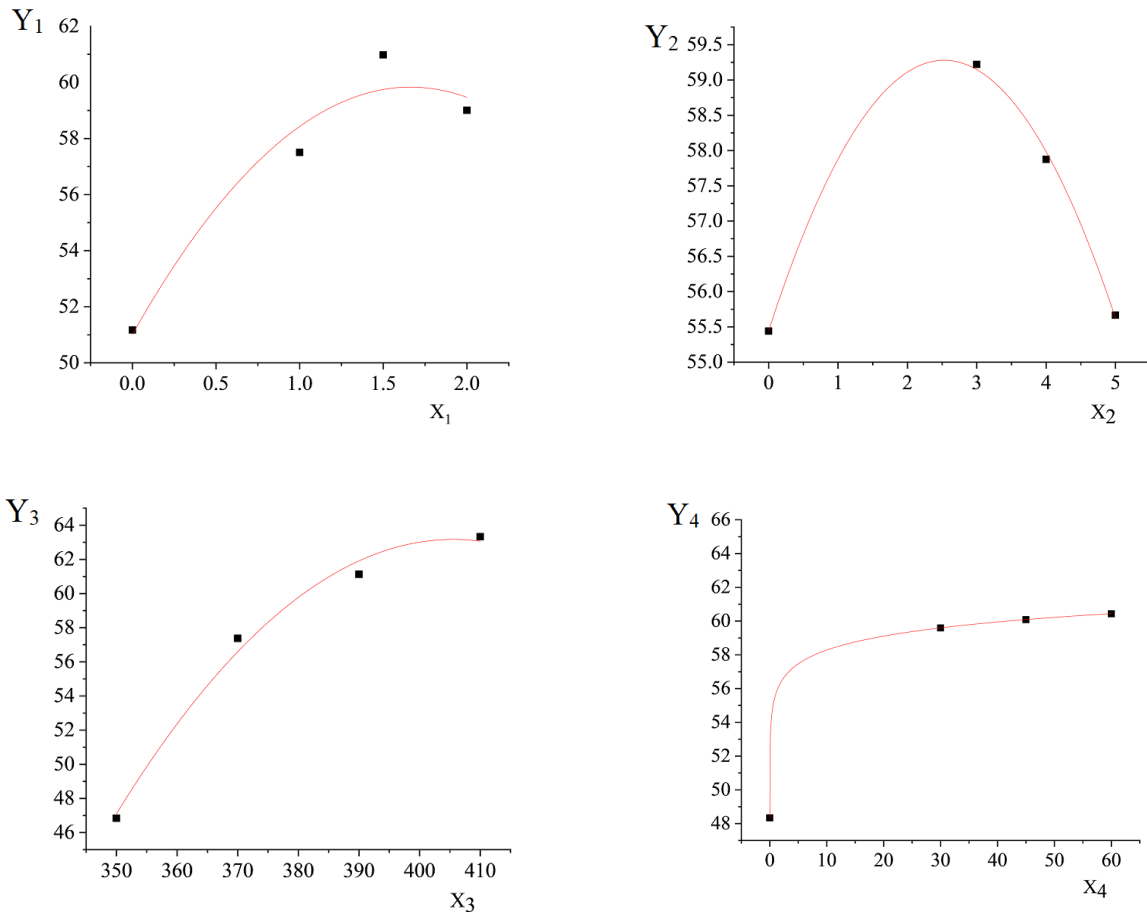
$$R = 0.66; t_r = 3.7.$$

x_1 — amount of catalyst 1 added to the oil sludge; x_2 — initial hydrogen pressure, MPa; x_3 — temperature, T°C; x_4 — duration, min.)

Figure 1. Partial dependencies of catalytic hydrogenation of the oil sludge
($Y_{1,2,3,4}$ — yield of the raction up to 350 °C, %)
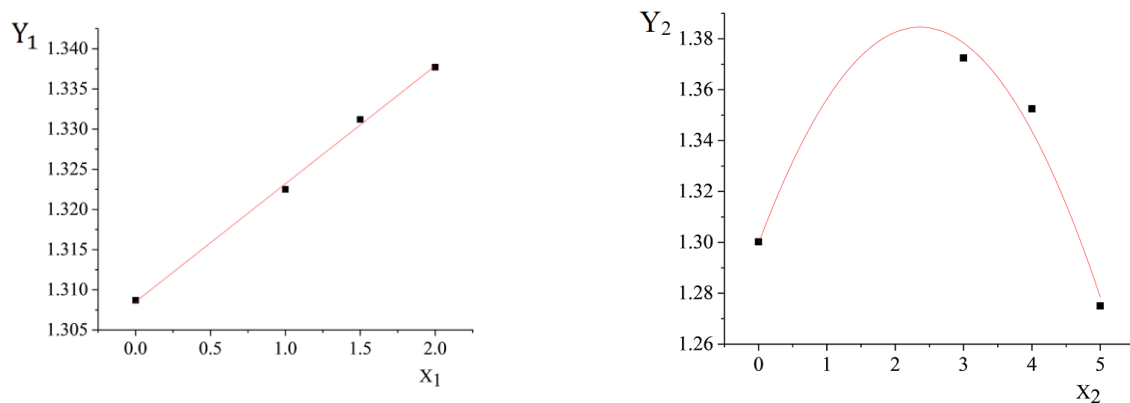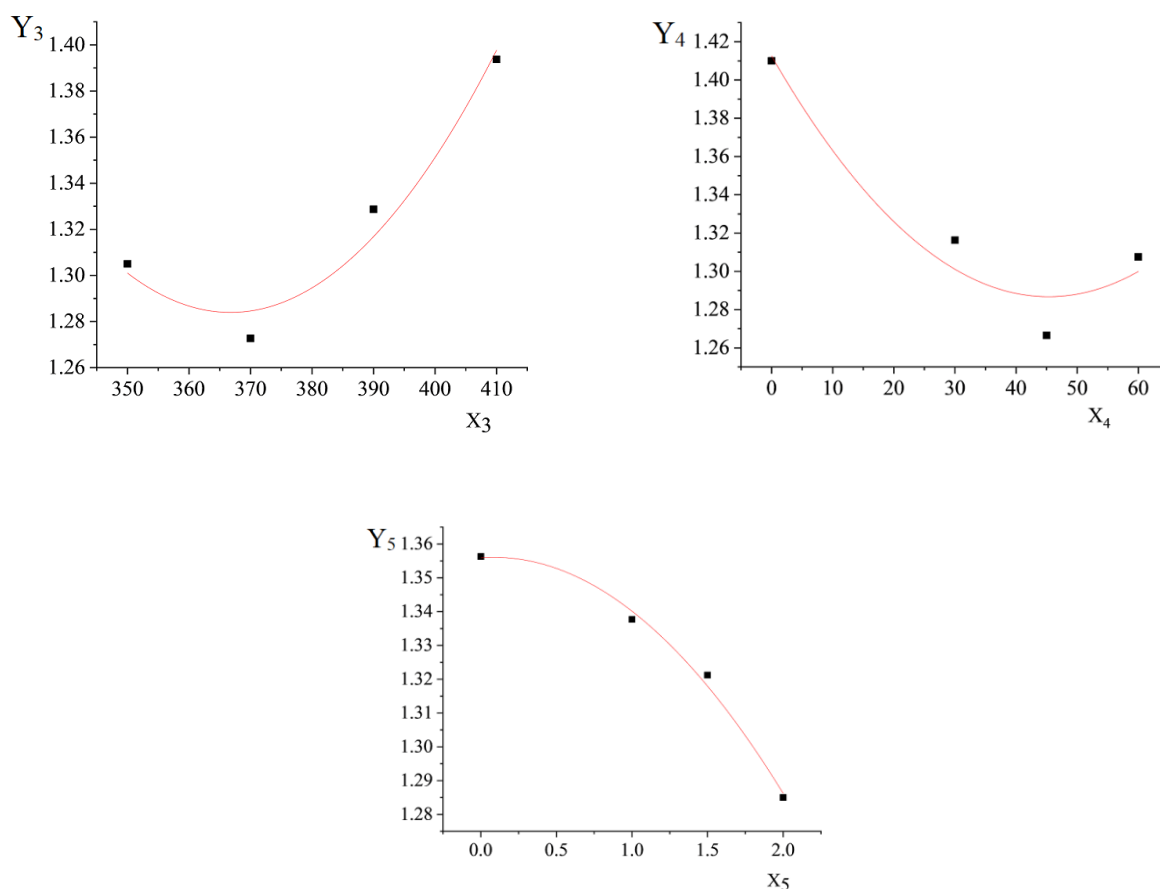
Figure 2. Partial dependencies of changes in kinematic viscosity of the fraction up to 350 °C on the various factors
(x_1 — amount of catalyst 1 added to the oil sludge; x_2 — initial hydrogen pressure, MPa;
x_3 — temperature, T°C; x_4 — duration, min; x_5 — amount of catalyst 2 added to the oil sludge)

The generalized equations (2) and (3) were tested for significance by comparing the results of that with experimental data. The generalized Protodyakonov-Malyshev equations (2), (3) are adequate for all R and t_r response functions. The obtained particular equations can be used both for optimizing the process and for technological modeling of the process of catalytic hydrogenation of oil sludge in enlarged laboratory conditions. It follows from these data that under experimental conditions the initial hydrogen pressure and the amount of catalyst 1 added have the greatest effect on the average fraction yield from the oil sludge. The change in the kinematic viscosity of the middle fraction is affected by the amount of catalyst 1 added to the oil sludge and the process temperature.

The generalized multivariate equation of fraction yield before 350 °C from oil sludge is

$$Y_P = \frac{(-3.192x^2 + 10.615x + 51.005)(-0.5993x^2 + 3.0321x + 55.444)}{(0.266x - 43.911)^{-1}(55.619x^{0.0203})^{-1}57.14^3}, \tag{4}$$

at standard deviation of 1.81 %. The calculation of this equation (4) showed at 410 °C temperature, the process time was 60 minutes, the amount of nanocatalyst 1 (cobalt-supported microsilicate 1.5 %) to be added was 2 %; initial hydrogen pressure 5.0 MPa, the amount of nanocatalyst 2 added (nickel-supported microsilicate 1.5 %) — 2 % is respectively 71.4 %.

The generalized multivariate equation changes in the kinematic viscosity of the middle 350 °C fraction from oil sludge is

$$Y_P = \frac{(1.309 + 0.01467X_1)(-0.01524X_2^2 + 0.07196X_2 + 1.3)6.081*10^{-5}X_3^2 - 0.04461X_3 + 9.464}{(6.122*10^{-5}X_4^2 - 0.00555X_4 + 1.413)^{-1}(1.285 + 0.03549X_5)^{-1}1.325^4} \tag{5}$$

at standard deviation of 0.014 %. Calculation of this equation (5) showed that at 410℃ temperature, process time was 0.0 min, the amount of nanocatalyst 1 (cobalt-supported microsilicate 1.5 %) to be added

was 1.5 %; initial hydrogen pressure 3.0 MPa, the amount of nanocatalyst 2 added (nickel-supported microsilicate 1.5 %) — 0.000 % was respectively 1.50 %.

Based on the conducted experimental research, the following optimal conditions have been established:

a) Yield of the middle fraction of oil sludge: amount of added nanocatalyst 1 — 1.2–1.5 %; initial hydrogen pressure 2.5–3 MPa; temperature 400–410 °C; process duration 50-60 minutes.

b) Change in the kinematic viscosity of the middle fraction obtained from oil sludge: amount of added nanocatalyst 1 — 0.5 %; initial hydrogen pressure 4.5 MPa; temperature — 370 °C; process duration — 45 minutes; amount of added catalyst 2 — 2.0 %.

During hydrogenation of oil sludge, the maximum total yield of light fractions of 62.1 % and a decrease in the kinematic viscosity value from 2.2 to 1.2 mm^2/s were achieved.

This is explained by changing the content of aromatic hydrocarbons in the initial fraction to 350 °C — 14.08 % (individual chemical composition is presented: toluene — 3.07 % and others), paraffinic hydrocarbons — 57.6 (individual chemical composition is presented: heptane — 3.02, 1-nonadecene — 1.52 %, decane — 7.59, dodecane — 4.51, heptadecane — 3.19, hexadecane — 2.37, nonane — 5.96, octadecane — 6.87 and others), unsaturated hydrocarbons — 15.7 % (individual chemical composition is presented: 1-decene — 1.09, 1-hexadecene — 1.1 and others), naphthenic hydrocarbons — 35.97 % (individual chemical composition is presented: 1.3-dimethylcyclohexane — 2.57 %, 1-ethyl-3-methylcyclohexane — 1.25 %, cyclododecane — 0.56 %, cyclohexane, (1-methylpropyl) — 4.89 % and others), polyaromatic hydrocarbons — 9.56 % (individual chemical composition is presented: naphthalene, 1,4,6-trimethyl — 1.33, naphthalene, 2,7-dimethyl — 2.59 %, naphthalene, decahydro-2-methyl — 1.8 % and others).

The group and individual chemical composition of the hydrogenate of the fraction with the end of boiling 350 °C obtained during catalytic hydrogenation from oil sludge is characterized by the following composition: aromatic hydrocarbons — 12.94 % (individual chemical composition is represented by: toluene — 1.97 %, benzene, 1-ethyl-3-methyl — 1.68 % and others); paraffinic hydrocarbons — 80.72 % (individual chemical composition is next: 1-heptadecene — 0.36 %, 2-Bromo dodecane — 0.22 %, Decane — 9.89 %, Dodecane — 11.47 %, Heptadecane — 5.27 %, Heptane — 2.65 %, Hexadecane — 5.36 % and others); unsaturated hydrocarbons — 9.31 % (individual chemical composition is represented by: 1-Decene, 5-methyl- — 0.19 %, 1-Tridecene — 0.65 %, 2,4-Hexadiene — 2.33 %, 2-Heptene — 0.14 %, 2-Tetradecene — 0.66 %, 3-Dodecene — 1.16 % and others); naphthenic hydrocarbons — 34.48 % (individual chemical composition is following: Cyclodecane — 0.4 %, Cyclodecane — 1.18 %, 0.33 Cyclododecane, ethyl- — 0.8 %, Cyclohexane, (1-methylpropyl)- — 0.12 %, Cyclohexane, (2-methylpropyl)- — 1.36 %, Cyclohexane, 1,1,2,3-tetramethyl- — 0.34 %, Cyclohexane, 1,2,3-tri-methyl- — 2.18 % and others); polyaromatic hydrocarbons — 4.27 % (individual chemical composition is represented by: Naphthalene, 1,2,3,4-tetrahydro-6- — 0.25 %, Naphthalene, 1,4-dimethyl- — 0.26 %, Naphthalene, 2,3,6-trimethyl- — 0.39 %, Naphthalene, 2,7-dimethyl- — 0.84 %, Naphthalene, decahydro-2-methyl- — 2.58 % and others); iso-Alkanes — 41.19 % (individual chemical composition is presented: Octane, 2,6-dimethyl- — 0.23 %, Nonane, 4-methyl- — 0.22 %, Nonane, 2,6-dimethyl- — 0.57 %, Decane, 5-methyl- — 0.33 %, Decane, 4-methyl- — 0.18 %, Decane, 2-methyl- — 0.41 %, Heptane, 3-ethyl-2-methyl- — 0.58 %, Undecane, 2-methyl- — 1.78 %, Undecane, 2,6-dimethyl- — 1.87 %, Tridecane, 2-methyl- — 1.23 % and others).

The obtained fraction composition of the hydrogenate up to 350 °C shows that the use of the nanocatalyst 1 in small amounts of 1.2-1.5 % allows increasing the yield of the fraction to 350 °C and components of the diesel fraction.

Conclusions

Thus, by the use of probabilistic-deterministic design of experiment, optimal conditions for the process of the oil sludge hydrogenation in the presence of a nanocatalyst (cobalt-coated microsilicate) and the change in the viscosity of the middle fraction from various factors were determined. In our hydrogenation conditions, the maximum total yield of light fractions (62.1 %) was achieved. It was established in the experimental conditions, the initial hydrogen pressure and the amount of added nanocatalyst, cobalt-coated microsilicate (catalyst 1), have the greatest effect on the yield of the middle fraction from oil sludge. It has been shown the catalyst 1 also increases the yield of diesel fraction components.

References

1 Dzhusupbekova, U. Zh., Chernyakova R. M., Kaiynbaeva R. A., Sultanbaeva G. Sh., & Agataeva A. A. (2020). Metody obezvrezhivanie i utilizatsii nefteshlamov [Methods for the neutralization and disposal of oil sludge]. *Khimicheskii zhurnal Kazakhstana – Chemical Journal of Kazakhstan, 1*, 15–30.

2 Marinaite, I. I., Sorokovikova, L. M., Sinyukovich, V. N. et al. Oil Products in Lake Baikal and Its Tributaries. *Water Resour 49*, 458–466 (2022). https://doi.org/10.1134/S0097807822030101

3 Lyubimenko, V. A., Frolov, V. I., Krestovnikov, M. P., & Lesin, S. V. (2016). Mathematical Modeling of Thermal Cracking of Oil Sludge Activated by Electromagnetic Radiation. Chemistry and Technology of Fuels and Oils, *52*(2), 134–140. https://doi.org/10.1007/s10553-016-0683-4

4 Barshabayeva, A., Balpanova, N.; Aitbekova, D.; Baikenov, M.; Aubakirov, Y.; Khalikova, Z. S.; Tusipkhan, A.; Tulebaeva, B.; Gulzhan, T. (2022). The influence of various factors on nanocatalyst activity during benzothiophene hydrogenation. *Applied Sciences 12*, 24, 12792. https://doi.org/10.3390/app122412792

5 Satybaldin, A., Tusipkhan, A., Seitzhan, R., Tyanakh, S., Baikenova, G., Karabekova, D., & Baikenov, M. (2021). Determination of optimal conditions for processing oil bottom sediments using electrohydraulic effect. *Eastern-European Journal of Enterprise Technologies, 5*(6 (113), 3–38. https://doi.org/10.15587/1729-4061.2021.241763

6 Tyanakh S., Baykenov M. I., Tusipkhan A., Aitbekova D. E., Balpanova N. Zh., Ma Fan Yung (2022). Kinetic study of the thermolysis process of oil sludge (Atasu-Alashankou) with nickel, cobalt and iron deposited on microsilicate. *Eastern-European Journal of Enterprise Technologies 2*(6 (116), 19–24. https://doi.org/10.15587/1729-4061.2022.255666

7 Tyanakh, S., Baikenov, M. I., Gulmaliev, A.M., Ma, Feng-Yun, Musina, G., Khamitova, T. O., & Bolatbay, A. N. (2022). Kinetics of thermolysis of a low-temperature tar in the presence of a catalyzer agent with deposited metals. *Bulletin of the University of Karaganda Chemistry, 108(4)*, 89-98. https://doi.org/10.31489/2022Ch4/4-22-19

8 Malyshev, V. P., Katkeeva, G. L., Zubrina Yu. S., et al. (2017). Razrabotka kompleksnoi veroiatnostno-determinirovannoi modeli protsessov izmelcheniia i flotatsi. kompleksnoe ispolzovanie mineralnogo syria [Development of a complex probabilistic-deterministic model of grinding and flotation processes]. Complex use of mineral raw materials [in Russian].

9 Malyshev, V. P. (1994). Veroiatnostno-determinirovannoe planirovanie eksperimenta [Probabilistic-deterministic mapping]. Almaty: Nauka [in Russian].

10 Fomin, V. N., Kovaleva, A. A., & Aldabergenova, S. K. (2017). Using multivariate variables in probabilistic-deterministic design of experiments. *Bulletin of the University of Karaganda Chemistry*, *3*(87), 91–100. https://doi.org/0.31489/2017Ch3/91-100

11 Beliaev, S. V., & Malyshev, V. P. (2008). Puti razvitiia veroiatnostno-determinirovannogo planirovaniia eksperimenta [Ways of stochastic-determinated design of experiments development]. *Informatsionnye tekhnologii v mineralnosyrevom komplekse — Information technologies in the mineral-raw complex, 8,* Almaty [in Russian].

12 Fomin, V. N., Aynabaev, A. A., Kaykenov, D. A., Sadyrbekov, D. T., Aldabergenova, S. K., Turovets, M. A., & Kelesbek, N. K. (2021). Optimization of coal tar gas chromatography conditions using probabilistic-deterministic design of experiment. *Bulletin of the University of Karaganda — Chemistry, 104*(4), 39-46. https://doi.org/10.31489/2021Ch4/39-46

Information about authors*

Tyanakh, Sairagul (*corresponding author*) — Master, doctoral student Karagandy University of the name of academician E.A. Buketov, Universitetskaya street, 28, 100024, Karaganda, Kazakhstan; e-mail: saika_8989@mail.ru; https://orcid.org/0000-0001-5343-4695;

Baikenov, Murzabek Ispolovich — Doctor of Chemical Sciences, Professor, Karagandy University of the name of academician E.A. Buketov, Universitetskaya street, 28, 100024, Karagandy, Kazakhstan; e-mail: murzabek_b@mail.ru; https://orcid.org/0000-0002-8703-0397;

Ma, Feng-Yun — PhD, Professor, Xinjiang University, Urumqi, Nan Min Lu street, 666, Xinjiang Uygur Autonomous Region (XUAR) People's Republic of China (PCR); e-mail: ma_fy@126.com;

Fomin, Vitaliy Nikolaevich — Candidate of chemical sciences, head of LEP "PCMI" of Karagandy University of the name of academician E.A. Buketov, Universitetskaya street, 28, 100024, Karaganda, Kazakhstan; e-mail: vitaliynikolaevich.fomin@mail.ru; https://orcid.org/0000-0002-2182-2885;

Baikenova, Gulzhan Gausilevna — Doctor of Chemical Sciences, Professor, Karaganda Economic University of Kazpotrebsoyuz, Karaganda, Kazakhstan; South Ural State University, Chelyabinsk, Russia; e-mail: murzabek_b@mail.ru; https://orcid.org/0000-0002-2816-3341;

Ashimhanov, Anuar Sultanovich — Master student, Karagandy University of the name of academician E.A. Buketov, Universitetskaya street, 28, 100024, Karaganda, Kazakhstan; e-mail: anuar.ashimhanov@mail.ru; https://orcid.org/0000-0001-9509-6495;

Seitzhan, Raikhan Sarsenkyzy — Master of engineering sciences, Karagandy University of the name of academician E.A. Buketov, Universitetskaya street, 28, 100024, Karaganda, Kazakhstan; e-mail: Raikhan.Seitzhan@mail.ru; https://orcid.org/0000-0003-2362-6383

_____

*The author's name is presented in the order: *Last Name, First and Middle Names*